Fire risk management of Li-ion batteries

Department of Chemical Engineering Materials and Environment

PhD in Chemical Processes for the Industry and the Environment

XXXVI cycle

Dr. Sofia Ubaldi

Supervisor

Prof. Ing. Paola Russo

Academic Years 2022-2023

Abstract

The growing use of Lithium-ion batteries (LIBs) in various applications, such as small portable devices, electric vehicles (EVs), and energy storage systems (ESS), is due to the better performance of these devices compared to the previous technologies available. However, this phenomenon also begins to show the disadvantages of these devices. In fact, the number of accidents along the whole life chain of LIBs, from production to use up to final disposal, is increasing. The fire hazard of LIBs, in terms of severity of the fire and products emitted, is strictly dependent on the internal chemical composition, the kind of abuse that was perpetrated, and the voltage stored inside the battery, the so-called state of charge (SoC). For this reason, it is important to evaluate the thermal stability of LIBs and to investigate not only the exothermic reactions that occur inside them, but also the composition and the properties of the hazardous products. These are both gases, such as hydrofluoric acid (HF) and carbon monoxide (CO), and solid, such as metallic aerosol particles, that can be released during the thermal runaway (TR).

The thermal stability of LIBs is defined by the reactions that can occur inside the cell between the internal components and the activation of the safety devices, such as the current interrupt device (CID), during a TR. It is possible to define three key events that occur during the abuse of LIBs: the activation of the safety devices, the venting, and the TR. Unfortunately, there are many variables that influence the temperatures and the products emitted during those events, such as the internal composition, the SoC, and the kind of abuse, which is either electrical, mechanical, or thermal. Even if the internal composition is one of the fundamental parameters, it is difficult to find it as it is only partially expressed on the product safety data sheets (SDS) and even a slight change in the composition, such as the electrolyte composition, may affect the final products ejected. The limitation of the available studies on TR behavior is due to the fact that they all refer to works conducted on different cells characteristics, such as geometry, chemistry, SoC, with a different instrumentation to perpetrate the abuse, such as direct flame or electrical heating, and different sensors and techniques to characterize the products.

In this optic, the present work was carried out with the aim of standardizing the information on the thermal stability and the TR behavior of different cylindrical cells (18650) currently available on the market, i.e., Lithium Nickel Cobalt Aluminum Oxide (NCA), Lithium Titanate Oxide (LTO), Lithium Iron Phosphate (LFP), Lithium Nickel Manganese Cobalt Oxide (NMC), and Lithium Cobalt Oxide (LCO). To do that, thermal stability tests, according to UN regulation, and thermal abuse tests were conducted in the same reactor and under the same conditions of abuse to have comparable data for the different chemistries analyzed. The test conditions were optimized to define a unique procedure to monitor all the parameters and to analyze the collected products, such as gases, solid, and liquid. So, for each thermal abuse test it was possible to obtain information on the temperature and pressure of the key events, the composition and the

quantification of the emitted gaseous species by continuous Fourier-transform infrared spectroscopy (FT-IR) analysis, and the composition of the solid and liquid emissions by FT-IR, scanning electron microscope coupled with energy dispersive X-ray analysis (SEM-EDX), inductively coupled plasma (ICP) and atomic absorption spectroscopy (AAS) analyses. The physicochemical analyses were also applied to LIBs (as received) to have a more precise characterization of the internal composition.

In this way it is possible to compare the data obtained and highlight common or significantly different behaviors for the LIBs depending on the internal chemistry, not only in terms of the temperature reached during the TR, but also by the dangerousness of the substances that can be emitted and dispersed in the environment in the short and long term. In fact, these released substances can have extremely dangerous effects on the environment and the people: be it intervening firefighters or people involved in the accident. In the case of gases, the concentration values of toxic species, such as CO and HF, during the TR must be evaluated. In fact, these substances can present toxic effects even in case of short-term exposures (30 min); therefore, already in the stages of the fire. In the case of solid particle emissions, however, the parameters to be evaluated are the composition and the particle size. The composition can be traced back to the transition metals used to make the cathode, while the dimensions of the particulate can vary in the respirable range. A graphical abstract of the present work is reported in Figure 1.
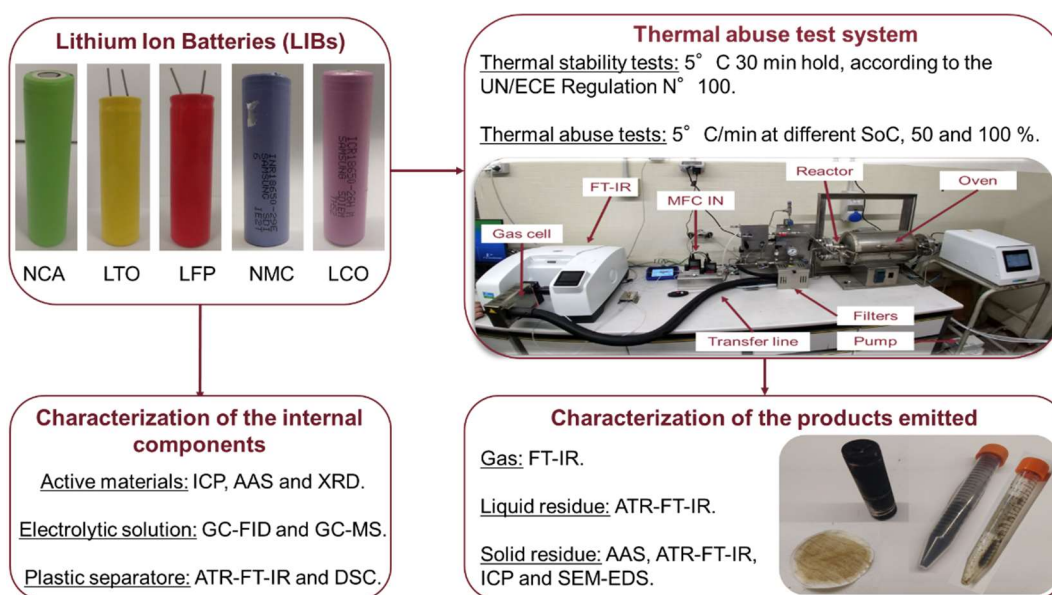

Figure 1: Characterization techniques and lab test apparatus for thermal abuse tests.

With time other issues started to emerge, such as the search for new materials to enhance the LIBs performance and the choice of a fire extinguishing agent to suppress a LIB fire. The research is now aimed to increase performance by optimizing the active materials of LIBs, using for example nanomaterials (NMs). The main NMs currently under investigation are silicon (Si), graphite, and LTO. However, even if the NMs show an increase in performance, the reduction in the size may induce a more explosive behavior

and more toxic effects on humans and environment. For this reason, during the doctorate the research activity was also focused on the evaluation of the physicochemical characteristics, explosivity risk, and ecotoxicity of pure materials and nanomaterials for LIBs. These assessments can lead to a more informed choice of manufacturer when selecting materials for cell assembly. A graphical abstract of this topic is reported in Figure 2.
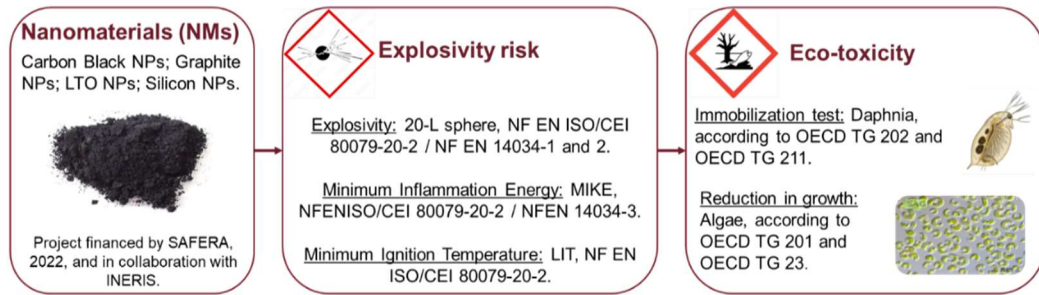

Figure 2: Characterization methods for explosivity and ecotoxicity of nanomaterials (NMs) for electrodes.

Another aspect that is also investigated in this thesis is the choice of an extinguishing agent to suppress a LIB fire which is much debated due to the different nature of this fire. In fact, the extinguishing agents currently used are classified based on the type of fire, but the LIB fire is not actually classified neither as a fire of flammable liquids neither of metals nor of electrical equipment.

Preliminary fire tests were conducted to evaluate the effectiveness of three different extinguishing agents, at different physical states. A unique procedure was also defined for the collection of both solid and liquid residues, remaining after the fire that must be characterized to be properly treated and disposed of, to limit the risk of release of dangerous substances into the environment. The graphical abstract of this subject is reported in Figure 3.
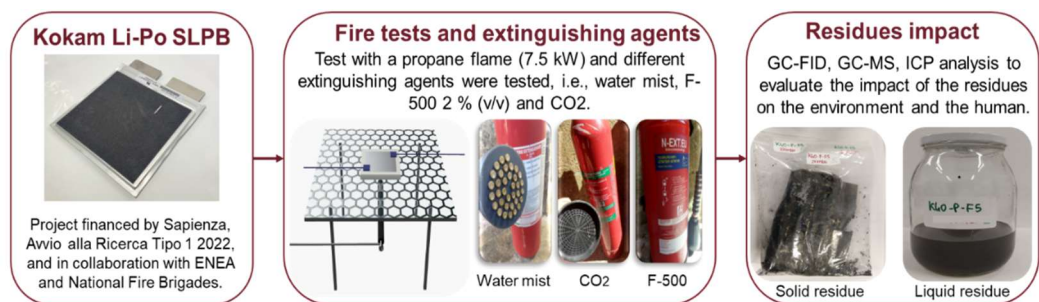

Figure 3: Fire test apparatus and extinguishing agents for LIBs and relevant characterization methods for fire residues.

Table of contents

List of Figures

List of Tables

List of Abbreviations

A

AAS: Atomic Absorption Spectroscopy;
AAS-OES: Atomic Absorption Spectroscopy Optical Emission Spectrometer;
ATEX: Explosive Atmosphere;
ATR-FT-IR: Attenuated total reflection Fourier-transform infrared spectroscopy;

B

BET: Brunauer-Emmett-Teller;
BMS: Battery Management System;
BP: Battery Packages;
BSE: Backscattered Electron;
BTEX: Benzene, toluene, ethylbenzene, xylene;

C

CB: Carbon Black;
CH_4: Methane;
CID: Current interrupt device;
CO: Carbon monoxide;
CO_2: Carbon dioxide;

D

DEC: Diethyl carbonate;
DLS: Dynamic Light Scattering;
DMC: Dimethyl carbonate;
DSC: Differential Scanning Calorimetry;
DTGS: Deuterated Triglycine Sulfate;

E

EC: Ethylene carbonate;
EC_{10}: concentration that caused a modification/reduction in 10 % of the population;
EC_{100}: concentration that caused a modification/reduction in 100 % of the population;
EC_{50}: concentration that caused a modification/reduction in 50 % of the population;
ECHA: European Chemicals Agency;
EMC: Ethyl-methyl carbonate;
EPA: U.S. Environmental Protection Agency;
ESC: External Short Circuit;
ESS. Energy Storage System;
EVs: electric vehicles;

F

FID: Flame Ionization Detector;
FOS: Fiber Optical Sensor;
FT-IR: Fourier-transform infrared spectroscopy;

G

GC: Gaschromatography;
GC-FID: Gas Chromatography-Flame Ionization Detector;

H

HCl: Hydrochloric acid;
HF: Hydrofluoric acid;
HNO_3: Nitric acid;

I

ICP: Inductively Coupled Plasma;
ICP-MS: Inductively Coupled Plasma Mass Spectrometry;
ICP-OES: Inductively Coupled Plasma Optical Emission Spectrometer;
IDLH: Immediately Dangerous to Life or Health;
ISC: Internal Short Circuits;
ISTD: Internal Standard;

K

Kmax: maximum rate of pressure rise;
Kst: Kmax index;

L

LCO: Lithium Cobalt Oxide;
LCT: Liquid Crystal Thermography;
LFP: Lithium Iron Phosphate;
$LiBF_4$: Tetrafluoroborate;
LIBs. Lithium Ion Batteries
$LiClO_4$: Lithium perchlorate;
$LiPF_6$: Lithium hexafluorophosphate;
Li-Po: Lithium-ion Pouch;
LMO: Lithium Manganese Oxide;
LOD: Limit of Detection;
LOQ: Limits of Quantification;
LPG: Liquefied Petroleum Gas;
LTO: Lithium Titanate Oxide;

M

MCT: Mercury Cadmium Telluride;
MEC: Minimum Explosivity Concentration;
MFC: Mass Flow Controller;
MIE: Minimum Ignition Energy;
MIT: Minimum Ignition Temperature;
MS: Mass Spectrometry;

N

NCA: Lithium Nickel Cobalt Aluminum Oxide;
NIA: Fire Investigation Unit;
NIOSH: National Institute for Occupational Safety and Health;
NMC: Lithium Nickel Manganese Cobalt Oxide;
NMR: Nuclear Magnetic Resonance Spectroscopy;
NMs: Nanomaterials;
NOEC: No-Observed-Effect-Concentration;
NPs: Nanoparticles;
NTA: Nanoparticle Tracking Analysis;
NTs: Nanotubes;
NW: Nanowire;

O

OC: Over-charge;
OD: Over-discharge;
OECD: Organisation for Economic Co-operation and Development;

P

PC: Propylene carbonate;
PCB: Protection circuit board;
PdI: Polydispersity Index;
PDMS: Polydimethylsiloxane;
PE: Polyethylene;
PEO: Polyethylene Oxide;
PF_5: Phosphorus pentafluoride;
PM 2.5: Particulate Matter 2.5 μm;
Pmax: Maximum Explosion Pressure;
POF_3: Phosphoryl fluoride;
PP: Polypropylene;
PPE: Personal Protective Equipment;
PTC: Positive Temperature Coefficient;
PVDF: Polyvinylidene fluoride;

R

ROS: Reactive Oxygen Species;
RTD: Thermal Resistance Detector;

S

SBI: Single Burning Item;
SDS: Safety Data Sheets;
SE: Secondary Electrons;
SEI: Solid Electrolyte Interphase;
SEM: Scanning Electron Microscopy;
SEM-EDX: Scanning Electron Microscope – Energy Dispersive X-ray;
SHR: Self-heating rate;
Si: Silicon;
SLPB: Superior Lithium Polymer Battery;
SLPM: Standard Liters Per Minute;
SoC: State of Charge;
SPME: Solid Phase Microextraction;
SPME-GC-MS: Solid Phase Microextraction-Gas Chromatography- Mass Spectrometry
SSA: Specific Surface Area;

T

TC: Thermocouple;
TCD: Thermal Conductivity Detector;
TEM: Trasmission Electron Microscopy;
TGA: Thermal Gravimetric Analysis;
TR: Thermal runaway;

V

v_c: Cooling rate;
VOCs: Volatile Organic Compounds;
VVF: Italian Fire brigade;

X

XRF: X-ray Fluorescence;
XRD: X-Ray diffraction analysis.

1. Introduction

Lithium-ion batteries (LIBs) are chosen in many fields, such as electrical vehicles (EVs), mobile device and energy storage system (ESS), due to their low weight, high energy density and charging capacity [1]. However, the principal disadvantage of these devices is the so-called thermal runaway (TR), that occurred when the device is subjected to an abuse. The term abuse indicates a change of the optimal conditions, such as electrical, mechanical, thermal, of use of the LIBs [2]. These conditions can be considered a direct cause of the TR of the LIBs [3] leading to the internal component decomposition, by multiple exothermic reactions in a wide range of temperatures [4], with the emission of smoke, gases, projection of fragments, fire and/or explosion [5]. The characterization of the products emitted can be done by various analytical techniques, according to the nature of the samples, giving back information on the dangerousness of the compounds, compared to the safety limits defined by the different regulation. To improve the battery safety, protection devices, such as positive temperature coefficient (PTC), current interrupt device (CID), top vent, bottom vent, and protection circuit, can be built-into commercial Li-ion cells, depending on the manufacturer [6]. Finally, the safety stability and the thermal behavior of the Li-ion cells can be evaluated both by standard stability test and by thermal abuse test in order to obtain information on the temperature of the key events, such as CID-vent disk activation , venting and TR, and the impacts of the products emitted on the health and the environment.

1.1. General composition of LIBs

The LIBs are general composed by four main components: anode, cathode, electrolyte and separator, as shown in Figure 4 [7]. At these can be included even additives to enhance the performance and the safety of the electrical devices, such as flame retardant or stabilizers [8].
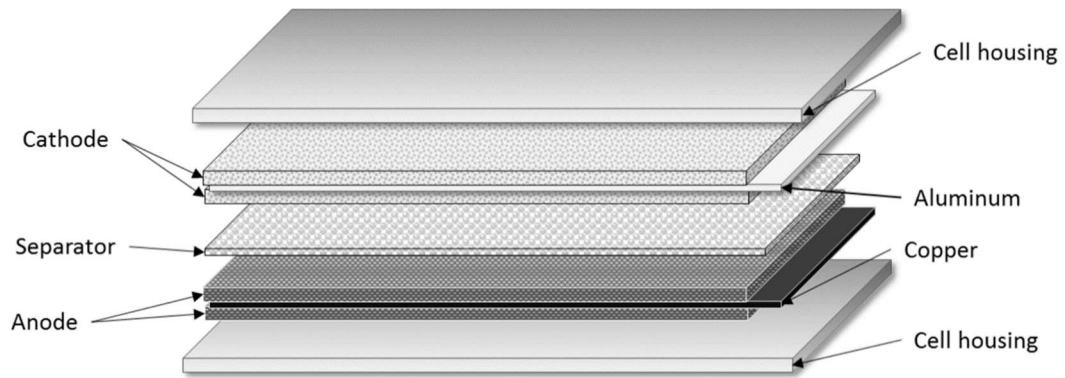
Figure 4: LIBs internal components [7].

Both the cathode and the anode are composed of two layers (deposited on opposite faces) of active material deposited on a metal foil acting as a current collector. Generally, the cathode is composed of mixed oxides of transition metals deposited on the aluminum current collector while at the anode the active layer material can be graphite or lithium titanate oxide (LTO) deposited on the copper current collector. The electrolyte is generally given by various organic carbonates, such as ethylene carbonate (EC), dimethyl carbonate (DMC), ethyl-methyl carbonate (EMC), diethyl carbonate (DEC) and propylene carbonate (PC), in which a lithium salt is dissolved, such as lithium hexafluorophosphate ($LiPF_6$), tetrafluoroborate ($LiBF_4$) or lithium perchlorate ($LiClO_4$) [9]. The main physical-chemical properties of some typical Li-ion cell organic electrolyte components are reported in Table 1 [10].

Table 1: measured flash points, auto-ignition temperatures, and heats of combustion of some typical lithium-ion cell organic electrolyte components [10].

Electrolyte	CAS	Molecular Formula	Melting Point (°C)	Boiling Point (°C)	Vapor pressure (torr)	Flash point (°C)	Auto-Ignition Temperature (°C)	Heat of Combustion (kJ/ml)
PC	108-32-7	$C_4H_6O_3$	-49	242	0.13 at 20 °C	135	455	-20.1
EC	96-49-1	$C_3H_4O_3$	36	248	0.02 at 36 °C	145	465	-17.2
DMC	616-38-6	$C_3H_6O_3$	2	91	18 at 21 °C	18	458	-15.9
DEC	105-58-8	$C_5H_{10}O_3$	-43	126	10 at 24 °C	25	445	-20.9
EMC	623-53-0	$C_4H_8O_3$	-14	107	27 at 25 °c	25	440	n.a.

n.a.: not available.

While, the separator is made of polymeric material, such as polyethylene (PE) and/or polypropylene (PP), which allows the electrical separation of the electrodes, to avoid internal short circuits (ISC), but at the same time porous in order to allow the passage, from anode to the cathode and vice versa, of the Li-ion dissolved in the electrolyte.

The LIBs are usually identified by an acronym, referring to the internal chemical composition, and a numerical code, referring to the geometric dimension of the cell. In fact, the current LIBs on the market are renamed according to the cathode composition, such as lithium iron phosphate ($LiFePO_4$, LFP), lithium nickel cobalt aluminum oxide ($LiNiCoAlO_2$, NCA), lithium cobalt oxide ($LiCoO_2$, LCO), lithium nickel manganese cobalt oxide ($LiNiMnCoO_2$, NMC) and lithium manganese oxide ($LiMn_2O_4$, LMO), while the lithium titanate oxide (Li_2TiO_3, LTO) is referred to the anode composition [11]. In Table 2 are reported the technical specifications of cylindrical cells for these chemistries [12].

Table 2: Technical specifications of cells for the different chemistries [12].

Specification	LTO	LFP	LCO	NCA	NMC	LMO
Nominal voltage (V)	2.40	3.20 - 3.30	3.60	3.6	3.6 - 3.7	3.7
Typical voltage (V/cell)	1.80 - 2.85	2.50 - 3.65	3.00 - 4.20	3.0 - 4.2	3.0 - 4.2	3.0 - 4.2
Specific energy (Wh/kg)	50 - 80	90 - 120	150 - 200	200 - 260	150 - 220	100-150

So, LIBs are characterized by high specific energy (100-200 Wh/kg), high power density (360 W/kg) and long life (500-2000 cycles) respect to traditional batteries, such as lead acid (20-35 Wh/kg; 180 W/kg; 200-2000 cycles), nickel-cadmium (Ni-Cd) (40-60 Wh/kg; 140-180 W/kg; 500-2000 cycles) and nickel-metal hydride (Ni-MH) (60-80 Wh/kg; 220 W/kg; < 3000 cycles) [13].

Another characteristic of the LIBs is the shape and the dimension. The cells can have cylindrical, coin, prismatic and pouch shape according to the final application and the voltage required. Independently from the external shape the

internal components are the same reported Figure 4, what is change is the disposition of the components, as shown in Figure 5 [14].

(a)

(b)

(c)

(d)
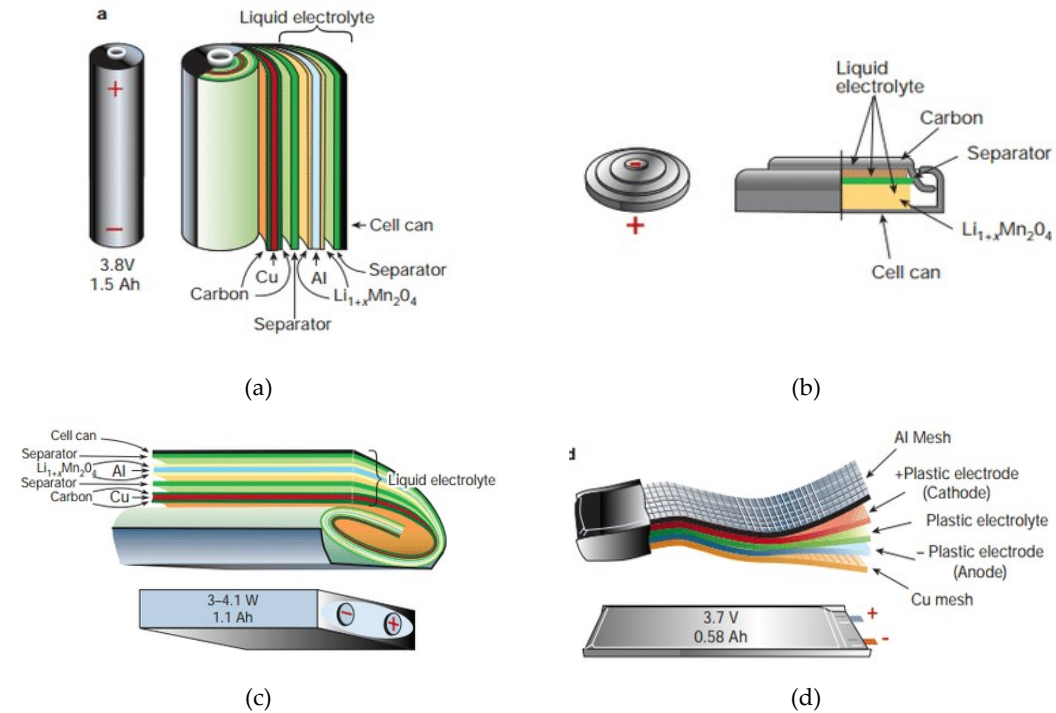
Figure 5: Different types of cell geometry: cylindrical (a); coin (b); prismatic (c); pouch (d) [14].

Indeed in the cylindrical cell the electrodes and the separator are long single sheets which are then rolled up; in the coin cell there is a single layer of each electrode placed at the two ends with the plastic separator in the middle; in the prismatic cell the sheets of electrode and separator components are folded on top of each other while in the cell pouch there are multiple sheets of the different components on top of each other.

For each shape and relative dimension there is a specific code. To indicate the cylindrical cells is used a code of 5 numbers, where the first two numbers indicate the diameter in mm, the following two number indicate the length of the cell, always in mm, while the last number, 0, indicates the cylindrical shape. The most common cylindrical cells are the 18650 and 21700, so cells with a diameter of 18 or 21 mm and a length of 65 or 70 mm. The coin cells are indicated by a code of 2 letters and 4 numbers, the two letters indicate the coin cell chemistry while the first 2 number indicate the maximum diameter, expressed in mm, and the last 2

numbers indicate the height, in mm. The most popular coin cells are the CR2032 and CR1254, so coin cells with lithium manganese dioxide cathode with a maximum diameter of 20 or 12 mm and a height of 32 or 54 mm.

1.2. Safety devices

In addition to the internal components, necessary for the normal function of the cell, can be built-into commercial Li-ion cells some protection devices to improve the battery safety, such as PTC, CID, top vent, bottom vent, and protection circuit, depending on the manufacturer, as shown in Figure 6 [6].
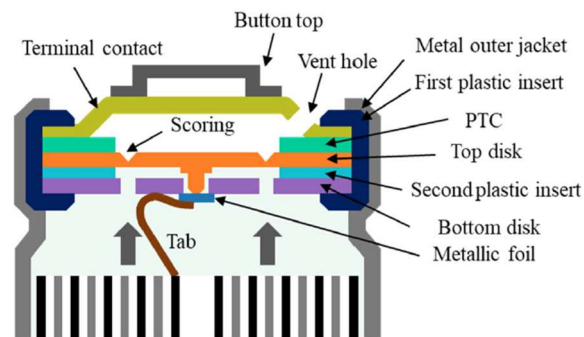
Figure 6: the cap structure of commercial 18650 Li-ion battery [6].

The CID breaks the internal circuit when the cell is overcharged by detecting an increase in the internal pressure in the cell, PTC protects the cell under external short circuit by detecting temperature rise caused by excessive current.

Only the CID and the top vent are mandatory in the 18650 cells while the other devices are optional. Once the abuse initiates the exothermic reactions, the heat produced increases the internal temperature and pressure causing the activation of the protection devices installed on the single cell [8]. If the protection devices activation is not sufficient to balance the pressure inside the cell, because of the faster temperature (and pressure) rise during the TR, the cell bursts.

1.2.1. Current interrupt device (CID)

The CID is composed by different components: top disk, second plastic insert, bottom disk and metallic foil, as reported in Figure 7a [6]. The activation of the CID is due to the increase in internal pressure, which leads to the opening of the

circuit at a pre-defined internal pressure of 1.0 - 1.2 MPa [15] with electrical insulation of one of the electrodes, as shown in Figure 7b [6].
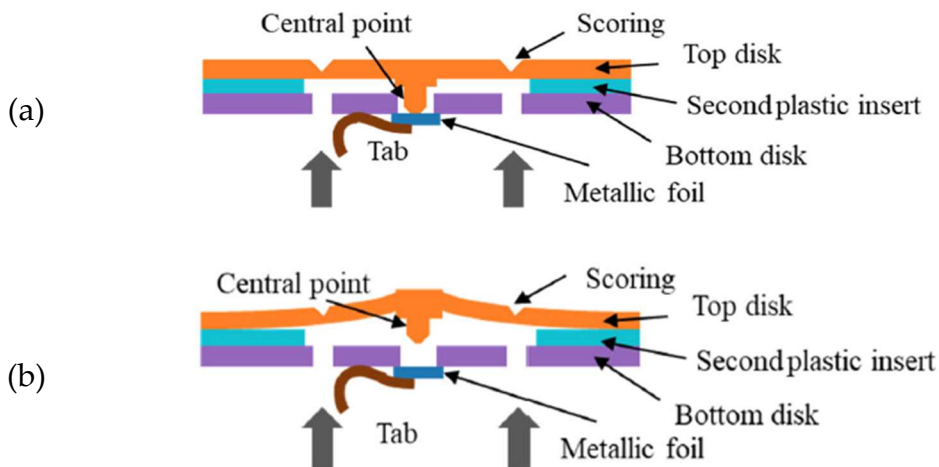
Figure 7: CID structure before (a) and after (b) being triggered [6].

In the normal condition the central point of the top disk, a conductive flexible membrane, is welded to the bottom disk and the two disks are electrically insulate by the second plastic insert, Figure 7a. This connection is the weak point in the current pathway and can be cut-off in case of abuse, Figure 7b. In fact, the abuse leads to the generation of a large amount of gas from the electrodes that caused the increase of the internal pressure that move upwards the top disk breaking the current connection. The activation of the CID causes the halted of both the current flow and the electrochemical reactions inside the battery. So, the CID interrupt the current flow inside the cell in the case of an abuse in an irreversible way.

1.2.2. Top vent

Venting is the *release of excessive internal pressure from a cell or a battery in a manner intended by design to preclude rupture or explosion*, definition provided by the International Electrochemical Commission 62133 standard [16]. The top vent is activated by a higher internal pressure value, in the range between 2.2 - 2.3 MPa [15], than the CID and the mechanism is shown in Figure 8.

In normal condition the components of the top vent, such as the terminal contact, vent hole and the top and bottom disk, work as conductors. In case of abuse the

6

weak point of the top vent is a *C shape scoring* on the top disk while the gas venting pathway of the top vent is indicated by the red arrow in Figure 8.
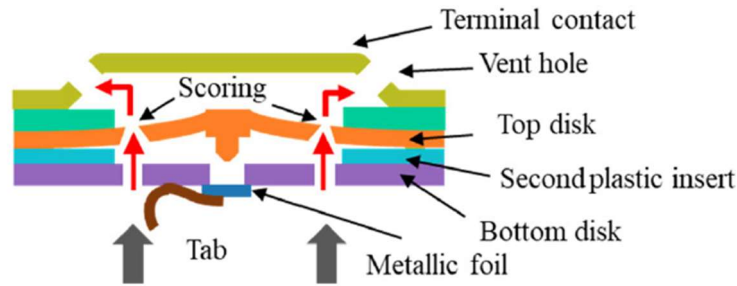
Figure 8: gas releasing pathway during venting [6].

The gas from the inside the cell passed through the peripheral holes on the bottom disk, the *C shape scoring* on the top disk and the vent holes on the terminal contact. During the venting both the battery cap or sidewall can be broken from an uncontrolled rupture and even the electrolyte and electrode materials, in addition to gaseous products, can be vented out through the releasing pathway. In the worst case, if the releasing pathway is clogged or cannot vent efficiently, the battery case may be ruptured or exploded increasing the emission products. So, even the top vent if activated is an irreversible safety device, as the CID. To avoid these adverse phenomena and enhance the safety the battery, manufacturers have introduced in the last cell even a bottom vent.

1.2.3. Bottom vent

The bottom vent has been designed to enhance the venting and increase the gas amount that can be released during this phase. In fact, the top vent can be clogged or insufficient to balance the internal pressure within milliseconds. So, another vent has been added on the bottom of the cell, as shown in Figure 9.

(a)   (b)   (c)
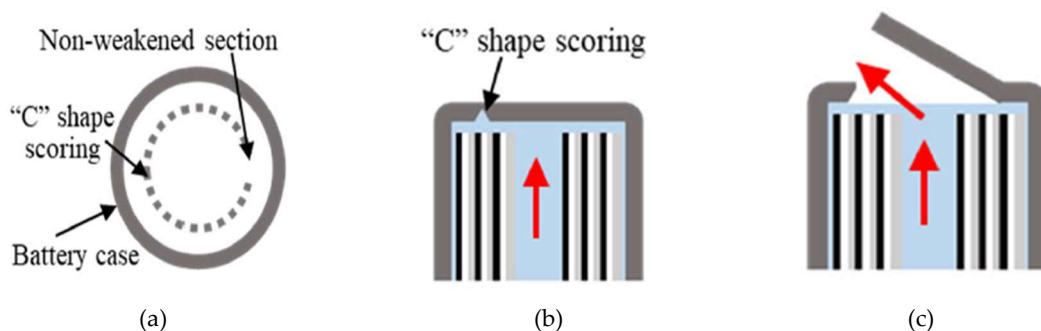
Figure 9: top view of the bottom vent (a) and bottom vent: (b) before and (c) after rupture [6].

During the normal use the bottom vent works has bottom case of the cell while in case of abuse can be broken to release the gas and reduce the pressure. In fact, bottom battery case has a *C shape scoring* inside or outside the battery case, Figure 9a, with a reduced thickness that corresponds to the weak point, Figure 9b, that can be broken if the pressure reached higher values, 2.47 MPa [17]. The gas venting pathway of the bottom vent is indicated by the red arrow in Figure 9c. When the specific level of pressure is reached the weak section, the *C shaped section*, opens outwards while the other section of the bottom disk remains attached preventing the disk flying out.

Even if is an irreversible safety device the bottom vent can reduce the risk of sidewall rupture and significantly decrease the impact to adjacent cells in a battery package by releasing generated gas through an alternative escape route. However, the total amount of gases and battery material that can be ejected during the venting is higher if this device is present.

1.2.4. Positive temperature coefficient (PTC)

The PTC is *a component that has the characteristics of a sudden large increase in resistance when the device reaches a specified temperature and/or current*, definition provided by the standard Institute of Electrical and Electronics Engineers 1725-2011 [18]. The PTC is an annular-shape disk in the top part of the cell, placed between the terminal contact and the top disk, as shown in Figure 10.
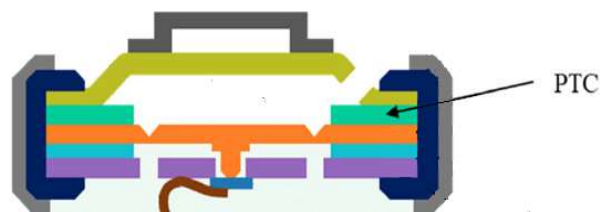
Figure 10: PTC structure [6].

In normal condition, the PTC is a annular-shape disk with a three-layer structure, one conductive polymer layer, such as polyethene polymer mixed with conductive particles, placed between two conductive and supporting metal layers [19]. The mechanism of this device is due to the change of the resistance of the conductive

polymer layer with the temperature increase. In fact, when the cell is subject to an abuse the internal temperature increases due to the exothermic reactions occurring inside the cell and this increase causes a higher resistance of the polymer layer. For temperature values around 100 °C the polymer expansion increases the distance between the conductive particles significantly reducing the current flowing through the cell.

This protection is reversible, so it is inhibiting current when the temperature is too high, but it returns to the initial position when the temperature is near the room temperature.

1.2.5. Protection circuit board (PCB)

The last protection device that can be installed on the cylindrical cell is the protection circuit. This device is located on each cell of the module and work as the battery management system (BMS) of the battery pack. Through sensors, controllers, actuators, and communicators the protection device can activate, if necessary, protection against overcharging, over-discharging, overcurrent and short-circuit with an enhance in the safety of the cell. Cells with this kind of protection can be considered smart cells that can be switches off if the condition inside the cells are considered a potential risk for a short circuit and/or a TR.

The protection device is fixed at the bottom of the battery by a plastic cover and is electrically connecting the positive and the negative pole by a metal wire. The control of the parameters, such as input power at negative and positive pin, current, voltage and charge and discharge current, is done by a controller chip.

This device is always working to monitor the parameters and being an electronic device if is damage by heat or aggressive vapors must be replaced.

1.3. Principle of function of LIBs

LIBs are defined as secondary batteries because these devices are rechargeable, in fact they discharge during use and are then recharged by connecting them to an

electrical grid [20]. So, the LIBs are able to convert the chemical energy products by the internal reaction in electrical energy and to use this one after to restart the process. This double mechanism is possible thanks to the movement of the Li-ions (Li^+), dissolved in the electrolyte, across the separator reaching the anode or the cathode layer according to the charging or discharging phase, in a process that is quasi-reversible. The displacement of the Li^+ and the consequent charge and discharge mechanism is illustrated in Figure 11 [21].

During the discharge phase, so when the device is used, the Li^+ passed from the active material of the anode (electron donor, electrochemical oxidation) to the active material of the cathode (electron acceptor, electrochemical reduction) passing through the plastic separator. This reaction is spontaneous, so is not necessary an external supply of energy, and cause the movement of the electrons on the external electrical circuit, converting the chemical energy in electrical energy.
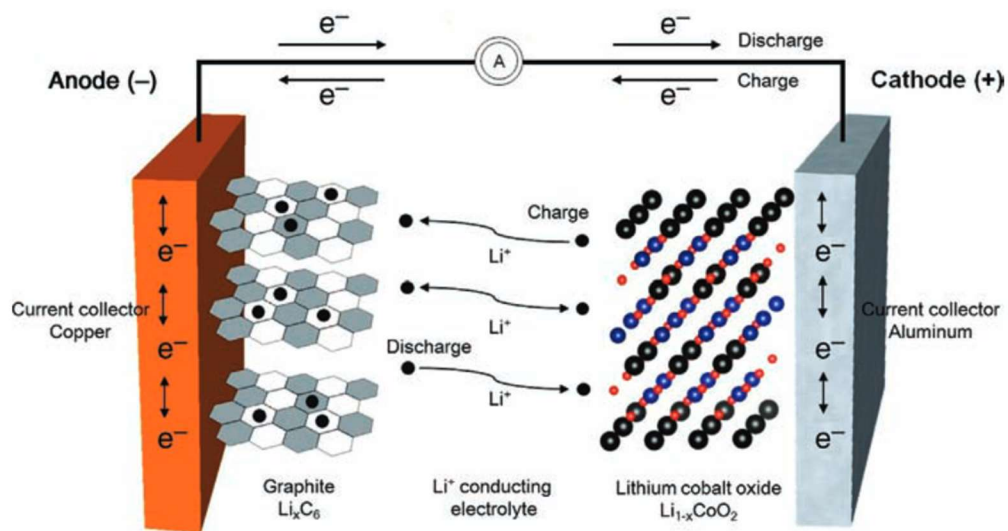
Figure 11: Charge-discharge mechanisms, movement of Li+ in an electrolyte and insertion/extraction of Li+ with in electrodes in LIBs [21].

The two half reactions that occur inside the cell are the de-lithiation of the anode, i.e. anode electrode is oxidized according to Equation (1), and the intercalation of the Li^+ in the cathode, i.e. cathode electrode is reduced, according to Equation (2).

$$Li_xC_6 \rightarrow x\ Li^+ + xe^- + C_6 \tag{1}$$

$$Li_{1-x}M_yO_z + x\ Li^+ + x\ e^- \rightarrow LiM_yO_z \tag{2}$$
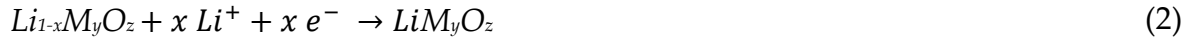
Where M indicates the generic metal, such as Ni, Co, and Mn.

The charging phase is the opposite of the discharging one and takes place when the device is connected to an electrical grid. In this case the reactions are not spontaneous and so needed an external electrical supply. The half-reactions are the de-lithiation of the cathode, cathode electrode is oxidized, Equation (4), and the intercalation of the Li^+ in the anode, anode electrode is reduced according to Equation (3).

$$x\ Li^+ + x\ e^- + C_6 \rightarrow Li_xC_6 \tag{3}$$

$$LiM_yO_z \rightarrow Li_{1-x}M_yO_z + x\ Li^+ + x\ e^- \tag{4}$$

Where M indicates the generic metal, such as Ni, Co, and Mn.

So, the full cell reaction, for the charge and discharge phases, is reported in Equation (5), and the process is reversible because the intercalation of the Li^+ in the electrodes active materials does not cause significant changes in the chemical structure of the cell components.

$$LiM_yO_z + C_6 \underset{\text{discharge}}{\overset{\text{charge}}{\rightleftharpoons}} Li_{1-y}M_yO_z + Li_xC_6 \tag{5}$$

Where M indicates the generic metal, such as Ni, Co, and Mn.

The more Li^+ the electrodes can absorb, the greater the total energy that the battery can store and therefore its duration. the reversible electrochemical intercalation of Li^+ into the graphite structure is limited to one lithium per six carbons (LiC_6) that results in a theoretical capacity of 372 mAh g^1 [22].

In conclusion, the two limit conditions for the LIBs are the completely charged, when the state of charge (SoC) is 100 %, and completely discharge, when the SoC is 0 %. The SoC is defined as the available amount of charge in a given battery related to the full amount of charge, which can be stored in this battery and is

usually expressed as a percentage and is calculated according to the Equation (6) [20].

$$SoC = \frac{Q_{remaining}(t)}{Q_{max}(t)} * 100 \%$$ (6)

Where $Q_{remaining}(t)$ is the remaining energy in the battery at a given time while $Q_{max}(t)$ is the maximum energy available for the cell.

1.4. Abuses of LIBs

In the previous section, Principle of function of LIBs, has been presented the normal mechanism of the LIBs, so when they are correctly used. Anyway, there are some conditions, defined as abuse, that can caused damage to the LIBs leading to secondary internal reactions, which caused the TR and the production of dangerous products [2]. Indeed, the internal components and the technical specifications define a safe and reliable operation range, limited by temperature and voltage. This range is the so-called safety window, green area in Figure 12, while all the conditions outside the safety window can cause the deformation of the cell, module, or battery, and/or the degradation of the internal components [23].
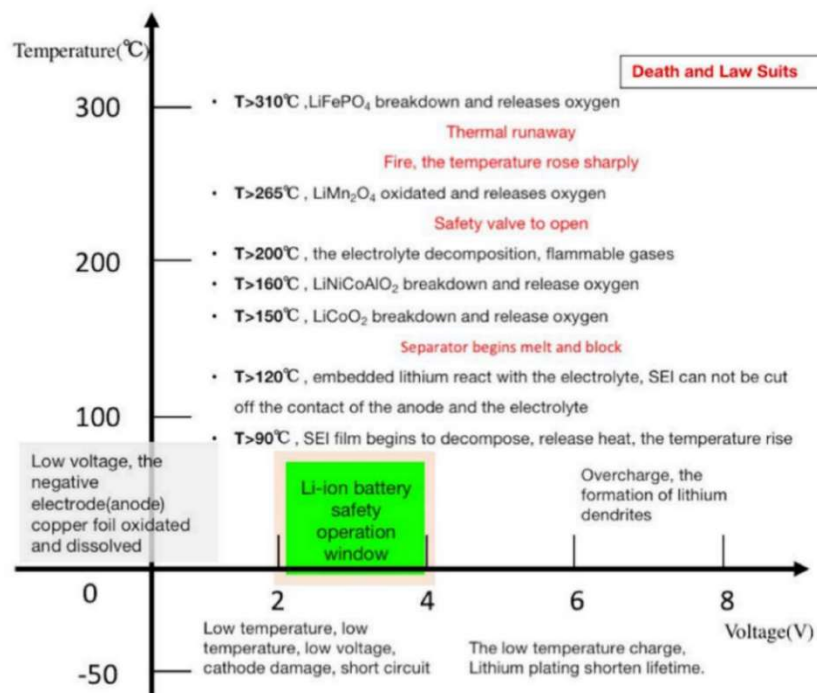
Figure 12: Safety operating window for LIBs [24].

12

According to the nature of the abuse the LIBs can be subject to electrical, mechanical or thermal abuse [25], as shown in Figure 13.

(a) "Large blaze in Shepherd's Bush high-rise yesterday was caused by failure of e-bike lithium-ion battery under charge." (London Fire Brigade, 22/06/2022) [26].

(b) "The impact in a fatal accident involving a Tesla electric car may have set off a fire in the vehicle's battery" (Reuters, 14/05/2018) [27].

(c) "The driver saw the overheated battery light on the dashboard come on and in a short time smoke began to come out from under the car." (Insideevs, 16/05/2023) [28].

Figure 13: Journal articles about accidents due to: (a) electrical; (b) mechanical; (c) thermal abuse.

Electrical abuse can be induced by improper charging, as in the case reported in Figure 13a, where an e-bike take fire during the charging phase in an apartment in Shepherd's Bush, a district of West London (England), the June 21st 2022 (source London Fire Brigade) [26].

Mechanical abuse can be caused by deformation or penetration of the battery pack, as in the case reported in Figure 13b, where an EV crush against the guard rail in a Switzerland highway, the May 16th 2018 (Source Reuters) [27].

Thermal abuse is usually related to an overheating, as in the case happened in Romania the May 16th 2023 (Source Insideevs) [21], Figure 13c, where during the use the BMS of an EV registering an anomaly in the temperature value of the battery pack turned on an error light on the dashboard. In few seconds the battery pack started emitting gases and after few minutes the car was completely disrupted.

So, independently from the nature of the abuse the LIBs reached the TR due to the heat production inside the cell that promote the secondary reactions between the materials, with release of gases, solids, fire and/or explosion [29].

1.4.1. Electrical abuse

The electrical abuse can be caused by over-charge (OC) or over-discharge (OD) and external short circuit (ESC) or ISC [30]. The OC and OD events are caused by improper charging, still forcedly charged the cell even after it had reached its nominal cut-off voltage, or discharging, still forcedly discharged the cell even below its cut-off voltage. The ESC can be caused by battery system failure and harsh operating conditions, while the ISC can be triggered by various conditions, such as internal defects, mechanical abuse, electrical or thermal abuse [31]. These kinds of abuses have a great impact on electrical and thermal performance causing a significantly change in the heat-generating characteristics of LIBs triggering, in the worst case, TR which leads to explosion and/or fire [30]. The general mechanism that occurred inside the cell, and that can lead to the TR, is the

formation of dendrites on the electrodes that can cause the loss of capacity, increasing the resistance, and/or the broken of the separator.

The OC negatively affects the cycling performance, cycle life and the safety directly triggering the TR. The main side events that can occurred inside the cell are the lithium plating and the solid electrolyte interphase (SEI) decomposition due to the cathode material destruction and decomposition. The lithium plating is caused by the cathode material destruction and decomposition that leads to the migration of the Li^+ and the dendrites formation on the anode surface which caused the separator piercing forming ISC [32]. The SEI film decomposition, between 80-120 °C, is caused by the increasing of the internal resistance that generate joule heat inside the cell. Without the SEI the lithiated anode can react with the electrolyte, accelerating the heat and the gas generation. In fact, these initial phenomena are then followed by additional complex side reactions, such as phase transition, transition-metal dissolution and electrode oxidation for the cathode and the separator melting [30].

The OD causes a continuously increase of the anode potential that leads to irreversible chemical reactions and internal structure damage. The continuous discharge of the cell causes a continuous anode potential increase and a gradual cathode potential decrease which possibly causes the cell polarity reversal. The higher potential at the anode causes the SEI breakdown and the copper current collector dissolution, around 4.8 V vs. Li/Li^+ [33]. When the copper dissolution potential is reached, the anodic corrosion of copper is triggered and the dissolved Cu^{2+} started migrating to the cathode and deposit on it. The continuous growth of copper dendrites on the cathode surface leads to the separator penetration and consequent ISC occurred [34]. The mechanism is due to the anode current collector and the experimental results reported that the LTO-based anode had a greater structural and thermal stability compared to the graphite-based anode [35].

ESC may be caused by battery system failure and harsh operating conditions that leads to an increase of the current accumulated inside the cell. The increasing current flow is not balanced by the short-circuit resistance outside the cell and by the heat dissipation rate of the cell [36]. So, if the heat produced during the current flow is not balanced, it that can leads to the lithium plating and the lithium dendrites growth. Both can growth rapidly due to the good condition, such as continuous transport of Li ions or the lower anode potential (under 0 V vs. Li/Li$^+$), causing in a short time a connection between the two electrodes that marks ISC forming.

Finally, as reported until now, the ISC can be caused by all the previously conditions [37] and even by other abuses, as reported in the next sections.

1.4.2. Mechanical abuse

The mechanical abuse can be caused by penetration, crash, drop, shock, vibration or immersion, all conditions that can happen during a collision accident. All these abuse caused a deformation of the external case of the cell, module or battery that leads to an ISC due to the intrusion of external object [38]. In fact, the critical point, for safety and energy storage performance, during a mechanical abuse is the integrity of the separators and electrodes.

The crush and collision are caused by the application to the cell of an external force that caused a destructive deformation of the external case first and of the internal material after, when the force is transmitted to the cell interior [39]. Applying a continuous force, the interlaying spacing between different layers gently shortens leading to a crack of the electrodes material, when the deformation limit is reached. By continuing to apply the external force, more and more internal layers will undergo deformation, also involving the plastic separator. Once the critical breaking point of the separator is also reached, the adjacent opposite electrodes will come into contact causing the ISC. Due to the ISC the flammable electrolyte can lacks from the cell triggering, in combination with air, a fire [31].

The penetration is caused by the perforation of the cell by an external object, such as nail, that passing through the internal components of the cell induced a quite immediate ISC. In fact, in this case, comparing to the crush or the collision cases, the deformation of the external case and of the internal layers of the cell is simultaneous and not consequential. Due to the nature of the external object that pass through the cell the effects can be even more severe, in fact, if the object is made of a conductive material, such as a metallic nail, penetrating the separator is causing an immediate ISC for the fact that is electrically connecting the adjacent opposite electrodes.

So, the main effect that occurred during a mechanical abuse is a localized ISC, defined as a pinpoint short-circuit, that evolve to a large short-circuit current with vigorous heat generation and a sharp temperature rise due to the contact between the electrodes inside the cell. The main difference between crush and penetration is the velocity at which the TR can be reached, which results more fast and severe in the second case compared to the first.

1.4.3. Thermal abuse

The thermal abuse can be caused by an external heating source or by an internal overheat caused by the previous abuses [40]. Independently from the heating source the thermal abuse is considered as the previous event before the TR. The critical point, for safety and energy storage performance, during a thermal abuse are the chain reactions that can occur with the rise of the temperature, such as electrolyte volatilization, the separator melting and the electrode decomposition [41]. The reactions that take place inside are spontaneous, uncontrolled, and exothermic, except for the melting of the separator, and are due to the SEI decomposition (> 90 °C), reaction between intercalated lithium and electrolyte (90-200 °C), melting of the separator (120–150 °C) and metal oxide cathodes decomposition with production of oxygen (> 150 °C) [42]. The temperature values, as shown in Figure 12, are different according to the chemical composition, in fact

the LFP are more stable compared to the LCO in terms of reaction temperature. During these phases the cell undergoes an increase in internal pressure with subsequent, depending on the shape of the cell, opening of the vent valve for cylindrical cell or of an area, placed between the two terminals, with a less resistance welding for pouch cell. Finally, the TR is characterized by a self-accelerating exothermic reaction inside the cell with high temperature and heating rate (10 °C/min or higher), gas ejection, projection of fragments, fire and/or explosion [4].

The first reaction, occurring around 90 °C, is the SEI decomposition on the anode electrode that leads to the increase in temperature and pressure inside the cell. The SEI layer on the anode is composed of stable, such as LiF and Li_2CO_3, and metastable components, such as polymers, ROLi and $(CH_2OCO_2Li)_2$, that can decompose exothermically a temperature higher than 90 °C, Equation (7) [43].

$$(CH_2OCO_2Li)_2 \rightarrow Li_2CO_3 + C_2H_4 + CO_2 + \tfrac{1}{2} O_2 \tag{7}$$
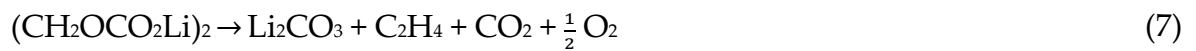
The breakdown of the SEI caused the reaction between the lithium intercalated in the anode and the organic carbon electrolytes, according to the type of solvent present in the electrolyte, such as EC in Equation (8), PC in Equation (9), or DMC in Equation (10).

$$2\,Li + C_3H_4O_3\,(EC) \rightarrow Li_2CO_3 + C_2H_4 \tag{8}$$

$$2\,Li + C_4H_6O_3\,(PC) \rightarrow Li_2CO_3 + C_3H_6 \tag{9}$$

$$2\,Li + C_3H_6O_3\,(DMC) \rightarrow Li_2CO_3 + C_2H_6 \tag{10}$$

The main products of these reactions are the flammable hydrocarbon gases, heat, and pressure.

In the range between 120 and 150 °C, the polymer separator melts. Even if is the only endothermic reaction that takes place inside the cell it can caused an ISC by the electrical contacts of the opposite electrodes.

The cathode breakdown occurs at higher temperature compared to the anode one but with similar effects, increase in temperature and pressure and release of reactive products, such as oxygen. The reactions varied according to the chemical composition of the cathode, between 140 and 160 °C for NCA as Equation (11), around 260 °C for NMC as Equation (12), or between 190 and 310 °C for LFP as Equation (13) [11].

$$Li_{0.36}Ni_{0.8}Co_{0.15}Al_{0.05}O_2 \text{ (NCA)} \rightarrow 0.18 \text{ Li}_2O + 0.8 \text{ NiO} + 0.05 \text{ Co}_3O_4 + 0.025 \text{ Al}_2O_3 \\ + 0.372 \text{ O}_2 \tag{11}$$

$$Li_{0.35}(NiCoMn)_{1/3}O_2 \text{ (NMC)} \rightarrow Li_{0.35}(NiCoMn)_{1/3}O_{2-x} + \tfrac{x}{2} O_2 \tag{12}$$

$$2 \text{ Li}_xFePO_4 \text{ (LFP)} \rightarrow Fe_2P_2O_7 + \tfrac{1}{2} O_2 \tag{13}$$
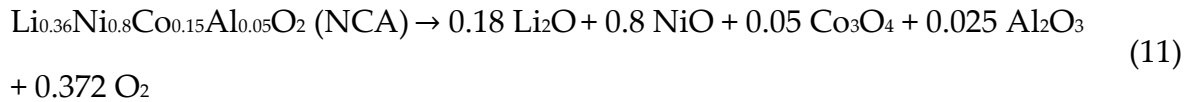
The oxygen production and the heat release provide the required conditions for combustion in the cell, leading to the TR.

These are the main reactions that occur during the abuse of the device, but even other reactions can take place according to the additives present in the chemical composition. The first one is the decomposition of the electrolyte while the second one is the reaction between the polyvinylidene fluoride (PVDF) binder and the anodic electrode.

The decomposition of the electrolyte, made of organic compounds and Li salt, can be observed at elevated temperatures, between 200 and 300 °C, and leads to flammable and/or toxic products, such as hydrogen fluoride (HF), phosphoryl fluoride (POF_3), phosphorus pentafluoride (PF_5) and carbon dioxide (CO_2) [4].

$$2 \text{ Li} + 2 \text{ C}_3H_4O_3 \text{ (EC)} \rightarrow Li\text{-O-}(CH_2)_4\text{-O-Li} + 2 \text{ CO}_2 \tag{14}$$

$$LiPF_6 \rightarrow LiF + PF_5 \tag{15}$$

$$Li\text{-O-}(CH_2)_4\text{-O-Li} + PF_5 \rightarrow Li\text{-O-}(CH_2)_4\text{-F} + 2 \text{ LiF} + POF_3 \tag{16}$$
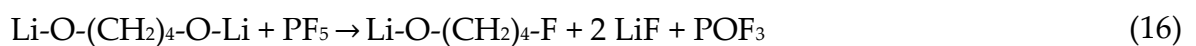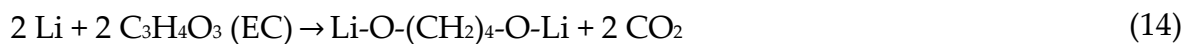
The second one occurs only when the anode is lithiated, so when the LIBs are charged. In this case the PVDF binder, present as protection for the active material

of the anode, in the presence of the electrolyte which acts as an acidic medium is dehydrofluorinated, Equation (17). Then the binder reacts with the Li intercalated in the anode, Equation (18).

$$-CH_2\text{-}CF_2 \rightarrow -CH = CF\text{-} + HF \tag{17}$$

$$-CH_2\text{-}CF_2 + Li \rightarrow LiF + -CH = CF\text{-} + \tfrac{1}{2} H_2 \tag{18}$$

However, during a real abuse the reactions not occurred one after one in order but even together due to the reactions between the different products present and the temperature increase [44], so the degradation reactions strictly depends on the chemical composition, the SoC, and the type of abuse perpetrated [45].

1.5. Safety regulation to simulate abuse condition

To evaluate the behavior to abuse and therefore to define the safety, various international, national, regional standards and regulations for cells (C), modules (M) or battery packages (BP) under mechanical, electrical and thermal abuse, had been published [46]. The final aim of each test is to identify the potential weak points and vulnerabilities when the device experiences real-life off-normal conditions. In the following are reported the main tests, dividing for kind of abuse, with the reference to the UN/ECE-R100.02:2022 approved by the United Nations in date 23 August 2022 and so applied in the European Union [47].

The various electrical tests can be conducted on the different level of the device, i.e., C, M and BP as follows:

a. ESC test: to evaluate the safety performance of the device when applying an external short circuit. The test can evaluate the activation of the overcurrent protection device, such as CID or PTC, or the ability of cells to withstand the current without reaching a hazardous situation. The UN/ECE-R100.02:2022 test procedure is reported in Annex 9F "External short circuit protection" [47].

b. ISC test: to evaluate the safety performance of the device when an internal short circuit occurs triggered by manufacturing imperfections, presence of impurities in the cells, dendritic growth of lithium etc. Due to the complexity of the process and the difficult to control the impurities inside the cell standard test for this kind of abuse are under development.

c. OC/OD test: to evaluate the functionality of the electrical protection system charging or discharging the device beyond the limits recommended by the manufacturer in the SDS and they can using charge-discharge test equipment. The UN/ECE-R100.02:2022 test procedure is reported in Annex 9G "Overcharge protection" and in Annex 9H "Over-discharge protection" [47].

Even the mechanical tests can be conducted on the different level of the device, i.e., C, M and BP, according to the final aim.

a. Mechanical shock test: to evaluate the robustness of a battery in situation of sudden acceleration and/or deceleration of a vehicle. To measure and determine the impact resistance of a C or M can be conducted vertical or horizontal shock test with a shock test system, while for BP can be used a battery crush chamber. The UN/ECE-R100.02:2022 test procedure is reported in Annex 9C "Mechanical shock" [47].

b. Drop test: to evaluate the fall behavior. For conducting this kind of test it can be used the traction battery drop test, anyway there are no indication in the UN/ECE-R100.02:2022.

c. Penetration test: to evaluate the reactivity of the components due to the electrical contact. The test can be conducted using a press combined with a nail that can be moved with different velocity and at different depth inside the device, such as the nail penetration test chamber, but even in this case there are no indication in the UN/ECE-R100.02:2022.

d. Immersion test: to evaluate the behavior of the device when is submerged or partially flooded, and ca be carried out with equipment like the battery seawater immersion testing. Also, in this case there are no indication in the UN/ECE-R100.02:2022 [47].

e. Crush test: to evaluate the response of the device when it is applied a crush force that emulates a vehicle accident or any external load force that may damage the battery enclosure causing its deformation. This test can be conducted on C, M and BP just modifying the characteristic of the crush equipment. The UN/ECE-R100.02:2022 test procedure is reported also in Annex 9D "Mechanical integrity" of the [47].

f. Rollover test: to evaluate the behavior of the device when is rotate, but there is no indication in the UN/ECE-R100.02:2022.

g. Vibration test: to evaluate the effect of long-term vibration profiles, representative of driving, on the BP, both in terms of the durability and in terms of identification of design flaws. The test can be performed with a battery vibration test equipment and the UN/ECE-R100.02:2022 procedure is reported in Annex 9A "Vibration test" of the [47].

Finally, the thermal tests that can be conducted on the different level of the device, i.e., C, M and BP, are the following:

a. Thermal stability test: to evaluate the safety performance and the thermal stability of a system under conditions of temperature change. The thermal stability test, according to UN/ECE-R100.02:2022 [47], permits to identify the temperature at which the TR started by increasing the temperature of 5 °C with a holding time of 30 min between each incremental step, until the temperature reaches 200 °C above the maximum operating temperature of the battery or until a catastrophic event occurs.

b. Thermal shock test: to evaluate changes in the integrity of the device arising from expansion and contraction of cell components upon exposure to

extreme and sudden changes in temperature and potential consequences. The test can be performed inside a thermal shock chamber and the relative UN/ECE-R100.02:2022 procedure is reported in Annex 9B "Thermal shock and cycling test" [47].

c. Overheat test: is conducted to evaluate the effect of temperature control failure or failure of other protection devices against internal overheating, due to a rapid charge/discharge, cycling without thermal management, single point thermal control system failure or over-temperature protection test. The test can be performed with in a thermal shock chamber and the UN/ECE-R100.02:2022 procedure is reported in Annex 9I "Over-temperature protection" [47].

d. Extreme cold temperature test: to evaluate the effect of possible exposure of the device to low temperatures. The lower temperature caused a decrease in the electrical performance with side reactions, such as lithium plating and lithium dendrites growth, but the standard test for this kind of abuse are under development.

e. Fire test, to evaluate the risk of explosion of the device when exposed to a fire. The fire test can be conducted using as ignition source a gasoline pool fire or a liquefied petroleum gas (LPG) burner. The UN/ECE-R100.02:2022 procedure is reported in Annex 9E "Fire resistance" [47].

In conclusion, for each abuse test usually there is the specific equipment and the standard procedure, and for a single device more tests can be done subsequently to have a more complete idea of the behavior.

1.6. TR products characterization

Independently from the type of abuse, the LIBs reached the TR due to the degradation reactions occurring inside the cell between the internal components which leading the emission of smoke, gas, fire, explosion and projection of solid [5], as shown in Figure 14.

(a) "A fire broke out around 4:30 p.m. on Monday January 16 in a warehouse containing 12,250 automotive lithium batteries, propagating to the near industries." (actu.fr, 16/01/2023) [48].

(b) "In the 26 second video clip, plumes of smoke can be seen bellowing out of the scooter which is parked by the side of the highway" (ETAuto, 29/03/2022) [49].

(c) "The battery pack of Audi, an electric vehicle, was ejected from the vehicle and caught fire." (Sicurauto.it, 03/02/2023) [50].

Figure 14: Main products of LIBs TR: (a) fire; (b) gases; (c) solid material and/or particulate.

From these journal articles is possible to observe not only the different products that can be emitted from the TR but even the severity, the total amount, and the relative risks for human security. Due to potentially hazardous materials, such as highly flammable electrolytes, corrosive and toxic components, the concentration limits, such as the Immediately Dangerous to Life or Health (IDLH), defined by

the National Institute for Occupational Safety and Health (NIOSH), can be overcome [51].

So, it is crucial, during the abuse tests, on laboratory scale, the characterization of the products emitted by different techniques both on-line, by linking the instruments to the reaction chamber, and off-line using instruments not directly linked to the chamber. The on-line measurements permit to obtain a profile of the values during the test time while the other analysis permit to obtain information about the whole event.

1.6.1. Temperature devices: monitoring and recording

As shown in Figure 14a one of the most dangerous products of the TR is the flame coming from the cell. The main parameter that can be evaluated is the flame temperature. Obviously, the temperature values can be significantly different depending on the place where the values are monitored, in fact, there is a difference between the internal and surface cell temperature and the gas temperature, but the first one to be measured needs the opening of the device (more invasive procedure), while the second and third one is easier and there are many sensors that can be used.

The sensors that can be used to measure the surface cell temperature and gas temperature around the device are thermocouple (TC), thermal resistance detector (RTD), fiber optical sensor (FOS), impedance temperature measurement, infrared thermography and liquid crystal thermography (LCT) [25], and infrared thermal imaging camera. With these sensors it is possible to monitor the temperature on the surface of the cell in a fast and reproducible way. The TCs are the most used device for this kind of measurements due to the high sensitivity, small size, fast response time and low cost. The quick response to temperature change is due to the resistance change and permits to obtain fast response that can be usually recorded by external data logger or computer software. The LCT devices can be used to have not a single point evaluation but the characterization of the surface

temperature distribution. The most promising sensor actually under investigation is the FOS due to a typically lightweight, smaller physical dimension and the ability to withstand harsh environments at elevated temperatures [52]. Finally, infrared thermal imaging cameras can detect thermal radiation and process it into thermal images or videos, which can clearly show the temperature distribution on the surface of an object [53].

1.6.2. Gaseous emissions: identification and quantification

In Figure 14b is reported the second typical products of the TR, the gas emissions. The main gases produced by the decomposition of the electrolyte and the reaction between the active materials are carbon monoxide (CO), CO_2, methane (CH_4), HF, the electrolytic solvents, and a variety of hydrocarbons [54], as shown in Figure 15 [55].

From Figure 15 it is possible to observe the variation of the gas composition according to the range of temperature. The main reactions that can occur during these phases, such as SEI decomposition, venting and thermal runaway were already presented in the previous section, Abuses of LIBs.
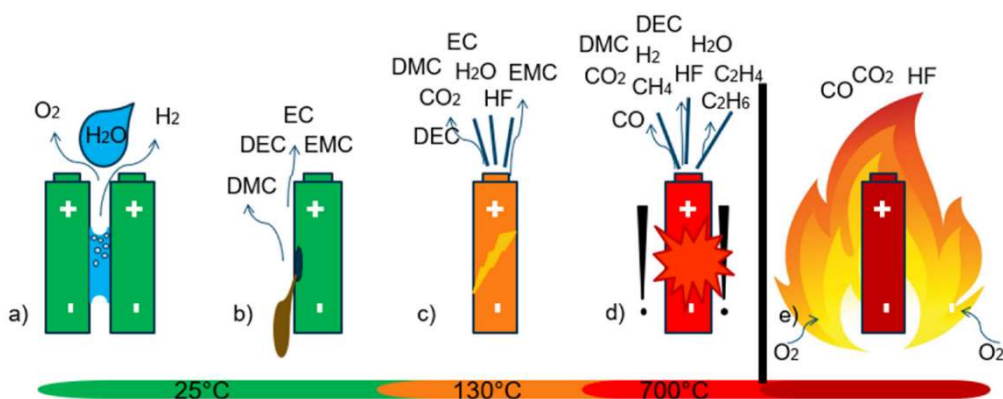
Figure 15: gases emission at various temperatures: (a) around 25 °C; (b)around 100 °C; (c) around 130 °C; (d) around 700 °C; (e) over 700 °C [55].

At about 25 °C (Figure 15a) if the cell is under voltage (in a module and/or in a battery pack) an unwanted electrolysis of liquid coolant or condensed water can take place. The product of the electrolysis process of water molecules is pure oxygen and hydrogen, with all the safety problems concerning the release of pure

H_2 in the atmosphere due to the broad flammability range [55]. If the temperature increases between 55 and 130 °C (Figure 15b), it can be observed the vaporization of the electrolyte. If the temperature continues to increase, over 130 °C (Figure 15c) the venting will occur releasing in the atmosphere the products of the reactions between the different internal components, such as anode and electrolyte, as reported in Equations (8), (9), and (10). A rapid increase in temperature, due to the exothermicity of the reactions, will bring the system to the TR, at temperature of about 700 °C (Figure 15d), with the release of other gaseous products by the reaction between the internal components and the previous products, i.e. flammable hydrocarbons (C_2H_4, C_3H_6) and lithium carbonate (Li_2CO_3). The process will end with the total combustion of the cell (Figure 15e) due to the production of oxygen from the electrolyte, as reported in Equations (11), (12), and (13).

Even if the mechanism of the safety devices, such as venting, and the relative reactions occurring inside the cell are almost clear the final products, in term of total amount released and relative danger, are not still well investigated. In fact, in literature there are many works studying the behavior of the single components or the whole Li-ion cell when subject to a thermal abuse anyway the comparison between them is not actually possible due to the different parameters that affects the TR products, such as chemical composition, SoC, abuse conditions, and measurement system. The TR products are strictly dependent on the component characteristics, so according to them the reactions occurring inside the cells and the composition of the gases can vary. The higher SoC, so the level of energy available inside the cell, can triggered the internal reactions causing the production of different products compared to lower SoC. The abuse conditions, such as the oxidative atmosphere (air) or the inert atmosphere (N_2) can lead to the complete combustion of the products, more CO_2 instead of CO. Finally, the heating source (electric heating or direct flame) can effect the severity of the TR and the relative products.

The thermal abuse test on the single components of the Li-ion cells given back information about the thermal stability of the single material, such as anode or cathode active material, and according to the techniques applied the results can be expressed in terms of temperature and enthalpy of the reaction, using the differential scanning calorimetry (DSC) [56], or in mass lost, thermal gravimetric analysis (TGA) [57]. Instead, the thermal abuse test on the assembled cell given back the thermal stability of the cell considering all the materials and even the electrical energy storage inside, indicated by the SoC. The test in this case can be performed by the single burning item (SBI) [58], the calorimeter cone [59], the combustion chamber [60] to obtain information on the temperature, the time, the gas released and the mass loss. Comparing these two kinds of tests, the tests conducted on the single components or on whole cells leads to different thermal response [61], in fact it emerged that full cell presents a higher temperature than the anode and the electrolyte reactions, but lower than the cathode decomposition [62]. These changes are due to the more complex system present inside the assembled cell and the secondary reactions that can take place between the products of the first reactions and the components. Improving cathode stability there is an increase in the thermal stability with both higher thermal runaway temperature and a reduction of peak heating rate. Comparing the commercial chemical composition it emerged that the LFP are the most thermally stable while the LCO presented the lower onset temperature coupled with the highest self-heating rate [63]. The greater stability of the LFP is given by the fact that the production of oxygen inside the cell, due to degradation of the internal materials, occurs above 500 °C, also causing a slower heating rate [62].

Regarding Li-ion cell characteristics the principal factors that must be considered are the SoC and the internal chemical composition. For a fully charge (100 % SoC) the oxygen consumption is higher than for other SoC levels, the temperatures increase sharply after the onset temperature of TR leading to a higher maximum

temperature and a variation in the gas production [61]. With regards to the gases produced during TR they are mainly CO, CO_2, CH_4, fluorinated compounds such as HF, POF_3 and PF_5 [64] and the electrolytic solvents, such as DMC, EC, and DEC [65]. The production of fluorinated compounds, such as HF, POF_3 and PF_5, is due to the decomposition reaction of the PVDF binder, the Li-salt used and the active cathode material [64]. There are conflicting data on the trend of these compounds from the results presented by Larsson (2016), the greater quantity of HF occurs due to low SoC while Peng (2020) shown that the increase in SoC also increases the production of HF and the toxic or highly toxic properties of gases [66].

To analyze the emitted gases, according to the nature of the gases species, different analytical techniques can be used, such as Fourier transform infrared spectroscopy (FT-IR) or gas chromatography (GC) and both these techniques can be connected online [42], [58], [67]. In the literature these techniques can be applied on continuous gases, so the instrument is positioned at the exit of the test chamber, or collecting them in gas bags before analysis, to have an overview of the gases emitted. The difference between the two methods is given by the information that can be obtained, an emission profile in the first case or a total emission in the second case.

The FT-IR can identify trace contaminants in high-purity gas samples but even the different components in gases produced during combustion process. The main advantages of infrared spectroscopy are the simultaneous measurement of many frequencies within a single scan, providing information for many types of chemical bonds, it is non-destructive technique and can provides a precise measurement in a short time as 5 scans/second. Due to the speed of the measurement the gas flow, such as the flow exit from a test chamber, can be monitored continuously, providing a concentration versus time trend chart [68]. In fact, by using the standard gas it is possible to obtain extremely stable calibrations lines that can be used on the real sample to obtain the calibration of the species in

a very wide range of concentration [64]. To increase the wavenumber spectra range, until 4500 cm^{-1}, and to enhance the resolution of the instruments, 1 cm^{-1}, a mercury cadmium telluride (MCT) detector cooled by nitrogen can be installed instead of the traditional deuterated triglycine sulfate detector (DTGS) [42].

The GC can be coupled with different detectors, such as the mass spectrometry (MS), flame ionization detector (FID) or thermal conductivity detector (TCD). This technique permits to separate the gases species present in a complex mixture and to identify and quantify them according to the retention time (t_R) and the compositional, mass, or thermal properties. The main species that can be analyzed are the volatile organic compounds (VOCs), the hydrocarbons and the carbonates. Even for these techniques it is possible to quantify the substances identify according to calibration lines or to addition of a known quantities of internal standard (ISTD) to the sample. A precaution that must be taken regard the compatibility between the column used for the GC separation and the nature of the gases, in fact since the GC uses corrosion sensitive columns, the gas must be purify before the injection, such as using water washing bottles [42]. For this reason, toxic species, such as the fluorinated compounds, cannot be analyzed by GC.

So, to have more complete information about the TR process and the relative products it is better to perform the thermal abuse test on the whole cells.

Another evaluation that can be considered to, regarding the safety aspect, is the total amount of flammable and/or toxic gases produced during TR [63]. In fact, the measured values must be compared with the flammability limits or the regulation limits, such as the IDLH defined by the NIOSH [51].

1.6.3. Particle emissions: identification and quantification

Finally, the last typology of products that can be emitted during a TR are the particle emissions. The risk for the safety can be of double nature. The first one is about the chemical composition and the size of the emitted particles, that can be in

the respirable size range, particulate matter with a diameter lower than 10 and 2.5 μm (PM10 and PM 2.5), and the second one about the composition of the solid particles.

As reported in the literature [69], the most common solid sample that is ejected during the TR is made of thinner particle, comparable to an aerosol, in which the particles have a diameter in the range between 8.5 and 300 μm. The main aspects that must be evaluated in this case are the physical-chemical properties, such as the diameter of the particles and the chemical composition of it. Generally, the solid particles collected after TR can be composed of carbon, organic compounds (i.e., carbonates), transition metals, transition metal oxides and other species, in composition and particle sizes depending on the type of cell and the abuse conditions [70].

One important aspect about the particle emissions that must be evaluated, after the chemical composition, is the shape of the cell such as cylindrical, pouch, coin or prismatic. In fact, according to the shape of the Li-ion cells different safety device have been improved to contrast the different abuse conditions. The response to overheating, and consequent overpressure inside the cells, in the case of the cylindrical and prismatic Li-ion cells is due to the rupture of a valve disk while in the case of the pouch there is a less resistance part in the welded ends. In both cases the result is the emission of gases to reduce the inner pressure and to mitigate the TR consequences. The two technologies present differences in the function and in the emissions, in fact the vent disk supports a higher internal pressure before the rupture compared to the pouch opening, and this effect the quantities of materials released. In fact, the vent disk causes a higher velocity of the release in a short time, producing more incomplete combustion products [71]. However, theoretical values of internal activation pressure at which CID-vent disk activation and/or venting can occur are indicated in the literature. In any case, in

the studies conducted so far no pressure values inside the cell have been measured neither gas released during venting and/or TR outside the cell.

The mechanism of production of the particles in the case of the cylindrical and prismatic cells, shown in Figure 16, is caused by the rupture of the cathode materials, due to a different pressure in the cell, while the chemical composition of particles depends from the original composition of the cathode [72].
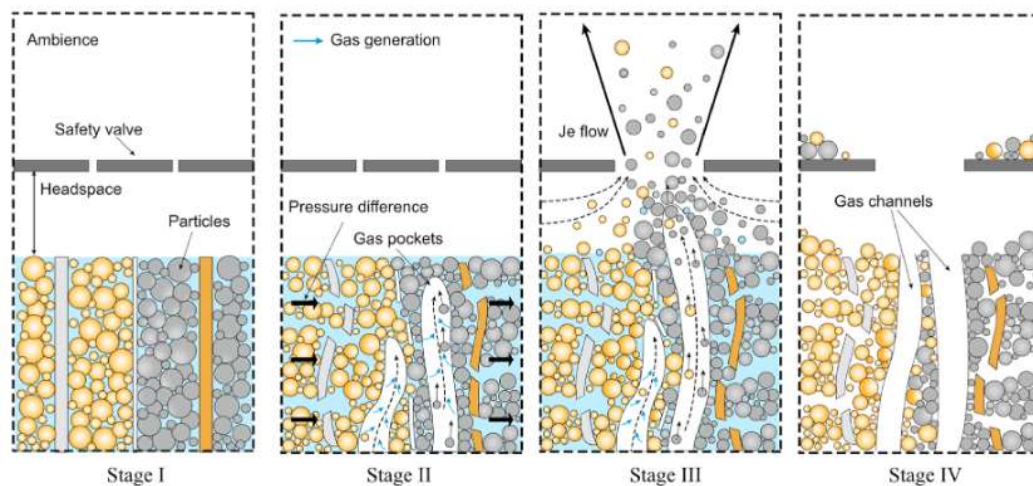
Figure 16: Mechanism of particle's ejection from lithium-ion batteries during TR, where the yellow particles represent the cathode active material on the aluminum foil while the gray particles represent the anode active material on the cupper foil [72].

In stage I the cell is intact, so all the components are at the initial state and the safety devices are not activated. Due to abuse the thermal degradation reactions start occurring causing the release of massive gases and temperature increasing, as shown in stage II. These increases cause a pressure difference between the component layers leading to fracture of the electrode materials. Another reaction that can take place, at this temperature, is the binder debonding. So, these reactions lead to the interparticle fracture and pulverization with the subsequently gas pockets formation that increase the pressure gradient.

Stage III reports the movement caused by the internal degradation reactions, in fact the fragmented electrode materials are in motion with the gas pockets. So, the particles can be transported and projected first from the interior of the jelly roll to the headspace of the cell and then from the headspace to the free space through

the safety valve. In the ejection phase the particles are accelerated due to the increasing momentum at the nozzle. At the end, stage IV, the ejected particles leave numerous channels of gas pockets, which explains the collapse in the structure of the spiral wound layers.

The main reactions that can occur during the collapse of the layers and the ejection of the particles into the environment depend on the internal chemical composition, as reported in the following Equations regarding the LCO and NCM reactions. In the case of the LCO, at high temperature the lithium metal oxides ($LiCoO_2$), can be reduced to cobalt (Co) metal and lithium carbonate (Li_2CO_3) by the reaction with the graphite (C) and this reaction can take place under different conditions even under an oxygen-free atmosphere (Equation (21).

$$4\ LiCoO_2 + 2\ C \rightarrow 4\ Co + 2\ Li_2CO_3 + O_2 \tag{19}$$

$$2\ LiCoO_2 + 2\ C \rightarrow 2\ Co + Li_2CO_3 + CO \tag{20}$$

$$4\ LiCoO_2 + 3\ C \rightarrow 4\ Co + 2\ Li_2CO_3 + CO_2 \tag{21}$$

The metal carbonate can undergo a chain degradation reaction which leads to the production of metal oxide (CoO), CO_2, CO and O_2.

The NCM decomposition reactions are similar to the LCO ones. So, the first reaction, (Equation (22) is a disproportionation followed by autocatalytic reactions of Ni and Mn oxides (Equation (23) and Equation (24).

$$Li_{1-x}(Ni_{1/3}Mn_{1/3}Co_{1/3})O_2 \rightarrow Li(Ni_{1/3}Mn_{1/3}Co_{1/3})O_2 + Ni_2O_3 + Mn_3O_4 +$$

$$Co_3O_4 + O_2 \tag{22}$$

$$Ni_2O_3 \rightarrow 2\ NiO + \tfrac{1}{2}\ O_2 \tag{23}$$

$$Mn_3O_4 \rightarrow 3\ MnO + \tfrac{1}{2}\ O_2 \tag{24}$$
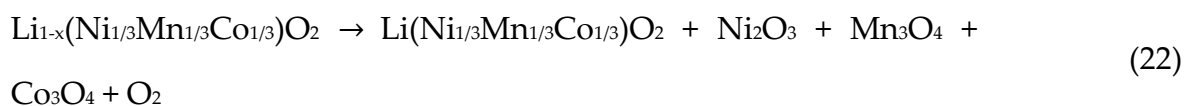
The few studies available in the literature [69] confirm that the particles are mainly composed of metals, due to the active material cathode degradation and it is dependent on the initial composition of the cell. LFP cells showed very

homogenous particles composed by cenospheres of carbon, silicon, and fluorine while NMC and LTO particles are composed of various transition metals, such as cobalt, aluminum, and oxygen. Even the size plays an important role in the safety, a large number of particles are in the respirable size range.

To analyze the ejected solids particles, different analytical techniques can be used, such as X-ray fluorescence (XRF) [70], scanning electron microscopy (SEM) with X-ray energy dispersive spectrometry (EDX) [69] and inductively coupled plasma (ICP) or atomic absorption spectroscopy (AAS), but all these techniques cannot be connected online to the test chamber due to the pretreatment necessary to prepare the sample and/or the atmosphere in which the analysis must be taken [69], [70]. The main advantage of the XRF analysis is that these is non-destructive analytical techniques while ICP, AAS and SEM, just if the conductive layer is necessary, are destructive analytical techniques. So, the size diameter can be evaluated by the SEM analysis while the chemical composition can be evaluated by different techniques, such as XRF, XRD, SEM-EDX, ICP or AAS, obtaining different kind of information.

XRF is used to determine the elemental composition of materials by measuring the fluorescent X-ray emitted from a sample when it is excited by a primary X-ray source. So, the analysis permits to determine all the elements contained in the sample, such as carbon and aluminum [70].

SEM analysis permits to obtain microscopic picture of the distribution of the elements in the sample and to measure the diameter of the particles. According to the detection modes material contrast, imaging with backscattered electron (BSE), or topographic contrast, imaging with secondary electrons (SE), can be evaluated. Finally, if combined to the EDS detector it is possible to obtain even information on the elemental analysis, such as carbon, titanium, phosphate, and cupper [42], [69]. The limitation of these technique, correlated to the LIB fields, is that the presence of lithium cannot be verified by this analysis, in fact SEM-EDX only

detect the Z > 3, Li is too light and cannot be detected for the very low energy of characteristic radiation.

ICP and AAS permit to determine the elements present in the sample with a high sensitivity and to quantify the concentration due to the stability of the calibration lines. Due to the acid digestion, in regia water (3:1 volume over volume (v/v) nitric acid (HNO_3): hydrochloric acid (HCl)) usually, used to dissolve the metals, this technique can be used both for solid and liquid samples and permits to eliminate the organic interference. So, the contribution of the electrolyte components cannot be evaluated by this technique.

Anyway, a comprehensive safety assessment is still lacking, with few investigations regarding the size and the chemical composition of the particles produced during the TR.

1.7. Nanomaterials (NMs) as active materials for LIBs and safety concerns

The increasing use of LIBs in a huge variety of applications requires an increase in capacity, longevity, and charge/discharge rate [73]. To reach this goal the materials currently used as active materials for both anode and cathode must be improved. In fact, the limitation in capacity of the actual LIBs materials is due to the micrometer size of both the anode and cathode active materials particles and of the pores of the plastic separator. The introduction of nanomaterial (NMs) in the internal chemical composition shows improvement on the global capacity of the LIBs enhancing the performance of these devices [74]. At the same time the NMs decreasing the safety properties of the pristine materials increases the explosivity risk [75] and impact on the aquatic system, defined as eco-toxicity [76]. The aim is to guarantee a safety increase of the performance of the new electrical devices.

1.7.1. Nanomaterials (NMs) as active materials for LIBs

The limitation of the actual materials available both as active powder materials for the anode and the cathode is due to the space and the density volume. In fact, the actual materials have micro-size dimension that limits the intrinsic diffusivity of

the Li-ion that can be intercalated in the solid state on the anode and that can pass through the separator. Although the battery has a high energy density but is a low-power device, expressed as slow charge/discharge rate [73]. To increase both the rate of intercalation/deintercalation rate and the charge/discharge rate, the micro powders used as active materials must be replaced by the same materials or even different ones under NMs [77]. In fact, due to the smaller size these materials showed a shorter diffusion length and a higher contact area between active materials and electrolyte [78] that can enhance the performance and the storage battery capacity with a reduction of the batteries dimension [74].

With the term NMs are indicated the substance with an outer diameter of at least one nanometer [74]. The European Commission standardized the terms in the Commission Recommendation of the June 10th 2022 [79]:

"'Nanomaterial' means a natural, incidental, or manufactured material consisting of solid particles that are present, either on their own or as identifiable constituent particles in aggregates or agglomerates, and where 50 % or more of these particles in the number-based size distribution fulfil at least one of the following conditions:
(a) one or more external dimensions of the particle are in the size range 1 nm to 100 nm;
(b) the particle has an elongated shape, such as a rod, fiber or tube, where two external dimensions are smaller than 1 nm and the other dimension is larger than 100 nm;
(c) the particle has a plate-like shape, where one external dimension is smaller than 1 nm and the other dimensions are larger than 100 nm."

According to the articles available in literature different NMs have been evaluated for both the positive and the negative electrodes. These NMs can have various morphology such as nanoparticles (NPs), nanotubes (NTs), nanowire (NW), hallow nanosphere, porous nanostructure and can be used as pristine or as a mixing or by coating. The NMs can be applied both to the anode and the cathode and in Table 3 is reporting a summary of the main NMs under investigation, with the relative application and reference study.

Table 3: brief summary of the nanomaterials under investigation, with the relative application and reference.

Material	Application	Reference
Si	Anode	Wang et al.; [80]
Si	Anode	Chen et al.; [81]
Carbon coating on the Si surface	Anode	Wang et al.; [80]
Mixing Si with C-based	Anode	Chen et al., 2014; [81]
Mixing Si with C-based	Anode	Chen et al., 2017; [82]
Si with polymer and chemical bonding	Anode	Erk et al.; [83]
Si with polymer and chemical bonding	Anode	Assresahegn et al.; [75]
Hybrid 0D and 1D Si	Anode	Pinilla et al.; [84]
SiO_2	Anode	Al Ja'farawy et al.; [85]
$Li_4Ti_5O_{12}$	Anode	Hudak et al.; 2014 [86]
$LiFePO_4$	Cathode	Hudak et al.; 2014 [86]

The most interesting and developed NMs for the cathode is the $LiFePO_4$ [86]. The principal advantages of these materials are the intrinsically low ionic, the electronic conductivity, the high theoretical capacity for full de-lithiation (170 mAh g^{-1}), and the degree of reversibility, due to the cycling mechanism for this material. In fact, the mechanism is based on a phase transformation between two phases, $LiFePO_4$ and $FePO_4$, with a very similar structure that permits to obtain a theorical reaction potential for lithiation/de-lithiation of almost 3.45 V Li/Li^+. While, the two main possibilities for the anode active material are the are the titanium (Ti) and silicon (Si) based NMs. In the case of the titanium-based NMs different forms are under investigation [86]. The principal form is the $Li_4Ti_5O_4$ but can be even used various form of TiO_2. The $Li_4Ti_5O_{12}$ cycling mechanism is quite similar to what has been reported for the $LiFePO_4$, in fact the Li^+ insertion due to the formation of $Li_7Ti_5O_{12}$ at 1.55 V versus Li/Li^+ with a theoretical capacity of 175 mAh g^{-1} and a high degree of reversibility. The material applied is the lithium titanate spinel in nanocrystalline or nanoparticulate to achieve a higher charging rates and extended cycle life compared to the same material in micron size. In literature most of the studies are developing material made of or with silicon to substitute the graphite powder in the anode composition. The Si-NPs choice is due to the highest gravimetric and volumetric capacity among all the elements actually developed for this rule [87] and the lighter batteries produced. The shape, dimension, and combination in which the Si-NPs can be applied as anode

materials are various and can be classify as zero-dimensional (0D) NPs, one-dimensional (1D) NWs/NTs, two-dimensional (2-D) nanosheets, and three-dimensional (3D) porous structures. Si is very attractive since it comes from an abundant source, it is cheap, and has a high theoretical capacity of 4200 mAh g^{-1}, and it is reacting with lithium forming the alloy SiLi$_x$, with $0 < x < 4.4$. However, Si-NPs have two major drawbacks, the first is the volume change during lithiation and de-lithiation (with an expansion/contraction of about 300 – 400 % in volume) and the second being the unstable SEI [22]. In fact, the large amount of lithium involves large structural changes, expressed in volume, that can reach up to 400 %. This volume expansion represents the main disadvantages of silicon NMs because this cause an irreversible loss of capacity due to the continuous SEI formation and a poor retention capacity due to the pulverization of the Si-NPs [88]. These are the main reasons why Si is considered in various morphologies containing also other species, such as carbon coating on the Si-NPs surface, mixing the Si-NPs with C-based NMs, new polymer binders and chemical bonding to decrease the Si degradation and enhance the electronic conductivity and structural stability [89].

1.7.2. Safety concern about NMs as active materials for LIBs

The increasing in performance anyway must be balance with the safety characteristics in terms of thermal behavior and eco-toxicity of the pristine NMs. In fact, the reduction of the size can significantly affect the well-known properties of the respective material in micro scale for the explosivity and the eco-toxicity. The reduction of the size increases the specific surface area (SSA) of the material increasing the reactivity, while in an organism the size reduction enhances the capabilities of the NMs to bind with toxic pollutants that can be inhaled, travelling freely in the blood reaching the main organs and be accumulate inside it [76]. So, the NMs characterization, the relative explosivity risk, and the eco-toxicity must be evaluated again.

1.7.2.1. Characterization on the NMs

The NMs characterization and the relative safety are necessary to a proper risk assessment due to the use of these materials in the LIBs. First, it is necessary to characterize the NMs according to the physical-chemical properties, such as size distribution, composition, dispersibility, agglomeration, surface area, porosity, and shape [90]. These properties can be divided in intrinsic and extrinsic, where the first term is referring to the characteristics of the material, such as size, surface area and composition, while the second term is referring to the reactivity of the material according to the medium, such as surface charge, surface chemistry and aggregation. So, the behavior of the NMs, both as pristine (as produced) and as mixture, is given by the combination of a high number of properties. These properties can be evaluated according to different techniques and can change compared to the same material on micro-scale [73].

- Composition analysis, by XRD, ICP-MS or ICP-OES, Raman, and SEM-EDX, returned the information on the bulk, core and shell, composition. Some methods return event the atomic composition or the structural details.
- Crystal structure can be evaluated by XRD, and transmission electron microscopy (TEM) to evaluate the structure.
- Primary particle size and distribution measurement can be evaluated by hydrometric size, such as dynamic light scattering (DLS) and nanoparticle tracking analysis (NTA), or by microscopy method, such as SEM and TEM.
- Specific surface area can be evaluated by Brunauer-Emmett-Teller (BET) or liquid nuclear magnetic resonance spectroscopy (NMR).
- Surface charge can be evaluated by the measurement of electrophoretic mobility by optical or acoustic methods, such as zeta potential.

As reported below in some cases the same technique can be applied to evaluate more properties [91]. For example, the XRD can provides information on the

crystalline structure, nature of the phase, lattice parameters and crystalline grain size. The solid sample can be analyzed in form of powder and the composition of the particle can be obtained by the comparison with the reference patterns available. The most important parameter that must be evaluated is the NPs size, in fact due to the higher surface-to-volume of the NMs compared to the micro-ones the reactivity at the molecular level increase exponentially. This property can be evaluated by different techniques, such as BET, TEM, and XRD. The main problem of the size determination is the agglomeration tendency of the NPs. TEM and XRD can be applied by especially for the spherical shape.

1.7.2.2. Explosivity risk

The flammability behavior and the explosivity risk for the NMs is strictly linked to the particle physical-chemical properties [90] and to the dispersion conditions. An explosion can occur when the NMs are dispersed into an atmosphere containing sufficient oxygen to permit combustion and ignition source of appropriate energy is present. The expansion of hot gaseous products generates a pressure wave. The mechanism behind the flame acceleration process in dust explosions is essentially the same as for gas explosions, so the expansion of combustion products introduces flow which generates turbulence enhancing the heat and mass transfer. The turbulent flow results in a higher rate of combustion, which creates more expansion, which creates more turbulence, etc. [92]. The decrease of the particle size leads to an increasing of the SSA with an increase in sensitivity to explosion and a significant change of the explosion severity [92]. Moreover, several studies demonstrated that a significant increase in explosion severity occurs as the particle size decreases to nano meters with a plateau for smaller particle sizes [93].

However, if for some materials the behavior has been already investigated it is important to take in account that the decreasing of the particle size, from a microscale to a nanoscale, determined a significant variation in the ignition and explosion behavior [75]. In fact, a higher potential of ignition and explosion risks

have been determined for nano-materials than for micrometer sized materials [93]. The explosivity and severity of an explosion can be expressed by various parameters that can be evaluated by laboratory-standardized explosivity tests, such as the minimum ignition energy (MIE), the minimum ignition temperature (MIT), the minimum explosivity concentration (MEC) and the explosivity factor, with the instruments shown in Figure 17.

(a)   (b)   (c)
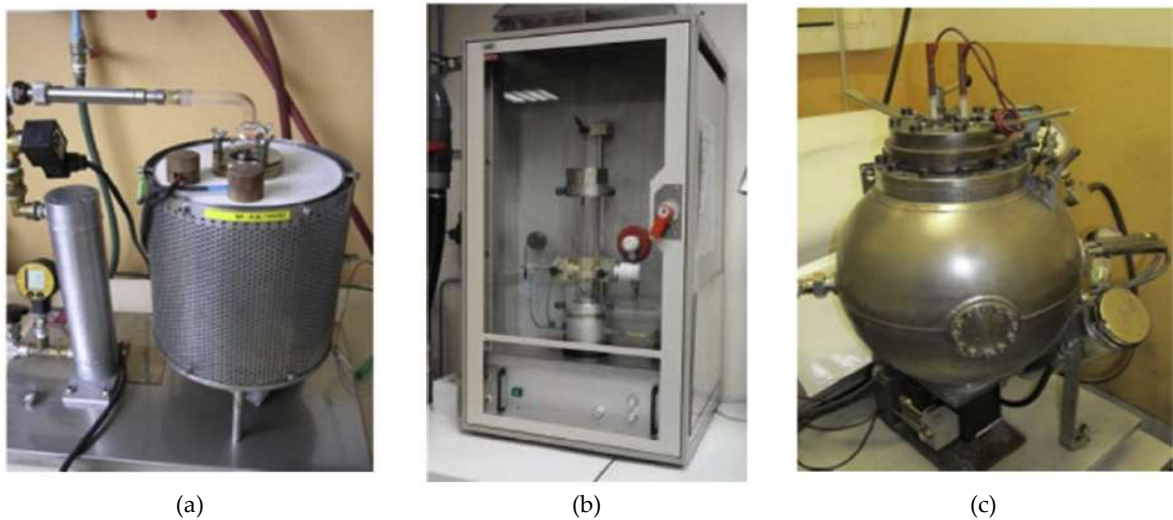
Figure 17: (a) Godbert-Greenwald furnace or BAM; (b) Hartmann tube or Mike III tube; (c) 20-L explosion sphere.

The MIT assessed the lowest temperature at which flame is observed and can be evaluated by the Godbert-Greenwald furnace [94], called even BAM and shown in Figure 17a, according to the NF EN ISO/IEC 80079-20-2, Explosive atmospheres – Part 20-2: Material characteristics – Combustible dusts test methods [92]. The apparatus consists of a cylindrical furnace held in a constant temperature furnace, with 600 °C as maximum temperature value, into which the dust is suspended at different concentrations to determine the lowest temperature of ignition. The MIE assessed the electrostatic ignition risk [93] and can be evaluated by the Hartmann tube [95], called even MIKE and shown in Figure 17b, according to the standard references, such as the NF EN ISO/IEC 80079-20-2, *Explosive atmospheres – Part 20-2: Material characteristics – Combustible dusts test methods* [96]. The apparatus consists of a 1.2-L cylindrical glass chamber into which dust is dispersed and then ignited by an electrical spark of know energy, with 1 J as maximum ignition value

[97]. The ignition source is mainly a capacitor discharge spark igniter, and the test consists in observing for a given powder concentration the flame propagation at least 6 cm away from the spark electrodes, to evaluate the ignition energy necessary for explosion to occur [94]. The MEC and the explosivity factors, such as maximum explosion pressure (Pmax), assessed the severity of the explosion and can be evaluated by conducting the experiments inside a 20-L sphere apparatus, shown in Figure 17c, according to the NF EN ISO/IEC 80079-20-2, *Explosive atmospheres – Part 20-2: Material characteristics – Combustible dusts test methods* [96], and the NF EN 14034, *Determination of explosion characteristics of dust clouds*, in part 1, *Determination of the maximum explosion pressure pmax of dust clouds*, part 2, *Determination of the maximum rate of explosion pressure rise (dp/dt)max of dust clouds*, and part 3, *Determination of the lower explosion limit LEL of dust clouds* [98]. This apparatus is used to determine dust explosivity parameters based on overpressure, and/or rate of pressure rise, $(dP/dt)_{max}$, development. The material is dispersed in the 20-L sphere, from an external reservoir where is pressurized with air, and then ignited by the ignitor [99]. The ignition source, placed in the center of the sphere, is an electrical igniter with an energy between 2 and 10 kJ according to the analysis [97]. The minimum amount required to initiate an explosion for many dusts is strictly correlated to the dust layer thickness. So, the MEC can be defined as the minimum layered dust raised into suspension to form a dust cloud that can be ignited by a sufficiently energetic ignition source, and can be calculated according to the Equation (25) [100].

$$C = (\rho_{bulk}) * (h/H) \tag{25}$$

where C is the resulting dust concentration (g/m³), ρ_{bulk} is the bulk density of a dust layer (kg/m³), h is the layer thickness (mm) and H is the height of the dust cloud produced from the layer (m).

So, dust explosions do not require so deep layers of combustible material and the MEC is directly proportional to the bulk density. From the determination of the maximum explosion pressure, Pmax, and the maximum rate of pressure rise,

(dP/dt)$_{max}$, it is possible to calculated the explosivity factor (K$_{st}$), even called explosion severity factor, from the cube-root law reported in Equation (26).

$$K_{st} = \left(\frac{dP}{dt}\right)_{max} * V^{1/3} \tag{26}$$

where V is the volume of the vessel (m³), t is the time (s) and $\left(\frac{dP}{dt}\right)_{max}$ is the maximum rate of pressure rise (bar/s).

The value obtained from Equation (26) give back the size-normalized maximum rate of pressure rise for a constant-volume explosion. The severity of the explosion can be classified according to the following classes; if the value is 0 the explosion feature is nil, for values between 1 and 200 the feature is weak, between 201 and 300 is strong while when the valuer is higher than 300 the explosion feature is classified has very strong.

Even if the MEC, MEI, P$_{max}$, and (dP/dt)$_{max}$ can be determined, it must be underlined that these explosivity parameters are strongly dependent on both the material characteristics, such as particle size or SSA, and experimental conditions, such as, turbulence, vessel volume or applied ignition energy. So, the principal properties that can affect the explosivity parameters are the particle size, concentration, ignition energy and turbulence [101]. The most important property that must be evaluated and considered in the dust explosion, especially for the nanomaterials, is the dust particle size. In fact, a decrease in particle size causes an increase in the surface area with an enhancement of dust explosivity [97]. According to the production and the environmental conditions the particles can create agglomeration modifying the initial particle size distribution. So, in the case of the dust is measured the polydispersity in order to evaluate the degree of heterogeneity of particle size, according to the Equation (27) [102].

$$\sigma_D = (D_{90} - D_{10})/D_{50} \tag{27}$$

where σ_D is the particle size polydispersity, D_{90} is the diameter greater than 90 volume % of the particles (μm), D_{10} is the diameter greater than 10 volume % of

the particles (μm) and D_{50} is the diameter greater than 50 volume % of the particles (μm).

This property significantly affects the explosivity of NMs, in fact a decrease of σ_D leads to a significantly lower value of K_{st} and a higher value of MIE compared to samples with higher σ_D.

The ignition energy must be sufficient to initiate combustion of dust dispersion. The ignition of dust explosion can be of different in origin and nature, such as electrical (electrical sparks), mechanical (impact sparks), or thermal (flames and direct heat). These are all high energy able to ignite the dust particle but especially for nanoparticles the energy required to obtain the ignition is lower than micrometer particles (< 1 mJ vs 20 mJ).

The turbulence is referred to the rapid movement of the small elements inside the dust cloud. In the case of dust explosion there are two different turbulence that must be considered, the first before the ignition, called pre-ignition or initial, and the second one after the ignition, called post-ignition or explosion generated. The pre-ignition is generated by the industrial process while the post-ignition is caused by the combustion process [99]. The turbulence is due to the movement of unburn dust ahead of the propagation flame. A higher turbulence of the dust on one hand can makes ignition more difficult, but on the other hand can accelerate the combustion leading to higher overpressures and rates of pressure rise [97].

So, in conclusion the nanosized sample is clearly ignitable at lower ignition energies and significantly lower dust amounts than is the micrometer sample. In any case, even if many standard references have been developed to evaluate the dust explosion parameters these must be correlated to the physical-chemical properties of the NMs.

1.7.2.3. Eco-toxicity on the NMs

Eco-toxicity evaluates the biological, chemical, or physical stressors caused by natural or artificial pollutants on the ecosystem population, so microorganisms,

plants, and animals, including humans. In fact, these stressors, such alteration of the parameter or concentration in the environment, affect the natural uptake mechanisms and the influence of environmental factors on bioavailability [103]. With the aim of protecting individuals, ecotoxicity looks at various trophic organism levels, to find a correlation between the potential pollution agents and the toxic effect on the organism to calculate the dangerous concentration [104].

Specifically, the aquatic toxicity can be evaluated by test on microorganisms, aquatic plants, algae and cyanobacteria, aquatic invertebrates and fish. According to the typical food chain, reported in Figure 3 [105], algae and daphnia, which are at the base of the aquatic alimentation pyramid, can assess the health of a freshwater system. By ensuring that the lower parts of the food chain are healthy, the higher ordered organisms, like fish, whales and even humans will be protected. For this reason, is important to understand the role and the function that regulated the aquatic ecosystem to evaluate the diffusion of the pollution across the different species levels [106]. The aquatic food chain can be summarized as a prey species–predator species loop in which the nutrients and the energy are transferred in continuous. The organic matter present dissolved in water, the nutrients, can be used by the algae, circle in red in Figure 3, to produce their own food and growth.
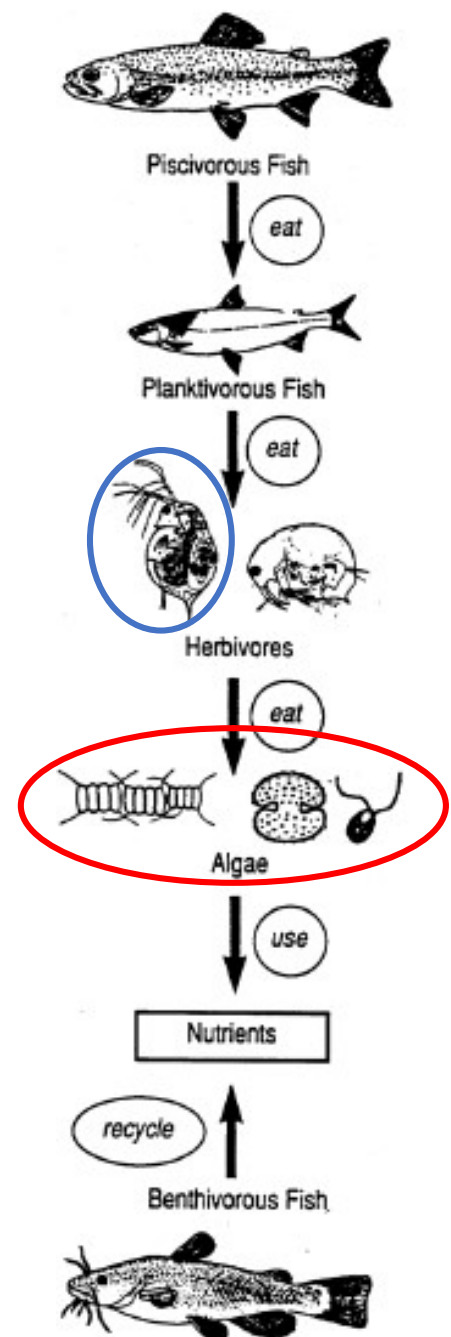
Figure 18: a typical aquatic food chain [105].

The edible algae can be eaten by the other microscopic animals, such as the rotifers. One of the most important rotifers is the Daphnia Magna, circle in blue in Figure 3. Daphnia Magna can be considered a fresh-water filter-feeding organism due to the sensitive to water pollution; in fact, can ingest nano- and micro-sized (20 nm to 70 µm) particles present in water [107]. The microscopic animals are then food for the macroscopic fishes and in turn are then eaten by humans. During the lifetime macroscopic fish release nutrients in water that can feed the growth of algae. For this reason, the aquatic food chain can be defined as a prey species–predator species loop.

The basic organisms that can be tested to evaluate the eco-toxicity of the NPs are the daphnia and algae. In fact, even if Daphnia and algae are relatively simple organisms, they shown a high bioaccumulation of the of NPs on their organism that leads to modification in the identity, stability and absorption and excretion of organisms, which are all parameters that can be evaluated experimentally.

All these parameters can be evaluated experimentally following the guideline emitted by the Organisation for Economic Co-operation and Development (OECD) for each organism [103]. Independently form the species, the eco-toxicity can be assessed by defining conventional ecotoxicological endpoints, such as lethality or immobilization, or more sensitive, sublethal endpoints, such as heartbeat rate feeding activity and reactive oxygen species (ROS) [108]. The eco-toxicity is then expressed by the following parameters, the concentration that caused a modification/reduction in 100 % of the population (EC_{100}), in 50 % of the population (EC_{50}), in 10 % of the population (EC_{10}) or no-observed-effect-concentration (NOEC). The toxicity results are affected by the intrinsic and the extrinsic properties due to the interaction between the material and the medium in which it is dispersed. In fact, the intrinsic properties of the material, such as size, surface coating, solubility, and pH, affect the dispersion of the material in the medium. So, the final evaluation on toxicity is not just correlated to the exposure

route but even to the physic-chemical properties, such as core the hydrodynamic size and the aggregation state [109].

For the daphnia the relative standard references are the OECD TG 202 [110], Daphnia sp. Acute Immobilization Test, and the OECD TG 211 [111], Daphnia magna Reproduction Test. In this case, the parameter affected by the interaction between the pollution material and the daphnia is the mobility, in fact water pollution brings to both changes to the organism at internal cellular levels and at the physical level that affect the ability to swim. So, the ecotoxicological end point after the 48 h of test is the immobilization of the organisms. While for the algae the relative standard reference is the OECD TG 201 [112], Freshwater Alga and Cyanobacteria, growth Inhibition Test, and the parameter affected by the interaction with the material is the growing rate, due to the cell membrane morphology cell apoptosis, cell death, genotoxicity, mitochondrial damage, and ROS. So, to evaluate the impact on the algae of the material the ecotoxicological end point after the 72 h of test is the reduction of the growth rate.

The guidelines mentioned are standardized for the micro pollution materials but in the case of NPs there may be some problems with dispersion of the material in the matrix and with stability during the test time, due to the structural and surface properties changing [104], [108]. For these reasons the OECD TG 23 [113, p. 23], Guidance Document on aquatic toxicity testing of difficult substances and mixtures, has been developed to indicate some extra procedure that can be applied when difficult substances are tested. The term difficult substance indicated all the substances which are volatile, strongly adsorbing, colored, having a low solubility in water or substance that may affect the availability of nutrients or minerals in the test solution, so-called medium.

In fact, in the case of NMs the number of parameters that must be evaluated increase due to the dispersion, stabilization, agglomeration, and aggregation of the NMs in the medium. The principal problem is given by the different size between

the pristine powder and the powder dispersed in the medium, where the size plays a fundamental rule in the uptake mechanism and the relative kinetics of the NPs in the organism due to the higher permeability across the cell barriers [114]. For example, in eco-toxicity test TiO_2, with an initial particles size of 20 nm, showed in the test solution a medium size of 1000 nm [115], which is not considered anymore nanomaterial according to the definition reported in the Commission Recommendation of the 10 June 2022 [79]. Another property that affects directly the eco-toxicity is the surface chemistry which controls the interaction of the NM with the receptors in the cells or the organisms [116]. The aggregation/deposition is due to the reduction of the size that leads to a variation of the SSA of the NMs, the zeta potential on the surface of it, and the electrostatic attraction with the medium used [117]. So, the NPs can be easily making aggregate (80-100 nm) or agglomerate (> 1 µm) or be coated by different type of biomolecules present in the matrix [118] affecting the dispersion and the interaction between NPs and matrix's receptors. Finally, even the stability of the NMs dispersion during all the test time, in fact, the composition of the test solution must remain stable for at least the entire time of the eco-toxicity test.

So, the main problems that can be encountered during both the preparation of the test solution and the execution of the test with NMs are due to the aggregation and deposition of the NMs [119] which affect the size of the particles dispersed in the medium and the following interaction with the biological system (uptake) and the kinetics [108].

According to these problematics it is necessary to actuate some additional steps to the standard procedure, as indicated in the OECD TG 23 [113, p. 23]. Firstly, to prepare an efficient suspension it is necessary to broke the inter-particle interactions between the NPs and one way to obtain that is a ultrasonic bath passage [120]. Even, if necessary, the sonication must not be too much aggressive and long otherwise the structural properties of the NPs can be damage modifying

the ecotoxicity results [114]. Finally, the poorly solubility in water of the NPs can be enhanced by different techniques such as the addition of some external solvents, such as acetone and tertbutyl alcohol, or dispersant agents, such as hummic acid [121] or gum arabic [117]. If the substance is ionizing, it can be added even some buffer solution to maintain the pH at a good value to permit the organisms growth. Both the sonication, the stirring, and the addition of external species were performed to achieve a good dispersion stability.

Comparing the first results on the NMs with the available European Chemicals Agency (ECHA) report [122], for each materials it is emerging that the nanometer size increase the toxicity of materials due to the higher surface area that leads to a higher accessibility to critical biological functions and activities [76]. Anyway, a complete comparison is not possible between materials tested by different works because each result is strictly correlated to the key parameters, such as solubility, shape, and agglomeration [123].

Unfortunately, in a real-world situation it is also highly likely that multiple species coexist and the simultaneously exposure to different species, such as NPs and heavy metals, can leads to co-exposure effects on various target organisms [124]. The exposition routes can be different, i.e., oral, inhalation, dermal or parenteral, according to the physical state of the substance, such as solid dispersed in aerosol or liquid/solid contamination [125]. Each contaminant has a preferential target organism with specific typology and severity of the damage, such as damage of cell or tissue white acute, sub-chronic, chronic, carcinogenicity or genetic toxicity. So, the simultaneously exposure to different substances lead to a mixed exposures with different effects according to the interaction between the substances. The main co-exposure effects are the additive, synergistic and antagonistic ones. The additive effect is due to the sum of the effects of each single compounds, synergistic effect is an enhance of the effects sum while the antagonistic effect is a reduction of the total effect due to the competition of the compounds for the

organism target site. For example, in the case of Si-NPs, these particles can react with the metal cathodes, such as Cd^{2+} and Pb^{2+}, increasing the co-exposure effects, synergistic effect [124].

1.8. Fire extinguishing agents for LIBs fire

The growing use of LIBs has also marked an increase in the number of accidents and relative fire highlighting an important aspect, the fire management involving LIBs. The term management includes the procedure for extinguishing a fire and the collection and disposal of residues. The first topic concerns the most efficient extinguishing agent that can be applied by firefighters during the extinguishing operations while the second concerns the management of residues released during the fire, whether solid or liquid, to reduce the dispersion of dangerous species in the environment, in the form of solid particulate or exhausted extinguishing liquid and contact with humans. Indeed, due to the complexity of battery component, such as flammable liquid, metal components, and electrically connection, the fire classification of LIBs is controversial. Finally, even the information on the environmental impact of LIB residues after the application of extinguishing agents is of considerable interest especially for post-fire soil management in case of major accidents for human health and environmentally safety.

1.8.1. Fire extinguishing agents

Fire extinguishing agents are classified according both to their physical state, such as gaseous, aqueous, dry powders and foams, and to the action of fire. In fact, there are different extinguishing mechanisms, such as by cooling, by suffocation and by chemical reaction, which can be combined in some extinguishers. The agents that extinguish the fire by suffocation prevent the contact between the fuel and air, the agents for cooling instead subtract heat from the fuel to make it fall below the ignition temperature, while the agents acting for chemical reaction react directly with the fuel, blocking those chain reactions that occur during combustion, by so-called negative catalysis [126].

The most common agent used is the water, due to the low cost, the large availability, high thermal capacity, and latent heat of vaporization. The water extinguisher is a permanent pressurization system, while the water lance consists of a system which allows the water to flow out as a nebulized jet to produce greater heat exchange and greater heat absorption. The extinguishing efficiency of water is in fact due to its enormous ability to absorb heat (latent heat of vaporization). If the volume is sufficient, the water simply removes heat faster than the fire can regenerate it, and so the fire is extinguished. This agent can apply efficiently on the fire of solid fuels while must be avoided on the electrical fire due to the high conductivity of the medium [127]. Another possibility is mixed water with film-forming substances and special additives. Some additives that can be mixed with the water include, fluorocarbon surfactant, hydrocarbon surfactant, chelating agents, anti-burning agents, emulsifiers, thickeners and antifreeze substance that can enhance the efficiency of the firefighting [128].

The fire-fighting powder is composed of various chemical substances mixed with the addition of additives to improve the qualities of fluidity and water repellency and acts by inhibition of the still unburned material [129]. The powders can be divided according to the class fire on which they can be applied, such as ABC powder, so acting on the solid/liquid/gases fuels, D powder, so acting on combustible metals, and BC powder, so acting on liquid/gas fuels. The different class means even different chemical composition, in fact, the ABC powder is composed of ammonium dihydrogen phosphate and ammonium sulfate, while the D is composed just of sodium chloride (NaCl) and the BC is sodium bicarbonate ($NaHCO_3$). As they do not contain water, they are suitable for electrical appliances and metals. The extinguishing action on the fire occurs mainly by suffocation, cooling and chemical inhibition. The suffocation is obtained by the melting powder that create a glassy film that prevents the contact with the

air. There is also a mild cooling action, caused by the absorption of heat in the decomposition of the powders in contact with the flaming fuel.

Carbon dioxide, CO_2, gaseous extinguishant, is an odorless, colorless, inert, non-electrically conductive gas. It does not corrode, does not conduct, and does not leave residues, making it suitable for extinguishing electrical appliances and solid perishable materials. The CO_2 is compressed and liquefied in the extinguisher and is emitted as carbon snow or dry ice. CO_2 acts both by suffocation, due to the greater specific weight compared to that of air, which determines its stratification at the bottom, and by intense cooling, due to the rapid expansion of the gas.

The foam extinguisher is made up of a foaming liquid diluted in water in a percentage that varies between 1 and 10 % [130]. The extinguisher dispensing device is made up of a tube at the end of which a shower head in anti-corrosion material is connected, at the base of which there are air inlet holes. When the fire extinguisher is activated and the foaming liquid solution comes out at the same time, air will enter from the small holes located at the base of the lance due to the venturi effect which, mixing with the liquid in passage, will produce the foam which will be directed towards the fire.

According to the physical state of the agents the lance and the fire extinguisher structure changes, as shown in Figure 19, in fact the different lances allow to obtain different spread and size of the agent while the structure must be suitable for the pressure and volumes contained inside thee extinguisher.

According to the type of fuel the European Committee for Standardization has established a classification for fires, by letter (A, B, C, D and F) and pictogram, as shown in Figure 20, which are reported on the label of the extinguisher. For each class of fire a corresponding list of extinguishing agents that can be used is drawn up [131].

Figure 19: Common types of fire extinguisher and relative lance: dry power, foam, carbon dioxide, water and wet chemical [132].
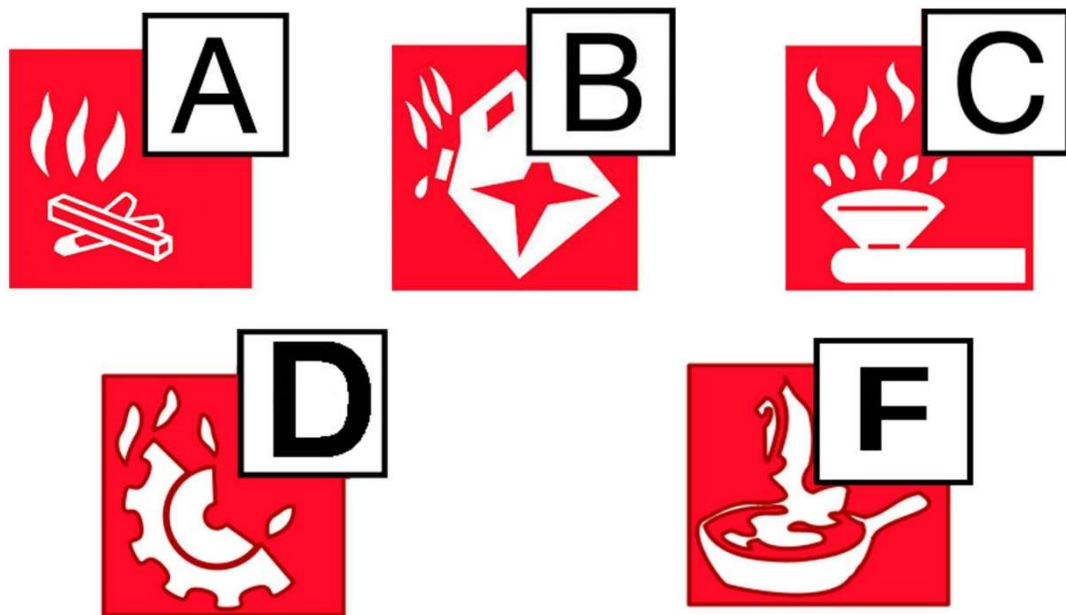
Figure 20: fire classes pictograms [131].

Class A fires are generated by solid fuels, such as wood, paper, textile materials, leather, and rubber except metals. For such fires, powder, or foam extinguishers (separation action) or water (cooling action) can be used. Class B fires are generated by liquid and liquefiable solid fuels, such as solvents, mineral oils, hydrocarbons, and petrol. For the conditions of this scenario, it is recommended to use foam, CO_2, and chemical powder extinguishers (suffocation/separating action). Water can only be used if it is a fractional or nebulized jet (cooling action). Class C fires are generated by gaseous fuels, such as hydrogen, methane, acetylene, and other gases. In this case, water can be applied, if it is a fractional or nebulized jet, to cool the pipes or gas cylinders. As for fire extinguishers, it is possible to use powder ones and CO_2 (separation action).

Class D fires are generated by combustible metals, such as potassium, magnesium, zinc, and titanium. such fires can be extinguished with carbon dioxide, since it is a substance that does not conduct electricity, or with dielectric powders.

Class F fires are generated by kitchen appliances, such as oils and fats. In this case only foam filled fire extinguishers should be used (suffocation/separating action).

1.8.2. LIBs fire

As reported in the previous section, Abuses of LIBs, the causes of battery fires can be many, such as electrical, mechanical or thermal abuse, and also the moment in which they can occur, in the charging phase, in the phase of use or during storage [133]. In this section, a specific incident is reported that shows why it is so important to evaluate the effectiveness of fire extinguishing agents for LIBs fire. The incident took place in Ganzhou city in east China's Jiangxi province on June 4 2018 [134] and was recorded by surveillance cameras. The most significant images of the accident and of the subsequent safety operations are shown in Figure 21.

While the electric scooter was travelling some gases started to be emitted from the BP, Figure 21a, and within seconds the electric scooter caught fire, Figure 21b. The driver and the passenger managed to leave the vehicle while two policemen intervened on the fire with a fire extinguisher. The chemical composition of the fire extinguisher is not known but from what the images show it could be a powder agent, due to the color and the residues remaining after the applications. The policeman going around the burning electric scooter applied the extinguishing agent on the entire surface, Figure 21c, but shortly after the flames reappeared from the scooter, Figure 21d. A second application of the same extinguishing agent was done to extinguish the flames, Figure 21e, but the flames reappeared again, Figure 21f, until the fire was finally extinguished after 20 min.

(a)

(b)

(c)

(d)

(e)

(f)
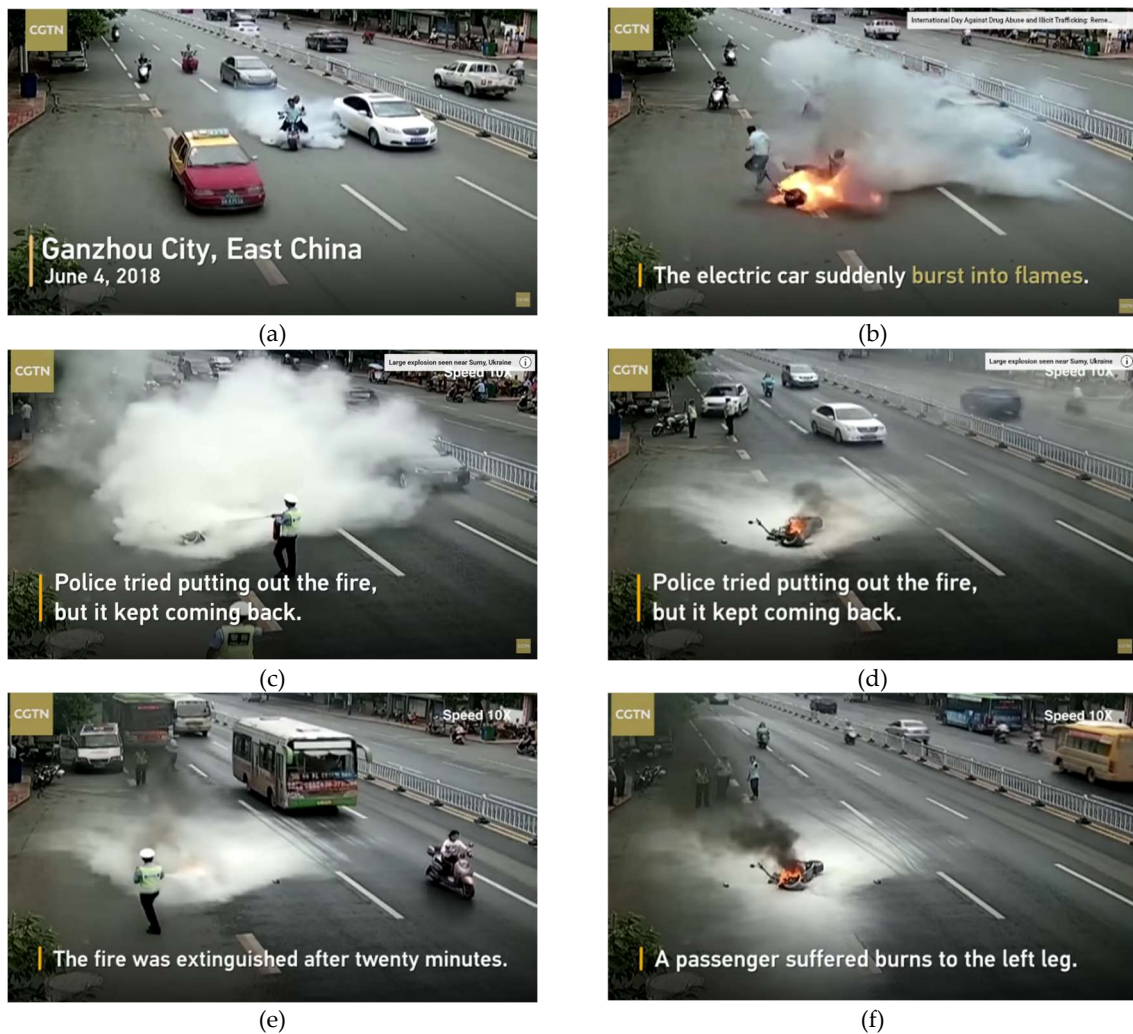
Figure 21: main events of an electric scooter catches fire in Ganzhous City, East China, June 4th 2018, source CGTN (Speed 10x) [134].

What happened at the beginning of the accidents it is well known, as explained in the previous sections, Abuses of LIBs and TR products characterization. Indeed, due to the complexity of battery components, such as flammable liquid, metal components, and electrical component, the fire classification of LIBs is controversial. In fact, LIBs fire is a complex fire, which involve class A-D fire due to the presence at the same time of solid material, such as the plastic pouch and the plastic separator (class A), flammable liquids such as electrolyte (class B), and electrodes and electrical devices containing metals (class D). Due to this, there are no unified and specific requirements for LIB fire suppression and effective LIB firefighting technology is still a challenge. In fact as reported in Table 4, the fire extinguishing agents suggested depends on the LIBs manufacturer.

From the Table 4 is possible to observe how for the same chemistry, such as LCO, one company indicates as agent: water, CO_2, foam, powder and halon, another one just some of these, while another one whatever suitable. Since battery fires have not yet been classified within any of the classes described above.

Furthermore, as will be explained in the next section, the action that must be applied on fires of LIBs must be a combination of a cooling and suffocation action. The discrepancy relating to the extinguishing agent to be applied for LIBs fires creates problems in their management by the rescue teams, as shown for the accident in Figure 21.

Table 4: List of fire extinguishing agents suggested by LIBs manufacturers in MSDS [135].

Company	Country	Year	Battery	Chemistry	Water	CO₂	Foam	Powder	N₂	Sand	Halon*	Whatever suitable
Yuka Energy	China	2011	Pack	LCO		x	x	x		x		
Makita	USA	2013	Pack	NCO	x		x	x				
Enertech	Korea	2017	Pack	NMC	x			x		x		
Samsung	Korea	2011	Cell	NMC	x			x				
Samsung	Korea	2016	Cell	NMO	x	x	x	x	x			
Saft	France	2009	Pack	LCO	x	x		x			x	
Bipower	USA	2017	Pack	LCO	x	x		x				
LG Chem	Korea	2013	Cell	NMC								x
Motorola	USA	2017	Pack	LCO	x	x	x	x				
Ideal	USA	2010	Cell	LCO		x	x	x				
SDPT	China	2016		LCO	x	x						
Bren-Tronics	USA	2013	Pack	LCO	x	x	x	x				
Advanced Energy	USA	2011		LCO								x
Leo Energy	Singapore	2014		NMC	x		x					
IDX	Japan	2016	Pack	LMO	x	x	x	x	x			
Panasonic	USA	2015		NMC	x	x	x	x				

* Note that Halon-based products deplete the ozone layer and are prohibited.

1.8.3. Fire extinguishing agents for LIBs fire

The fundamental properties required to a fire-extinguishing agent for LIBs are: high heat capacity, high wettability, low viscosity, low electrical conductivity, and a positive environmental impact [136]. It must be able to prevent the propagation of heat between the cells in a module and between the modules (as a cooling

agent) and to inhibit the chemical reactions that take place inside the cell (as an inhibiting agent) [135]. The main agents studied for LIBs fire are water, micro-encapsulation technology called F-500, dry powders, Novec and CO_2 [136]–[138].

As water-based extinguishing agent, water is the most used due to the high thermal capacity and latent heat of vaporization [139]. The most used physical status is the water mist, with diameter of 99 % of volume of droplets less than 1000 µm. This high surface/volume ratio causes greater heat absorption, a depth penetration into the fire plume, and the burning material [135]. The action on fire is due to a combination of cooling, dilution, and suppression. Water mist in fact cools and wets the fuel surface and the fire plume, the evaporation remove heat being an endothermic transformation and the oxygen is diluted by the steam, remove it from the system. The smaller diameter of the droplets permits to obtain a better penetration in the cells, the module, and the BP. On the other hand, water can react with Li salt, such as $LiPF_6$, forming toxic, i.e., HF, and flammable gases, i.e., H_2, and can conduct current causing ESC in a cell. So the problems linked to the application of water are the large amount requested and the generation of gas and smoke even after the extinction [136]. A possible solution that can be applied, to stop the fire and enhance the heat dispersion and penetration, is to immerse the EVs or the other electrical devise in a large amount of water, such as pool or container full of water. This procedure was applied by the fire investigation unit (NIA) of the Italian fire brigade (VVF) during a training with a prismatic cell after the TR and the extinction with water, as shown in Figure 22.
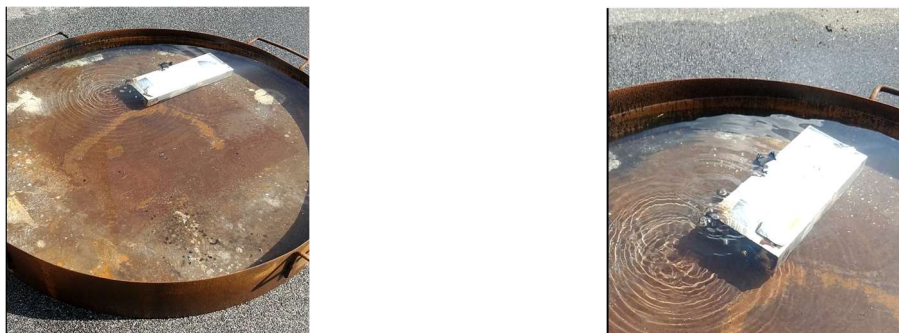
Figure 22: Prismatic cell immersed in water after TR.

From Figure 22 it is possible to observe both the advantages and the disadvantages of this technique. In fact, even if the fire is not present some bubbles were emitted from the cell. This means that some reactions occurred inside the cell with the production of gaseous products even after the extinction. These products can be produced both from the typical internal component reactions and from the reaction of the internal components with the water.

An additive that can be added to the water to enhance the efficiency is an encapsulating agent. A commercial encapsulating agent can be the F-500 that is a water-based extinguishing agent mixed with a surfactant, made by molecules with a hydrophilic and a hydrophobic part [140]. Due to this composition the extinguishing agent leads to the formation of micelles capable of encapsulating a variety of substances, such as liquid, gas and solid, by intensive mixing which are resulting not-flammable in the long term. F-500 forms a protective film layer on the surface of the burning material forming a spherical microcapsule which allows rapid cooling, inhibition of reactions and prevent the re-ignition [137]. So, the extinguishing agent therefore combines two extinguishing actions, that of cooling typical of water, and the action by separation, as the micelles that are formed around the hydrocarbon molecules prevent the contact with the comburent and the consequent combustion reaction. The ratio in volume can vary from 1 to 3 % of encapsulating agent in water.

The dry powders present on market are ABC powder, D powder and BC powder. In the case of LIBs fire, ABC powder is more widely used, due to the combination of more actions. In fact, the ABC powder acts as cooling and diluter, chemical suppressor, and suffocation agent. The first mechanism is due to the decomposition of the ABC powder, when it enters the flame zone, in ammonia gas and water vapor that can dilute the combustible gases and oxygen concentration in the flame zone. These decomposition products, at high temperatures, lead to the generation of many free radicals which can in turn react with other free radicals

present in the flame. These reactions cause chemical suppression, in fact, the reactions between free radicals lead to the arrest of the radical chain reactions that feed the flame and the fire. Finally, the layer of powder generated on the fuel could isolate the unburned fuel from the atmospheric oxygen. This effect can be enhanced by decreasing the particle size of the powder, so that the powder have a total flood extinguishing capacity, filling the entire space but only under specific conditions [135]. However, when applied on LIBs the ABC powder is not able to effect some critical problems such as the internal high temperature and the high risk of re-ignition [135]. In fact, the core of the battery is not reached by the extinguishing agent so the temperature remains high, and this could cause ignition of close batteries even after the application.

Another class of extinguishing agents that can be applied to LIBs fire is the gaseous one, such as Novec 1230 and CO_2. Novec 1230, perfluoro(2-methyl-3-pentanone) ($C_6F_{12}O$), is an environmentally friendly agent, with nearly zero ozone depletion potential which acts both by chemical and physical suppression. In fact, due to its low boiling point, 49.2 °C, can be effectively vaporized in a wide range of temperatures reducing the CO emissions [138] while the decomposition products, such as CF_3 and CF_2, not being radical compounds, reduce the concentration of free radicals available in the flame. Anyway, the cooling efficiency is limited compared to other extinguishing agents. In fact, the experimental results indicated that the agent could control lithium-titanium battery fire within 30 s, but continuous spray of the agent on the battery surface is necessary to prevent the fire from re-ignition [138]. Even the products emitted are dangerous, in fact, the agent is not inert and reacting with the fuel in the burning reaction can releases toxic products, such as HF and CF_2.

The CO_2 as extinguishing agent replaces the oxygen in the combustion zone. It is suitable for electrical fires and does not leave residues. However, the extinguishing effect is limited because CO_2 decreases the surface temperature but

not the internal one, in fact the extinguishing efficiency of the agent highly depends on the tightness of the casing. The CO_2 acts as suppressor but not as cooler, in fact the impact of the endothermic transformations, such as the evaporation of liquid and sublimation of solid, is very low compared to the temperature of the flame. So, in the case of LIBs fire it is possible to observe the re-ignition of the flame and the re-increase of the temperature in a short time, due to the low heat and cooling capacity.

The efficiency of the extinguishing agents can be evaluated by conducting fire test on LIBs to evaluate the cooling capacity of the different agents and the long-term stability, so if the agents is able to stop the heat production and the fire in a definitive way. The test must be conducted following the same procedure to obtain comparable results, so the ignition source, the position of the monitoring system, the time of application of the agent and the duration must be the same as possible. In this way the results are strictly dependent on the agents applied and the chemical composition of the LIB under investigation. During the tests it is important to monitor the time and the relative temperature, using sensors such as TCs or infrared thermal imaging cameras, to have a response to all the events that can occurred. From the combination of data, it is possible to calculate the cooling rate (v_c), given by the Equation (28), of the extinguishing agent.

$$v_c = \left| \frac{T_{end\ extinction} - T_{start\ extinction}}{t_{end\ extinction} - t_{start\ extinction}} \right| \tag{28}$$

Where $T_{end\ extinction}$ is the temperature monitored on the LIB at the end of the extinction phase, $T_{start\ extinction}$ is the temperature monitored on the LIB just before start of the extinction, and $t_{end\ extinction}$ is the time at which the extinction end while $t_{start\ extinction}$ is the time at which the extinction starts.

Higher values of the v_c indicates a better cooling capacity compared to lower values, so the best extinguishing agent must show a higher cooling capacity. Anyway, another aspect that must be considered is even the amount of agent necessary to reach a safety temperature, under 100 °C. From the results reported in

the literature it emerges that the best class of extinguishing agents currently available for extinguishing LIB fires is the water-based one, on the base of the cooling rate, the non-reignition and the quantity of extinguishing agent used [136].

Furthermore, the environmental impact of the extinguishing agents after the application must be evaluated. The residues that remain after the extinction are not just the burnt LIBs but even the extinguishing agents, liquid in the case of water-based or solid in the case of foam or powder. In the case of the gaseous ones no residues remain on the scene but there is the release of gases that must be considered too. A scheme of the emission pathways from a LIBs fire is shown in Figure 23 [141].

The liquid residues can have a high impact on the environment due to the percolation through the soil, reaching underground aquifers or surface watercourses. The release of liquid in the environment is regulated and so, independently from the agent applied, first the agents must be analyzed. Then it must be considered that during the extinguishing phase the agent encounters a material under combustion with the relative products and with which the extinguishing agent itself can react to give other products. So, even the water that is the most eco-friendly extinguishing agents due to this contact will be present different species, such as VOCs or metals, not usually present in the composition and in concentrations higher than the limit values imposed for the release. The solid residues, i.e., the burnt LIBs, present a different composition comparing to the initial one due to the combustion reactions.

So, both the liquid and solid samples composition after the application of extinguishing agents must be analyzed and the concentration values of dangerous substances (organic and inorganic) should be compared to the regulation limits. Environmental information is of considerable interest especially for the post-fire soil management and to prevent risk for the human health. The characterization analyzes that can be performed on the samples are standardized by the U.S.

Environmental Protection Agency (EPA) while to classify waste, both solid and liquid, reference is made to European Regulation No. 2008/98/EC [142], and subsequent amendment to EU Regulation 1375/2014 [143], to which the Italian regulation refers, by the Legislative Decree no. 152 [144].
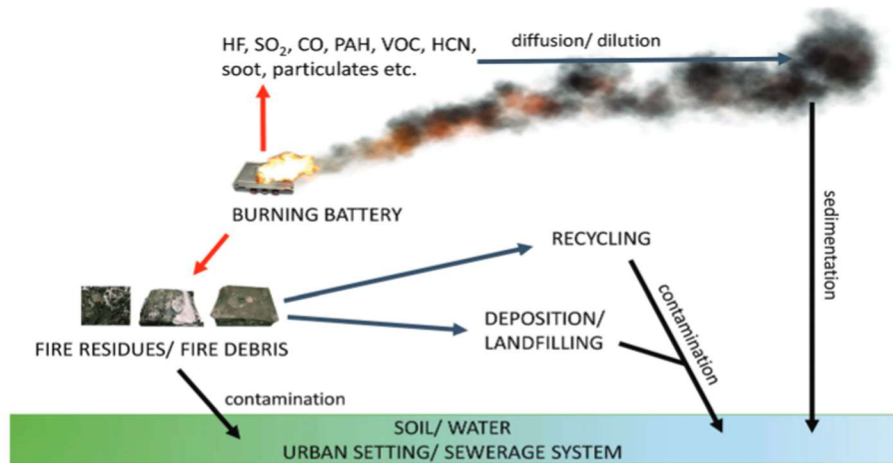
Figure 23: Emission pathways from a LIB fire [141].

The substances that must be analyzed in the samples are the nonhalogenated volatile organic compounds, the VOCs, and the metal elements. The concentrations of various nonhalogenated VOCs and semi volatile organic compounds can be determined quantitatively by the GC-FID according to the EPA method 8015D [145]. The method to determine VOCs in a variety of waste matrix is the EPA 8260D method [146]. This method allows to investigate the VOCs by different preparation techniques and extraction, such as air sampling trapping media, solvent extraction, and filter. One of the appropriate preparation techniques can use the equilibrium headspace analysis, such as the solid phase microextraction (SPME), according to the EPA 5021A method[147]. After the preparation the samples can be analyzed by GC-MS. So, combining the preparation with the analysis the waste can be analyzed by the SPME-GC-MS. The identification of the compounds can be done by the comparison of the mass spectra with the mass spectra available in the library, such as the NIST, while the quantification can be obtained by the addition in the sample a known quantity of an internal standard (ISTD). Finally, the determination of trace elements in waste

can be done by inductively coupled plasma, according to the EPA 200.8-1 method [148]. This procedure can be applied for the determination of dissolved elements in wastewater and soils samples. The detector coupled to the ICP, for the determination of the metals, can be the MS or the OES and the identification is made by the mass fragment or the wavelength, according to the detector, while the quantification can be made through the calibration line of the single metal. A pretreatment of the samples must be done to avoid external contamination due to the matrix and to dissolve the metals in an acid solution.

The dangerous of the solid and liquid samples post-extinction can be evaluated comparing the concentration obtained by the analysis with the limit value proposed by the EU Regulation 1375/2014 [143]. The dangerousness of the samples is classified according to the effects related to the physicochemical properties, such as explosivity or flammability, the effects on the human body, such as toxicity for reproduction or mutagenicity, and the impact on the environment, such as eco-toxicity. In Table 5 are reported the HP code for that waste classification in accordance with EU Regulation N. 1375/2014 [143]. The limit values for each code depends on the species considered and the waste matrix analyzed.

Table 5: HP code description according to EU Regulation N. 1375/2014 [133].

Code	Description	Code	Description
HP1	Explosive	HP9	Infectious
HP2	Oxidizing	HP10	Toxic for reproduction
HP3	Flammable	HP11	Mutagenic
HP4	Irritant - skin irritation and eye damage	HP12	Release of an acute toxic gas
HP5	Specific target organ toxicity (STOT) / Aspiration toxicity	HP13	Sensitizing
HP6	Acute toxicity	HP14	Eco-toxic
HP7	Carcinogenic	HP15	Waste capable of exhibiting a hazardous property listed above not directly displayed by the original waste
HP8	Corrosive		

Finally, if the residues, both liquid and solid, exceed the limits they cannot be classified as municipal solid waste or wastewater but require specific treatment and disposal based on their composition and relative hazard.

2. Aim of the thesis

The present work will touch many aspects regarding the LIBs, from the characterization of the internal components to the extinguishing capacity of some extinguishing agents during a LIBs fire passing through the identification of the key events and the main products that can be emitted during the TR of Li-ion cells.

This work aims to fill some gaps that emerged from the review of literature.

The first is the complete understanding of the internal composition of the cells in terms of components and quantities present and the related operational safety window. Preliminary analysis and tests were performed to characterize the principal components of Li-ion cells and to determine the thermal stability of the whole cell. The internal component's characterization, conducted in Chapter 3, has the scope to determine and precisely quantify the solvents and the metal elements present inside the cell because in many of the SDS available for the Li-ion cells the quantities of the components are expressed in a percentage range and some components are not specified. The most frequent example can be the electrolyte that is indicated as a mixture of organic carbonate without reporting the exact solvents used and their volumetric ratio.

The thermal stability test, reported in Chapter 4.2, as per UN/ECE-R100.02:2022, permits to obtain the limit temperature values for the safety window, meaning the temperature value after which the thermal stability of the cells is not more guaranteed. While the thermal abuse test, reported in Chapter 4.3, permits to obtain information about the cell behavior during a controlled thermal abuse. Combining the previous results, it is possible to identify the key events and especially the main products emitted during thermal abuse.

In fact, another gap is the complete characterization of thermal abuse in the same operating conditions for cells of different chemistry currently available on the market. In this way it was possible to quantify the gas released by the cell

following the venting and the TR events, but also to characterize the emitted gases, such as toxic (CO and HF) and flammable (electrolyte) compounds.

A lab scale apparatus has been set up, as described in Chapter 4.1, to induce an external heating by an electrical oven with a controlled heating rate (i.e., 5 °C/min), connected with thermocouples (TCs), and online analytical instrument (FT-IR) for continuous measurements while other instruments after the test (e.g., SEM-EDX , ICP-OES) were used to complete the characterization analysis of the liquid and/or solid resides. Due to this system, a complete investigation of the thermal parameters and the physical-chemical properties of the main products can be obtained for each Li-ion cell under investigation. In fact, the different sensors and the analytical analysis will provide specific information based on the nature:

- Cell surface temperatures, monitored by TCs placed on the surface of the cell, showed the onset of TR and maximum temperature values during TR.
- Pressure profile, monitored by a differential pressure transducer, showed the maximum pressure reached inside the reactor.
- Gas emission profiles, analyzed by FT-IR and quantified by relative software, showed the concentrations and the whole amount of produced gas along the whole test time.
- Particle emission analysis, obtained by SEM-EDX, AAS-OES, and ICP-OES, gave information on the particle size distribution and composition.

The concentration values obtained by the laboratory tests were compared with the regulation limits, i.e., IDLH defined by the NIOSH, to evaluate the risk for the human health due to the exposition to a LIBs accident.

Moreover, to increase the performance of the LIBs, new materials are under investigation. In fact, the use of NMs in the internal chemical composition, such as active materials, is showing an improvement on the global capacity of the LIBs enhancing the performance. At the same time, the NPs decrease the safety

properties of the device increasing the explosivity and thermal risks and the eco-toxicity impact. For these reasons, a study on the explosivity behavior, by the 20-L sphere and the Mike III tube, and the environmental impact, by evaluating the immobilization of the daphnia, of the most interesting NPs (i.e., Si, LTO and graphite) has been conducted in Chapter 5. The goal is to identify, already in the initial phase of the selection, the new NPs that can guarantee an improvement in the performance of the electrical device without losing in terms of safety.

Finally, another important aspect that must be considered is the LIBs fire management. At the moment, there is not a specific indication about the extinguishing agent that must be used to properly and efficiently extinguish a LIBs fire. Two typical agents (i.e., water mist and CO_2) and one innovative agent (i.e., F-500) were tested in Chapter 6 during a fire test to determine efficiency, in terms of cooling rate. Knowing the dangerousness of the species present inside the Li-ion cell and relative TR products, the global aim is not just to compare the efficiency of the extinguish agents, but also to analyze with different analytical techniques (i.e., GC-FID, SPME-GC-MS, ASS-OES, and ICP-OES) the dangerousness of the liquid and solid residues remaining after the fire. In fact, they are wastes and according to that they must be analyzed to be classified properly in accordance with the European Regulation No. 2008/98/EC.

Although the topics covered are broad and cover various problems related to the use and abuse of batteries, they all fall within the scope of an increasingly safe and conscious energy towards electrification. Often, in fact, conditions of abuse are reached due to users' unawareness of the risks related to batteries. Correct information and a more conscious use of these devices are the basis for correct use and obtaining maximum performance.

3. Li-ion cell characterization

The aim of these analysis is to determine and quantify the internal components of the cells. This is necessary because in many SDS available for the LIBs usually the quantities of the components are expressed as percentage and some components are not well identify, in fact usually the electrolyte is defined as mix of organic carbonate without reporting the exact solvents used and in which rate.

To analyze the internal component of the cell is necessary to disassembly it. Due to the flammability of the electrolyte, the cells must be disassembled in an inert environment, such as a glovebox filled with argon. After separation the electrodes were analyzed by ICP-OES and AAS-OES, the electrolyte was extracted and analyzed by GC-FID and SPME-GC-MS, while the separator was analyzed by DSC and ATR-FT-IR.

3.1. Material and Methods

3.1.1. Materials

3.1.1.1. Li-ion cells

The characterization analysis were conducted on Lithium-ion cylindrical cells, 18650, and the Kokam Lithium-ion pouch (Li-Po).

In Table 6 are reported the 18650 cells with the chemical composition and the technical specification reported in the relative SDS and the relative technical data sheet.

Usually, as mentioned in the Introduction, the different cells are labeled according to the cathode material, except for the LTO cell which is labeled according to the anode material. To avoid confusion during the discussion of the results of the analyzes on the individual components and on the entire cells, both information was inserted in the id-code of the cells under examination, anode material/cathode materials, such as for example C/NCA indicates the cell with carbon (graphite) as an anode material and NCA as a cathode material.

Table 6. cylindrical Li-ion cells and relative technical specification according to the SDS.

Li-ion cell	Id-code	Technical specification	
Anode: graphite (C) Cathode: Lithium nickel cobalt aluminum oxide (NCA)	C/NCA	**Parameter**	**Value**
		Rated Capacity[1]	Min. 3200 mAh
		Capacity[2]	Min. 3250 mAh Typ. 3350 mAh
		Nominal Voltage	3.6 V
		Charging method, current and voltage	CC-CV, Std. 1625 mA, 4.20 V, 4.0 hrs
		Weight	48.5 g
		Ambient temperature	Charge: 0 to 45 °C Discharge: -20 to 60 °C Storage: -20 to 50 °C
		Energy density[3]	Volumetric: 676 Wh/l Gravimetric: 243 Wh/kg

[1]at 20°C [2]at 25°C [3]energy density based on bare cell dimensions

Li-ion cell	Id-code	Technical specification	
Anode: Lithium titanium oxide (LTO) Cathode: Lithium nickel cobalt aluminum oxide (NCA)	LTO/NCA	**Parameter**	**Value**
		Rated Capacity	Min. 1300 mAh
		Capacity	Min. 1300 mAh Typ. 1350 mAh
		Nominal Voltage	2.4 V
		Charging	1.3 A / 1 C
		Weight	40.0 g
		Temperature	Charge: 0 to 50 °C Discharge: -35 to 75 °C Storage (1year): -10 to 20 °C Storage (3months): -10 to 45 °C

Li-ion cell	Id-code	Technical specification	
Anode: graphite (C) Cathode: Lithium iron phosphate	C/LTO	**Parameter**	**Value**
		Rated Capacity	Min. 1300 mAh
		Capacity	Min. 1300 mAh Typ. 1320 mAh
		Nominal Voltage	3.2 V
		Charging	650 mA/0.5 C
		Weight	40.0 g
		Temperature	Charge: 0 to 40 °C Discharge: -10 to 70 °C Storage (1year): -10 to 20 °C Storage (3months): -10 to 45 °C

The main difference between the 18650 cells is not just in terms of chemical composition and technical specification but even in terms of geometry. In fact, even if the cells are cylindrical they present different electrode pole disposition, as shown in Figure 24.

(a)   (b)
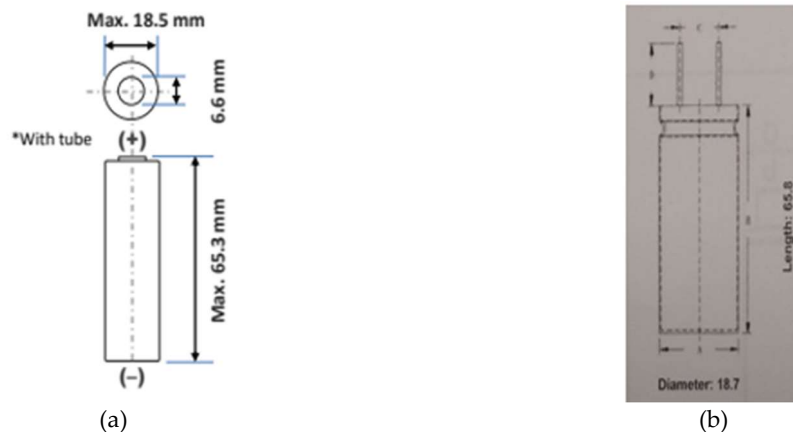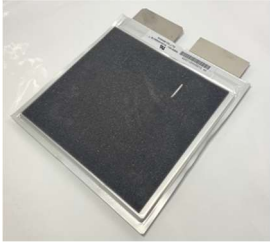
Figure 24: Scheme of cylindrical cell in the two possible dispositions: (a) electrode pole inside; (b) electrode pole outside.

In fact, in the case of the C/NCA the pole are placed on the opposite pole of the cell, as shown in Figure 24a, while for the LTO/NCA and C/LFP cells the poles are not placed on the two opposite ends but rather two pins come out of the same pole, as shown in Figure 24b, with a distance between them of 7.8 mm.

As pouch cells were selected the Kokam Lithium-ion pouch (Li-Po) battery Superior Lithium Polymer Battery (SLPB). In Table 7 are reported the two cells used in this study with the relative chemical composition and the technical specification reported in the relative SDS and the relative technical data sheet.

Table 7: pouch Li-ion cells and relative technical specification according to the SDS.

Li-ion cell	Id code	Technical Specification	
Anode: graphite (C) Cathode: Lithium nickel cobalt manganese oxide (NMC)	K25Ah (C/NMC)	Parameter	Value
		Rated Capacity	25 Ah
		Nominal Voltage	3.7 V
		Weight	555 g
		Dimension	Width 226 mm Length 227 mm Thickness 6.0 mm
Anode: graphite (C) Cathode: Lithium nickel cobalt manganese oxide (NMC)	K40Ah (C/NMC)	Parameter	Value
		Rated Capacity	40 Ah
		Nominal Voltage	3.7 V
		Weight	835.0 g
		Dimension	Width 226 mm Length 227 mm Thickness 9.1 mm

3.1.1.2. Solvents

The acids necessary for the sample digestion, HCl, 37 % and HNO_3, 65 % were purchased from Sigma Aldrich (Germany). The metal standard for the ICP-OES and AAS-OES were purchased from Thermo Fisher Scientific (USA).

3.1.2. Methods

Various analytical instruments were used, with different methods and in different configuration according to the nature of the sample. So, the methods are divided according to the final aims of the analysis.

3.1.2.1. *Disassembly of the cell*

The cells were carefully disassembled in a glove box filled with argon (O_2, $H_2O \leq$ 0.1 ppm). Depending on the geometry the tools used were different, in fact an electric Dremel® was used to open the cylindrical cells, while a ceramic knife was used to open the pouch cells. The difference is due to the different resistance of the external case, in the case of the 18650 the nickel-coated steel case is hard while the external aluminum foil that acts as a case for the pouches is less hard. The procedure was performed in collaboration with the NIA of VVF in Rome, and the various steps are shown in Figure 25 for the cylindrical cell and in Figure 26 for the pouch cell.

At the end of the disassembling operation the different components or the entire rolls were close in test tube or hermetic bag according to the subsequently analysis to avoid the degradation of the materials.

Figure 25: disassembly steps for cylindrical cell: external case incision (a); external case incision (b); removing the outer case (c); separation of the electrode sheets (d).
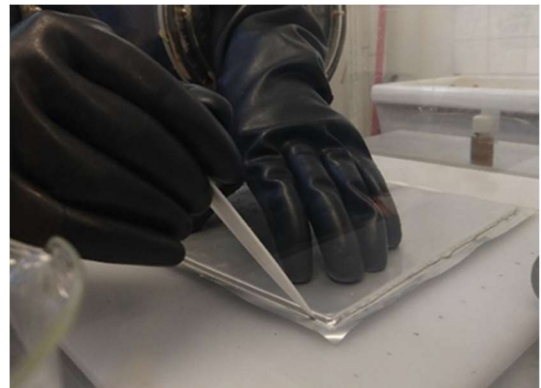
Figure 26: disassembly steps for pouch cell: pouch cell in glove box (a); lateral border incision (b); removing the outer case (c); separation of the electrode sheets (d).

3.1.2.2. Electrode's characterization

The electrodes were separated manually and were subsequently analyzed by X-Ray diffraction analysis (XRD) and ICP-OES and AAS-OES to evaluate the electrodes surface and the chemical composition.

3.1.2.2.1. XRD method

X-ray diffraction (XRD) is a flexible and non-invasive analytical method to study the material characteristics, such as phase composition and structure in powder, solid, or liquid samples. The method is based on the identification of the phases by comparing the X-ray diffraction pattern of an unknown sample to patterns stored in a reference database. Key applications of X-ray diffraction are both qualitative and quantitative analysis of phases in pure substances and mixtures, the influence of the effects of temperature, and the analysis of material microstructure, including aspects like crystallite size and preferred orientation effects [149].

The crystalline phases were determined by XRD using a Philips X'Pert diffractometer (PANalytical B.V.). The diffractometer operated at 40 kV and 40 mA in a continuous scan mode in the 2θ range from 10° to 90°, with a step size of 0.02° and counting time of 1 s. The monochromatic radiation adopted was CuKα1. The crystalline phases in the resulting diffractograms were identified through the COD database [150].

3.1.2.2.2. ICP-OES and AAS-OES method

Inductively coupled plasma optical emission spectroscopy (ICP-OES) and Atomic Absorption Spectroscopy Optical Emission Spectrometer (AAS-OES) are elemental analysis techniques.

The ICP-OES technique is applied for both quantitative and qualitative chemical analysis across diverse materials, both inorganic or organic matrix in liquid or solid phase. Typically, a mineralization step is performed, often involving dissolution in aqua regia (3:1 v/v HCl: HNO_3). This technique allows for the determination of numerous elements from the periodic table, with exceptions for some light elements or halogens. Detection limits vary based on atomic

characteristics, typically in the parts per billion (ppb) range, and the analysis is feasible on milligrams of materials. On the other hand, the AAS-OES technique is utilized to determine the qualitative and quantitative elemental composition of samples following a pretreatment process that includes mineralization. The analytical process involves introducing the sample into a nebulizer, where it transforms into an aerosol of droplets through nebulization. This aerosol is then directed to a burner, where the atoms and ions experience an excitation process, followed by the absorption of characteristic radiations. The resulting radiation is detected and converted into an electrical signal, which, upon constructing an appropriate calibration curve, enables the quantification of the analytes.

To identify and quantify the metals present in the electrode, analysis was carry out by ICP-OES or AAS-OES, according to the EPA 200.8-1 method [148, p. 200]. Samples were previously homogenized using a laboratory agate mortar to obtain a fine powder. 0.150 g were weighed on an analytical balance in a beaker and were then placed in the muffle for 8 h at 530 °C. Once the muffle had cooled down, the samples were removed and re-weighed to have the exact quantity of final sample. 10 ml of reverse aqua regia (3:1 v/v HNO_3:HCl) were added to each sample. The digestion was performed at room temperature (20 °C) for 3 h shaking the sample. At the end of digestion, the samples were filtered, using ultra slow filter, into a flask and diluted with ultrapure water up to a final volume of 100 ml. Other dilution, according to the sample have been carried out. The samples were analyzed by ICP-OES or AAS-OES. Standard solutions for each metal of interest were prepared at the following concentrations: 2 ppm, 1 ppm and 0.5 ppm.

3.1.2.3. *Electrolyte characterization*

The electrolyte was extracted from the cylindrical cells by centrifugation extraction. The samples were subsequently analyzed by GC-FID and SPME-GC-MS. This procedure was not performed for pouch cells due to the hybrid nature of

the electrolyte. In fact, for this type of cell the electrolyte is in gel form and therefore difficult to extract through the centrifugation process.

3.1.2.3.1. Centrifugation extraction method

The roll composed of anode, cathode and membrane was transferred as such into a 50 ml test tube, as showed in Figure 27. The tube was then centrifuged for 30 min at 4200 rpm with a CL10 Centrifuge, ThermoScientific [151]. At the end of the centrifuge, the roll was removed and 50 µl of the extracted electrolyte were transferred to a 1.5 ml gas chromatography vial and diluted with 950 µl of dichloromethane.

(a)   (b)   (c)
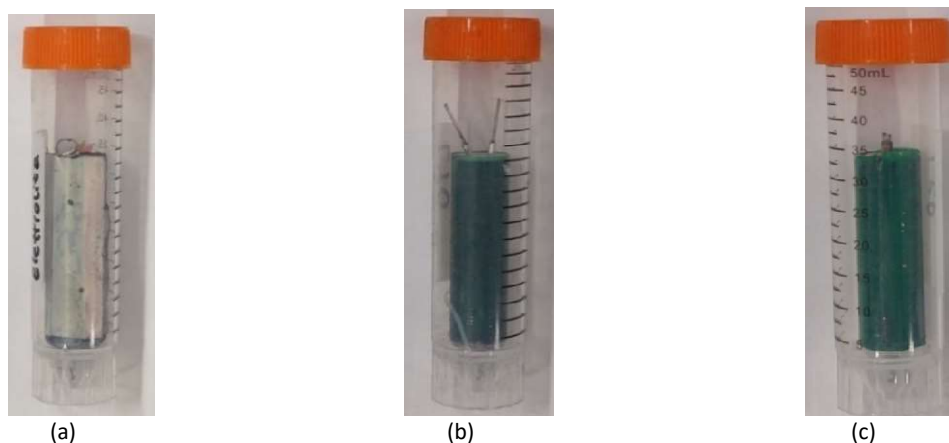
Figure 27: roll of the cyclindrical cells: NCA (a); LTO (b); LFP (c).

3.1.2.3.2. GC-FID method

Gas chromatography-mass spectrometry (GC-MS) is a versatile analytical technique employed for the identification and quantification of various molecules. GC-MS separates and analyzes mixtures, particularly volatile organic compounds (VOCs) like hydrocarbons. This technique combines chromatographic separation with qualitative information, obtained by the MS.

Similar to GC-FID, GC-MS mechanisms are the same. As individual components reach the column's end, the MS detector records data. This detector creates a unique mass spectrum for each compound, useful for the compound identification. MS analyzes the ionized fragments (ions) obtained from the fragmentation of the molecule by chemical ionization or electron impact. The

resulting ions are accelerated through a mass analyzer (quadrupole or ion trap), separating them based on mass-to-charge ratios (m/z) using a magnet. Different particles hit the detector at distinct locations due to variations in turning time. The fragmented molecules are thus separated and identified by their masses, appearing in the mass spectrometer's spectrum based on their m/z ratios. The mass spectra obtained by the sample analysis can be compared to the library mass spectra, such as the NIST library, to obtain a unique identification.

A GC-FID (Perkin Elmer) with a StabilWax-DA - Restek column (30 m x 0.25 mm i.d. x 0.25 µm) mounted inside was used for the analysis. Helium is used as carrier gas with a flow rate of 1 ml/min. The injector is held at 200 °C and 1.0 µl of sample is injected with a split ratio of 70:1. The analysis involves a programmed temperature: from 40 °C to 100 °C with a heating rate of 5 °C/min and from 100 °C (2.5 min) up to 200 °C (10 min) with a heating rate of 30 °C/min. The detector is set to a temperature of 270 °C [152].

3.1.2.3.3. SPME-GC-MS method

Gas Chromatography-Mass Spectrometry (GC-MS) is an analysis technique for identifying and quantifying concentrations of organic substances. GC-MS has a wide variety of applications because of its ability to detect various types of molecules with high accuracy. GC-MS is particularly useful in detecting and quantifying volatile organic compounds (VOCs), such as hydrocarbons. This technique is given by the combination of the chromatographic separation, quantitative information obtained by GC, and the detector analysis, qualitative information obtained by the MS.

The principals of the GC are the same reported for the GC-FID. When the individual components reach the end of the column, they are detected, and the data is recorded by the MS detector. This detector identifies different compounds separated in a gas chromatograph by creating a mass spectrum that is unique for every compound. Mass spectrometry also detects the quantities of the compounds

by producing peaks in the data. These peaks are proportional to the amount of the compound of interest. In mass spectrometry an electron or chemical ionization is used to ionize and fragment the compound. The fragmented molecules (ions) are then accelerated through a mass analyzer which includes either a quadrupole or an ion trap. In the mass analyzer, the ions are separated based on their mass-to-charge (m/z) ratios with the help of a magnet which bends the stream of the ions toward a detector. Bigger particles take longer to turn than smaller ones, which is why different particles hit the detector in different locations. Thus, the fragmented molecules can be separated and identified by their different masses and they appear as a function of their m/z ratios in the spectrum produced by the mass spectrometer. The peak areas in the MS spectrum are proportional to the quantity of the corresponding compound. A complex sample produces numerous different peaks in the gas chromatograph and each peak generates a unique mass spectrum. The identification and quantification of unknown compounds are done by comparing the mass spectra obtained to libraries of mass spectra, such as the NIST library.

A polyacrylate fiber (Supelco) was used for the SPME-GC/MS analysis. The fiber was conditioned for 30 min at 250°C. The vial containing the solution was stirred for 5 min inside the switched-off oven, then, still under constant stirring, the fiber was exposed for 1 min in the head space of the solution. The fiber was desorbed inside the injector for 2 min with a split ratio of 1:25.

For the analysis, a GC-MS (Agilent Technologies) connected to a Flex autosampler and an HP-5MS-Agilent Technologies, Inc. (30 m x 0.25 mm i.d. x 0.25 µm) column mounted inside the GC oven was used. Helium is used as the carrier gas with a flow rate of 1.6 ml/min and a purge flow of 3 ml/min. The analysis foresees a programmed temperature: from 50 °C (2.5 min) up to 300°C with a heating speed of 15 °C/min and maintained for 5 min. The total analysis time is 25 min.

The mass spectrometer works in electron ionization (EI) mode with the following parameters: ion source temperature set at 230 °C, interface temperature set at 280 °C and filament voltage set at 70 eV. The mass spectra were acquired in scan mode, with a mass range between 40 and 350 m/z [151]. In addition to comparisons with retention times of the standards, mass spectra were compared with mass spectra available in the NIST library.

3.1.2.4. Plastic separator characterization

The plastic separator was physical separated from the other internal components of the cell. The material was analyzed by DSC and ATR-FT-IR to obtain information on the thermal stability and the chemical composition.

3.1.2.4.1. Differential scanning calorimetry (DSC)

The thermal analysis is a technique in which a physical property of a substance is measured as a function of temperature while the sample is subjected to a controlled temperature program, such as heating, cooling or isotherm. Specifically, the Differential Scanning Calorimetry (DSC) quantifies the disparity in heat needed to raise the temperature of a sample compared to a reference. The properties of the sample that can be investigated are the chemical-physical transformations, the decomposition process, the quantitative composition information, the evaluation of reaction enthalpies and specific heat, and the studies of kinetics and reaction mechanisms.

5.0 mg of plastic separator was placed inside the aluminum capsule and crimped using a sealing tool provided by the PerkinElmer. All the tested samples were weighted before and after the experiment to test their actual hermetic closure. DSC measurements were performed using a conventional Perkin Elmer DSC equipment (model 8500) in nitrogen flow (40 mL/min) at 5 °C/min heating rate in the temperature range 25-350 °C. Experimental data were carefully analyzed by Pyris software provided by the PerkinElmer.

3.1.2.4.2. Attenuated total reflection Fourier transform IR (ATR-FT-IR)

Fourier transform infrared spectroscopy – attenuated total reflectance (ATR-FT-IR) provides information on the chemical composition by the identification of specific functional groups and the chemical structure of materials, both liquid and solid. Alterations in the wavenumbers, x-axes, and variations in relative band intensities, y-axes, indicate the changes in the chemical structure. ATR-FTIR spectroscopy is particularly valuable for discerning molecular conformations and/or the chemical structure of both solid and liquid materials. It provides information about the presence or absence of specific functional groups and reveals interactions between different components within the material [153].

The plastic separators were analyzed by the ATR-FT-IR, Perkin Elmer Spectrum 3TM FT-IR Spectrometer. Spectra were acquired using the following parameters: 4 cm^{-1} as resolution, spectral range between 4000 and 650 cm^{-1}; 8 scans per spectrum and with TGS as detector. Spectra were identified by comparison with spectra available in the Perkin Elmer library.

3.1.2.5. Charge-discharge cycles

Before being tested, a standard procedure consisting of five charge-discharge cycles [154] was carried out on the Li-ion cells, using the Battery Test System BaSyTec CTS of Thasar (Italy), shown in Figure 28, to ensure the correct formation of the SEI.

The cells were discharge at first with a discharge current until the completely discharged state (0 % SoC) and then charged imposing a maximum limit voltage until the completely charged state (100 % SoC) for 5 times. The limit voltage of charge and discharge are reported in Table 6 and Table 7, according to the cell. In Figure 29 is reported the voltage profile (V) of 9 C/LTO cells in series during the five charge-discharge cycles.

The thermal abuse tests were conducted on the cylindrical cells at different SoC, 100 and 50 %, while the fire test was conducted on the pouch cells at 100 % SoC. So, at the end of the five charge-discharge cycles the SoC desired was obtained.
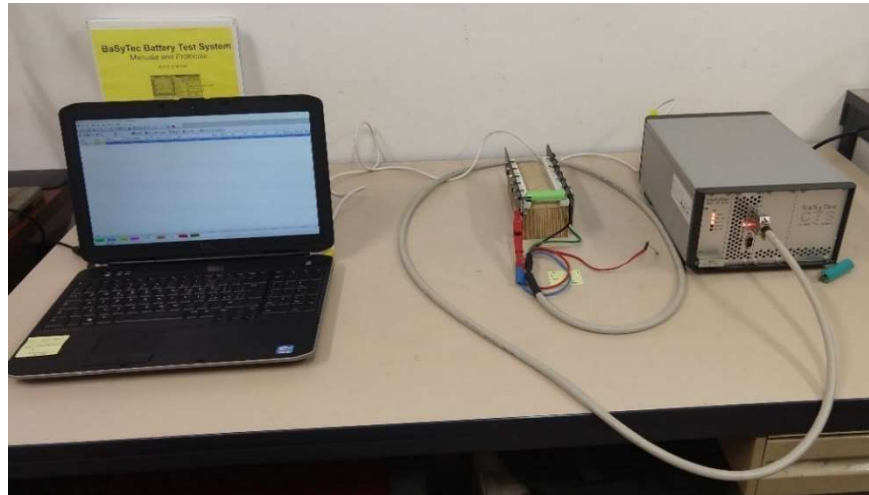
Figure 28: Battery Test System BaSyTec CTS (Thasar, Italy).
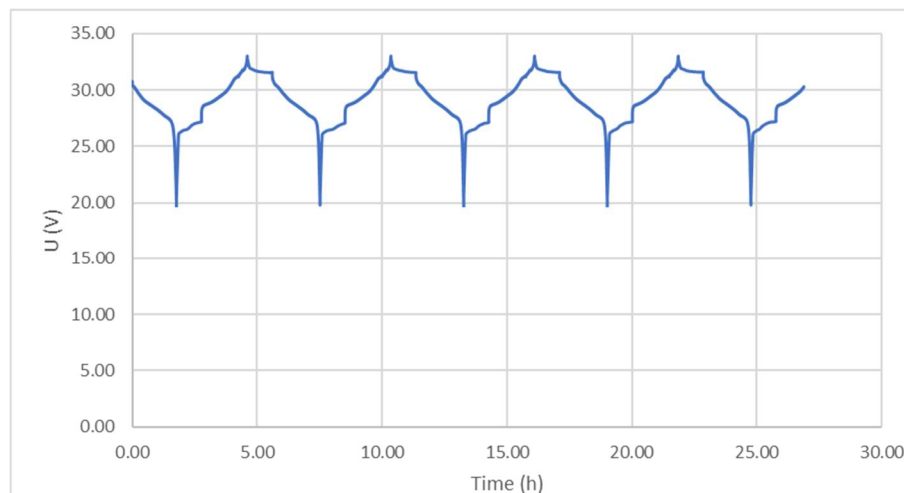
Figure 29: five charge-discahrge cycle for C/LTO cells in series.

3.2.   Results

According to the opening procedure the different components of the C/NCA, LTO/NCA and C/LFP 18650 cells and the Kokam 25 Ah and 40 Ah pouch cells were separated and analyzed through different techniques to define the internal chemical composition.

The following analysis were performed on the single components of the cell: ICP-OES and AAS-OES for the anode and cathode electrodes, ATR-FT-IR and DSC for the separator foil and GC-FID and SPME-GC-MS for the electrolyte..

3.2.1. 18650 cells

The 18650 cells have been open in the glovebox, has shown in Figure 25, and the different components were analyzed separately. First of all the external case, shown in Figure 30a, and the internal roll, shown in Figure 30b, were separated.

For C/NCA, Figure 30a, it is possible to recognize the following safety devices, the top vent on the right and the bottom vent on the left of the metallic case and the CID components, the blue and the orange disks in front in Figure 30a. Specifically, the blue disk is the second plastic insert while the orange one is the bottom disk of the CID, as shown in Figure 7.

(a)	(b)

Figure 30: C/NCA components: (a) external case with the safety devices; (b) internal roll.

A detailed description of the cell design has been reported in the literature by Finegan et al. [155]. In fact, the cells considered in this work have the septum of the CID and the vent disk coincident, as shown in Figure 31 [155].

(a)	(b)
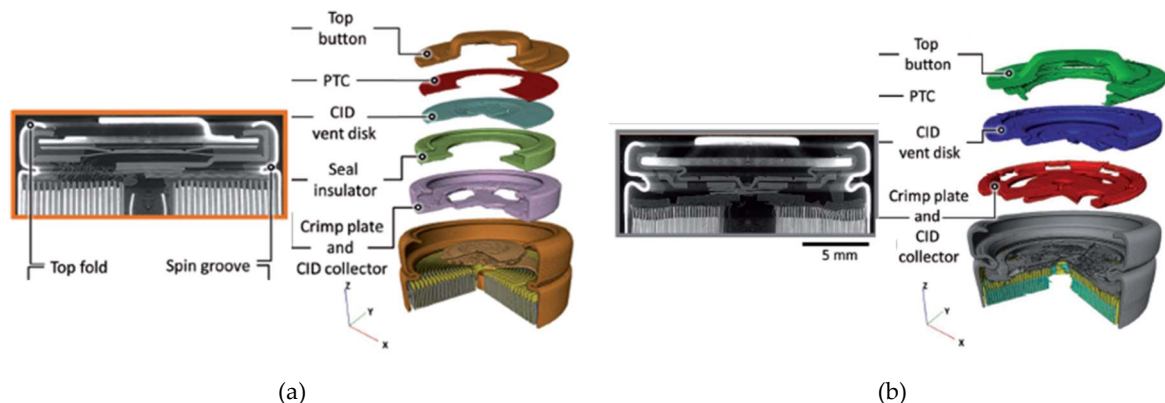
Figure 31: Greyscale XZ orthoslices from X-ray CT reconstructions and the relative placement of the integrated safety devices: (a) C/NCA; (b) C/NMC and C/LCO [155].

In particular, it is reported that the CID-vent disk on each cell consists of a conducting plate with a domed structure that is concave with respect to the

electrode assembly. When the pressure inside the cell increased due to gas generation, the domed disk become convex and disconnected the circuit, preventing further discharge. In addition, each CID disk contains a scored annulus that ruptured when a certain pressure is reached, initiating the venting process.

In the case of the LTO/NCA and C/LFP cells the identification of the safety device was more complicated due to the presents of the pins in one extremity.

Then the inner roll, the rolled-together components shown in Figure 30b, was first centrifuged to extract the electrolyte solution and then unrolled to obtain the individual sheets of anode, cathode, and separator. The weight of the single component after the dismantling of the cell was measured to obtain the weight percentage (w/w%), according to Equation (29), that can be compared to the concentration, expressed in percentage, reported in the relative SDS.

$$\%component = \frac{mass_{component}}{mass_{internal\ components}} * 100 \qquad (29)$$

Where the $mass_{component}$ is the mass of the single internal component while the $mass_{internal\ components}$ is the total weight of the internal components.

In the following tables, Table 8 for C/NCA, Table 9 for LTO/NCA, and Table 10 for C/LFP, are reported the component's weights, expressed in g, the w/w%, and the concentrations, expressed in percentage, reported in the relative SDS.

Table 8: weight (g) of the internal components and SDS specification for C/NCA cell.

C/NCA Component	Weight (g)	w/w%	SDS (%)
Anode and Cu foil	13.3551	41.5	31
Cathode and Al foil	17.4816	54.5	54
Separator foil	1.3198	4.1	3
Electrolyte	0.0614	0.19	12
Total internal components	32.2179	-	-
External case + safety device	8.3795	-	-
Total cell	40.5974		
Cell - before opening	45.7384	-	max 47.5 g

There is a discrepancy of 5.1410 g between the weight of the entire cell and the weight obtained summing the individual components. This difference can be due to losses during the cell opening operation of some materials, especially the electrolyte. In fact, comparing the percentage values of the individual components indicated on the SDS and the values obtained, it is evident that the quantity of electrolyte extracted is significantly lower than the expected value, while the other components have slightly higher values, therefore they are overestimated. So, it is plausible to assume that the missing grams are attributable to the electrolyte.

Table 9: weight (g) of the internal components and SDS specification for LTO/NCA cell.

LTO/NCA Component	Weight (g)	w/w%	SDS (%)
Anode and Cu foil	14.3258	47.8	n.a.
Cathode and Al foil	13.2016	44.0	n.a.
Separator foil	2.3796	7.9	n.a.
Electrolyte	0.0836	0.28	n.a.
Total internal components	29.9906	-	n.a.
External case + safety device	5.6879	-	n.a.
Total cell	35.6785	-	n.a.
Cell – before opening	40.2677	-	max. 37.5 g

n.a.: not available.

Even for LTO/NCA there is a discrepancy between the weight of the entire cell and the weight obtained summing the individual components of 4.5892 g that can be due to the loss of the electrolyte during the different operations.

Table 10: weight (g) of the internal components and SDS specification for C/LFP cell.

C/LFP Component	Weight (g)	w/w%	SDS (%)
Anode and Cu foil	11.4546	41.2	35
Cathode and Al foil	14.1625	51.0	45
Separator foil	2.1098	7.6	n.a.
Electrolyte	0.0427	0.15	10
Total internal components	27.7696	-	-
External case + safety device	5.1458	-	-
Total cell	32.9154	-	-
Cell – before opening	35.5858	-	max. 40 g

n.a.: not available.

In the case of C/LFP the discrepancy between the initial weight of the cell, and the weight obtained from the individual components is lower than previous ones of 2.6704 g.

The electrodes were analyzed by the XRD to evaluate the composition and then by the ICP-OES and AAS-OES to quantify the grams of metal present.

The surface composition of the electrodes, both anode and cathode, were obtained by the XRD analysis and are shown in Figure 32 for C/NCA, in Figure 33 for LTO/NCA and in Figure 34 for C/LFP.

XRD spectra relative to the NCA anode, Figure 32a, have a simple profile compared to the relative XRD spectra of the NCA cathode, Figure 32b, and with a higher intensity, 50000 counts vs 5000 counts. The peaks obtained in the anode are attributable to the chemical components: graphite, the active material of the anode, and copper, the metal current collector. The complexity of the cathode patterns, in terms of number of peaks and intensity, is due to the different transition metal oxides present in the initial chemical composition of active material.

Comparing the spectra obtained with the COD database [150] it was possible to define the chemical formula of the NCA cathode, as reported in Equation (30).

$$(Al_{0.15}Co_{0.15}Li_{0.99}Ni_{0.71})O_2 \tag{30}$$
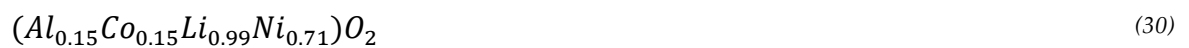
So, it is possible to confirm the internal composition of the C/NCA as cell with an anode in graphite and the cathode composed by lithium cobalt nickel aluminum oxide.
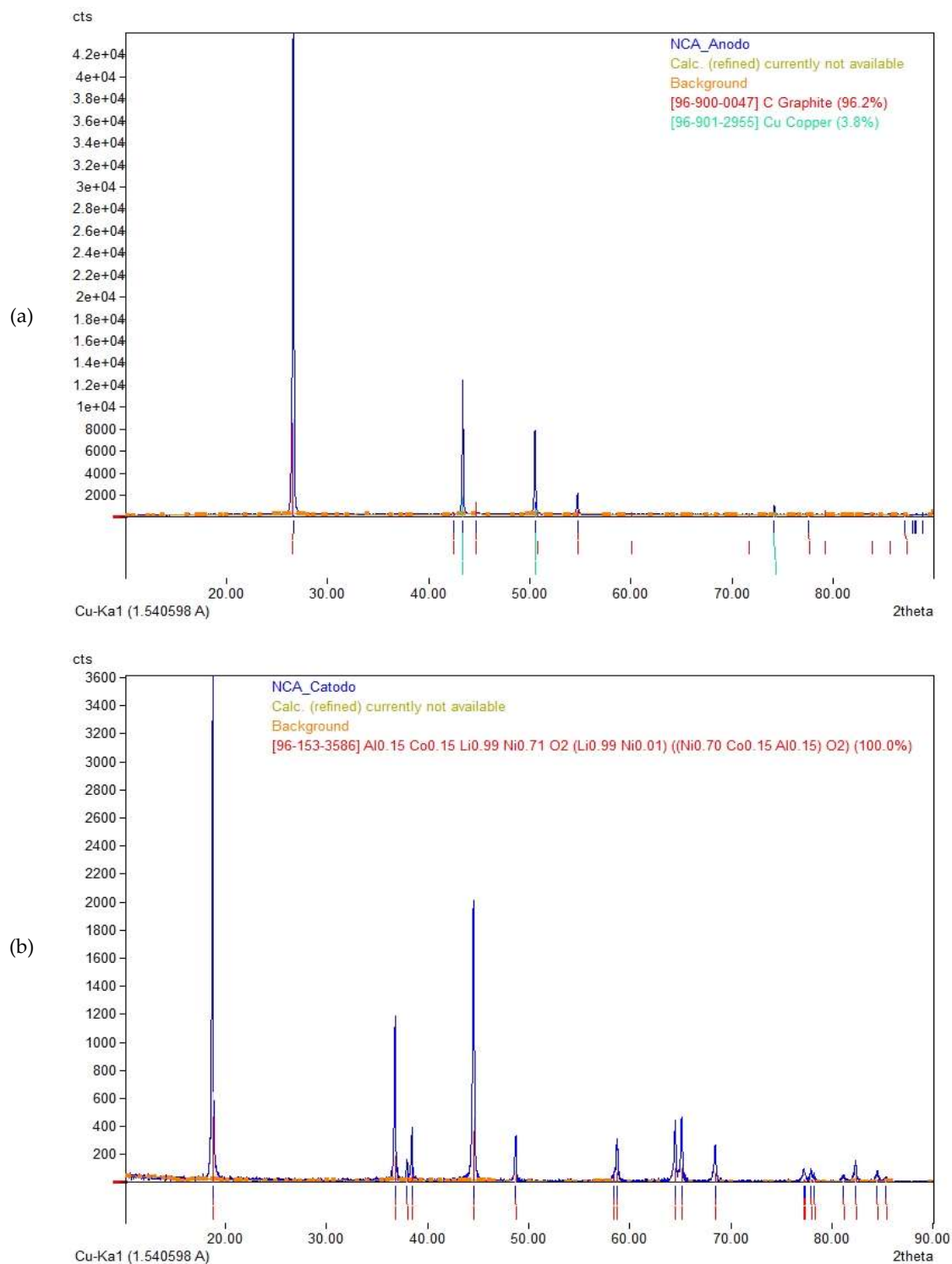
Figure 32: XRD spectra of C/NCA: (a) anode; (b) cathode.

XRD spectra relative to the LTO/NCA cell are shown in Figure 33a for the anode material and in Figure 33b for the cathode material. The spectra obtained were compared with the COD database [150] to define the chemical structure.
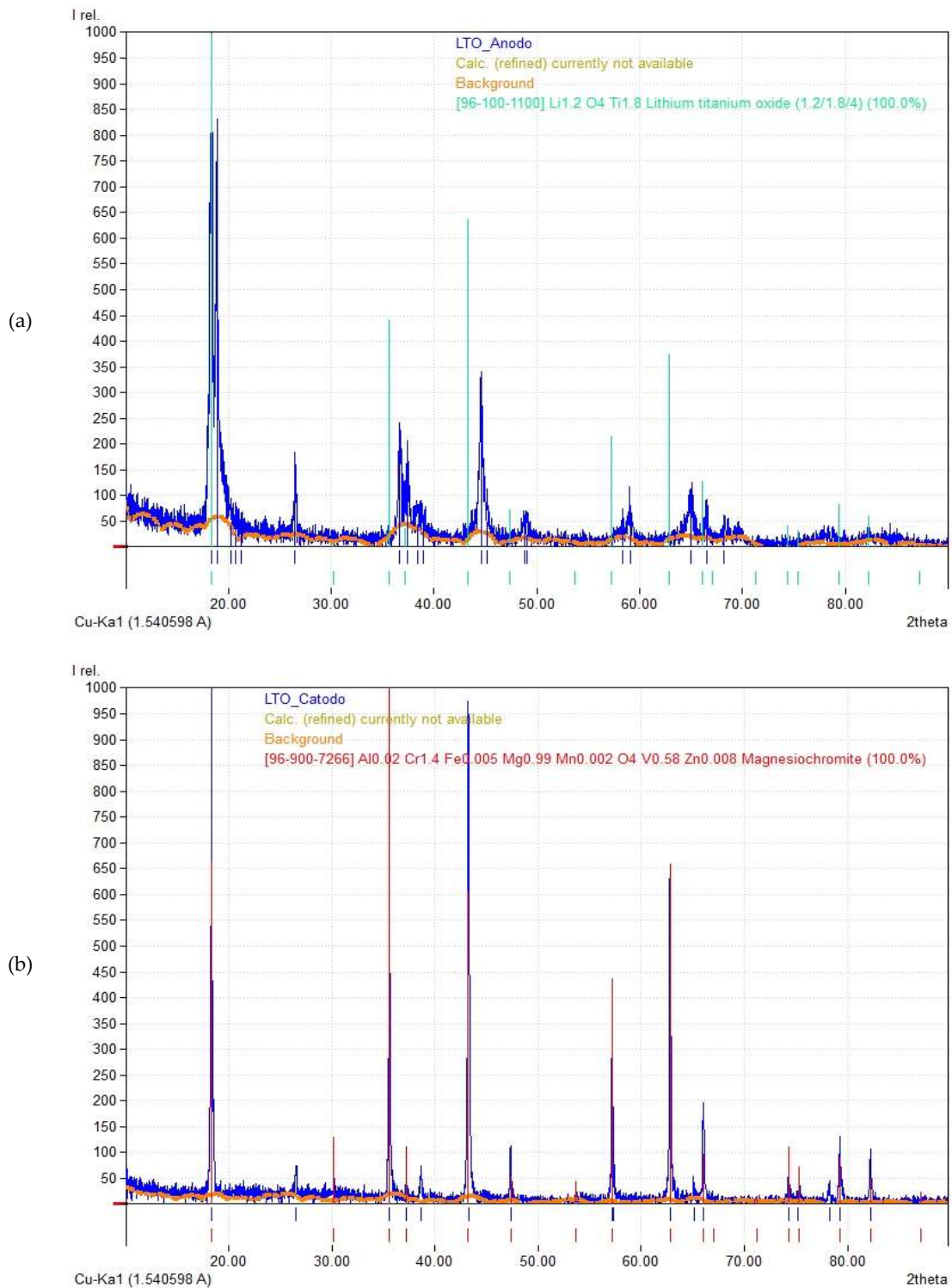
Figure 33: XRD spectra of LTO/NCA: (a) anode; (b) cathode.

Regarding the anode composition it was possible to identify two different ternary phases of Li-Ti-O: $Li_4Ti_5O_{12}$ and $Li_7Ti_5O_{12}$. The two phases are due to the intercalation of the Li-ion and electron into/extraction from the active material, as reported in Equation (31) [156].

$$Li[Li_{1/3}Ti_{5/3}]O_4 + Li^+ + e^- \underset{\leftarrow}{\rightarrow} Li_2[Li_{1/3}Ti_{5/3}]O_4 \qquad (31)$$
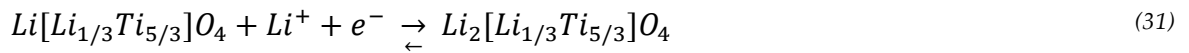
By XRD analysis it is possible to observe the structure change of the anode material during the Li intercalation/deintercalation, in fact the pattern shown in Figure 33a is the sum of the two phases [157]. So, the chemical formula of the spinel LTO that is used as anode material is reported in Equation (32).

$$Li_4Ti_5O_{12} \qquad (32)$$

In Figure 33b is shown the pattern obtained from the cathode analysis. In this case the identification is not unique. From further analyses, such as ICP-OES and AAS-OES, it was possible to identify the metals present, as reported in the Table 12, and it was therefore possible to confirm the NCA composition.

So, from the XRD analysis it is possible to confirm the chemical composition of the anode of the LTO/NCA cell, which is composed by lithium titanium oxide, while the cathode composition, made by lithium cobalt nickel aluminum oxide, will be confirm by following analysis.

XRD spectra relative to the C/LFP cell are shown in Figure 34a for the anode material and in Figure 34b for the cathode material. The complexity of the cathode patterns, in terms of number of peaks and intensity, compared to the pattern observed for the anode material, is due to the different metal present in the initial chemical composition of active material.
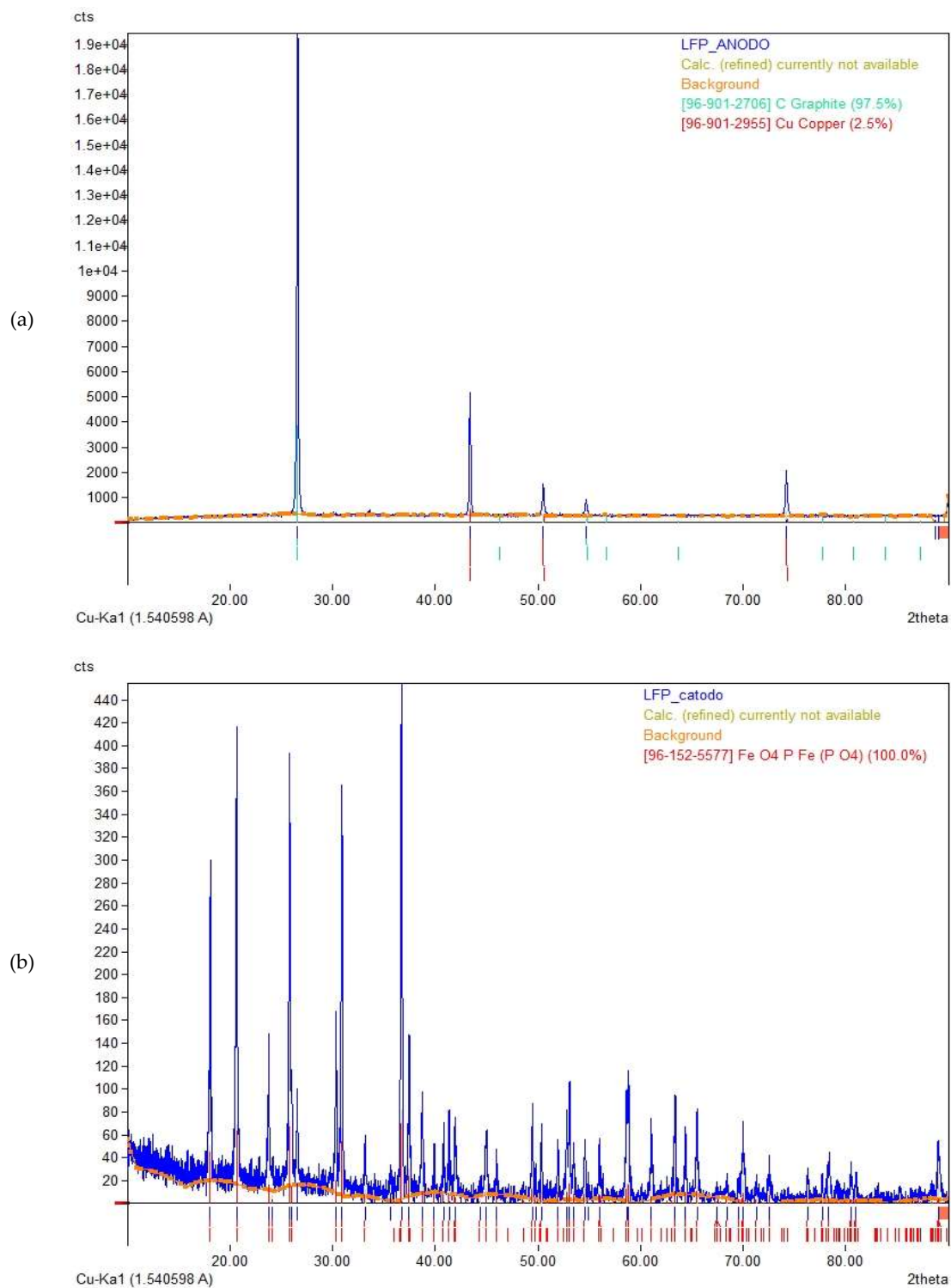
Figure 34: XRD spectra of C/LFP: (a) anode; (b) cathode.

The pattern obtained in the anode, Figure 34a, are attributable to the chemical components: graphite, the active material of the anode, and copper, the metal current collector.

Comparing the spectra obtained with the COD database [150] it was possible to define the chemical formula of the cathode, as reported in Equation (33):

$$LiFePO_4 \tag{33}$$

So, from these first data it is possible to confirm the internal composition of the C/LFP as cell with an anode in graphite and the cathode composed by lithium iron phosphate.

Then, the electrodes were analyzed by the ICP-OES and AAS-OES to quantify the metals present in the chemical composition, expressed in g over the total gram of each internal component, and reported in Table 11 for C/NCA, in Table 12 for LTO/NCA and in Table 13 for C/LFP.

Table 11: quantification (g) of metals in the C/NCA anode and cathode by ICP-OES and AAS-OES analysis.

	Al (g)	Co (g)	Cu (g)	Fe (g)	Li (g)	Mn (g)	Ni (g)	P (g)	Ti (g)
C/NCA Anode	-	-	5.53	-	0.21	-	-	-	-
C/NCA Cathode	4.73	1.58	-	-	0.30	< LOD	4.73	-	-

LOD: limit of detection.

Table 12: quantification (g) of metals in the LTO/NCA anode and cathode by ICP-OES and AAS-OES analysis.

	Al (g)	Co (g)	Cu (g)	Fe (g)	Li (g)	Mn (g)	Ni (g)	P (g)	Ti (g)
LTO/NCA Anode	-	-	3.22	-	3.63	-	-	-	4.77
LTO/NCA Cathode	5.33	1.37	-	-	0.28	0.05	5.61	-	-

Table 13: quantification (g) of metals in the C/LFP anode and cathode by ICP-OES and AAS-OES analysis.

	Al (g)	Co (g)	Cu (g)	Fe (g)	Li (g)	Mn (g)	Ni (g)	P (g)	Ti (g)
C/LFP Anode	-	-	8.47	-	0.25	-	-	-	-
C/LFP Cathode	4.27	-	-	3.04	0.09	-	-	0.44	-

In general, the analyses confirmed the chemical composition expected. The co-presence of Li both in anode and cathode material is due to the SoC of the cell opened, 50 % SoC, so, a part of the Li is intercalated in the graphite plane, anode material, and a part in the cathode material [158]. About the cathode, where the Mn is present the concentration values resulted very low, as for LTO cathode, or even under the limit of detection (LOD) of the instrument. About the graphite-

based anode, it has to be taken into account that this analysis does not give information on carbon. Similarly, for the cathode, there are not information about the oxygen.

The separator foils of the different cells are shown in Figure 35. The ATR-FT-IR analysis combined with the DSC analysis permitted to identify the polymers and the relative thermal stability.

(a)

(b)

(c)

Figure 35: separator foil: (a) C/NCA; (b) LTO/NCA; (c) C/LFP.

The C/NCA separators is made by a combination of PE and PP, the presence of two different polymers is visible even from Figure 35a where the two side of the separator have two different colors. The ATR-FT-IR analysis identified the white side as made of PE while the yellow one as made of PP. Through the DSC analysis is possible to determine the temperature of melting of the material, values that

affect the thermal stability of the material, as shown in the thermograms in Figure 36.
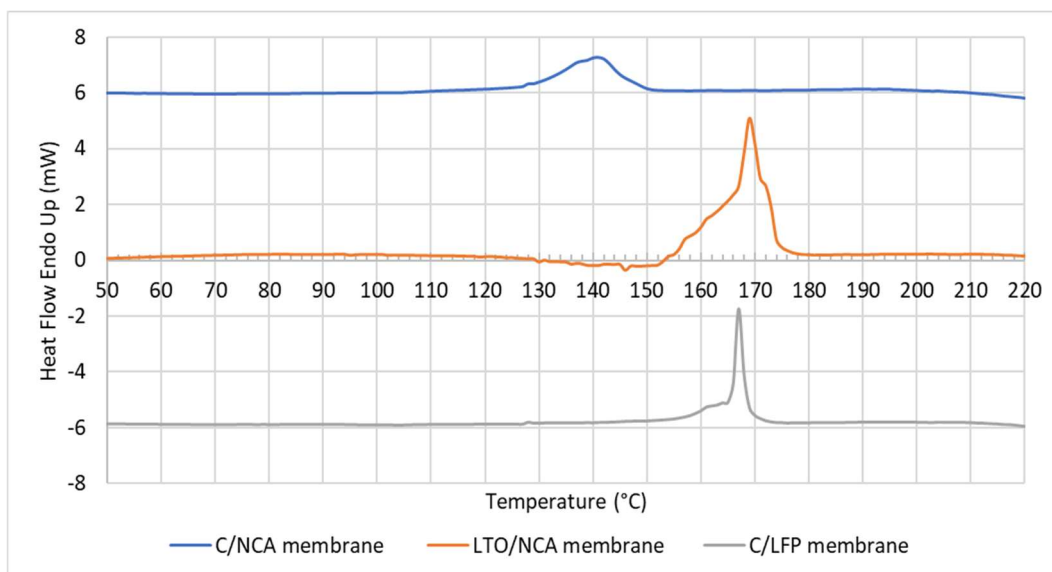
Figure 36: thermograms of the separators: (blue line) C/NCA; (orange line) LTO/NCA; (grey line) C/LFP.

In the C/NCA thermogram is observed just one endothermic peak at the temperature value of 141.28 °C with an enthalpy (ΔH) of 71.5802 J/g. The temperature value is between the range of melting of the two materials, 115-135 °C for the PE and 160-166 °C for the PP.

The LTO/NCA separator is made by just PP and the presence of just one polymer is visible even from Figure 35b where the two sides of the separator have the same color. About the thermal behavior, obtained by the DSC analysis, it is observed just one endothermic peak at 168.79 °C with a ΔH of 50.4101 J/g. The temperature value is near to the range of melting of the pure PP material, 160-166 °C.

Even the C/LFP separator which is made by PP and the presence of just one polymer is visible even from Figure 35c where the two side of the separator had the same color. From the DSC analysis is observed just one endothermic peak a 169.79 °C with a ΔH of 180.1280 J/g. The temperature value is near to the range of melting of the pure PP material, 160-166 °C. The higher temperature compared to the range can be to the presence of some additives to the material to enhance the

safety and the physical-chemical properties, as demonstrated in the next paragraphs.

Finally, the electrolyte has been analyzed by GC to quantify the organic carbonates and identify eventually additives. The organic carbonates identified by the GC-FID are reported in Table 14 for C/NCA, in Table 15 for LTO/NCA and in Table 16 for C/LFP with the relative t_R (min), concentration (ppm), percentual over the total and the relative ratio between the carbonates.

Table 14: compounds identification and quantification (ppm) by GC-FID in the C/NCA electrolyte.

t_R (min)	C/NCA Compounds	Concentration (ppm)	%	Ratio
3.948	DMC	1036.14	47.77	2
4.157	DEC	537.49	24.78	1
11.086	EC	595.24	27.44	1

Table 15: compounds identification and quantification (ppm) by GC-FID in the LTO/NCA electrolyte.

t_R (min)	LTO/NCA Compounds	Concentration (ppm)	%	Ratio
3.951	DMC	322.42	24.49	1
4.160	DEC	515.38	39.14	1.5
11.089	EC	478.95	36.37	1.5

Table 16: compounds identification and quantification (ppm) by GC-FID in the C/LFP electrolyte.

t_R (min)	C/LFP Compounds	Concentration (ppm)	%	Ratio
3.953	DMC	100.31	30.32	1.5
4.157	DEC	158.96	48.05	2
11.065	EC	71.56	21.63	1

In the cells analyzed the electrolyte is so composed by a mixture of DMC:DEC:EC in a different ratio. In fact, it is possible to observe that the carbonate predominant in the NCA is the DMC, in the LFP the DEC, while in the LTO both the DEC and the EC are in the same ratio. The percentage values and the ratio are calculated considering only the organic carbonates in the electrolyte, anyway other components can be added to the solution to increase the stability and the performance.

The identification of some possible additives compounds has been done by the SPME-GC-MS analysis, and the results, with the relative t_R (min) and the concentration (ppm), are reported in Table 17 for all the cells.

Table 17: compounds identification and quantification (ppm) by SPME-GC-MS in C/NCA, LTO/NCA, and C/LFP electrolyte.

t_R (min)	Compounds	C/NCA (ppm)	LTO/NCA (ppm)	C/LFP (ppm)
8.730	Urea, N,N-dimethyl	259.88	n.d.	n.d.
11.017	Dimethyl diglycol carbonate	61.64	n.d.	89.76
15.447	Tetrahydrofuran	198.90	400.33	n.d.

n.d.: not detected.

These compounds are not reported in any SDS, but they can be used as additives to increase the safety of the internal components enhancing the performance of the device, as reported in literature. The urea additive, such as urea, N,N-dimethyl, stabilized the Li-ion electrodes increases the electrochemical performance of the cells [159]. In fact, these additives could form a stable and uniform SEI film, which could effectively suppress the growth of Li dendrites and reduce the electrolyte decomposition improving the cyclability of LIBs. The dimethyl diglycol carbonate is part of the family of the glycols, also known as glycol diethers, which are added to the electrolyte to obtain a higher conductivity and a higher lithium cycling efficiency [153]. Finally, the tetrahydrofuran is added to the electrolyte [160] to decrease the electrolytic decomposition stabilizing the organic SEI constituents [161]. Anyway, apart the enhance in the performance it must be even considered the safety concerns, such as the flammability and/or the risk for the human health, as reported in Table 18.

From the physical properties and the hazard statements reported in Table 18 it emerges that the compounds added have some safety concerns, especially the tetrahydrofuran. In fact, the tetrahydrofuran has a boiling temperature of 65 °C, which cause the evaporation and the increase of the pressure inside the cell. The release of this compound can have effects both on the environment and on the health, due to the flammability of the compounds and the health hazard,

suspected of causing cancer. The other compounds released show less hazards, anyway their presence can affect the reactions and the gaseous emissions.

Table 18: boiling temperature (°C), hazard pictogram, and hazard statements of the Li-ion cells additives.

Compounds	Tboiling (°C)	Hazard pictogram	Hazard statements
Urea, N,N-dimethyl	268-270	-	H303: may be harmful if swallowed.
Dimethyl diglycol carbonate	n.a.	GHS07: harmful	H315: caused skin irritation.
			H319: caused serious eye irritation
			H335: may cause respiratory irritation.
Tetrahydrofuran	65	GHS02: flame	H225: highly flammable liquid and vapor.
			H302: harmful if swallowed.
		GHS07: exclamation mark	H319: causes serious eye irritation.
			H335: may cause respiratory irritation.
		GHS08: health hazard	H336: may cause drowsiness or dizziness.
			H351: suspected of causing cancer.

n.a.. not information available.

In conclusion, the compositions of the electrolyte for the three different 18650 cells are shown in Figure 37, where it is possible to observe that the half of the electrolyte is given by the organic carbonates, such as DMC, DEC, and EC, but even other organic components are present.
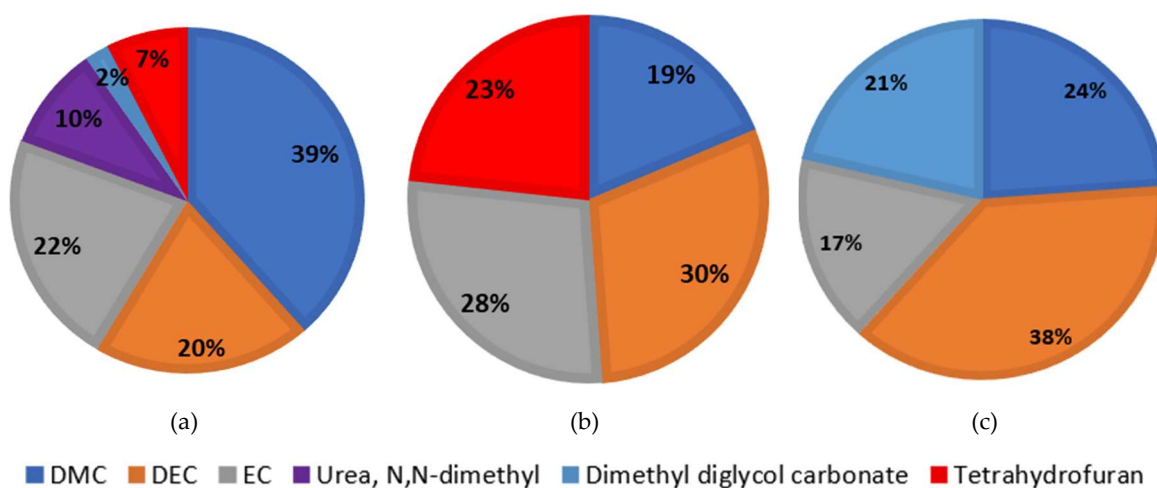
Figure 37: electrolyte composition in: (a) C/NCA; (b) LTO/NCA; (c) C/LFP cell.

Even if these substances are added to the chemical composition to enhance the safety and the performance of the cells, the recommendation is that their presence has to be reported in the SDS to have a better understanding of the reactions that

can occurred inside the cell and the species that can be released outside the cell during an abuse.

3.2.2. Pouch cells

A Kokam cell 25 Ah (K25) and a Kokam cell 40 Ah (K40) have been open in the glovebox, has shown in Figure 26 and the different extracted components, such as the anode, cathode and separator foils, shown in Figure 38, were analyzed separately.

In Table 19 and Table 20 are reported the weight (g) of the single component after the dismantling of the K25 and K40 cells, the w/w%, calculating according to Equation (29), and the concentration, expressed in percentage, reported in the relative SDS.

| (a) | (b) | (c) |
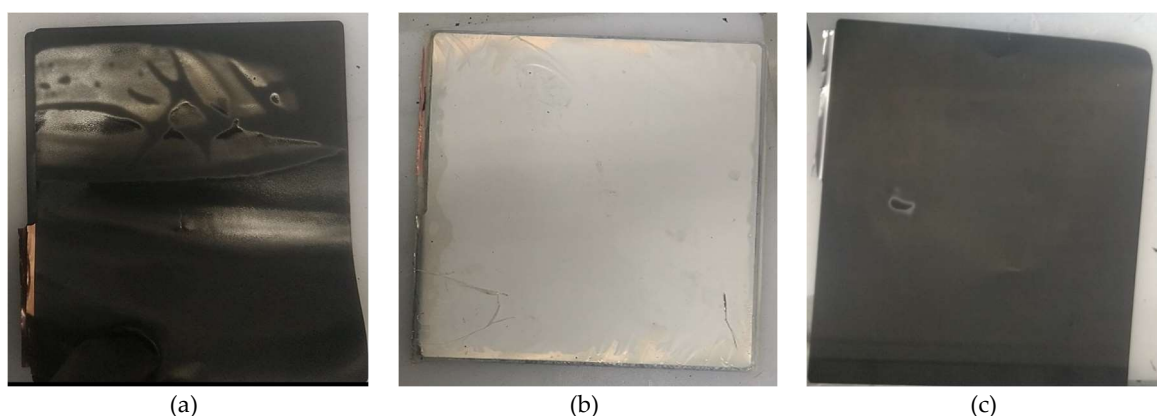
Figure 38: Kokam 25 Ah components: (a) anode foil; (b) separator foil; (c) cathode.

Table 19: weight (g) of the internal components and SDS specification for Kokam 25 Ah cell.

K25 Component	Weight (g)	w/w%	SDS Kokam 25 (%)
Anode and Cu foil	211.61	50.4	18-47
Cathode and Al foil	238.50	44.7	23-62
Separator foil	22.90	4.8	-
Electrolyte	-	-	10-28
Total internal components	473.01	-	-
External case + safety device	21.50	-	<5
Total cell	494.51	-	-
Cell – before opening	555.00	-	Max. 555 g

Table 20: weight (g) of the internal components and SDS specification for Kokam 40 Ah cell.

K40 Component	Weight (g)	w/w%	SDS Kokam 40 (%)
Anode and Cu foil	256.70	43.1	18-47
Cathode and Al foil	304.00	51.0	23-62
Separator foil	35.10	5.9	-
Electrolyte	-	-	10-28
Total internal components	595.8	-	-
External case + safety device	59.10	-	<5
Total cell	654.90	-	-
Cell – before opening	835.00	-	Max. 835 g

There is a discrepancy between the initial weight of the cell and the weight obtained from the individual components equal to 60.49 g, for 25 Ah, and 180.10 g, for 40 Ah. This difference is due to the electrolyte solution which was not collected and was lost during the opening and handling of the cells. So, it is plausible to assume that the missing grams are mainly attributable to the electrolyte solution. So, without the contribution of the electrolyte the other components have slightly higher values, therefore they are overestimated.

The electrodes were analyzed by the ICP-OES and AAS-OES and the quantification of the metals in the chemical composition, expressed in g over the total gram of each internal component, is reported in Table 21 for K25 and K40.

Table 21: quantification (g) of metals in the anode and cathode of the Kokam 25 Ah and Kokam 40 Ah.

Parts \ g	Al	Co	Cu	Fe	Li	Mn	Ni	P	Ti
K25 Anode	-	-	68.01	-	40.48	-	-	-	-
K25 Cathode	49.85	40.43	-	-	63.44	2.61	43.60	-	-
K40 Anode	-	-	82.50	-	49.11	-	-	-	-
K40 Cathode	63.54	51.53	-	-	80.86	3.32	55.71	-	-

The co-presence of Li both in anode and cathode material is due to the SoC of the cell opened, 50 % SoC, so, a part of lithium is intercalated in the graphite plane, anode material, and a part in the cathode electrode [158]. About the anode, the discrepancy between the initial grams of anode and the grams obtained by the

metal analysis is due to the absence of information about carbon. Another small discrepancy is obtained making the same calculation for the cathode, and this is due to the absence of information about the oxygen.

The ATR-FT-IR analysis combined with the DSC analysis permitted to identify the polymers of the separator, which is made by PE. From the DSC analysis is observed an endothermic peak at 140.19 °C with a ΔH of 103.2150 J/g. This temperature is near the range of melting of the pure material, 115-135 °C for the PE. The higher temperature compared to the range can be to the presence of some additives to the material to enhance the safety and the physical-chemical properties.

3.3.   Discussion

The characterization of the 18650 cells was useful to have a more precise information of the species present inside the cell. In terms of electrode composition, the SDS data were confirmed but by the additional analysis it was possible to determine the grams of each metal, by ICP-OES and AAS-OES, present in it and not just the percentage. The most interesting discovery regarding the electrolyte, in fact by the GC analysis was possible not only to identify the organic carbonate, i.e., DMC, DEC, and EC, and the relative ratio in each cell, but even the additives added to the electrolyte to enhance both the safety and the performance, such as the tetrahydrofuran. Even if, these substances are added to the chemical composition to enhance the safety and the performance of the cells it is recommended is that their presence must be reported in the SDS to have a better understanding of the reactions that can occurred inside the cell and the species that can be released outside the cell during a generical abuse.

Lastly, the characterization of the Kokam cells was valuable to have a more accurate idea of the metal quantities present in each electrode, by the ICP-OES and AAS-OES analysis. In the end, both the electrodes and the separator compositions reported on the SDS were confirmed.

4. Thermal stability and thermal abuse tests on 18650 cells

The thermal stability test on the cell, according to UN/ECE Regulation N°100 [47], allows to identify the temperature at which the main events occur. The test is conducted by sequentially increasing the temperature in 5 °C steps with a hold time of 30 min between each incremental step until the temperature reaches 200 °C above the maximum operating temperature of the battery or all events do not take place. While the thermal abuse test on the cell allows to study the interactions of the whole system when subjected to an external heating, subjected to continuous and non-gradual step heating.

Both the tests were conducted in a stainless-steel tubular reactor in a laboratory setup while the characterization of the products emitted were conducted by different instrumentation, such as FT-IR, SEM-EDX, ICP-OES, and AAS-OES, in order to identify and quantify the gases, the solid and the liquid ejected during the TR. In particular the temperature and pressure profiles are referring to the temperature on the cell surface during the heating while the pressure value is the internal pressure in the reactor. The gas emission profile has been obtained in continuous during the tests while the solids and liquids were collected at the end of each test.

From the combination of the physical parameters inside the reactor with the chemical composition of the products emitted from the cell it was possible to define the safety of the cell in terms both of thermal behavior, so the temperature and pressure reached, and the impact on the human heath, according to the properties of the products emitted.

4.1 Materials and Methods
4.1.1. Materials
4.1.1.1. Li-ion cells

The thermal stability and abuse tests were conducted on lithium-ion cylindrical cells, 18650, reported in Table 6 and in Table 22.

Table 22: cylindrical Li-ion cells and relative technical specification according to the SDS.

Li-ion cell	Id-code	Technical specification	
Anode: graphite (C) Cathode: Lithium nickel manganese cobalt oxide (NMC)	C/NMC	**Parameter**	**Value**
		Rated Capacity	2850 mAh
		Capacity	Min. 2750 mAh Typ. 2850 mAh
		Nominal Voltage	3.65 V
		Standard Charging Current	1,375 mA
		Weight	48.0 g
		Temperature	Charge: 0 to 45 °C Discharge: -20 to 60 °C Storage (1 year): -20 to 25°C Storage (3 months): -20 to 45 °C Storage (1 month): -20 to 60 °C
Anode: graphite (C) Cathode: Lithium cobalt oxide (LCO)	C/LCO	**Parameter**	**Value**
		Rated Capacity	2600 mAh
		Capacity	Min. 2550 mAh
		Nominal Voltage	3.63 V
		Standard Charging Current	1300 mA
		Weight	47.0 g
		Temperature	Charge: 0 to 45°C Discharge: -20 to 60°C Storage (1 year): -20 to 25°C Storage (3 months): -20 to 45°C Storage (1 month): -20 to 45°C

4.1.1.2. Solvents

The organic carbonates, constituting the electrolyte of the Li-ion cells, DMC (≥99 % anhydrous), EMC (99 %), DEC (≥99 % anhydrous) and EC (99 % anhydrous), were purchased from Sigma Aldrich (Germany).

The acids necessary for the sample digestion, HCl, 37 % and HNO_3, 65 % were purchased from Sigma Aldrich (Germany). The metal standard for the ICP-OES and AAS-OES were purchased from Thermo Fisher Scientific (USA).

4.1.1.3. Technical gases

The technical gases for the calibration of the FT-IR were CO 1000 ppmv in N_2, HCl 100 ppmv in N_2 and HF 811 ppmv in N_2 were purchased from Siad (Italy).

4.1.2. Methods

4.1.2.1. Laboratory setup for the thermal stability and the thermal abuse tests

Since the components of the electrolyte are flammable, the reactions that take part in thermal abuse are highly exothermic. For this reason, a pressure-tight stainless-steel reactor was built for carrying out the thermal abuse tests which is connected to a safety valve, for venting in the event of pressures exceeding 8.5 barg,. The reactor is connected, through a filter unit connected to a transfer line, to the FT-IR

gas cell. In Figure 39 is showed the stainless-steel tubular reactor for the thermal abuse test on the Li-ion cell.

Figure 39: laboratory setup for the thermal abuse test of the Li-ion cell.

4.1.2.2. Reactor and linked instruments

The reactor is placed in the center of a cylindrical furnace (900 W) Figure 40a, equipped with a PID controller, for temperature control and it contains a removable support for the cells were up three 18650 cells can be housed in a triangle configuration, Figure 40b.
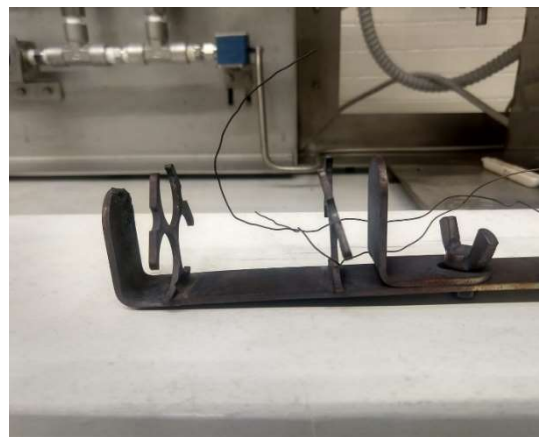
(a) (b)

Figure 40: reactor placed in the center of the cylindrical furnace (a); removable support for the 18650 cells (b).

The reactor inlet is connected to a gas supply line, through mass flow controller (MFC) to regulate and modify the composition of the atmosphere inside the reactor, Figure 41a. Furthermore, 4 TCs are installed which can be used to measure the temperature of the cell surface and that of the gases inside the reactor,

according to the position, as shown in Figure 41b. In the specific case, two TCs are located on the cell surface, TC_1 at 0.5 mm from venting valve (negative electrode side), TC_2 at 0.5 mm from the cell bottom (positive electrode side), TC_3 measures the gas temperature under the cell support while TC_4 measures the temperature of the gases in the reactor. The TCs are connected to a data logger which allows the continuous acquisition of temperature, pressure, and gas flow rate values. While a differential pressure transducer monitors the pressure inside the reactor.

(a)
(b)

(c)
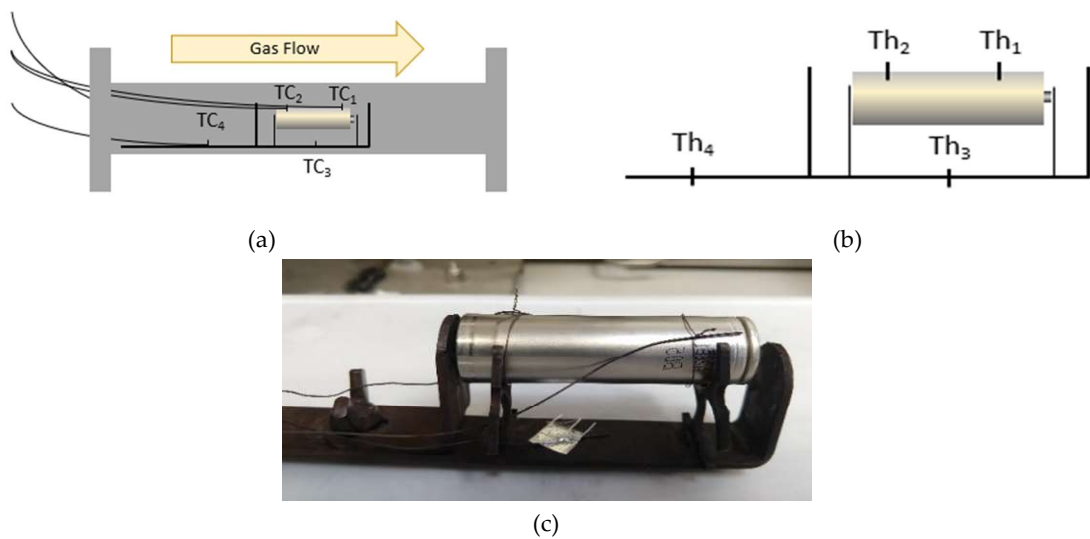
Figure 41: scheme of the position of the cell in the reactor (a); scheme of the TCs on the cell (b); TCs placed on the cell (c).

The gases produced during the thermal abuse test are flushed out of the reactor by a controlled draft system. The gases are purified of any particulate by passing through a filter unit, Figure 42a, which is connected to a transfer line which allows the entry to the cell for FT-IR gas analysis, Figure 42b.

(a)
(b)

Figure 42: Filter unit (a); transfer line linked to the gas cell of PerkinElmer Spectrum 3 MIR/NIR/FIR.

To avoid the condensation of the vapors, the filter, the transfer line, and the cell are heated up to 180 °C. The FT-IR employed is the Spectrum 3 MIR/NIR/FIR spectrometer (PerkinElmer) with MCT detector cooled with liquid nitrogen (N_2).

The gas cell is made of steel and has an optical path of 2 m. To ensure a permanent and fixed alignment, gold-plated mirrors are fixed to the internal walls of the cell and protected by a coating that protects them from acid gases. A pair of flat mirrors opposite each other and arranged diagonally on adjustable supports, placed outside the cell, allows the infrared ray to be directed from the outside to the inside and back to the outside again. An IR radiation is passed inside the cell, to obtain the infrared spectrum of the gases. Through the Time Base software, it is also possible to acquire the FT-IR spectra continuously to obtain the composition of the gases throughout the test time. Spectra were identified by comparison with spectra available in the Perkin Elmer library, while the quantification of gases are obtained by applying the calibration lines, obtained from the standard gas, and interpolating by SpectrumQuant software (Perkin Elmer).

The thermal stability tests are conducted by sequentially increasing the temperature in 5 °C steps with a hold time of 30 min between each incremental step until the temperature reaches 200 °C above the maximum operating temperature of the battery or all events do not take place, while the thermal abuse tests were conducted by a heating rate of 5 °C/min from 25 °C until the TR event do not take place. The specifications of the setup are reported in Table 23.

Instrumentation	Specification		
MFC IN	0.500 Standard Liters Per Minute (SLPM) (N_2 or AIR)		
Reactor volume	1.2 L		
MFC dilution	0.600 SLPM (N_2)		
Filter unit	Temperature: 180 °C Split: 30 %		
Primary filter	Filter (1.5 μm) with a diameter of 47mm.		
Secondary filter	Screen holding filter with fine and coarse mesh.		
Third filter	Cylindric filter in sintered stainless steel with a diameter of 15x25mm and 50μm porosity.		
Pump parameters	Sampling flow: 0.15 SLPM		
Sampling tubing	Temperature: 180 °C		
Gas cell	Volume: 98 ml Path length: 2.0 m Temperature: 180 °C		
Spectrometer	FT-IR Spectrum 3, Perkin Elmer	Spectrometer parameters	Resolution: 4 cm^{-1} Spectra acquisition frequency: 16 s Spectral range: 4500–650 cm^{-1} Scans/spectrum: 8 accumulation Detector: MCT
FT-IR software	TimeBase, Perkin Elmer	Software parameters	Data collection mode: continuous

Due to the high amount of gas released during the tests and to avoid saturation of the FT-IR detector, only a part of the emitted gas is sent to the FT-IR cell. In fact, after the filtering unit the gas is fractionated, a part is sent to the analyzer while a part vented to a hood.

The operating conditions were optimized through preliminary tests. The dilution of gases with nitrogen was inserted at the exit of the reactor in order to avoid saturation of the transmittance signal in the FT-IR spectrum especially during the TR and at the same time to avoid interference in the spectrum, because N_2 is both transparent to IR radiation and an inert gas. The acquisition frequency of FT-IR spectra is given by the best compromise between spectral resolution and acquisition time: high resolutions require longer acquisition times which however do not allow rapid events, such as TR, to be followed.

Once the instrumental parameters have been optimized, tests were conducted in the same operating conditions for two cells of the same type order to verify the reproducibility of the tests. As an example, the results obtained from two tests conducted on the 100% SoC C/NCA cell subjected to a heating rate of 5 °C/min are shown in Figure 43.

The temperature on the cell surface, expressed in °C, the pressure inside the reactor, expressed in barg, and the temperature of the oven during the thermal abuse tests are reported in Figure 43.
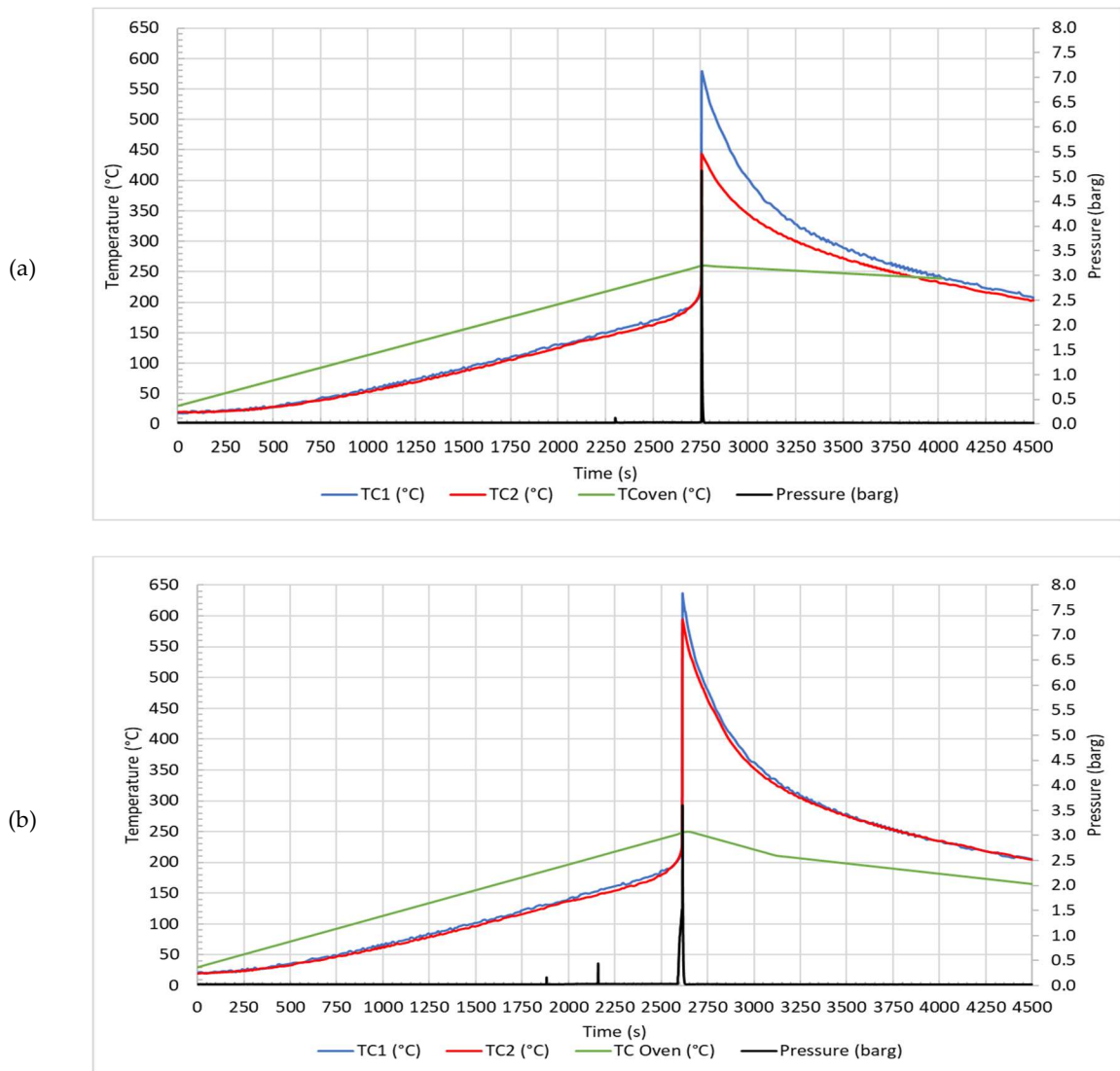
Figure 43: temperature (°C) and pressure (barg) profiles for thermal abuse tests on C/NCA at SOC 100 %.

The temperature profile of the oven shown in the graphs is due to the heating ramp of 5 °C/min which was set until the peak temperature on the cell surface is reached. After the peak temperature the ramp was interrupted, and the oven temperature set to 25 °C. Therefore, the oven temperature profile observed after the peak temperature is due to the inertia of the oven during the cooling step.

The first event observed is the CID-vent disk activation due to the increase in internal pressure. Then the venting occurs, which correspond to the emission of gases from the vent disk due to the increasing pressure inside the cell. Subsequently, the TR occurs when the temperature increases with a self-heating rate (SHR) higher than 10 °C/min. Then a maximum in temperature is observed followed by a temperature decrease. The parameters, in terms of temperature on the cell surface (°C) and pressure inside the reactor (barg) of the main events of thermal abuse tests are summarized in Table 24.

Table 24: temperature (°C) and pressure (barg) relative to the main events of the LTO/NCA thermal abuse tests.

Key event	C/NCA 100 %			C/NCA 100 %		
	t (s)	T (°C)	P (barg)	t (s)	T (°C)	P (barg)
CID-vent disk activation	2023	130 ± 5	0.175	1882	131 ± 3	0.167
Venting	2301	157 ± 2	0.125	2160	151 ± 4	0.445
TR	2731	207 ± 3	0.034	2590	204 ± 1	0.188
Peak	2751	579 ± 137	5.071	2615	615 ± 30	3.597

From the comparison, there are not significant differences in the parameters recorded for each event.

The products emitted during the thermal abuse test has been analyzed to evaluate the composition and the concentration. The main products are the gaseous vapors and the solid and liquid residues. To characterize the different products FT-IR spectrometer connected to the reactor outlet was used for online analysis of gases, while ATR-FT-IR, SEM-EDX, ICP-OES, and AAS-OES analysis have been conducted on solid and liquid samples.

4.1.2.3. Characterization of gases effluent produced during the thermal abuse test

The spectra were collected according to the spectrometer and software parameters reported in Table 23. The main gaseous products, according to the literature results and the chemical composition of the cells under investigation, are essentially composed by HF, CO, CO_2, CH_4, HCl and the electrolytic solvents DMC, EC and DEC. For this reason, the technical gases of these gases were purchased from SIAD (Italy), to obtain the standard spectra and the relative calibration lines. From the spectra of the pure gaseous species the main wavenumbers were identified, expressed in cm^{-1}, and of these the wavenumber that was univocal for each species. The standard spectra were then obtained at different concentrations to create the calibration line using the SpectrumQuant software (Perkin Elmer). The wavenumbers of each species are shown in the Table 25 and the unique value chosen for calibration and the relative linearity range of each gas are shown in bold.

Table 25: gases species with the relative linearity range and the typical wavenumber (cm^{-1}).

Compounds	Concentration range (ppmv)	Wavenumber (cm^{-1})
EC	31.72 – 277.55	1079, 1087, 1096; 1122, 1131, 1141; 1385; 1860, 1868, 1876, **3735**
DMC	23.25 – 271.25	917, 925; 985, 990, 996; 1295; 1455, 1463; 1768, 1780, **2199**
DEC	15.6 – 364.0	791; **862**; 1021; 1093; 1258; 1302; 1374; 1409; 1448; 1746, 1742
HF	29.0 – 811.0	4172-4175 (**4110**); 4202-4203
CO	1000 – 900000	2115; **2173**
CO_2	1600 – 900000	2343; 2360; **3731**
CH_4	100 – 10000	2989-2843; 3015; 3224-3029 (**3175**)

Once the wavenumber is identified, the absorbance relative to each peak was calculated and the calibration line was defined. Finally, the concentration of gases emitted during the thermal abuse tests are obtained by applying the calibration lines to all the spectra acquired during the time.

By quantifying the different species over time it is possible to obtain the concentration profile over time relating to each species. By integrating the area under the curve for each gas it is possible to obtain the total concentration emitted over the time of the test. To compare the concentration values obtained with the

IDLH limits reported by NIOSH for CO and HF it is necessary to consider 30 min. Then, the total amount of gas over time for each test was compared to 30 min in order to obtain an average concentration value to compare with the IDLH limit.

4.1.2.4. Characterization of liquid and solid ejected during the thermal abuse test
4.1.2.4.1. ATR-FT-IR

The procedure applied is the same reported for the characterization of the plastic separator in section, Attenuated total reflection Fourier transform IR (ATR-FT-IR) of the Plastic separator characterization section.

4.1.2.4.2. SEM-EDX

The solid samples, such as filters and solid powder, collected at the end of each thermal abuse test were analyzed at the SEM to evaluate the morphology of the solid particles and by the EDX to evaluate the chemical composition. Surface morphology analyses were performed with a FEG-SEM Tescan Mira3 (Tescan, Brno, Czech Republic) equipped with Edax Octane Elect EDS system and Hikari EBSD detector (Edax/Ametek inc.). SEM analyses were conducted on the primary (PTFE) filter both before and after abuse tests. A layer of carbon film was deposited on the filters to make the surface conductive for SEM analysis by Leica EM SCD005 top sputter coater. Compositional analyses were performed with EDS to verify the presence of other elements in the filter. SEM-EDX analyses were performed with a beam voltage of 15.0 kV and a working distance from the source of 15.00 mm, at different magnifications, depending on the size of the particles detected in the filter plots. EDS analyses were therefore conducted on the particles: point and area.

4.1.2.4.3. ICP-OES and AAS-OES

The procedure applied is the same reported in the section, Electrode's characterization, according to the EPA 200.8-1 method [148, p. 200].

4.2 Thermal stability test on 18650 cells
4.2.1 Results

The tests were conducted on each chemical composition but here are reported, as an example, the data obtained for C/NMC to explain how the temperature and

pressure have been evaluated and how the products, such as gases, solid or condensed phase, have been analyzed.

4.2.1.1. *Graphite/Lithium Nickel Manganese Cobalt Oxide (C/NMC)*

The cell surface temperature, the internal reactor pressure, and the oven temperature profiles are reported in Figure 44.

At the beginning of the heating step the temperature increased according with the oven heating while the pressure remained constant, around 0.013 barg. After an increase of the pressure is registered before 4000 s, due to the CID-vent disk activation and the venting of gas, while a sharp increase of the temperature and pressure, due to the onset of the TR, is observed after 7000 s.
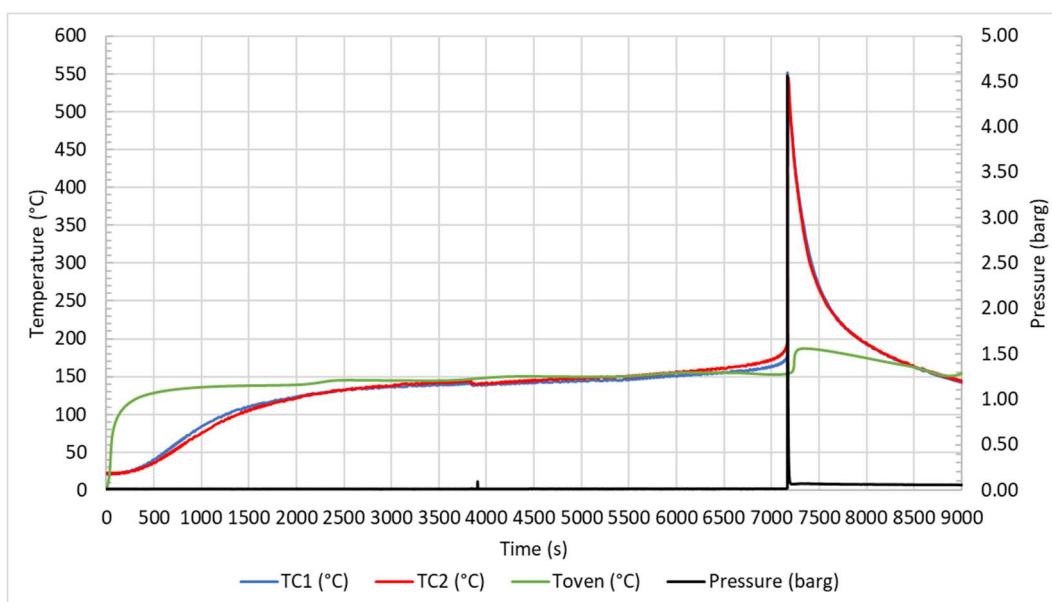
Figure 44: temperature (°C) and pressure (barg) profiles for C/NMC thermal stability test.

To analyze better the behavior a zoom of the most significant area, from 3500 to 8000 s on the x-axis, between 100 to 175 °C on the primary y-axis, and from 0.0 to 0.25 barg on the secondary y-axis, is reported in Figure 45, to highlight the variation in the pressure values during the three key events and the variation in the values of temperature according to the TCs.
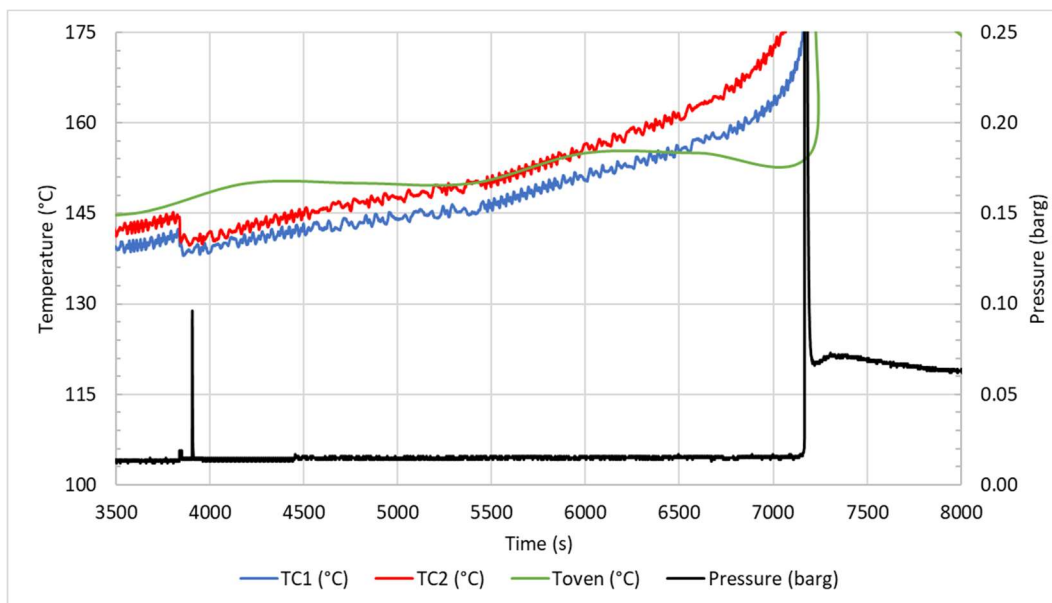
Figure 45: zoom of the most interesting area for C/NMC thermal stability test.

From Figure 45 it is possible to evaluate the time, temperature and pressure of CID-vent disk activation, venting and TR, as reported in Table 26.

Table 26: identification of the three key events from the thermal stability test of C/NMC.

Key event	Time (s)	Surface cell temperature (°C)	Pressure (barg)
Initial	0	22 ± 0.4	0.013
CID-vent disk activation	3839	140 ± 3	0.019
Venting	3907	142 ± 1	0.095
Onset TR	7167	187 ± 5	0.030

At a certain internal pressure the CID-vent disk activation occurred with a relative increase of the internal reactor pressure and a decrease of the temperature around the cell surface. The same behavior is observed for the venting, that in the case of C/NMC is close in terms of temperature, difference of 2 °C, and time, after 68 s, to the CID-vent disk activation parameters. The pressure increase is due to the release of gases species from the cell in the reactor while the decrease of the temperature is caused by the evaporation of the electrolyte when ejected from the cell. Finally, the TR onset temperature is reached with a consequent rapid increase in temperature, higher than 10 °C/min, and pressure.

A profile similar to the temperature and pressure profiles was also obtained for the gases analyzed through the FT-IR, as reported in Figure 46.
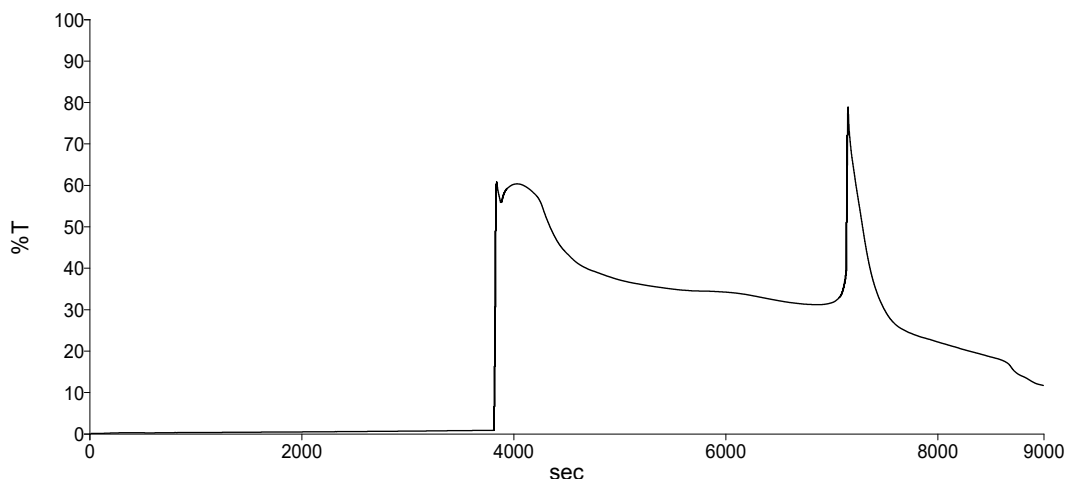
Figure 46: transmittance (%T) profile for the gas emitted during the thermal stability test on C/NMC.

In Figure 46 is reported the emission of gas monitored during the test in term of total transmittance (%T) over the time, where a T% near 0 is equal to no emission while higher values means that some compounds are flowing in the gas cell. So even from the gas profile can be identified three different peaks corresponding to the CID-vent disk activation , before 4000 s, venting, after 4000 s and TR, around 7000 s.

Appling the calibration lines, one for each gas CO, CO_2, CH_4, HF, DEC, EC, and DMC, to each single spectra obtained in the time it is possible to quantify the gases emitted during the thermal abuse test, as reported in Figure 47.
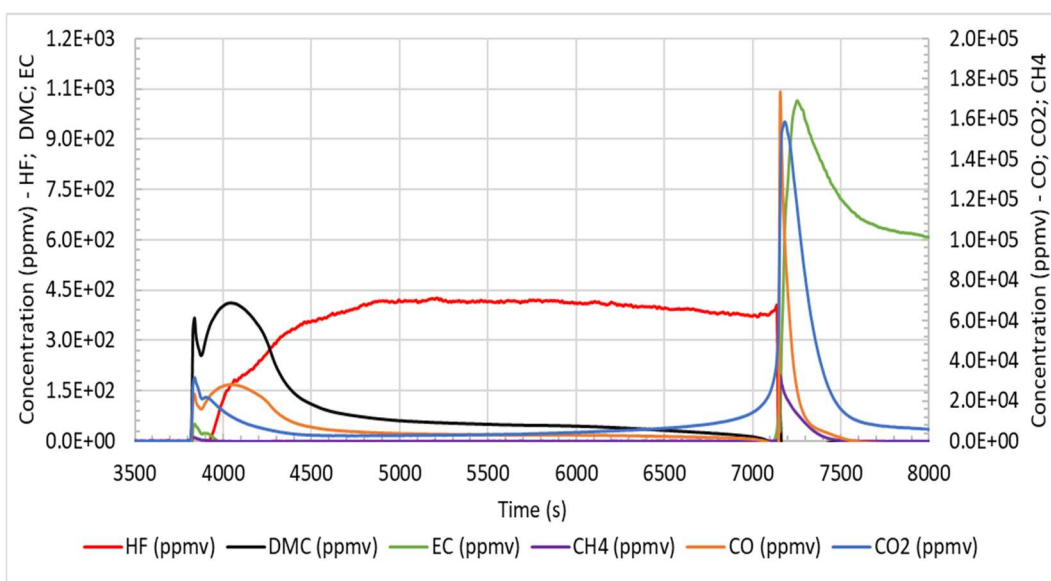
Figure 47: gases concentration profile (ppmv) for the thermal stability test on C/NMC.

From Figure 47 it is possible to observe that the release of almost all the gas compounds started with the CID-vent disk activation and finished after the end of the TR, except for EC. The CID-vent disk activation peak is very narrow with an increase for the electrolytic compounds of the order of 10^2 ppmv and for the CO and CO_2 around 10^4 ppmv. As obtained before for the C/NMC the CID-vent disk activation and venting occurred very close in the time, this means that the CID-vent disk activation did not balance enough the pressure inside the cell leading to the venting through the vent disk. The venting corresponded to a higher rate compared to the CID-vent activation, leading to a more prolonged release over time. From the venting time the quantity of HF remained constant around $4.5*10^2$ ppmv until the TR occurred. This behavior can be due to the different fluorinated compounds present inside the cell, such as the Li-salt and the PVDF binder, comparing to the other species. At a certain time, the temperature increased with a rate higher than 10 °C/min, temperature of onset of TR, and the maximum temperature and pression values were reached in few seconds. After that the temperature dropped up to the room temperature. And even the concentration dropped to zero except for the EC. This phenomenon may be due to the higher vaporization temperature of this carbonate, around 248 °C, compared to the other carbonates which therefore vaporize only once the TR has been triggered [162].

According to the integration method it is possible to concentration values obtained with the IDLH limits reported by the NIOSH. The quantities of gases in 30 min, expressed in ppm, are reported in Table 27.

Table 27: concentration (ppm) of gas emitted for the thermal stability test on C/NMC.

ppm \ Cell	DMC	EC	HF	CH_4	CO	CO_2
C/NMC	131	46	503	1418	13234	20873
IDLH [51]	-	-	30	-	1200	-

The amounts of CO and HF emitted significantly exceed the IDLH values reported by the NIOSH set at 30 ppm for HF and 1200 ppm for CO of one order of magnitude [51].

When the temperature returned to the room temperature, the reactor is opened and the residues were collected for the subsequent analysis to characterize the organic and metallic components, by ATR-FT-IR, ICP-OES, and AAS-OES. For this test the amounts of collected materials, the initial weight of the cell (g), the final weight of the cell (g), the loss Δcell (g), the total amount of gases emitted (g), the condensate phase on the filter (g), the solid ejected (g) in the reactor and the eventually liquid (g), are reported in Table 28 and shown in Figure 48.

Table 28: weight of the cell and the products collected (g) after the thermal stability test on C/NMC.

Initial cell weight (g)	Final cell weight (g)	Δcell (g)	Gases weight (g)	Condensate phase weight (g)	Solid weight (g)	Liquid weight (g)
45.0404	22.3834	22.6570	9.0476	n.p.	11.4932	n.p.

n.p.: not present.

The mass cell loss, indicated by Δcell, is of 22.6570 g and it is due to the gaseous emissions, 9.0476 g, and the solid collected after the test, 11.4932 g.

(a)   (b)

Figure 48: solids collected after the thermal stability test on C/NMC: cell (a); solid ejected from the cell (b).

Due to the metallic nature and the black color of the powder the ATR-FT-IR analysis has not been conducted. The ICP-OES and AAS-OES analysis were conducted to identify the metallic ejected and the relative quantities, as reported in Table 29 where the metals are expressed as wt% of metal in the total solid ejected.

Table 29: quantification (mg and wt%) of metals in the solid residue collected after the thermal stability test on C/NMC.

Metals	Al	Co	Cu	Li	Mn	Ni	P
mg	64.2	49.6	120	31.355	5.2	210.5	0.6
wt%	0.559	0.432	1.044	0.273	0.045	1.832	0.005

The higher concentration values are due to the Ni, one of the metal oxides in the active material of the cathode, and Cu, the anode metallic collector. The low value of P is due to the combustion of both the PVDF binder and the solid electrolyte ($LiPF_6$) decomposition. $LiPF_6$ salt is thermally stable up to 107 ∘C in a dry inert atmosphere, and its decomposition path is a simple dissociation producing lithium fluoride (LiF) as solid and PF_5 as gaseous products. P is usually present in the electrolyte so the lower values is due to the decomposition of this salt during the thermal abuse test. The total amount quantified in the solid emitted is approximately 5.97 g. This value is significantly lower than the total quantity, 11.4932 g, and it can be due to the presence of both carbon, from the anode, and the oxygen, from the cathode oxides, that cannot be quantified with this analysis.

4.2.1.2. Comparison between cells of different chemistries

The thermal stability tests were conducted for all the chemical compositions of cells under the same operating conditions, and the same analyses were carried out. Therefore, not all the results are shown but the comparisons of the various analyses are reported below to understand how the chemistry affects the temperature values of the key-events, such as CID-vent disk activation, venting and TR, and the relative emissions composition and quantities.

The first data are the ones for the temperature and the pressure at which the three key events occur according to the chemistry, as reported in Table 30.

Table 30: Temperature (°C) and pressure (barg) values for the thermal stability test on the different chemistries.

	T_{CID} (°C)	P_{CID} (barg)	T_V (°C)	P_V (barg)	$T_{onsetTR}$ (°C)	$P_{onsetTR}$ (barg)
C/NCA	88 ± 2	0.701	144 ± 1	1.259	200 ± 1	0.421
LTO/NCA	165 ± 2	0.039	184 ± 3	0.043	194 ± 5	0.177
C/LFP	170 ± 1	0.013	183 ± 1	0.035	216 ± 5	0.130
C/NMC	140 ± 3	0.019	142 ± 1	0.095	187 ± 5	0.030
C/LCO	150 ± 2	0.025	168 ± 2	0.032	226 ± 2	0.038

The data reported in Table 30 show the different thermal stability of the cell under investigation: comparing the temperature and the pressure values at which the CID-vent disk activation occurred the C/NCA resulted the most dangerous cell. In fact, the activation of the first safety device occurred at a very low temperature, about 88 °C, compared to the other chemistries, not before 140 °C. This means that the safety operating window for the C/NCA is much narrower than for other chemistries that showed higher values for this event. For the other cells the CID-vent disk activation is observed above 140 °C, with the higher temperature recorded for the LFP at 170 °C. For the second event, the venting, similar temperature values are obtained for all the chemistries, between 142 and 168 °C, with a higher value even this time recorded for the LFP, 183 °C, but even for the LTO/NCA, 184 °C. The main difference between the cells in this case are for the pressure values, in fact the venting occurs at significantly different values. Even if the pressure values are referring to the pressure inside the reactor and not inside the cell, the venting of the C/NCA and C/NMC caused a higher pressure compared to the other due to a higher emission from inside the cell to the reactor chamber. Finally, the main event, the TR, occurred in a very wide range of temperatures, between 187 °C for C/NMC and 226 °C for C/LCO. In conclusion, based on the temperature values, the safest cell is LFP while the most unstable are C/NCA for the CID-vent disk activation temperature and C/NMC for the proximity of the first two events.

Anyway, the temperature and the pressure provide information on the thermal stability but not on the dangerousness of the emissions. To this aim the main gaseous emissions were analyzed during the thermal stability test, by FT-IR as reported in Table 31, while the solid residues were collected at the end of each thermal stability test, as reported in Table 32, to be analyzed by different techniques, such as ATR-FT-IR, ICP-OES, and AAS-OES.

The gaseous emissions were identified by the FT-IR analysis and quantified by the relative quantification software. The profiles were similar to the profile reported in Figure 46. So, each key event causes a release of gases in the reactor with a higher increase during the TR. The species detected are similar for the different chemistries, such as CO, CO_2, CH_4, DMC, EC, and HF.

The concentration of the gases, expressed in ppm, are compared with the IDLH limits reported by the NIOSH, as reported in Table 31.

Table 31: concentration (ppm) of gas emitted during the thermal stability tests for the different chemistries.

ppm / Cells	DMC	EC	HF	CH_4	CO	CO_2
C/NCA	243	124	411	144	8862	10591
LTO/NCA	162	189	169	511	1302	3208
C/LFP	n.d.	12	180	31	n.d.	7078
C/NMC	131	46	503	1418	13234	20873
C/LCO	46	n.d.	263	103	2494	3493
IDLH	-	-	30	-	1200	-

n.d.: not detected.

Some similar trends can be observed comparing the results reported in Table 31. The first concern is about the electrolyte, in fact usually the DMC is always detected while the EC is correlated to the temperature reached during the TR, that must be higher than the boiling temperature of the carbonate. The second concern is about the concentration of the HF which is due to the huge quantity available inside the cell and the main reaction, Equation (17), that can produce and release it. Finally, the total amount of CO_2 and CO given back information both on the

combustion, in fact, CO is produced when the combustion reactions are not complete and on the combustion properties of the electrolyte. Regarding combustion, for all the cells, except C/LFP, the CO production is due to the high amount of products emitted that cannot react completely even if the test are conducted in air and the cathode degradation reactions produce oxygen. In the case of C/LFP the cathode metal is stable until 500 °C, so the amount of products emitted are not so high so the combustion is total, without unburned products. About the total amount released, C/NCA and C/NMC shown the higher values while the C/LFP and the LTO/NCA the lower ones in terms of concentration of each species. However, as regards the combustion properties of the electrolyte components, it emerged that the combustion of different electrolytes, such as DMC, DEC and EC, leads to different products. In fact, the combustion of the two most volatile components, DMC and DEC, tends to produce CO_2 at temperatures around 200 °C while the combustion of EC, a high-boiling component, leads to the formation of CO at temperatures between 400 and 500 °C [163]. Therefore, the different composition of the electrolyte in the cells in terms of both organic carbonates and the ratio between them causes, in case of TR, a significant variation in the CO and CO_2 emitted.

Some species are defined as toxic and for them the maximum values of exposition are regulated. For the HF, the NIOSH-defined IDLH value is 30 ppm, which is significantly exceeded, while for the CO, on the other hand, the defined IDLH value is 1200 ppm and is even widely exceeded. Therefore, the safest cell from the point of view of emissions is the LFP while the most dangerous for humans is the NMC as the concentration values significantly exceed both the IDLH values reported for HF and for CO of 1 order of magnitude [51].

Furthermore, the residues collected were weighed, as reported in Table 32, to obtain information on the initial weight of the cell (g), the final weight of the cell

(g), the loss Δcell (g), the total amount of gases emitted (g), the condensate phase on the filter (g), the solid ejected (g) from the reactor.

Table 32: weight of the cells and the products collected (g) after the thermal stability test on the different chemistries.

g / Cells	Initial cell weight	Final cell weight	Δcell	Gases weight	Condensate phase weight	Solid weight
C/NCA	45.6600	41.3400	4.3200	5.0917	0.0100	n.p.
LTO/NCA	38.4374	31.7944	3.6430	1.3847	0.0107	n.p.
C/LFP	35.0402	31.8008	3.2394	1.8246	0.0010	n.p.
C/NMC	45.0404	22.3834	22.6570	9.0476	n.p.	11.4932
C/LCO	43.6374	38.9411	4.6963	1.5991	0.2618	n.p.

n.p.: not present.

During the thermal stability test the residues change according to the different chemistry composition of the cells and the loss can be related to the gas emissions rather than to the emission of solid compounds, as shown in Table 32. In fact, just the C/NMC released a solid residue, in fact in the other case a condensate phase has been collected on the filter. In Figure 49 are shown the filters collected at the end of each thermal stability test and it is possible to observe the difference between the solid emissions, black powder for the NMC and a condensate phase, such as a brown liquid for the other cells.

For this reason, the two types of filters have been analyzed with different instruments, the powder has been analyzed by the ICP-OES and AAS-OES to quantify the metal while the other has been analyzed by the ATR-FT-IR for the organic identification.

The ATR-FT-IR spectra of filters are shown in Figure 50 while the peaks with the relative identification and force, such as very weak (*vw*), weak (*w*), medium (*m*), strong (*s*), or very strong (*vs*), are reported in Table 33.

(a) C/NCA (b) LTO/NCA (c) C/LFP

(d) C/NMC (e) C/LCO

Figure 49: filters collected after the thermal stability test of: (a) C/NCA; (b) LTO/NCA; (c) C/LFP; (d) C/NMC; (e) C/LCO.
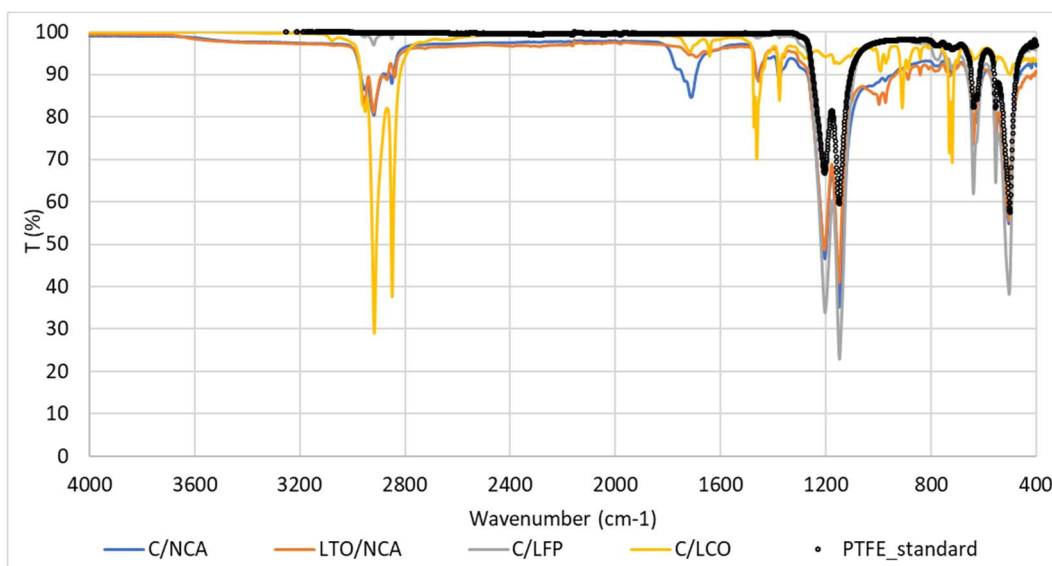
Figure 50: spectra of filters obtained by the thermal stability tests: C/NCA (blue line); LTO/NCA (orange line); C/LFP (gray line); C/LCO (yellow line); PTFE standard (black line).

The spectra of C/NCA, LTO/NCA and C/LFP cells are quite similar while the spectra of C/LCO cell showed more intensive peaks, for some specific wavenumbers. This difference is due to the fact that in the case of C/NCA, LTO/NCA and C/LFP cells the quantities released were minimal and scattered over the entire surface of the filter unlike the filter relating to the C/LCO cell which instead has all the solid residue concentrated in the central point of the filter, as shown in Figure 49. So, the peaks in the C/LCO are due just to the collected

117

material while in the other spectra the more intensive peaks are given by the filter material (PTFE), as shown by the comparison with the reference spectra in black reported in Figure 50.

The most intense peaks identified in the C/NCA, LTO/NCA and C/LFP cells are attributable to the composition of the PTFE filter, while the other peaks, even if lower in T% and force can be attributed to the presence of paraffin oil and polyethylene oxide (PEO), as for the C/NMC. These two materials can be used in the cell composition to enhance its properties. In fact, the paraffin oil can be referred to the use of paraffin wax as a protective layer of the anode material or separator [164]. The paraffin oil is released during the increase of cell temperature: at about 55 °C the wax melts and subsequently (> 240 °C) it starts to decompose [165]. In addition to paraffin oil, the main peaks due to PEO were identified [166]. PEO is usually applied as a multifunctional binder to partially replace the commonly used PVDF binder. PEO has the advantages of a good adhesive quality, high ionic conductivity, high flexibility, low cost, excellent processing property and environmental friendliness. The utilization of high-conductivity binders can significantly improve the battery cycling performance [167].

Table 33: wavenumbers (cm^{-1}) found in each filter with the relative force (vw, w, m, s or vs) and the identification.

Identification		C/NCA		LTO/NCA		C/LFP		C/LCO	
Paraffin oil	s	2954.42	w	2951.75	m	2950.95	vw	2951.68	s
Paraffin oil – PEO	vs	2918.32	w	2918.75	m	2918.99	w	2916.79	vs
Paraffin oil – PEO	vs	2850.04	w	2839.67	w	2848.87	vw	2848.79	vs
PEO	w	1711.82	w	n.d.	-	n.d.	-	1715.12	w
PEO	w	n.d.	-	n.d.	-	n.d.	-	1642.91	w
Paraffin oil – PEO	s	1459.75	w	1455.84	w	n.d.	-	1461.97	m
Paraffin oil – PEO	m	1377.39	w	1376.12	w	n.d.	-	1375.14	m
PTFE Filter	vs	1203.95	s	1205.12	s	1202.86	vs	n.d.	-
PTFE Filter	vs	1148.78	vs	1150.06	vs	1148.15	vs	n.d.	-
PEO	w	n.d.	-	n.d.	-	n.d.	-	909.35	w
Paraffin oil	w	n.d.	-	887.37	w	n.d.	-	n.d.	-
Paraffin oil	m	n.d.	-	728.45	w	n.d.	-	729.98	m
Paraffin oil – PEO	s	719.83	w	n.d.	-	720.06	w	719.34	m
PTFE Filter	m	638.77	w	639.06	m	638.76	m	n.d.	-
PTFE Filter	m	554.08	m	554.39	m	554.04	m	n.d.	-
PTFE Filter	vs	504.08	s	502.88	s	502.97	vs	n.d.	-

PEO: polyethylene oxide. n.d.: not detected.

Anyway, the PEO can be even decomposition product of the internal components of the cells, such as electrolyte and separator. Specifically, the formation of PEO-like oligomers can be obtained by the ring-opening polymerization of EC, a carbonate present inside the electrolyte, as reported in Equation (34) [168].

$$n \ \text{(EC)} \longrightarrow (-CH_2-CH_2-O-)_n + n \ CO_2 \tag{34}$$
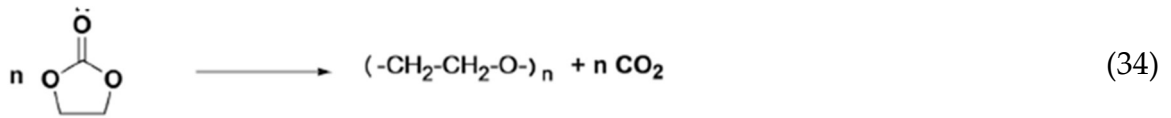
The ICP-OES and AAS-OES analysis permits to obtain information on the metallic composition of the solid residues and has been conducted on the sample residue. The metal quantifications are reported in Table 29 and are expressed as grams of metal in the total solid collected.

4.2.2 Discussion

The thermal stability test on cells, according to UN/ECE Regulation N°100 [47], permits to identify the temperature where the main events occurred. The temperature at which the key events can occur is an important parameter to evaluate the safety of the battery but even the characterization of gases and solids emitted permit to obtain information on the impact on the environment and the human health.

From the data on the temperature values for the key events, summarized below and extracted from Table 30, the safest cell can be considered the LFP. In fact:

T_{CID}: C/LFP (170 °C) > LTO/NCA (165 °C) >> C/LCO (150 °C) > C/NMC (140 °C) >> C/NCA (88 °C).

T_V: LTO/NCA (184 °C) > C/LFP (183 °C) >> C/LCO (168 °C) > C/NCA (144 °C) > C/NMC (142 °C).

T_{TR}: C/LCO (226 °C) > C/LFP (216 °C) >> C/NCA (200 °C) > LTO/NCA (194 °C) > C/NMC (187 °C).

The pressure values, even if referred to the internal pressure of the reactor and not to the cell, permitted to control the amount of gases released from the Li-ion cell.

The higher values were recorded for the C/NCA, 1.259 barg during the venting, while the other cells showed values lower than 0.177 barg, with a difference around one magnitude order.

The difference can be correlated to the separator and the electrolytic composition. In fact, the first affects the temperature at which the two opposite poles can enter in contact, causing an internal short circuit, while the second determines the vaporization of the electrolyte inside the cell, which causes the increase of pressure necessary for the CID-vent disk activation. The identification and the quantification of these materials has been conducted in the Li-ion cell characterization and the main results are summarized in Table 34.

Table 34: separator and electrolyte characterization for the NCA, LTO, and LFP.

	Plastic separator		Electrolyte	
	Materials	Tmelting (°C)	Organic compounds	Ratio
C/NCA	PE-PP	141	DMC:DEC:EC	2 : 1 : 1
LTO/NCA	PP	169	DMC:DEC:EC	1 : 1.5 : 1.5
C/LFP	PP	170	DMC:DEC:EC	1.5 : 2 : 1

From the data reported in Table 34 it is possible to observe that the C/NCA separator has a lower melting temperature, 141 °C, due to the co-presence of the PE and the PP compared to the other two cells in which the separator is made just of PP, about 169 °C. While the electrolyte composition and the relative ratio of the organic compounds can effect both the evaporation and the reactions that can occur between the electrolyte, the SEI, and the electrode. In the three cells the main components are the same, DMC, DEC, and EC, anyway the different ratio can affect the liquid/vapor release characteristics, such as the total amount released, and its physical state, which effect the reactivity of the cell. The release characteristics are related to the boiling temperature of each organic solvent, in fact a lower boiling temperature causes an increase in the internal pressure of the cell at a lower temperature. In the specific case the boiling temperatures of the organic solvents are 90 °C for the DMC, 125.8 °C for the DEC, and 243 °C for the EC. So, the DMC is the first compound that, with the increase of the cell

temperature, can evaporate followed by the DEC and finally the EC. The higher amount of DMC has been calculated in the C/NCA, in the C/LFP the more abundant electrolyte is the DEC, while in the LTO/NCA the DEC and the EC have a similar ratio. The higher amount of the DMC in the C/NCA can cause an increase of the internal pressure high enough to activate the CID around the 88 °C, while for the other cells the CID-vent disk activation occurred in correspondence of the separator melting and the DEC boiling temperature.

Another parameter that can be evaluated is the composition and the concentration of the gases emitted during the key events, performed by FT-IR analysis. The concentration values considered are refer to a period of 30 min, which has to be compared with the IDLH values and all the values are reported in Table 31. From these concentration values it can be concluded that a safe cell cannot be defined, in fact all the chemistry emitted gases substances that can be toxic and/or flammable. When comparing the concentration values of the toxic compounds, i.e., HF and CO, with the IDLH limits, it can not be defined a safer cell because for all the chemistries the concentration values exceed the limit values of at least one order of magnitude. Anyway, it can be identified the worst cell that is the C/NMC, due to the higher amount of HF, 503 ppm, and CO, 13234 ppm, released compared to the other cells.

In addition to the gaseous emissions, solid residues of different nature can also be emitted, as shown in Figure 49, specifically black powder in the case of the C/NMC and a brown condensate phase in the case of the other cells. Due to the different nature the residues were analyzed differently. The condensate phase on the filters is a mixture of paraffin oil and PEO, used as protective layer to enhance the performance of the cell, while the black powder is a mixture of vary metal oxide and carbon produced by the degradation of both anode and cathode. Due to the amount released, 11.4932 g compared to amounts under 0.2618 g for the other

cells, and the composition, C/NMC is the dangerous cell in comparison to the other chemistries under investigation.

Therefore, evaluating all the results obtained by the characterization analysis, the safest cell turns out to be the C/LFP compared to the C/NMC which is the most dangerous.

In conclusion, the thermal stability test returns an idea of the critical internal temperature of the cell, of the pressure ejected, and of the product's composition. Though, in a real case, to observe the degradation of the LIBs, they must be subjected to an external abuse, such as electrical, mechanical, or thermal, which changes the normal operating conditions. In the case of thermal abuse, an external source supplies the energy necessary for the LIB to initiate key events. The heat, though, is not constant, as is in the stability test, but has a heating rate.

Depending on the external heating system, the heating rate can change, and the environmental conditions can influence the evolution of events. So, the purpose of the thermal abuse tests is to study the behavior under faster heating conditions than thermal stability tests and to evaluate the effect of the temperature also on the composition of the products emitted.

4.3   Thermal abuse tests on 18650 cells

The thermal abuse tests were conducted in the stainless-steel tubular reactor and the relative temperature and pressure profiles with the gas emission profile and the consequent characterization analysis were obtained for all the chemistries, C/NCA, LTO/NCA, C/LFP, C/NMC, and C/LCO, at two different SoC, 50 and 100 %.

To discuss the data obtained the Results are divided in more sections in order to evaluate the effect of the anode composition and the effect of the cathode composition on the thermal behavior and the product's composition. In fact, the C/NCA and the LTO/NCA cells have the same cathode composition, $(Al_{0.15}Co_{0.15}Li_{0.99}Ni_{0.71})O_2$, but a different anode composition: graphite in the case of NCA cells and lithium titanium oxide in the case of LTO. While C/NCA, C/LFP, C/NMC, and C/LCO have different transition metal oxides as cathode materials but all of them have graphite as anode material.

In this way, from the first comparison it will be possible to have information on the impact of anode composition on the behavior of cell under thermal abuse, while from the second comparison it will be possible to obtain information on the cathode effects during the TR, both related even with the SoC.

For sake of clarity, first the results of the C/NCA cell are reported below, than for the other chemistries the data are summarized in tables. All the graphs are available in the respective appendices at the end of the manuscript.

4.3.1   Results: Anode composition effect

In this section the results obtained from the study of C/NCA and LTO/NCA cells, at different state of charge, are reported. First the results for C/NCA cells will be discussed than those obtained for LTO/NCA will be presented in order to highlight the effect of anode composition on the thermal behavior of cell and also on the composition of emissions.

The temperature on the cell surface, expressed in °C, the pressure inside the reactor, expressed in barg, and the temperature of the oven are reported in Figure 51a for 50 % SoC and in Figure 51b for 100 % SoC respectively, during thermal abuse test.
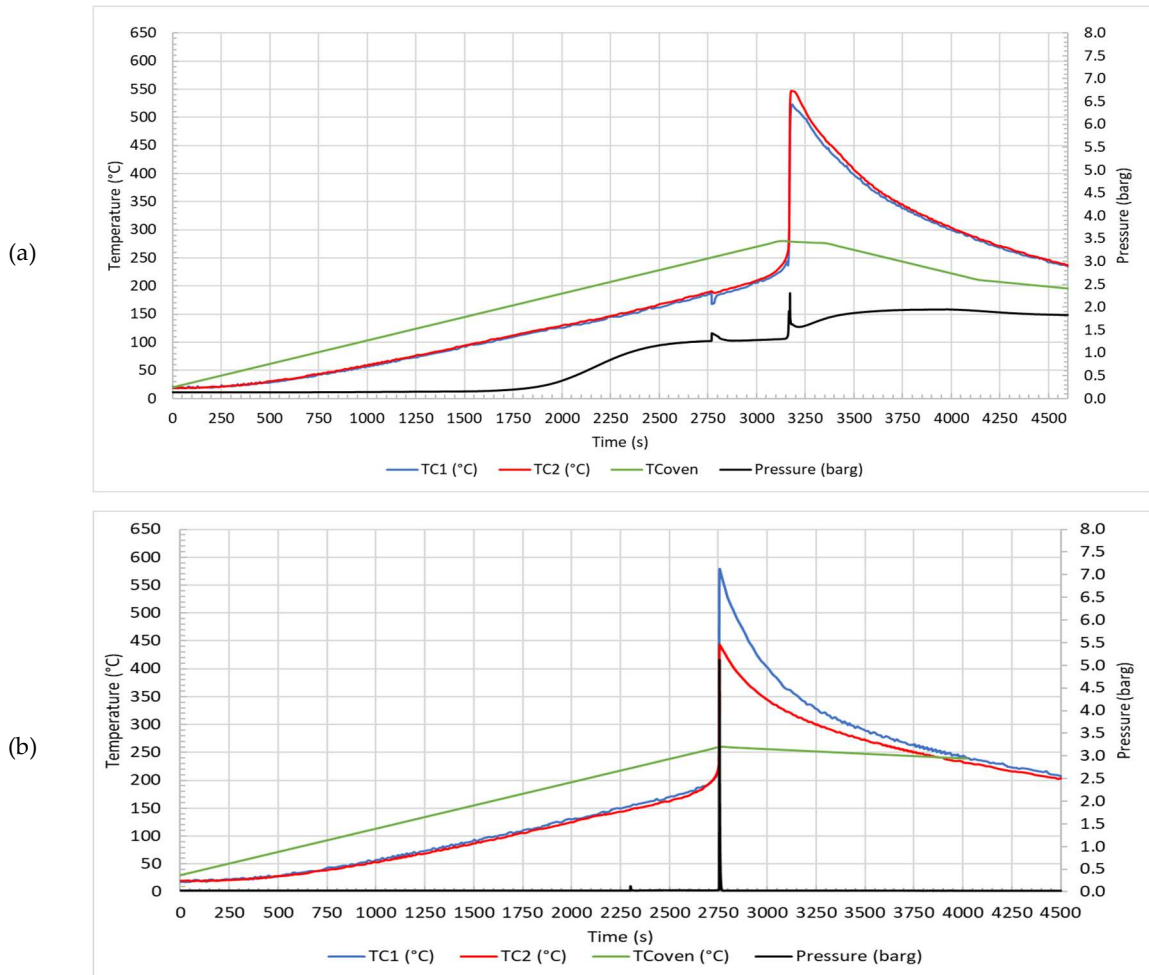
Figure 51: temperature (°C) and pressure (barg) profiles for thermal abuse test on C/NCA at SOC: (a) 50 %; (b) 100 %.

From a first comparison between the graphs it is possible to observe that the temperature and pressure values obtained for the 100% SoC (Figure 51b) are higher than the corresponding ones for the 50% SoC (Figure 51a) and the events take place in a shorter period of time.

In fact, the first event observed, which is the CID-vent disk activation, occurred at 1672 s when the temperature on the cell surface is around 106 ± 2 °C for the 50 % SoC and at 2023 s at a temperature of 130 ± 5 °C for the 100 % SoC. The increase of

the pressure inside the cell, which leads to the opening of the circuit with electrical insulation of one of the electrodes, caused an increase even of the internal pressure of the reactor, more evident for the 50 % SoC, 0.175 barg, than for the 100 % SoC, 0.028 barg. The different behavior is due to the amount of gas released during this phase, in fact, as will be shown later by the gas analysis, in the case of 50% SoC the release of hydrofluoric acid is starting from the CID-vent disk activation, while in the 100% SoC this acid is released together with the electrolyte from the venting.

The venting, the second event, occurs at 2770 s and 179 ± 16 °C for the 50 % SoC and 2301 s and 157 ± 2 °C for 100 % SoC, with a further increase of the pressure inside the reactor. In correspondence of the venting, it can be observed both an increase of the internal reactor pressure (0.030 barg for the 50 % SoC and 0.125 barg for the 100 % SoC) and a decrease in the surface temperature of the cell, registered by the TC_1 and TC_2. This phenomenon is due to the release of the electrolyte solution that vaporizes at such temperatures and absorbs heat due to the endothermic phase change occurring during the vaporization. After the evaporation the temperature starts to increase again. Subsequently, the onset of the TR occurs at 3122 s, 230 ± 6 °C on the cell surface and with an internal pressure of the reactor of 1.503 barg for the 50 % SoC and at 2731 s, 207 ± 3 °C and 0.034 barg for the 100% SoC. The main difference between the two SoCs are given by the maximum values of temperature and pressure reached at the peak (535 ± 17 °C and 2.312 barg for the 50 % SoC and 579 ± 137 °C and 5.071 barg for the 100 % SoC). The differences observed between the two SoCs in terms of temperature and pressure are significant both for the CID-vent disk activation and the venting. In fact, the CID-vent disk activation occurred around 20 °C before for the 50% SoC while the venting occurred 18 °C before for the 100 % SoC.

Finally, the highest temperature is reached for the 100 % SoC due to the higher level of energy available in this case compared to the 50 % SoC which provide the activation energy for an increasing number of the reactions that can occur inside

the cell. In fact, higher charge levels make the duration of total abuse shorter as the reactions are concentrated, there is in fact enough energy for the fuel to react completely.

In summary in the case of 100 % SoC, because of the higher energy content the cell requires less energy (i.e., lower temperatures) to initiate the reactions between cell components than cell at 50% SoC that are completed in a shorter time.

As mentioned before even the gas emission profiles are different depending on the SoCs. The concentration profiles (ppmv) of the main species, such as HF, EC, DMC, CO, CO_2, CH_4, are reported in Figure 52 for both the SoCs.
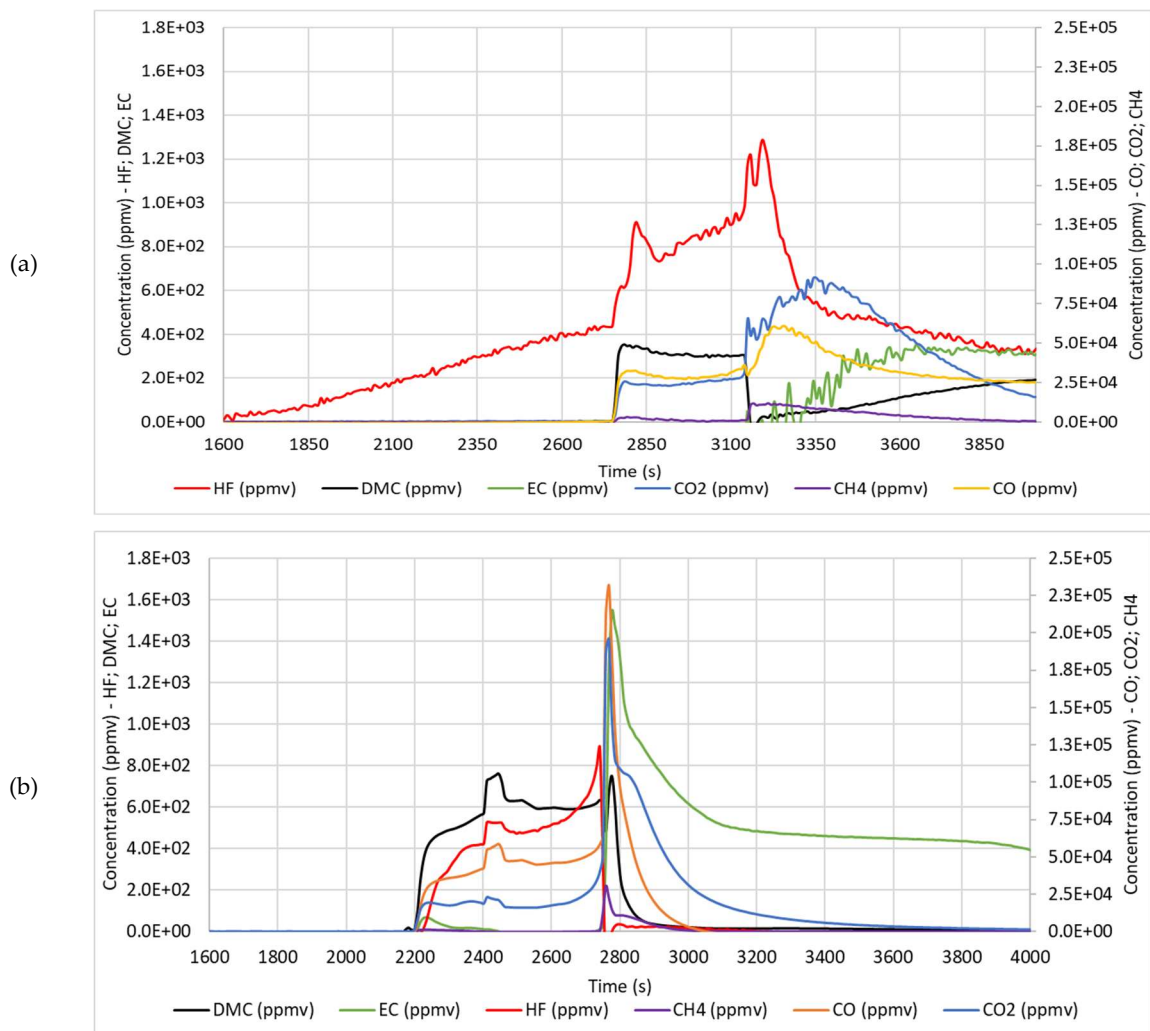
Figure 52: concentration profiles (ppmv) of DMC, EC, HF, CH_4, CO and CO_2 for thermal abuse test on C/NCA at SoC: (a) 50 %; (b) 100 %.

From a first comparison between the graphs it is possible to observe that the concentration values obtained for the 100% SoC (Figure 52b) are in a narrow range, while for the 50% SoC (Figure 52a) the gases are emitted in a wider range, above all the HF which is emitted starting from the CID-vent disk activation up to the maximum peak. The concentration profiles obtained for the two SoCs are significantly different but in line with what was previously observed for the pressure profile. In the case of 50 % SoC, the pressure value begins to increase upon CID-vent disk activation and does not return close to zero until the end of the test. This constant increase is due to a continuous release of gaseous compounds from the cell, which is initially only made of HF (at about 1600 s) and continues from venting onwards also with formation of other gases.

For HF and CO the total amount released in 30 min was compared to the values of the IDLH limits reported by the NIOSH. The total quantities of the gases, expressed in ppm, are reported in Table 35.

Table 35: concentration (ppm) of gas emitted for thermal abuse test on C/NCA at 50 and 100 % SoC in 30 min.

ppm Cells	DMC	EC	HF	CH_4	CO	CO_2
C/NCA 50 %	55	n.d.	344	349	10462	13118
C/NCA 100 %	146	185	101	885	15532	16043
IDLH [51]	-	-	30	-	1200	-

n.d.: not detected.

From the values reported in Table 35, it is possible to affirm that, independently from the SoC, the concentration values significantly exceed, by an order of magnitude, the IDLH values reported by the NIOSH set at 30 ppm for HF and 1200 ppm for CO in 30 min [51].

For these tests the quantities of collected condensate phase and solid are reported in Table 36 and showed in Figure 53.

g Cells	Initial cell weight	Final cell weight	Δcell	Gases weight	Condensate phase weight	Solid weight
C/NCA 50 %	45.6600	39.8367	5.8223	6.3433	0.0504	n.p.
C/NCA 100 %	45.6600	27.3000	18.3600	8.2230	n.p.	4.0103

n.p.: not present.

From the data reported in Table 36 it is shown that higher SoC caused an increase in the loss of material, indicated by the Δcell, in form of solid, liquid, and gases emitted. In the case of 100 % SoC most of the material is loss as gases and solid products while in the 50 % SoC is mainly constituted by gases and the condensate phase on the filter. Even the nature of the residues is different, in fact, for the 50 % SoC the solid residue is a condensate phase collected on the filter similar to a brown liquid (Figure 53b), while for the 100 % SoC the solid residue is a black powder (Figure 53d).

(a)

(b)

(c)

(d)
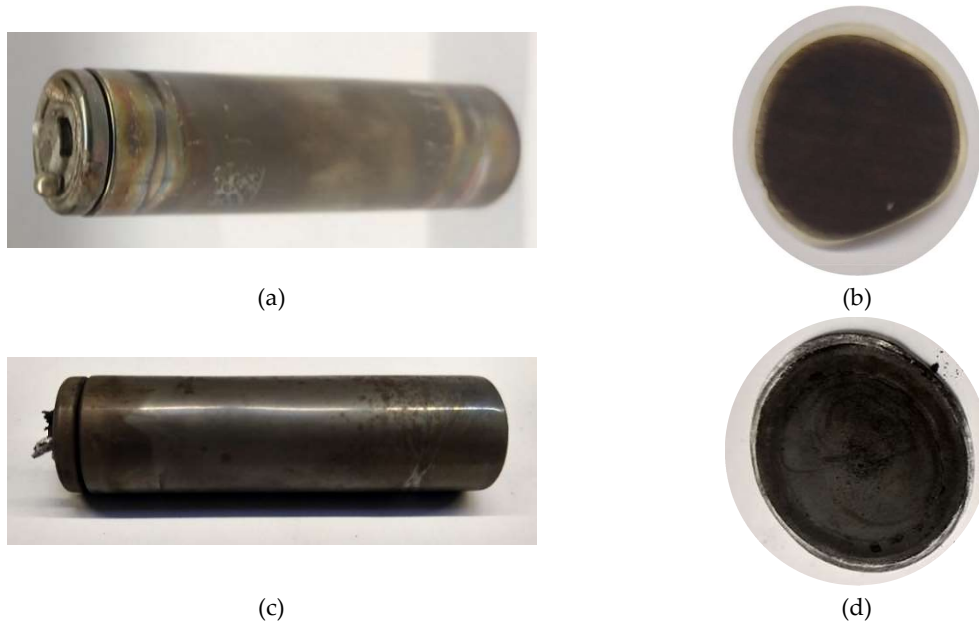
Figure 53: solid collected after the thermal abuse tests on C/NCA: (a) cell and (b) filter 50 %; (c) cell and (d) filter 100 %.

From the comparison of the cells (Figure 53a and Figure 53c) at the end of the tests is possible to observe that the 50 % SoC cell has some "droplet" in correspondence of the venting valve, probably due to the high temperature reached, while the cell of 100 % SoC presents the ejection of some internal components from the venting valve, probably due to the high pressure reached in the cell. In terms of solid

emissions collected on the filter at the exit of the reactor it is brown for the 50 % SoC cells while it is a black powder for the 100 % SOC cell.

The characterization of the solid emissions permit to obtain information on the composition, by ATR-FT-IR analysis, and the concentration of metals , by ICP-OES and AAS-OES analysis, and the size of the particle emitted, by SEM-EDX analysis. The ATR-FT-IR analysis was reported just for the filter of the thermal abuse test at 50 % SoC, due to the organic nature of the sample, rather than the inorganic nature of the residue obtained by form test at 100 % SoC. The ATR-FT-IR peaks with the relative identification and force such as very weak (*vw*), weak (*w*), medium (*m*), strong (*s*), or very strong (*vs*), are reported in Table 37.

Table 37: wavenumbers (cm⁻¹) of the filter of C/NCA at 50 % with the relative force (vw, w, m, s or vs) and identification.

Identification		C/NCA 50 % - filter	
Paraffin oil	*s*	2951.19	*m*
Paraffin oil – PEO	*vs*	2918.01	*vs*
Paraffin oil – PEO	*vs*	2849.62	*s*
Paraffin oil	*vw*	2737.23	*vw*
PEO	*w*	1714.37	*m*
PEO	*w*	1642.61	*vw*
Paraffin oil – PEO	*s*	1461.66	*s*
Paraffin oil – PEO	*m*	1376.06	*s*
Paraffin oil	*w*	1267.92	*vw*
PEO	*w*	1163.74	*m*
Paraffin oil	*vw*	1068.87	*vw*
PEO	*w*	909.60	*w*
Paraffin oil	*w*	886.26	*w*
Paraffin oil	*m*	729.99	*m*
Paraffin oil – PEO	*s*	719.27	*m*

PEO = Polyethylene oxide

The peaks identified are attributable to the presence of paraffin oil [164] and PEO [166]. These two materials can be used in the cell composition to enhance the properties, as already explained during the evaluation of the thermal stability products. PEO can be produced even by the EC degradation process.

Finally, the results obtained by the ICP-OES and AAS-OES were reported in Table 38 as milligrams of metal in the solid.

Table 38: quantification of metals (mg) in the solid ejected during the thermal abuse tests on C/NCA 50 and 100 % SoC.

	Al (mg)	Co (mg)	Cu (mg)	Li (mg)	Mn (mg)	Ni (mg)	P (mg)
C/NCA 50 %	0.0057	< LOD	< LOD	0.0012	< LOD	0.1505	< LOD
C/NCA 100 %	324.1	266.9	480.2	172.1	0.08	< LOD	< LOD

LOD: limit of detection.

The lower amount of metals obtained at 50 % SoC is due to the lower amount of material ejected from the cell and the different nature compared to the 100 % SoC. For the 100 % SoC there is a discrepancy between the total solid emitted and the total amount of metals quantified as 2.7667 g. This difference is due the carbon and the oxygen contribution that are not considered in the ICP-OES and AAS-OES analysis but as shown after by the SEM-EDX are widely present in the solid sample. The low concentration of Mn is due to the lower percentage in the cathode initial composition compared to the other metals while the not detection of P, under the LOD of the instrument, is due to the nature of this metal. In fact, the P in the LIBs is present as salt ($LiPF_6$) dissolved in the electrolyte or as electrode binder so it can be lost during the pretreatment at high temperature before the analysis.

Compositional analyses were performed with EDX to verify the presence of other elements in the filter. SEM-EDX analyses were performed with a beam voltage of 15.0 kV and a working distance from the source of 15.00 mm, at different magnifications, depending on the size of the particles detected in the filter plots. Then, EDX analyses were therefore conducted on the particles. In Figure 54a is reported the SEM images of the filter at 50 % SoC, while in Figure 54b is shown the EDX-map with the elements percentage.

Both from the microscope image, via SEM-BSE, and from the mapping of the elements, via EDX, it is possible to observe how the distribution of the material on the filter is uniform and less than a few small agglomerates. So, specific analyzes for determining the composition and size of the particles or agglomerates were conducted on these sites.
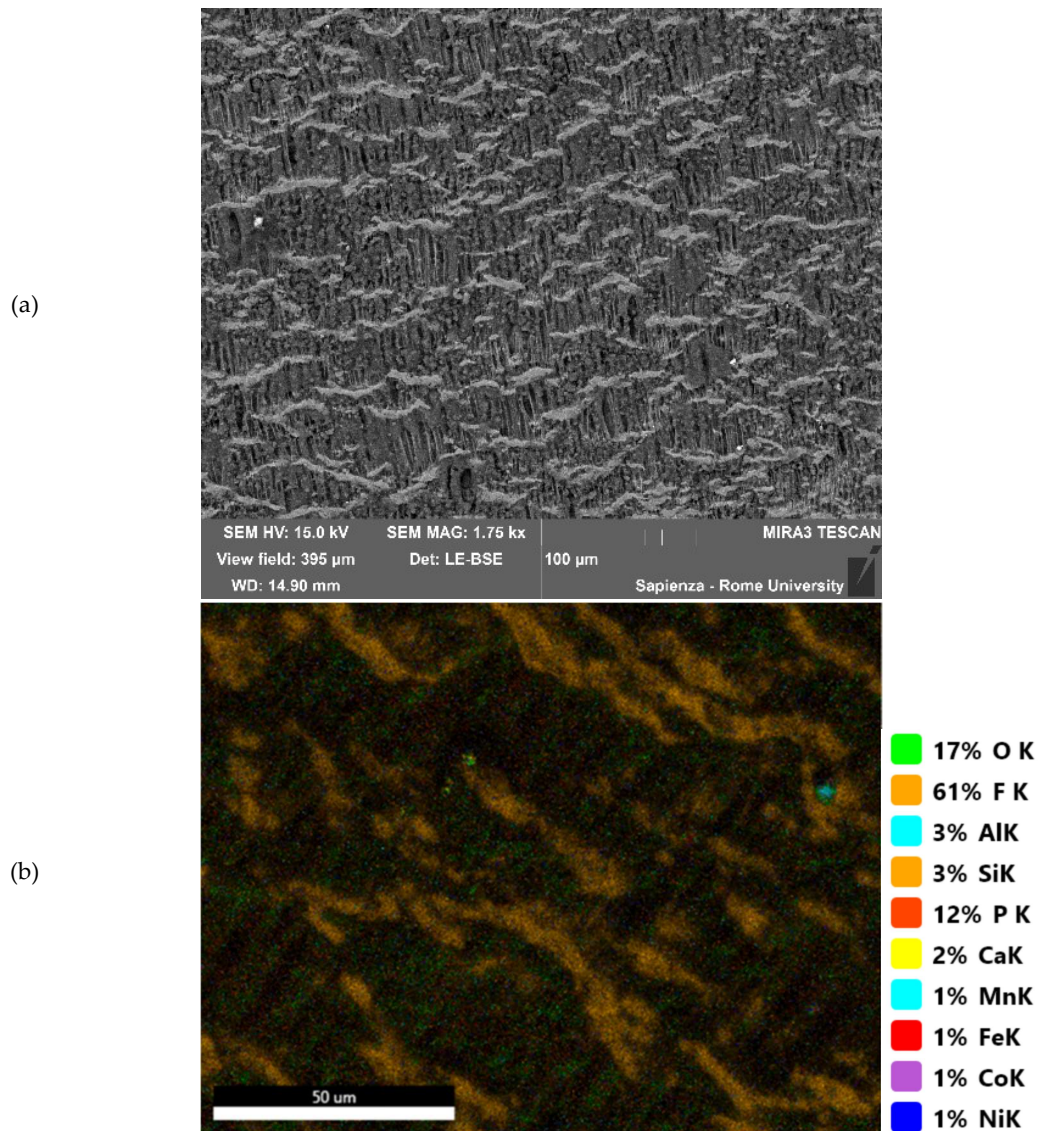
Figure 54: filters after the thermal abuse test on C/NCA at 50 % SoC: (a) SEM-BSE; (b) EDX-map.

For this latter are also reported the spot and/or area analyzed, the diameter of the particles and the respective EDX spectra for compositional analysis, as shown in Figure 55. The presence of lithium cannot be verified by this analysis, in fact SEM-EDX only detect the Z > 3, Li is too light and cannot be detected for the very low energy of characteristic radiation.

(a)

(b)

Element	C K	O K	F K	Al K	P K	Co K	Ni K
Weight %	37.6	13.11	18.39	0.22	12.09	1.86	16.69
Atomic %	55.61	14.54	17.18	0.14	6.92	0.56	5.04

(c)
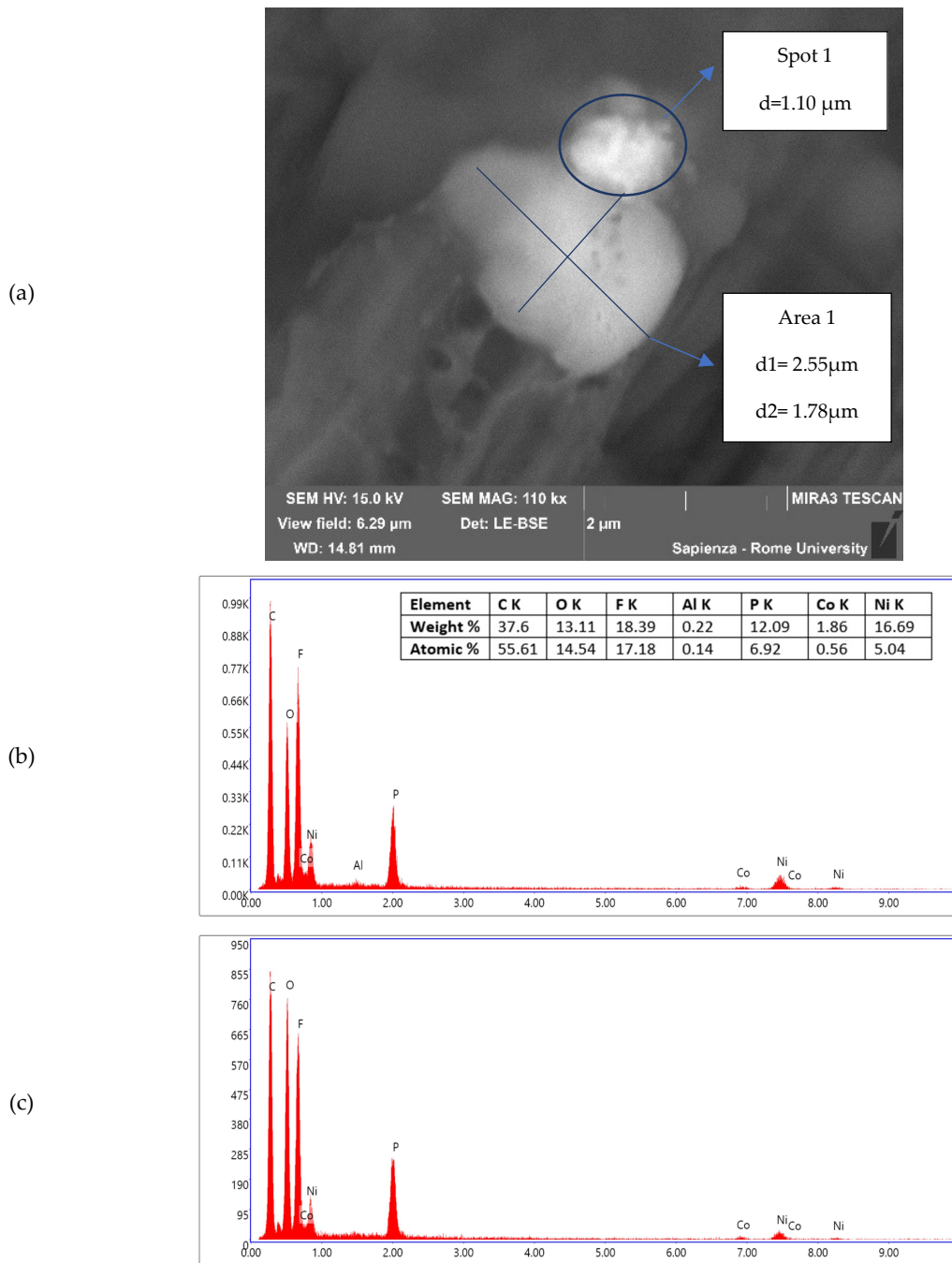
Figure 55: Condensed phase collected during the test on C/NCA at 50%. (a) Areas analyzed by EDX with dimension of the particles; (b) EDX of Spot 1; (c) EDX of Area 1.

The agglomerate in Figure 55a can be divided into two distinct particles, the upper one with a d = 1.10 μm and the inferior one with a d_1 = 2.55 μm and d_2 = 1.78 μm. The main difference between the two in terms of composition is the presence of Al in the upper one and a greater amount of oxygen in the inferior one. The P and F are attributable to the electrolyte salt while the material coming from the electrodes, specifically the cathode, is confirmed by the copresence, in Spot 1, of

Ni, Co and Al, presumably in oxidized form, while in Area 1 to the copresence of Ni and Co.

For LTO/NCA cell the results of thermal abuse tests are reported in Figure 88 (Appendix 1) for both the SoCs, 50 % and 100 % respectively, while in Table 39 are summarized the parameters of the main events.

Table 39: temperature (°C) and pressure (barg) relative to the main events of the LTO/NCA thermal abuse tests.

Key event	LTO/NCA 50 %			LTO/NCA 100 %		
	t (s)	T (°C)	P (barg)	t (s)	T (°C)	P (barg)
CID-vent disk activation	2683	183 ± 15	0.051	n.d.	n.d.	n.d.
Venting	2695	179 ± 18	0.088	2484	187 ± 4	0.089
TR	n.d.	n.d.	n.d.	2803	233 ± 8	0.060
Peak	n.d.	n.d.	n.d.	2805	310 ± 41	0.108

n.d.: not detected.

From the comparison, there are significant differences in terms of events occurring, in fact, the TR not occurred for the lower SoC while the CID-vent disk activation was not registered for the higher SoC.

In fact, the CID-vent disk activation has been registered only for the 50 % at 2683 s when the temperature of the cell surface is 183 ± 15 °C and at a pressure of 0.051 barg. In the case of the 50 % SoC the CID-vent disk activation is followed immediately, 12 s, by the venting when the temperature on the cell surface is 179 ± 18 °C and the pressure inside the reactor is 0.088 barg. The temperature measured during the venting is lower than the temperature of the CID-vent disk activation due to the release and the evaporation of the electrolyte solution that vaporizes at such temperatures and absorbs heat. The venting occurs in similar conditions for the cell at 100 %SoC

The main and most important difference between the two SoCs is now observed. In fact, after the evaporation the temperature on the cell surface starts to increase again, according with the heating rate of 5 °C/min. Subsequently, the onset of the

TR occurs only for the cell at 100 % SoC and not for the 50 % SoC, even if in the second case the oven heating continued well beyond the TR temperature observed during the thermal stability test, 194 ± 5 °C. For the 100 % the TR onset is registered at 2803 s, 233 ± 8 °C and pressure of the reactor of 0.060 barg, while the maximum peak for the temperature is at 310 ± 41 °C and a pressure of 0.108 barg.

In summary, the differences between the two cells at different SoCs in terms of temperature and pressure are significant both for the CID-vent disk activation and for the TR occurrence. In fact, the CID-vent disk activation occurred just in the case of the cell at 50 % SoC while for the 100 % SoC it was not registered. It cannot be excluded that since the two events are so close in time, for the highest SoC they occurred simultaneously due to the highest energy level present in the cell. While the TR occurred just for the 100 % SoC and not for the 50 %SoC and this may be due to the different level of energy present inside the cell. In fact, the electrical energy stored inside the battery can triggered more reactions inside the cell.

The SoC affects even the gas emission of the main species, such as HF, EC, DMC, CO, CO_2 and CH_4, whose profiles are reported in Figure 89 (Appendix 1), expressed in ppmv. The concentration profiles obtained for the two SoCs are significantly different reproducing the event observed during the tests. As an example, for the 100 % SoC cell emission peaks are well defined and in a very narrow range of time and once the gaseous species have been emitted the value returns to almost zero, therefore the emissions are concentrated. The only exception is given by the EC and it is probably due to the temperature reached during the TR compared to the boiling point of this organic carbonate, 248 °C. In fact, the EC is the carbonate with the highest boiling temperature among those used in the electrolyte and therefore, being released only during the TR, its emission is shifted in time compared to the other carbonates. One of the most significant difference between the cell at different SoC is given by the HF, which

reached higher concentration in the 50 % SoC, $1.5*10^3$ ppmv, compared to the 100 % SoC, $8.00*10^2$ ppmv.

The quantities of the gases, expressed in ppm, for an average 30 min period are reported in Table 40 and are compared with the IDLH limits reported by the NIOSH

From the values reported in Table 40, it is possible to affirm that the IDLH values reported by the NIOSH set at 30 ppm for HF and 1200 ppm for CO in 30 min are exceeded for both the SoCs by one order of magnitude [51].

Table 40: concentration (ppm) of gas emitted for thermal abuse tests on LTO/NCA at 50 and 100 % SOC in 30 min.

ppm / Cells	DMC	EC	HF	CH_4	CO	CO_2
LTO/NCA 50 %	218	184	155	n.d.	10392	14400
LTO/NCA 100 %	192	434	184	258	17851	14748
IDLH [51]	-	-	30	-	1200	-

Another evaluation that can be done is about the total amount released during the thermal abuse test at different SoCs. In fact, even if the two profile were significantly different the total amount of gases are similar in order of magnitude, except for the methane that does not appears in the 50 % SoC test (Figure 89 in the Appendix 1).

For these tests the quantities collected of residues and their typology are reported in Table 41 and showed in Figure 56.

Table 41: weight of the cell and the products collected (g) after the thermal abuse test on LTO at 50 and 100 % SoC.

g / Cells	Initial cell weight	Final cell weight	Δcell	Gases weight	Condensate phase weight	Solid weight	Liquid weight
LTO/NCA 50 %	39.4373	32.0086	7.4287	6.3347	n.p.	n.p.	0.5410
LTO/NCA 100 %	39.0736	30.2755	8.7981	8.4168	0.1313	n.p.	n.p.

n.p.: not present.

From the data reported in Table 41 it is shown that the increase of the SoC causes a variation both in the weight loss and in the typology of residues ejected. In fact, higher SoC caused an increase of the total weight loss (Δcell), while the products

emitted, except for common gaseous products, are of different nature. In Figure 56 it is possible to observe that the plastic septum, the venting disk in this kind of cell, collapsed completely in the case of 100 % SoC and partially for the 50 % SoC. In addition, at higher SoC the release of gas is occurred even by the bottom vent (Figure 56e). Regarding the products released, for the 100 % SoC it is observed the accumulation of a condensate phase on the filter (Figure 56f) while the 50 % SoC released a brown liquid collected in the reactor (Figure 56b) with negligible traces of condensed phase on the filter (Figure 56c).

| (a) | (b) | (c) |

| (d) | (e) | (f) |
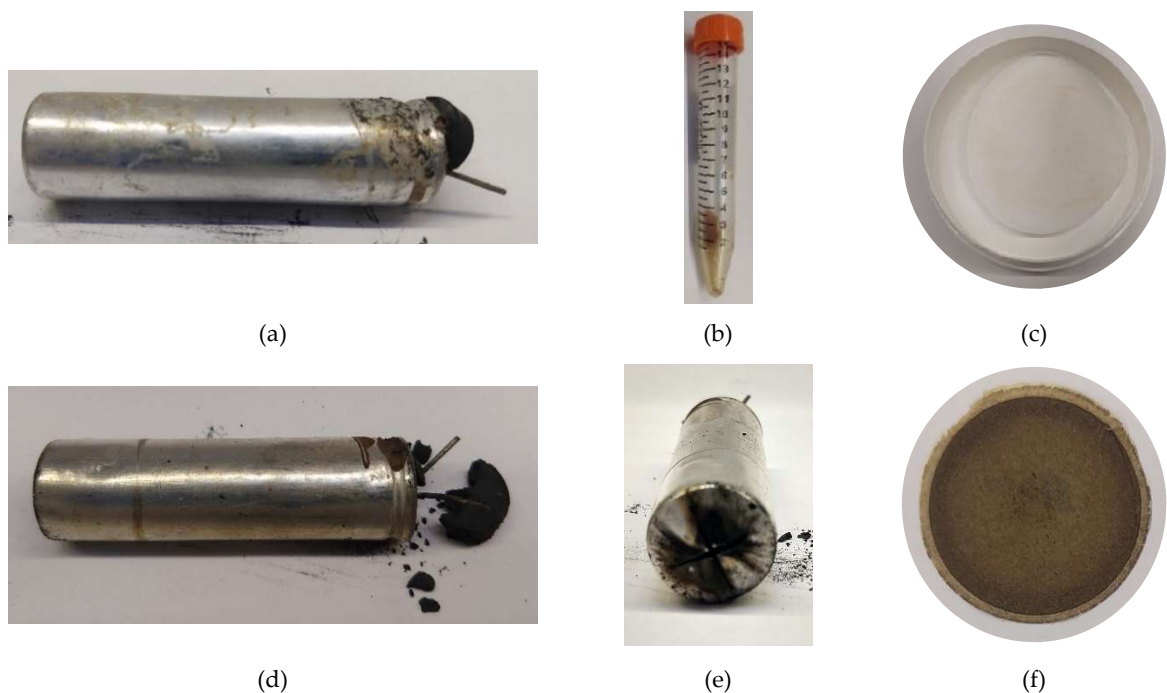
Figure 56: solids collected after the thermal abuse tests on LTO/NCA: (a) cell 50 % SoC; (b) liquid 50 %SoC; (c) filter 50 % SoC; (d) cell 100 %; (e) bottom part of cell 100 % SoC; (f) filter 100 % SoC.

In both cases the residues are due to the leakage of the electrolyte from the cell. In the case 100 %SoC cell the electrolyte solution evaporated in the reactor and flows into the filter where it condensed, while for 50 % SoC cell the electrolyte solution was released from the cell into the reactor but does not reach the filter. This difference could be due to the fact that in the latter case it was not observed the TR, therefore the temperatures and pressure did not reach values such as to allow complete evaporation and push gases towards the filter.

The composition of the liquid was obtained by the ATR-FT-IR analysis, the spectra of the liquid is shown in Figure 90 (Appendix 1) while peaks with the relative identification and force, such as *vw*, *w*, *m*, *s*, or *vs*, are reported in Table 42. Similarly, the spectra for the solids are shown in Figure 91 (Appendix 1) while peaks with the relative identification and force, are reported in Table 43.

Table 42: wavenumbers (cm^{-1}) of the liquid collected for LTO at 50 % with the relative force and identification.

Identification		LTO/NCA 50 % - liquid	
EC	*w*	2996	*w*
EC	*w*	2933	*w*
EC	*w*	1963	*w*
EC	*vs*	1793	*vs*
EC	*vs*	1770	*vs*
EC	*w*	1553	*w*
EC	*m*	1481	*m*
EC	*w*	1421	*w*
EC	*s*	1390	*s*
EC	*w*	1354	*w*
EC	*vs*	1155	*vs*
EC	*vs*	1066	*vs*
EC	*m*	971	*m*
EC	*m*	893	*m*
EC	*m*	845	*m*
EC	*s*	771	*s*
EC	*s*	715	*s*
EC	*w*	558	*w*
EC	*w*	526	*w*
EC	*w*	488	*w*
EC	*w*	451	*w*

The peaks identified and the superimposition of the spectra uniquely identified the liquid as EC, the highest boiling component of the electrolyte solution (boiling temperature 248 °C). This result confirms the hypothesis that the electrolyte in the case of the 50 % SoC test has not completely evaporated due to the low temperatures and is therefore condensed in the reactor itself and not on the filter, as is the case with the 100 % SoC.

The ATR-FT-IR analysis on the filters did not provide interesting information as the main peaks were those attributable to the filter alone. While due to the greater quantity and color of the condensed phase, for 100% SOC sample it is not possible to unambiguously identify the material filtered.

Table 43: wavenumbers (cm^{-1}) of the filter of LTO at 50 % and 100 % with the force (vw, w, m, s or vs) and identification.

Identification		LTO/NCA 50 % - filter		LTO/NCA 100 % - filter	
PP	s	n.d.	-	2950.77	s
PTFE Filter	m	2949.23	w	n.d.	-
PTFE Filter	s	2919.36	w	n.d.	-
PP	vs	n.d.	-	2918.11	vs
PTFE Filter	m	2871.54	w	n.d.	-
PP	m	n.d.	-	2867.48	m
PP	m	n.d.	-	2839.13	m
Not identified	-	n.d.	-	1685.68	m
Not identified	-	n.d.	-	1575.92	vw
Not identified	-	n.d.	-	1509.80	vw
PTFE Filter	m	1455.65	w	n.d.	-
PP	s	n.d.	-	1452.26	m
Not identified	-	n.d.	-	1434.85	m
PTFE Filter	m	1376.20	w	n.d.	-
PP	vs	n.d.	-	1375.71	s
PTFE Filter	vs	1203.96	vs	n.d.	-
PP	m	n.d.	-	1166.96	m
PTFE Filter	vs	1149.41	vs	n.d.	-
Not identified	-	n.d.	-	1112.15	m
PP	m	n.d.	-	997.40	m
PP	m	n.d.	-	972.10	m
PP	m	n.d.	-	841.20	m
Not identified	-	n.d.	-	728.91	vs
PTFE Filter	m	638.77	m	n.d.	-
PTFE Filter	m	554.29	m	n.d.	-
PTFE Filter	vs	503.10	s	n.d.	-

PP: polypropylene. n.d.: not detected.

Finally, the ICP-OES and AAS-OES analysis were conducted on the filter collected for the 100 % SoC, to identify the composition and the relative quantities, while the SEM-EDX returned the composition and the diameter of the particles. The results obtained by the ICP and AAS were reported in Table 44 as milligrams of metal on the total gram of solid. The filter for the 50 % SoC was not analyzed due to lower amount of the condensate phase.

Table 44: quantification of metals (mg) in the solid residue collected for the thermal abuse tests on LTO/NCA 100 % SOC.

Cell mg	Al	Cu	Li	Mn	Ti
LTO/NCA 100 %	3.3270	0.5370	0.6418	0.0223	0.3013

There is a discrepancy between the total solid emitted and the total amount of metals quantify of 0.1262 g. This difference is due the loss of the organic material during the pre-treatment, in fact before the digestion the sample were heated in a

muffle at 530 °C for 8 h to remove the organic compounds which could interfere with the ICP-OES and AAS-OES analyses. So, in this pre-treatment all the components due to the electrolyte, such as Co and O, are lost.

This information can be obtained by the SEM-EDX analysis. In fact, compositional analyses were performed with EDX to verify the presence of other elements in the filter. SEM-EDX analyses were performed (beam voltage of 15.0 kV and a working distance from the source of 14.66 mm) at different magnifications, depending on the size of the particles detected in the filter. In Figure 57a is reported the SEM images of the filter at 100 % SoC, while in Figure 57b the EDX-map.

(a)

(b)
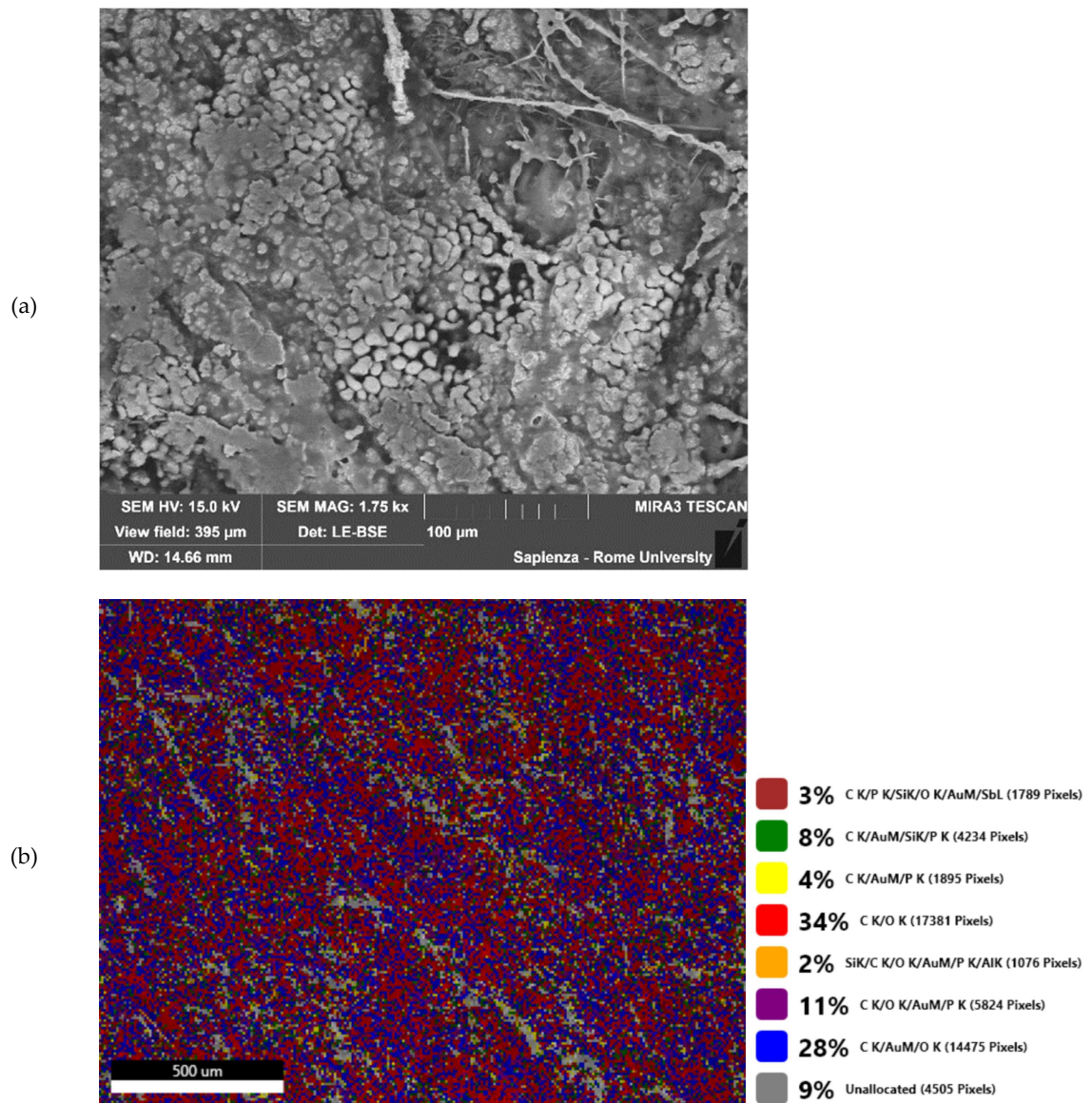
Figure 57: filters after the thermal abuse test on LTO/NCA at 100 % SoC: (a) SEM-BSE; (b) EDX-map.

From Figure 57a it is possible to observe that the distribution of the condensed compounds on the filter is homogeneous over the texture of the porous filter. The same dispersion and composition have been obtained even via EDX-map.

Finally, EDX analyses were therefore conducted on the agglomeration of the condensate phase and the most significant image for the filter is reported in Figure 58.

(a)

(b)

Element	C K	O K	F K	P K
Weight %	93.08	4.59	0.50	1.84
Atomic %	95.42	3.52	0.32	0.74

(c)

Element	C K	O K	F K	Al K	P K
Weight %	84.20	5.82	4.36	1.04	4.57
Atomic %	89.99	4.67	2.95	0.49	1.89
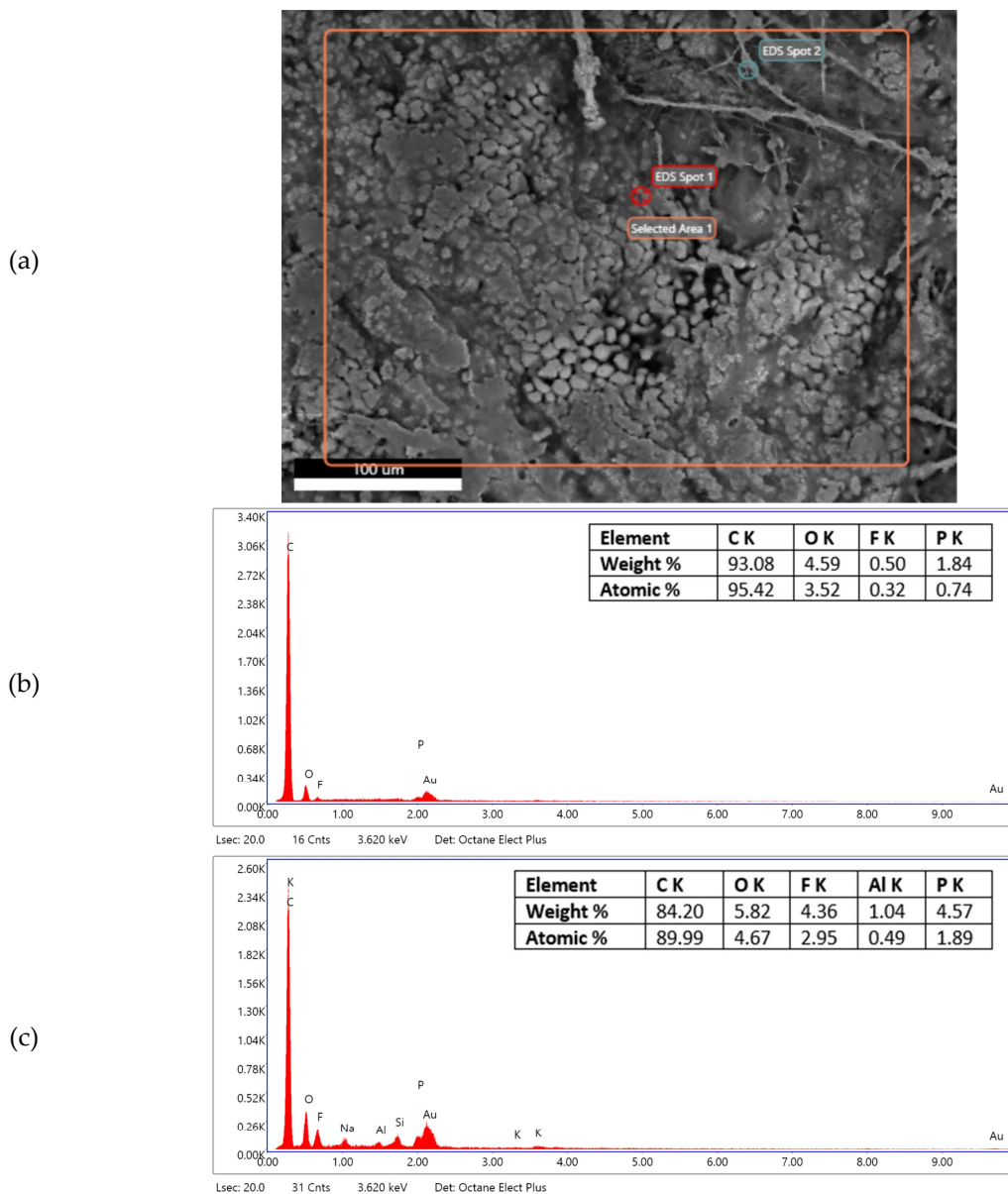
Figure 58: Condensed phase collected during the test on LTO/NCA at 100% SoC. (a) Areas analyzed by EDX; (b) EDX of Spot 1; (c) EDX of Spot 2.

The condensate phase shown in Figure 58a forms a film over the filter surface without creating particles and/or agglomerates, so any diameter can be calculated. The main components are the compounds of the electrolyte, such as C, O, F, and P. The only difference is the trace of Al in the spot 2, that can be due to the current collector of the cathode.

4.3.2 Discussion: Anode impacts on the thermal behavior

The two chemistries investigated so far have the same cathode composition, NCA, with a different composition of the active anode material. In fact, the anode of the C/NCA cell is made of graphite while the LTO/NCA is made of lithium titanium oxides, both deposited on a copper current collector. So, a first comparison can therefore be made on the effect of the composition of the anode on the thermal behavior of Li-ion cells, according to the SoC.

In fact, the first thing that it is possible to observe is the effect of the SoC on the temperature and pressure profiles obtained and the products emitted. The SoC s defined as the amount of electrical charge stored in the battery respect to the nominal electrical charge. This value can determine the strength of the electrical abuse when the opposite poles enter in contacts due to the melting of the separator. For each cell the relative voltage range is indicated in the SDS, and reported in Table 45.

Table 45: voltage (V) at 50 and 100 % SoC for the C/NCA and LTO/NCA cells.

Voltage (V)	C/NCA	LTO/NCA
Soc 50 % (V)	3.60	2.20
SoC 100 % (V)	4.20	2.80

From Table 45 it is possible to observe that the voltage range for the two chemistries considered are significantly different, with higher voltage values for the C/NCA than the LTO/NCA, so the voltage can give back a first evaluation of the TR strength.

A first comparison can be made between the temperatures of the main events for the thermal abuse tests at different SoC and the temperatures obtained by the

thermal stability tests UN/ECE Regulation N°100 for the relative chemical composition. The comparison between the temperature of CID-vent disk activation, venting and TR for the two anode composition is shown in Figure 59, Figure 59a for C/NCA and Figure 59b for LTO/NCA.

(a)

(b)
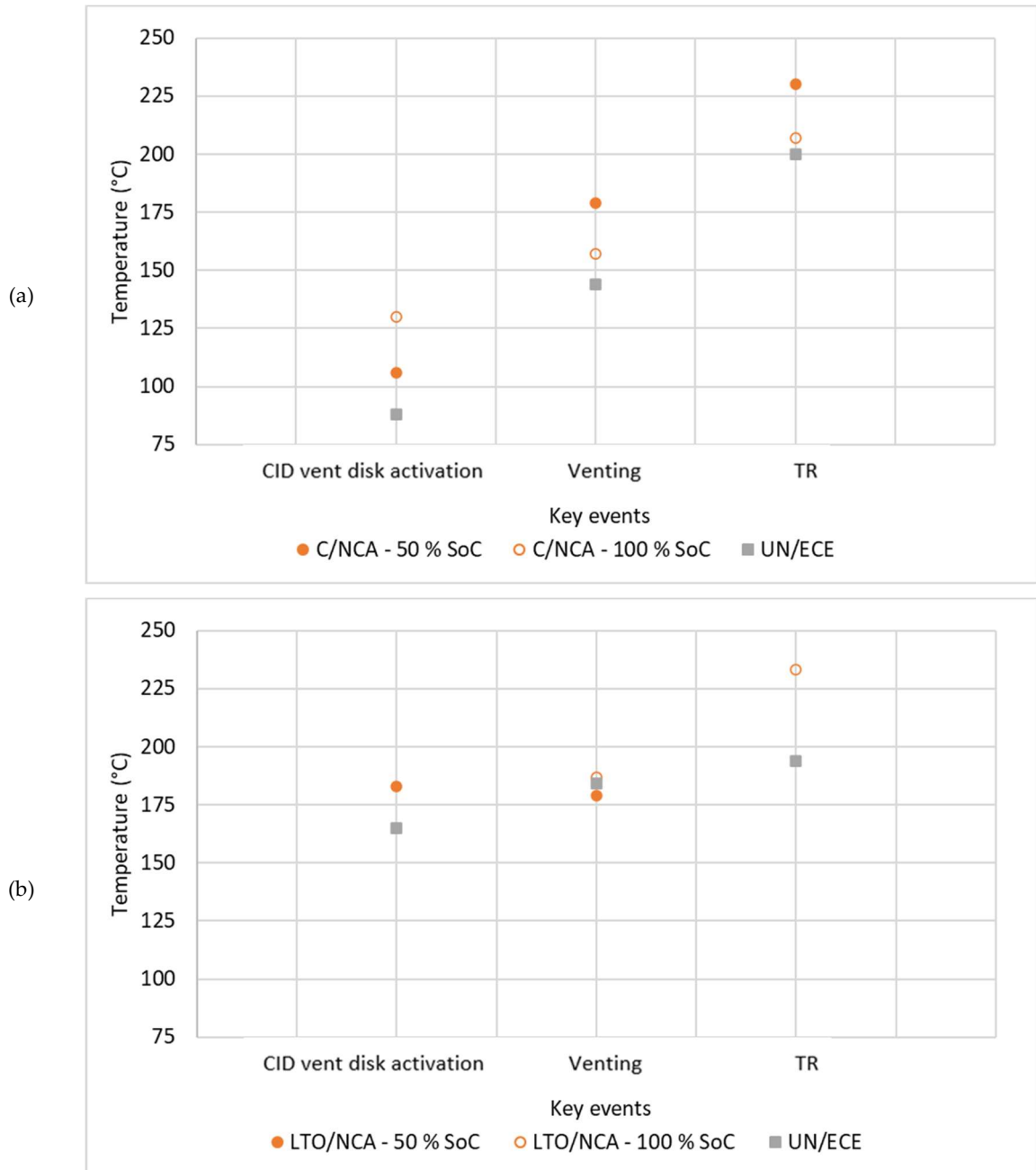
Figure 59: Comparison between the temperatures obtained by the UN/ECE N°100 and thermal abuse tests for: (a) C/NCA; (b) LTO/NCA.

The values recorded for the CID-vent disk activation for all the conditions investigated are higher than the limit values obtained by applying the thermal

stability test reported in the UN/ECE Regulation N°100. The same trend is observed for the venting and the TR for the C/NCA cell, while for LFP/NCA the venting temperature values during the stability and the thermal stability tests are very similar.

A comparison, in terms not just of maximum temperature reached but even of the products emitted, between the two chemistries of cells is reported for both the SoCs in Table 46. The table is divided in five sections, the first reports the electrical energy available, the second describes the main events reached during the abuse with the relative temperature and pressure reached, while the other three report the physical-chemical characterization of the emission, gas, solid and liquid.

Table 46: Comparison between the NCA and the LTO thermal abuse tests at 50 and 100 %.

Parameters	C/NCA – 50 %	C/NCA – 100 %	LTO/NCA – 50 %	LTO/NCA – 100 %
Voltage (V)	3.60	4.20	2.20	2.80
CID-vent disk activation	106	130	183	n.d.
Venting	179	157	179	187
TR	230	207	n.d.	233
Tmax (°C)	535	579	325	310
	(self heating)	(self heating)	(external heating)	(self heating)
SHR (°C/s)	0.300	0.600	n.d.	2.400
P_{max} (barg)	2.312	5.071	0.088	1.446
Weight loss (g)	5.8223	18.3600	5.4287	8.7981
Total gas (g)	6.3433	8.2230	6.3347	8.4168
C_{CO} (ppmv) - 30 min	10462	15760	12232	14747
C_{HF} (ppmv) - 30 min	344	101	706	184
Total solid (g)	0.0504	4.0103	n.p.	0.1313
Organic part	PEO and paraffin	-	-	PP
Inorganic part	Al, Cu, Ni	Al, Co, Cu, Li, Mn	-	Al, Li, Cu, Ti, Mn
Particle size (μm)	1.633	n.a.	-	n.d.
Total liquid (g)	n.p.	n.p.	0.541	n.p.
Organic part	-	-	EC	-

n.a.: not available. n.d.: not detected. n.p.: not present. - : no information.

The electrochemical difference between the two cells is due to the electrical energy stored by the cell. As already highlighted, the energy available, correlated to the SoC, can influence the strength of the TR, in term of energy available for the activation of the different reactions.

The effects of this difference can have repercussions both on the thermal behavior of the cells when subjected to thermal abuse and the products emitted. For example, the C/NCA reached the TR independently from the SoCs, while in the case of the LTO/NCA the TR is reached only for the higher SoC. So, the anode composition effect on the TR evaluation can be obtained considering the two SoCs separately.

For SoC of 50 %, it is observed that the TR occurred only for the C/NCA and not for the LTO/NCA and the products emitted were different in terms of nature and total amount. In fact, the TR in the case of the C/NCA occurred with a SHR of 0.300 °C/s with a maximum of 535 °C and 2.312 barg which caused the loss in weight of 5.8223 g from the cell, in the form of gases and solids. In the case of the LTO/NCA, even if the heating of the oven was maintained over 300 °C the TR was not detected, with the emission of gaseous and liquid products.

Independently from the temperature reached in both the conditions different products were emitted, such as gases, liquid, and solid, and the weight loss of the cell, before and after the thermal abuse test, is about 5 g. The difference between the typology of products is: gas and solid for the C/NCA and gas and liquid for the LTO/NCA. About the gas the total amount is comparable, around 6 g, but the most important aspect that must be evaluated is the concentration of the toxic gases, HF and CO, emitted in 30 min, which are 1 order of magnitude higher compared to the limits imposed by the NIOSH (30 ppm for HF and 1200 ppm for the CO). The solid particles are present only in the case of C/NCA and their environmental and human health impact is given both by composition and size. The composition is mainly given by metal oxides while the average size is 1.633 μm, a highly dangerous size falling within the respirable fraction (particles with a diameter less than 4 μm). While the liquid emission is observed only in the LTO/NCA, due to the lower temperature reached during the thermal abuse test that not permitted the complete evaporation of the EC.

For the 100 % SoC cells, the TR is reached for both the chemistries even if the temperature and the pressure values reached are significantly different. In fact, in the case of the C/NCA the maximum temperature reached is higher compared to the LTO/NCA, 579 vs 310 °C, and even the increase of the internal pressure of the reactor is higher, 5.071 vs 1.446 barg. These values caused a significant increase of the weight loss of the C/NCA compared to the LTO/NCA, with a difference of 10 g, due to solid and gases ejection. Due to the higher temperature reached by self-heating, SHR of 2.400 °C/s, the LTO/NCA in the case of the 100 % did not shown the liquid ejection but gases and solid emission as the C/NCA. Anyway, the amount of solid ejected in the case of the C/NCA is higher compared to the LTO/NCA, 4.0103 vs 0.1313 g, and even the composition is different, due to the initial chemical composition of the active materials of the cells and the organic fraction. In fact, for the LTO/NCA cell trace of the plastic separator has been identify in the condensate phase on the filter, added to the metallic particles due to the anode materials. In fact, in the LTO/NCA there is the presence of the Ti that is related to the anode composition. The size of the particles was not possible to measure because the solid ejection of the LTO/NCA is more a condensate phase that a powder.

So, with the same cathode the more stable anode material, according to the Li-ion cells under investigation, between the graphite (NCA) and the spinel $Li_4Ti_5O_{12}$ (LTO) resulted the second one, for the lower temperature and pressure reached during the TR, observed only for the higher SoC, and the typology of products emitted, liquid and condensate phase compared to respirable metallic powder.

The C/NCA thermal behavior can be due to the lower melting point of separator (141°C vs 169°C) (Table 34) and the higher flammability of electrolyte, with higher percentage of DMC characterized by a lower flash point than the other carbonates. This can be a first explanation of the lower temperature observed for the CID-vent disk activation and the venting than the LTO/NCA cell (Table 34). In the case of

the C/NCA the higher voltage value and the lower temperatures of melting of separator and evaporation of electrolyte can cause an internal increase of the pressure inside the cell which leads to the CID-vent disk activation and the venting at lower temperatures on the cell surface compared to the other chemistry (Table 46). Even the maximum temperature reached during TR can be correlated to the internal components due to the higher voltage value and the reactivity of the compounds with respect to LTO/NCA cell.

4.3.3 Results: Effect of Cathode composition

This section reports the results obtained from conducting thermal abuse tests on cells with the same anode composition, graphite anode, but different cathode composition, i.e., LFP, NMC, and LCO.

4.3.3.1. *Graphite/Lithium Iron Phosphate (C/LFP)*

Results of thermal abuse tests on C/LFP cell are reported in Figure 92 (Appendix 2) for the 50 % and the 100 % SoC while in Table 47 are reported the parameters of the main events.

Table 47: temperature (°C) and pressure (barg) relative to the main events of the C/LFP thermal abuse tests.

Key event	C/LFP 50 %			C/LFP 100 %		
	t (s)	T (°C)	P (barg)	t (s)	T (°C)	P (barg)
CID-vent disk activation	2185	154 ± 19	0.021	2259	164 ± 3	0.045
Venting	2680	198 ± 18	0.026	2488	197 ± 1	0.073
TR	n.d.	n.d.	n.d.	2658	234 ± 20	0.080
Peak	n.d.	n.d.	n.d.	2693	310 ± 36	0.108

n.d.: not detected.

From a first comparison between the data obtained at different SoCs it is possible to observe that with the increase of the SoC the TR occurred in both cases, even if the maximum temperature value is 310 ± 36 °C.

Specifically, the first event, the CID-vent disk activation , occurred for both the SoCs at same temperature (154 ± 19 °C and for the 50 % SoC and 164 ± 3 °C for the 100 % SoC) and this behavior was observed also for the second event, the venting (197 ± 18 °C for the 50 % SoC and 197 ± 1 °C for the 100 % SOC). During venting

the major difference is in the pressure increase, in fact the values is significantly higher for the 100 % SoC compared to the 50 %, 0.073 barg vs 0.026 barg. Then, increasing the temperature, in the case of the 50 % SoC the TR was not triggered, even if the oven temperature was brought up to 350 °C, a value well above the temperature value of 216 °C obtained for the TR during the thermal stability tests. Anyway, an increase in the pressure is observed at 3640 s with a pressure peak of 0.09 barg, as shown in Figure 92a. This trend can be due to the constant release of gases from the safety valve after the CID-vent disk activation which is not anyway sufficient to trigger the TR and to ignite a flame. In the case of the 100 % SoC, the onset of TR is reached at 234 ± 12 °C at 2658 s. The subsequently peak of the temperature and the pressure is observed at 2775 s, where the thermocouples registered a temperature on the cell surface of 310 ± 36 °C and an internal pressure of 0.108 barg. Even if the TR occurred the temperature and the pressure reached are not significantly higher compared to the onset parameters.

The difference of events that occurring between the two conditions can be due to the energy available inside the cells and the reactivity of the material which composed the cathode. In fact, a higher amount of electrical energy inside the cell caused an increase in the thermal and the pressure response, as reported for the 100 % SoC. Anyway, during the TR the temperature and pressure values reached are not significantly higher compared to the temperature at the onset of the TR and this can be due to the lack of oxygen produced until 500 °C by the LFP material.

The increase of pressure in correspondence of the main events is due to the release of HF, EC, DMC, CO, CO_2, and CH_4, as shown in Figure 93 (Appendix 2).

As the temperature-pressure profiles were different, the profiles of the gases emitted also differ significantly based on the SoC. For the same time interval shown in the graphs on the x axis, in the case of 50 % SoC the release is in a wider interval time, as shown in Figure 93a, than in the case of the 100 % SoC (Figure

93b). Even the maximum concentration values reached varied with the SoC, in fact in the 50 % SoC the HF maximum is $2.57*10^3$ ppmv, a valuer one magnitude higher compared to the $9.00*10^2$ ppmv obtained for the 100 % SoC. The opposite trend is observed for the CO_2, with a higher value, $1.60*10^5$ ppmv, for the 100 % SoC compared to the $7.50*10^4$ ppmv for the 50 % SoC. The difference in the gases amount is correlated with the reactions that can occurred inside the cell with the increasing of the temperature. In fact, reaching higher temperature in a shorter time, in the 100 % SoC the combustion is complete with the release of higher amount of CO_2.

The total quantities of the gases, expressed in ppm, are reported in Table 48 and compared with the IDLH limits reported by the NIOSH.

Table 48: concentration (ppm) of gas emitted for thermal abuse tests on C/LFP at 50 and 100 % SoC in 30 min.

ppm / Cells	DMC	EC	HF	CH_4	CO	CO_2
C/LFP 50 %	89	4	133	n.d.	7036	10325
C/LFP 100%	103	95	187	1188	10952	14106
IDLH [51]	-	-	30	-	1200	-

n.d.: not detected.

So, the average concentration values of HF and CO significantly exceed the IDLH values reported by the NIOSH [51].

Regarding the residues after tests, the quantities collected and the typology are reported in Table 49 and showed in Figure 60.

The increase of the SOC cause an increase in the loss of material from the cell in terms of solid and gases products, 12.3725 g for the 100 % SoC and 4.286 g for the 50 % SoC.

Table 49: weight of the cell and of the products collected (g) after the thermal abuse test on LFP at 50 and 100 %.

g / Cells	Initial cell weight	Final cell weight	Δcell	Gases weight	Condensate phase weight	Solid weight	Liquid weight
C/LFP 50 %	34.9370	30.5485	4.3885	4.3182	0.0017	0.3984	0.3984
C/LFP 100 %	35.1023	22.7298	12.3725	6.6576	0.0660	0.0453	0.0453

Even in this case the difference between the 50 and 100 % SoC cells are related to the activation of the safety devices, in fact for the 100 % the residues were released even by the bottom vent (Figure 60d).
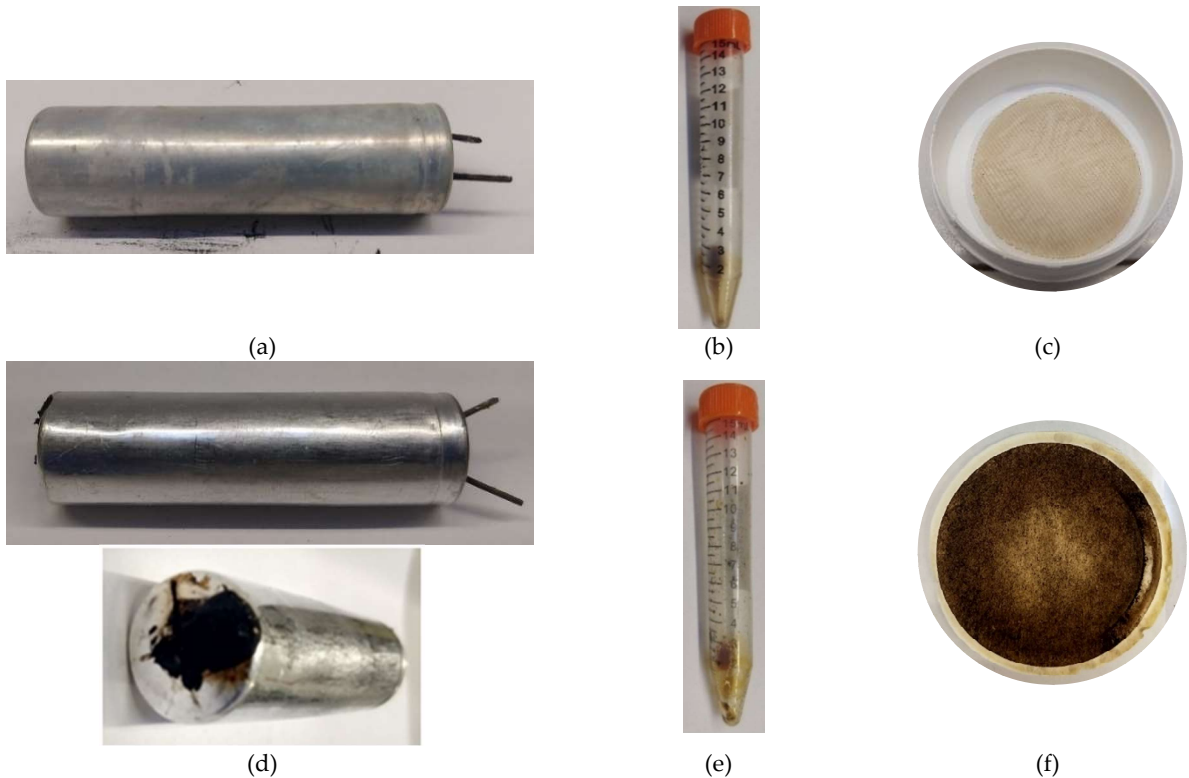
Figure 60: Materials collected after the thermal abuse test on C/LFP: (a) cell 50 % SoC; (b) liquid 50 %; (c) filter 50 % SOC; (d) cell 100 % SoC; (e) liquid 100 %SoC; (f) filter 100 % SoC.

From the Figure 60c and Figure 60f it is possible to observe a residue on the filter similar in the nature (brown color) but different in the amount.. Similarities are observed also for the liquid residues, Figure 60b and Figure 60e, in terms of color and amount.

The characterization of both the solids and the liquids were carried out . The ATR-FT-IR spectra for the liquid samples are shown in Figure 94 (Appendix 2) while the peaks with the relative identification and force are reported in Table 50. The liquid ejected from the LFP can be identify as EC used as solvent with in the electrolyte, around 248 °C. The presence of the higher amount of liquid in the test at 50% SoC than at higher SoC is probably due to the fact that TR was not reached while in the test at 100 % SoC, even if reached the temperature are not higher than 350 °C, so not all the EC present in the solution vaporizes.

Table 50: wavenumbers (cm⁻¹) found in the C/LFP liquids at 50 % and 100 % SoC with force and identification.

Identification		C/LFP 50 % - liquid		C/LFP 100 % - liquid	
EC	*vw*	3532.35	*vw*	3530.05	*vw*
EC	*vw*	2998.43	*vw*	2998.09	*w*
EC	*vw*	2931.45	*vw*	2925.92	*w*
EC	*w*	1964.00	*w*	1960.02	*w*
EC	*vs*	1794.67	*vs*	1797.05	*vs*
EC	*vs*	1770.75	*vs*	1771.57	*vs*
EC	*w*	1553.56	*w*	1554.11	*w*
EC	*m*	1481.94	*m*	1481.90	*m*
EC	*w*	1454.95	*w*	1455.47	*w*
EC	*m*	1390.31	*m*	1390.23	*m*
EC	*w*	1283.57	*w*	1260.76	*w*
EC	*s*	1156.33	*vs*	1158.80	*vs*
EC	*vs*	1067.72	*vs*	1069.86	*vs*
EC	*s*	971.24	*s*	971.76	*m*
EC	*m*	893.59	*m*	893.60	*m*
EC	*m*	844.69	*m*	845.69	*m*
EC	*s*	772.12	*s*	773.14	*s*
EC	*s*	715.69	*s*	716.12	*s*
EC	*m*	558.62	*w*	558.54	*w*
EC	*w*	526.37	*w*	n.d.	-
EC	*w*	488.53	*w*	449.05	*vw*

EC = ethylene carbonate. n.d.: not detected.

The ATR-FT-IR spectra for the filters are shown in Figure 95 (Appendix 2) while the peaks with the relative identification and force are reported in Table 51.

Table 51: wavenumbers (cm⁻¹) found in the C/LFP filters at 50 % and 100 % SoC with force and identification.

Identification		C/LFP 50 % - solid		C/LFP 100 % - solid	
Paraffin oil	*s*	n.d.	-	2952.36	*m*
PTFE Filter	*m*	2923.17	*w*	2922.26	*m*
Paraffin oil – PEO	*vs*	n.d.	-	2853.87	*w*
Paraffin oil – PEO	*vs*	n.d.	-	2552.80	*w*
Paraffin oil	*vw*	n.d.	-	1719.98	*w*
Paraffin oil	*w*	n.d.	-	1682.76	*vw*
n.i.	-	n.d.	-	1575.54	*w*
n.i.	-	n.d.	-	1509.59	*w*
PTFE Filter	*m*	1428.94	*w*	n.d.	-
n.i.	-	n.d.	-	1426.46	*m*
Paraffin oil – PEO	*m*	n.d.	-	1376.78	*s*
n.i.	-	n.d.	-	1278.85	*s*
PTFE Filter	*vs*	1203.46	*vs*	n.d.	-
PTFE Filter	*vs*	1148.32	*vs*	n.d.	-
PEO	*w*	n.d.	-	1111.39	*w*
n.i.	-	n.d.	-	1019.07	*w*
n.i.	-	n.d.	-	928.54	*w*
n.i.	-	n.d.	-	781.58	*m*
Paraffin oil	*m*	n.d.	-	729.74	*m*
PTFE Filter	*m*	638.79	*m*	n.d.	-
PTFE Filter	*m*	554.12	*m*	n.d.	-

PEO = Polyethylene oxide. n.i.: not identified. n.d.: not detected.

In the case of solid material, the spectra are not completely superimposable indeed they show significant differences in the wavenumber of the peaks. The different nature of the sample was already visible from the Figure 60b and d. From the interpretation of the spectra, it is possible to state that in the case of the 50 % SoC test the peaks are due to the PTFE filter, in fact the condensed phase is low concentrated and highly dispersed on the entire surface. While in the case of the 100 % SoC test the attribution is more complex and not completely solved. The major peaks identified in the 100 % are attributable to the presence of paraffin oil [164] and PEO [166]. These two materials can be used in the cell composition to enhance the properties, as already explained during the evaluation of the thermal stability products. However, there are also peaks which are not due to either paraffin or PEO and which may be due to organic residues present on the filter. The difficult understanding at low wavenumbers is due both to the co-presence of multiple species and to the color of the compound. In fact, in the area of the fingerprint, at low wavelengths each compound has a specific pattern that allows it to be identified, but if more spectra are added this information is lost and the area is no longer easy to understand. Finally, the dark color tends to absorb the IR ration at low wave numbers, so the determination of the remaining organic component on the filter cannot be done more in-depth.

The results obtained by the ICP-OES and AAS-OES on both the filters are reported in Table 52 as milligrams of metal in the gram of solid collected.

Table 52: quantification of metals in the solid collected (mg) after the thermal abuse tests on LFP at 50 and 100 % SoC.

mg / Cells	Al	Cu	Fe	Li	P
C/LFP 50 %	0.016	0.001	0.007	0.001	< LOD
C/LFP 100 %	0.780	0.065	0.440	0.016	0.135

LOD: limit of detection.

Higher amounts of all metals are filtered in the case of tests at 100 % SoC. The low values of P compared with the other materials is given by the initial state of the phosphorus. In fact, phosphorus in the cell is present as $LiFP_6$ salt in the electrolyte

151

and the melting of this salt and the decomposition to PF$_5$ occur at about 200°C, as reported in literature.

SEM-BSE analyses were also performed on the filter relevant to 100% SoC test, as shown in Figure 61a, while in Figure 61b is shown the mapping of the elements obtained by the EDX.

(a)

(b)
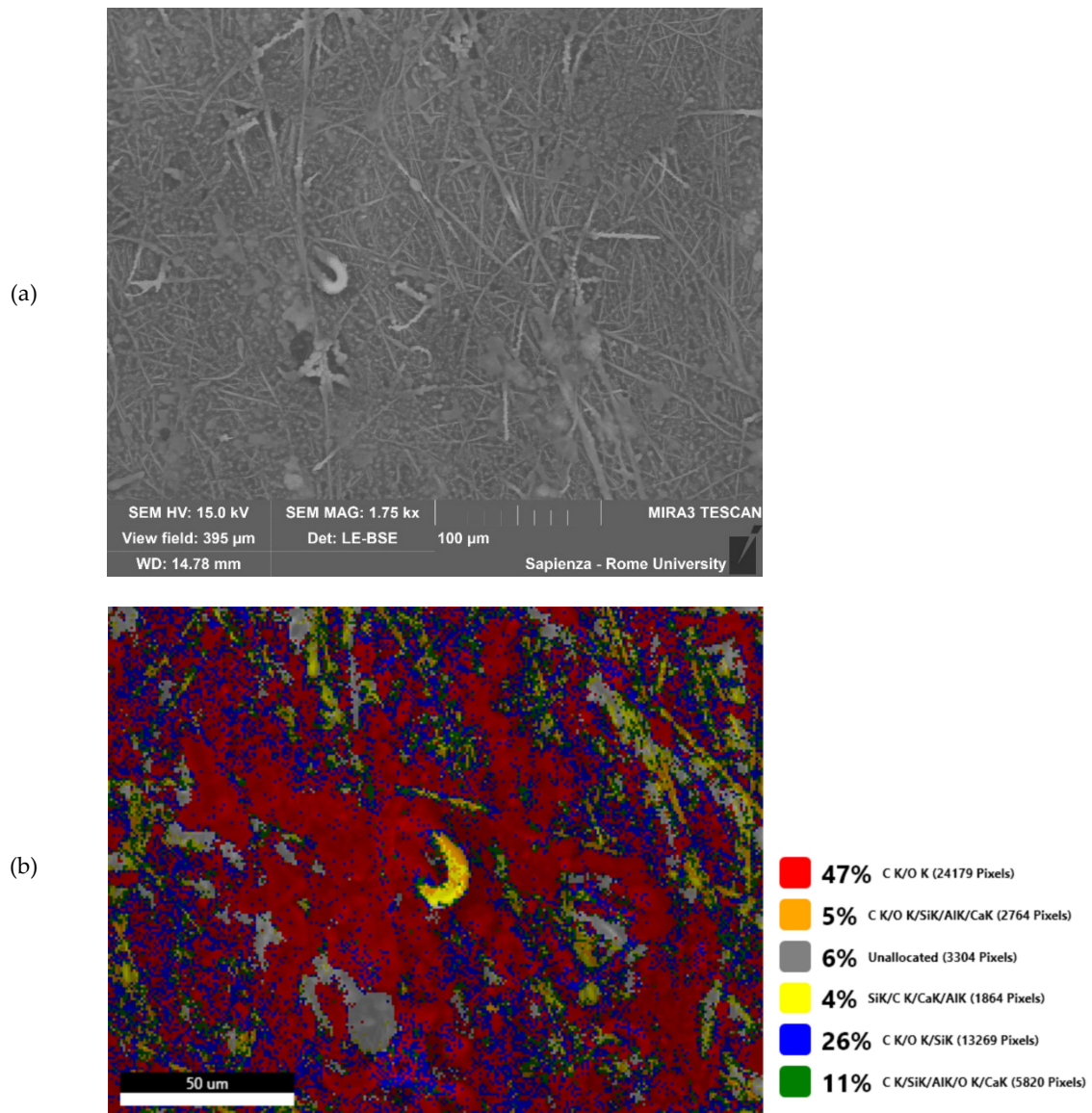
Figure 61: filter after the thermal abuse test on C/LFP at 100 % SoC: (a) SEM-BSE; (b) EDX-map.

From Figure 61a it is possible to observe the texture of the filter fibers covered by material of different sizes. By EDX it was possible to observe a small agglomeration with a significantly different chemical composition. So, specific

analyzes for determining the composition and size were conducted on this agglomeration, as shown in Figure 62.

(a)

(b)

Element	C K	O K	F K	P K
Weight %	96.79	2.83	0.02	0.34
Atomic %	97.71	2.15	0.01	0.13

(c)

Element	C K	O K	F K	Al K	P K	Fe K	Cu K
Weight %	96.85	1.51	0.05	0.72	0.19	0.42	0.28
Atomic %	98.28	1.15	0.03	0.32	0.07	0.09	0.05

Figure 62: powder after the thermal abuse test on C/LFP at 100 %. (a) Areas analyzed by EDS and dimension of the particles; (b) EDX of Spot 1; (c) EDX of Spot 2.

The particles detected in Figure 62a have a medium size of 4.89 ± 1.92 μm and are mainly composed by carbon and oxygen with some traces of the electrolyte, such as P and F. In addition, in the Spot 2 even some metals have been detected, specifically the Al and the Fe are from the cathode while the Cu is from the anode.

Anyway, both the particles are composed for more than the 95 % in weight by carbon, the active material of the anode.

4.3.3.2. *Graphite/Lithium Nickel Manganese Cobalt Oxide (C/NMC)*

Results of thermal abuse tests for C/NMC cell are reported in Figure 96 (Appendix 3) for the 50 % and the 100 % SoC, while the parameters of the main events are reported in Table 53.

Table 53: temperature (°C) and pressure (barg) relative to the main events of the C/NMC thermal abuse tests.

Key event	C/NMC 50 %			C/NMC 100 %		
	t (s)	T (°C)	P (barg)	t (s)	T (°C)	P (barg)
CID-vent disk activation	2522	169 ± 4	0.045	2589	170 ± 5	0.017
Venting	2630	174 ± 4	0.065	2591	169 ± 5	0.029
TR	2925	255 ± 3	0.066	2767	202 ± 6	0.045
Peak	2960	491 ± 41	0.880	2787	721 ± 55	5.858

n.d.: not detected.

From a first comparison the two SoCs shown a similar behavior when subject to a thermal abuse test. The most significantly difference is in the maximum temperature and pressure values reached according to the SoC, in fact in the case of the fully charged cell the maximum values were 721 ± 55 °C and 5.858 barg, compared to the 491 ± 41 °C and 0.88 barg reached with the half charged cell.

For the 50 % and the 100 % the first two events occurred almost at the same temperature, at about 170 °C. These data therefore demonstrate that in the case of C/NMC cells the first two events are not conditioned by the SoC and that the internal pressure limit values for the activation first of the CID and then of the venting are very close, especially in the case of the 100 % SoC. The lower temperature registered on the cell surface at the venting, for the 100 % SoC, compared to the temperature at the CID-vent disk activation is probably due to the evaporation of the electrolyte emitted by the cell in that moment, which evaporate and absorb the heat from the surface of the cell. The subsequent event, the TR, instead is affected by the SoC and in fact occurred at different time and temperature and leading to significantly different maximum peaks. The onset

154

conditions for the TR for the in the 100 % SoC compared to the 50 % SoC are reached before in time, 2767 s vs 2925 s, at a lower temperature, 202 ± 6 °C vs 255 ± 3 °C, and with an internal pressure smaller, 0.037 barg vs 0.066 barg. The SoC influences, also the maximum peak reached by both temperature and pressure: higher temperature and pressure are reached in the case of 100 % SoC (712 ± 55 °C 5.858 barg) than 50% SoC (491 ± 41°C and 0.880 barg). Therefore, the SoC influenced significantly the TR behavior instead of the safety devices activation.

Another aspect that must be considered is even the gases emitted and the relative concentration values. The gases emission profile of the main gases, HF, EC, DMC, CO, CO_2, CH_4, are reported in Figure 97 (Appendix 3), with the concentration values expressed in ppmv.

Significantly differences are observable according to the SoC, such as the duration of emission and the maximum peak of concentration the gas products. Although the three main events for both SoCs are recognizable from the temperature and pressure profile, in the case of gases not all of them are identifiable. In fact, in the 50 % SoC case the CID-vent disk activation and venting occur too close together to be visibly separated. As observed for other chemistries of the cell, the duration of the emissions shows how in the case of 100 % SoC they occur in a short period of time and with an increasing trend up to the maximum peak and then decreasing. However, the emission for 50% SoC is broader and less linear due to the lower temperatures during TR that do not allow the species are completely exhausted during the TR. In fact, from the graph it is possible to observe how after the maximum peak, the CO_2 and EC present a new peak which is lower in value but still pronounced. This peak is due to the continuous release of the EC from the cell which, when evaporating in the reactor, reacts with oxygen giving combustion reactions with the production of CO_2. The different quantity of CO_2 and CO produced, especially at the maximum peak, is an indicator of the degree of combustion, in fact, while in the case of 50 % SoC the CO_2 peak corresponds to the

consumption of CO, in the case of 100 % SoC a peak is observed for both to the TR. This is given by the fact that at high SoCs the gaseous species are released simultaneously and in large quantities, therefore, the total combustion of the products is not observed while in the case of lower SoCs the events are dilated over time allowing a complete combustion reaction.

The concentration of the gases emitted in 30 min, expressed in ppm, are reported in Table 54, compared with the IDLH limits reported by the NIOSH.

Table 54: concentration (ppm) of gas emitted for thermal abuse test on C/NMC at 50 and 100 % SoC in 30 min.

ppm / Cells	DMC	EC	HF	CH_4	CO	CO_2
C/NMC 50 %	81	134	155	632	2693	10204
C/NMC 100 %	56	767	612	2465	8303	24999
IDLH [51]	-	-	30	-	1200	-

So, the concentration values are significantly higher for fully charged cells and the IDLH values NIOSH set at 30 ppm for HF of one order of magnitude and 1200 ppm for CO in 30 min are significantly exceeded [51].

The quantities collected and the typology of residues are reported in Table 55 and showed in Figure 63.

Table 55: weight of the cell and the products collected (g) after the thermal abuse test on C/NMC at 50 and 100 % SoC.

g / Cells	Initial cell weight	Final cell weight	Δcell	Gases weight	Condensate phase weight	Solid weight	Liquid weight
C/NMC 50 %	44.8784	35.9856	8.8928	6.9489	0.0876	n.p.	n.p.
C/NMC 100 %	45.1015	27.7674	17.3341	9.1373	n.p.	5.4487	n.p.

n.p.: not present.

In the case of 100 % SoC the solid residues correspond to a high percentage of the total cell loss, 31.43 %, compared to 50 % SoC, 0.99 % of the total loss, that on the contrary is mainly due to gas emissions.

From the Figure 63b and Figure 63d it is possible to observe the difference in solid emissions. In the case of 50 % SoC it is a brown condensate phase, probably due to

the electrolyte, while in the case of 100 % the emission is a black powder due to the active materials of the electrodes as found by characterization analyses.

The ATR-FT-IR analysis was performed on the filter at 50 % SoC: ATR-FT-IR spectra are shown in Figure 98 (Appendix 3) while the peaks with the relative identification and force are reported in Table 56.

| (a) | (b) |
| (c) | (d) |
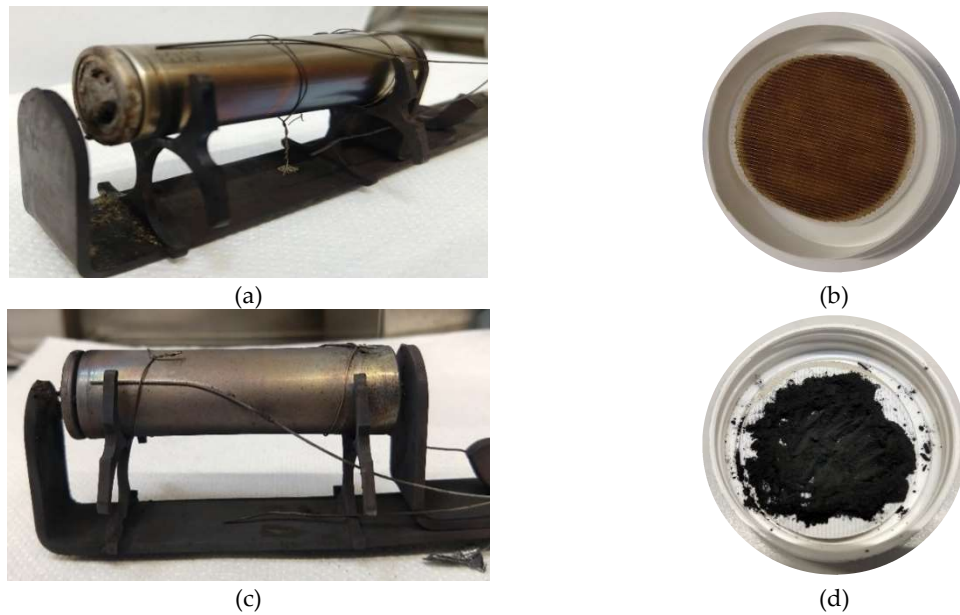
Figure 63: solids collected after the thermal abuse tests on C/NMC: (a) cell 50%; (b) filter 50%; (c) cell 100%; (d) filter 100%.

Table 56: wavenumbers (cm⁻¹) found in C/NMC at 50 % filter with force (vw, w, m, s or vs) and identification.

Identification		C/NMC 50 % - filter	
Paraffin	s	2958.35	w
Paraffin	vs	2918.65	m
Paraffin	vs	2850.09	m
Paraffin	w	1695.13	w
Paraffin	s	1462.61	w
Paraffin	w	1376.03	w
PTFE Filter	m	1205.10	m
PTFE Filter	m	1149.36	m
Paraffin	m	730.63	w
Paraffin	m	719.74	w
PTFE Filter	m	638.92	m
PTFE Filter	m	554.28	m
PTFE Filter	vs	502.11	m

The peaks identified are attributable to the composition of the PTFE filter and the presence of paraffin oil. The paraffin oil can be referred to the use of paraffin wax as a protective layer of the anode material or separator [74]. The paraffin oil is

released during the increase of cell temperature: at about 55 °C the wax melts and subsequently (> 240 °C) it starts to decompose [75].

The results obtained by the ICP-OES and AAS-OES analysis on filter relevant to both SoC tests were reported in Table 57 as milligrams of metal in the gram of solid collected.

Table 57: quantification of metals (mg) in the solid collected after the thermal abuse tests on NMC at 50 and 100 % SoC.

Cells ⟍ mg	Al	Co	Cu	Li	Mn	Ni	P
C/NMC 50 %	0.1055	< LOD	< LOD	< LOD	< LOD	< LOD	< LOD
C/NMC 100 %	421.7039	28.3424	20.9876	163.4820	1.6130	1539.3448	0.2318

LOD: limit of detection.

The lower concentration values for the 50 % SoC are due to the lower amount of material ejected from the cell compared to the 100 % SoC. In the case of the 50% the only metal detected is the aluminum, this can be due to the high amount present both as cathode collector. In the 100 % SoC the metals detected are all due to the internal composition of the electrodes, the lower concentration of P compared with the other materials is given by the initial state of the phosphorus, as discussed previously. There is a discrepancy between the total solid collected and the total quantified mg for both the SoCs, 0.0873 g for 50 % SoC and 3.266 g for 100 % SoC respectively, which can be attributed to the lack of information regarding carbon and oxygen.

SEM-EDX analyses were conducted on the powder collected after the thermal abuse test at 100 % SoC and the condensate phase at 50 % SoC. In Figure 64 are shown the SEM images of the surface of the filters at different SoC and the EDX map for the test at 100 %.

(a)

(b)

(c)

4%	O K/AlK/C K/F K (2189 Pixels)
40%	C K/O K (20535 Pixels)
14%	Unallocated (6920 Pixels)
1%	NiK/O K/C K/AlK/F K/MnK/CoK (654 Pixels)
4%	O K/C K/AlK/F K (2047 Pixels)
1%	AlK/C K/O K (730 Pixels)
8%	C K/O K/AlK/F K (4251 Pixels)
27%	C K/O K (13861 Pixels)
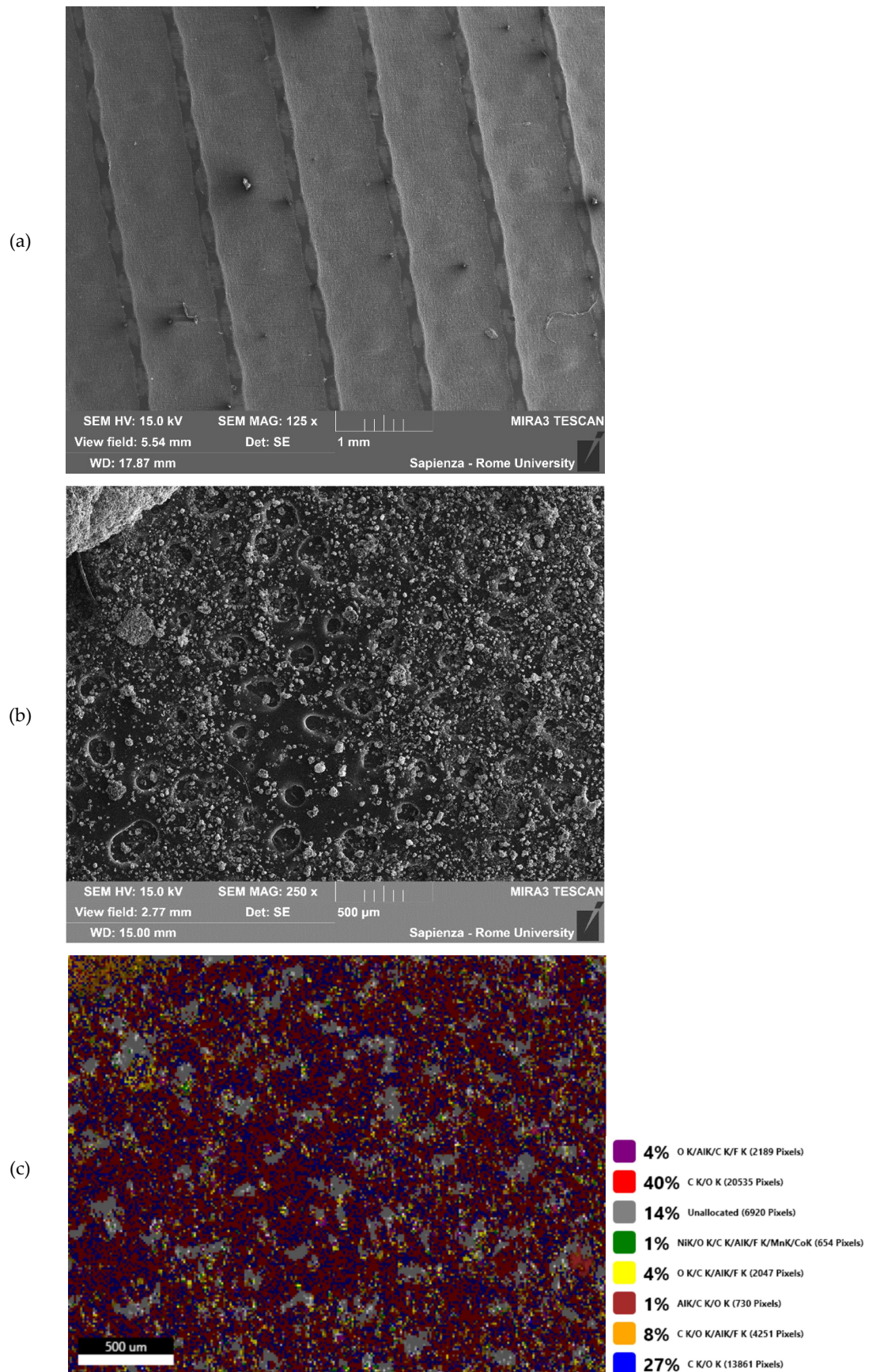
Figure 64: solid collected after the thermal abuse test on C/NMC: (a) SEM-BSE at 50 %; (b) SEM-BSE at 100 % SoC; (c) EDX-map at 100 %.

159

In the case of 50 % SoC, Figure 64a, the filter textures are visible on which there is only few agglomerates while for 100 % SoC, Figure 64b, the material is composed of several particles of similar size and composition. Anyway the chemical composition on the filter surface is homogeneous, as observed by the EDX-map, Figure 64c.

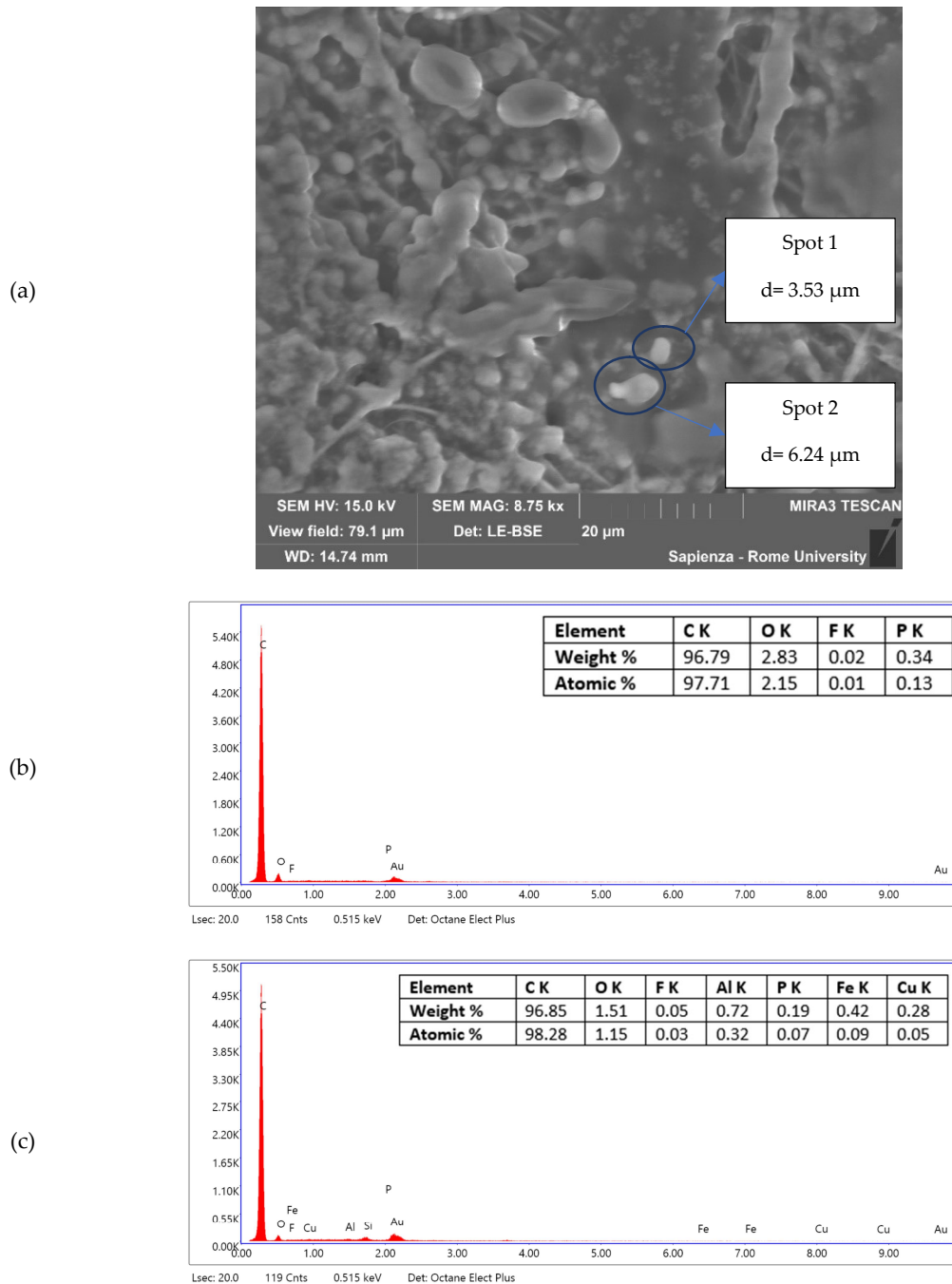The most significant image for the filter is reported in Figure 65 while for the powder is reported in Figure 66.
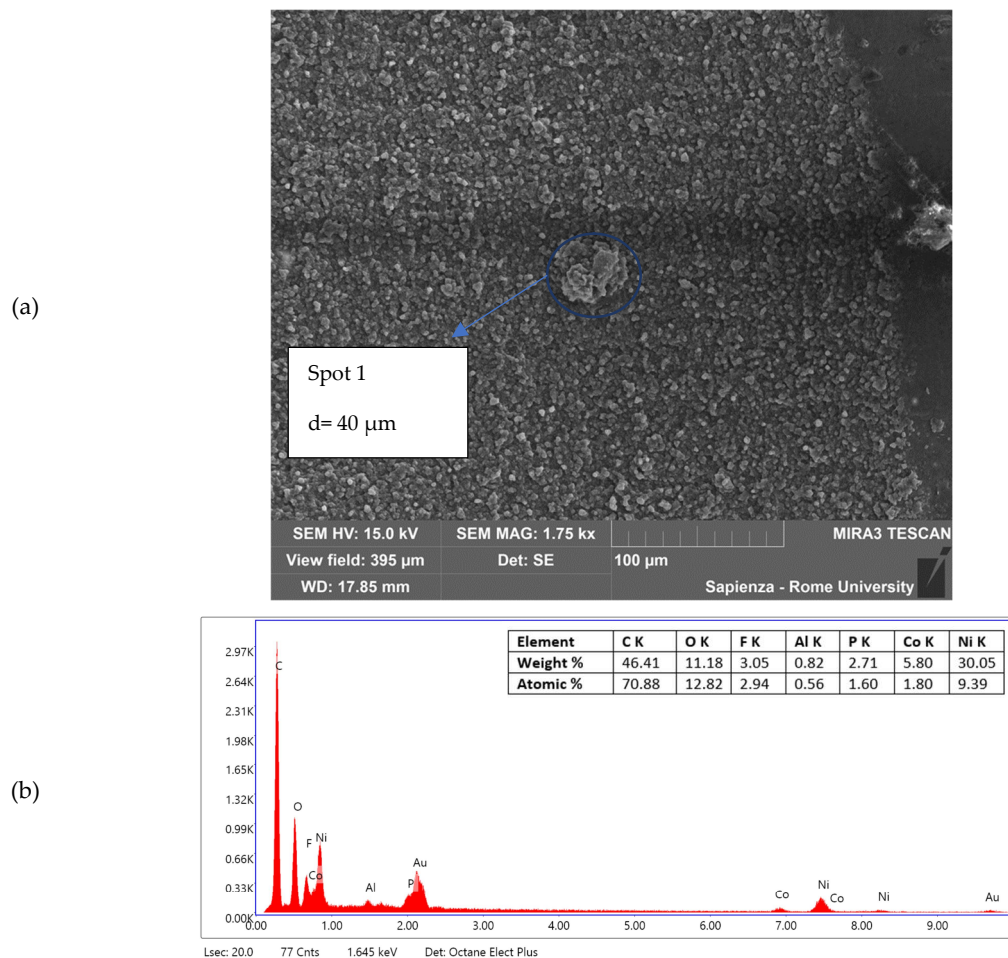
Figure 65: filter after the thermal abuse test on C/NMC at 50 % SoC. (a) Areas analyzed by EDS and dimension of the particles; (b) EDS of Spot 1.

The particle in Figure 65a has a diameter of d= 40 μm. For the chemical composition the elements are due to the anode material, such as C, the cathode material, such as Al, Co, Ni and O, and the electrolyte, such as C, O, P and F. The

most abundant elements, according to the weight percentage, are the C and the Ni while the less abundant are the P and the Al.

(a)

(b)

Element	C K	O K	F K	Al K	P K	Mn K	Co K	Ni K	Cu K
Weight %	7.14	27.30	2.51	17.16	0.08	5.34	6.92	28.97	4.56
Atomic %	15.43	44.31	3.43	16.51	0.07	2.52	3.05	12.81	1.86

(c)

Element	C K	O K	F K	Al K	Mn K	Co K	Ni K
Weight %	11.18	17.67	0.69	11.22	6.07	8.96	44.22
Atomic %	26.57	31.52	1.03	11.87	3.15	4.34	21.50
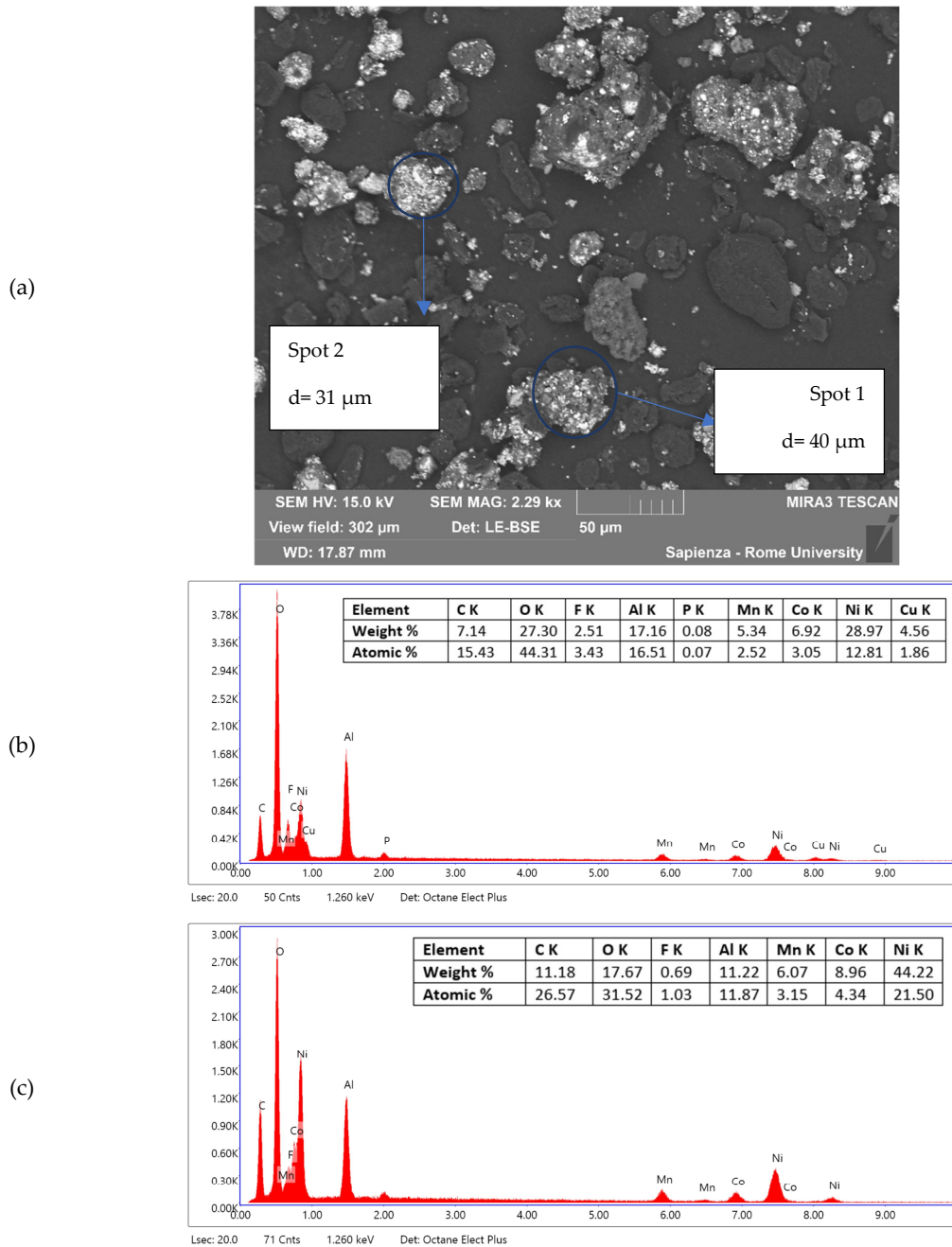
Figure 66: solid after the thermal abuse test on C/NMC at 100 %. (a) Areas analyzed by EDS and dimension of the particles; (b) EDS of Spot 1; (c) EDS of Spot 2.

The two particles in Figure 66a have a similar diameter, d1= 40 μm and d2 = 31 μm, with an average diameter of 35.5 μm. Even the chemical composition is quite similar in term of the chemical composition and the percentage in weight. For the chemical composition the elements are due to the anode material, such as C and

Cu, the cathode material, such as Al, Co, Mn, Ni and O, and the electrolyte, such as C, O, P and F. The only difference between Spot 1 and Spot 2 is given by the absence in the second of P and Cu. About the weight percentages for the two particles, the most abundant elements in both the particle are Ni and O while the less abundant are the P and F for the Spot 1 and the F and Mn for the Spot 2.

4.3.3.3. Graphite/Lithium Cobalt Oxide (C/LCO)

In Table 58 are reported the parameters of the main events occurring during thermal abuse tests of C/LCO cell (see Figure 99 Appendix 4).

Table 58: temperature (°C) and pressure (barg) relative to the main events of the LCO thermal abuse tests.

Key event	C/LCO 50 %			C/LCO 100 %		
	t (s)	T (°C)	P (barg)	t (s)	T (°C)	P (barg)
CID-vent disk activation	n.d.	n.d.	n.d.	2524	195 ± 1	0.043
Venting	2756	205 ± 20	0.029	2550	194 ± 3	0.064
TR	n.d.	n.d.	n.d.	2734	228 ± 5	0.066
Peak	n.d.	n.d.	n.d.	2783	563 ± 12	3.692

n.d.: not detected.

In fact, in the case of the half charged cell the CID-vent disk activation and the TR are not detected while the venting occurred at 2756 s at the temperature on the cell surface of 205 ± 20 °C and with an internal pressure value of 0.029 barg, while in the case of the fully charged these all the three events occurred. Specifically, for 100% SoC the CID-vent disk activation and the venting occurred almost at the same time, between 2524 s and 2550 s, and so almost at the same temperature, between 195 and 194 °C. The CID-vent disk activation temperature is defined by a small increase of the reactor pressure values, around 0.043 barg, while the venting temperature is defined by a decrease of the cell surface temperature and an increase of the reactor pressure value, until the maximum value of 0.064 barg. Then the onset temperature of TR is reached, just in the case of the fully charged cell, at 228 ± 5 °C with a maximum temperature of 563 ± 12 °C and a maximum pressure of 3.692 barg. After the TR the temperature dropped down returning around the environmental one. More complex is the behavior of the 50 % SoC. In

the case of the half charged cell nothing occurred until 255 ± 8 °C where there is another emission of liquid that vaporized decreasing the cell surface temperature and increasing the pressure until a maximum value of 0.746 barg. This event cannot be considered the TR because the temperature values did not increase with a SHR higher than 10 °C/min. The different behavior can be due to the lower energy available in the 50 % cell compared to the 100 % SoC which does not allow the achievement of temperatures such as to cause the degradation of internal materials and internal short circuit .

The gases emission profiles of the main species, such as HF, EC, DMC, CO, CO_2, CH_4 are reported in Figure 100 (Appendix 4) and shown the concentration values of expressed in ppmv. The gas concentration profiles reflect the temperature and pressure profiles, in fact an increase in concentrations can be observed in correspondence of the time of the key events, but the gases for 100 % SoC are emitted in a narrow time range. Different emission time also means different reactions that can occur and this is why the profiles of the same species at the two SoCs present some differences. In fact, CO shows two different profiles according to the SoC, in the case of the 50 % SoC the maximum peak is relative to the venting, $1.3*10^5$ ppmv at 2756 s, while in the case of the 100 % SoC the maximum peak is relative to the TR, $1.2*10^5$ at 2816 s. Even the other species present a similar trend, higher values during the venting in the case of 50 % SoC while in the case of 100 % SoC higher values at the TR. The only exception is given by the CO_2 that for 50% SoC present a higher peak in correspondence with the maximum pressure value, and this can be due to the complete combustion reactions of the species emitted from the cell. The concentration of the gases, expressed in ppm, are reported in Table 59 and are compared with the IDLH limits reported by the NIOSH..

Table 59: concentration (ppm) of gas emitted for thermal abuse tests on C/LCO at 50 and 100 % SoC in 30 min.

ppm / Cells	DMC	EC	HF	CH$_4$	CO	CO$_2$
C/LCO 50 %	177	173	276	59	1203	15837
C/LCO 100 %	94	146	298	907	10106	23173
IDLH [51]	-	-	30	-	1200	-

Similar values of HF are observed for the two SoCs significantly exceeding the IDLH values reported by the NIOSH while for CO the limit values is exceeded only for 100% SoC [51].

Regarding to the residues collected after the tests, the quantities collected and the typology are reported in Table 60 and showed in Figure 67.

Table 60: weight of the cell and the products collected (g) after the thermal abuse test on LCO at 50 and 100 %.

g / Cells	Initial cell weight	Final cell weight	Δcell	Gases weight	Condensate phase weight	Solid weight	Liquid weight
C/LCO 50 %	43.5783	39.2923	4.2860	4.4294	0.0058	n.p.	0.1409
C/LCO 100 %	43.6214	31.2489	12.3725	8.6807	n.p.	1.8706	n.p.

n.p.: not present.

Similar results were observed as for the previous cells, Table 60 shows a higher weight loss for the higher SoC and about the nature of the residue samples, liquid and condensate phases for the 50 % SoC and just solid for 100 % SoC, as shown in Figure 67. This different nature and composition of the residues released on the filter is shown in Figure 67c and Figure 67e.

In the case of 50 % the emission is a brown condensed phase, due to the electrolyte as the liquid collected inside the reactor Figure 67b, while in the case of 100 % the emission is a black powder due to the active materials of the electrodes, as confirmed by further characterization analyses.

(a)	(b)	(c)

(d)	(e)
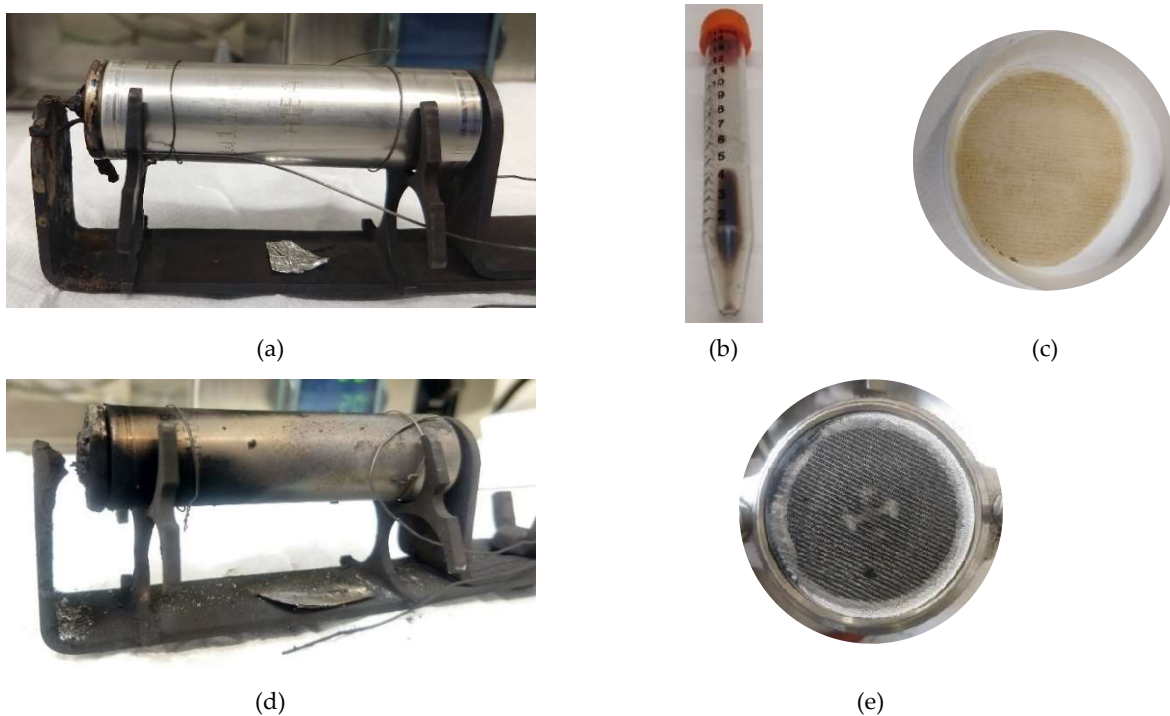
Figure 67: solids collected after the thermal abuse tests on LCO at: (a) cell 50 %, (b) liquid 50 %; (c) filter 50 %; (d) cell 100 %; (e) filter 100 %.

The ATR-FT-IR analysis was performed on the filter and the liquid of the thermal abuse test on C/LCO at 50 % SoC. The ATR-FT-IR spectra are shown in Figure 101 (Appendix 4), while in Table 61 are reported the peaks with the relative identification and force.

In the case of the liquid residue this is given by EC, the highest boiling component of the electrolyte solution (boiling temperature 248 °C). As previously discussed, the presence as liquid is due to the fact that in the test on LCO at 50 % SoC did not reach the TR so the temperature did not increase to values so high that all the EC present in the solution vaporize. About the condensed phase on the filter, from the ATR-FT-IR analysis is not possible to draw conclusions on the composition since the quantities released were minimal and scattered over the entire surface of the filter. So, the principal and more intense peaks are due to the PTFE filter.

Table 61: wavenumbers (cm⁻¹) of the filter and the liquid at 50 % with the force (vw, w, m, s or vs) and the identification.

Identification		C/LCO 50 % - solid		C/LCO 50 % - liquid	
EC	*vw*	n.d.	-	3532.35	*vw*
EC	*vw*	n.d.	-	2998.43	*vw*
PTFE Filter	*m*	2951.23	*s*	n.d.	-
EC	*vw*	n.d.	-	2933.72	*vw*
PTFE Filter	*s*	2916.38	*s*	n.d.	-
PTFE Filter	*m*	2866.11	*w*	n.d.	-
PTFE Filter	*m*	2837.87	*w*	n.d.	-
EC	*w*	n.d.	-	1964.02	*w*
EC	*vs*	n.d.	-	1795.62	*vs*
EC	*vs*	n.d.	-	1768.97	*vs*
EC	*w*	n.d.	-	1553.35	*w*
EC	*m*	n.d.	-	1481.78	*m*
PTFE Filter	*m*	1455.43	*w*	n.d.	-
EC	*w*	n.d.	-	1421.59	*w*
EC	*m*	n.d.	-	1391.54	*m*
PTFE Filter	*m*	1374.71	*w*	n.d.	-
EC	*w*	n.d.	-	1285.66	*w*
PTFE Filter	*vs*	1203.80	*vs*	n.d.	-
EC	*s*	n.d.	-	1155.03	*s*
PTFE Filter	*vs*	1149.03	*vs*	n.d.	-
EC	*vs*	n.d.	-	1066.46	*vs*
EC	*s*	n.d.	-	971.29	*s*
EC	*m*	n.d.	-	894.17	*m*
EC	*m*	n.d.	-	844.00	*m*
EC	*s*	n.d.	-	772.00	*s*
EC	*s*	n.d.	-	715.94	*s*
PTFE Filter	*m*	639.00	*m*	n.d.	-
EC	*m*	n.d.	-	558.42	*m*
PTFE Filter	*m*	554.39	*m*	n.d.	-
EC	*w*	n.d.	-	526.47	*w*
PTFE Filter	*vs*	503.10	*vs*	n.d.	-
EC	*w*	n.d.	-	488.86	*w*

n.d.: not detected.

The ICP and AAS analysis were conducted on the filter at 100 % SoC. The results are reported in Table 62 as milligrams of metal in the solid collected.

Table 62: quantification of metals (mg) in the solid collected after the thermal abuse tests on LCO at 50 % and 100 %.

Cells \ mg	Al	Co	Cu	Li	Mn	Ni	P
C/LCO 50 %	0.1399	0.0423	0.0521	0.0158	0.0031	0.1650	0.0107
C/LCO 100 %	0.5449	0.0106	0.0288	0.0259	0.0221	2.9834	< LOD

LOD: limit of detection.

Higher amount of some metals, such as Al, Mn, and Ni, are measured for the higher SoC cells because of the higher emission rate during TR.

SEM-EDX analyses were conducted on the filter collected after the thermal abuse test at 100% SoC. In Figure 68a is shown the SEM image of the surface of the filter, while Figure 68b is shown the EDX map.
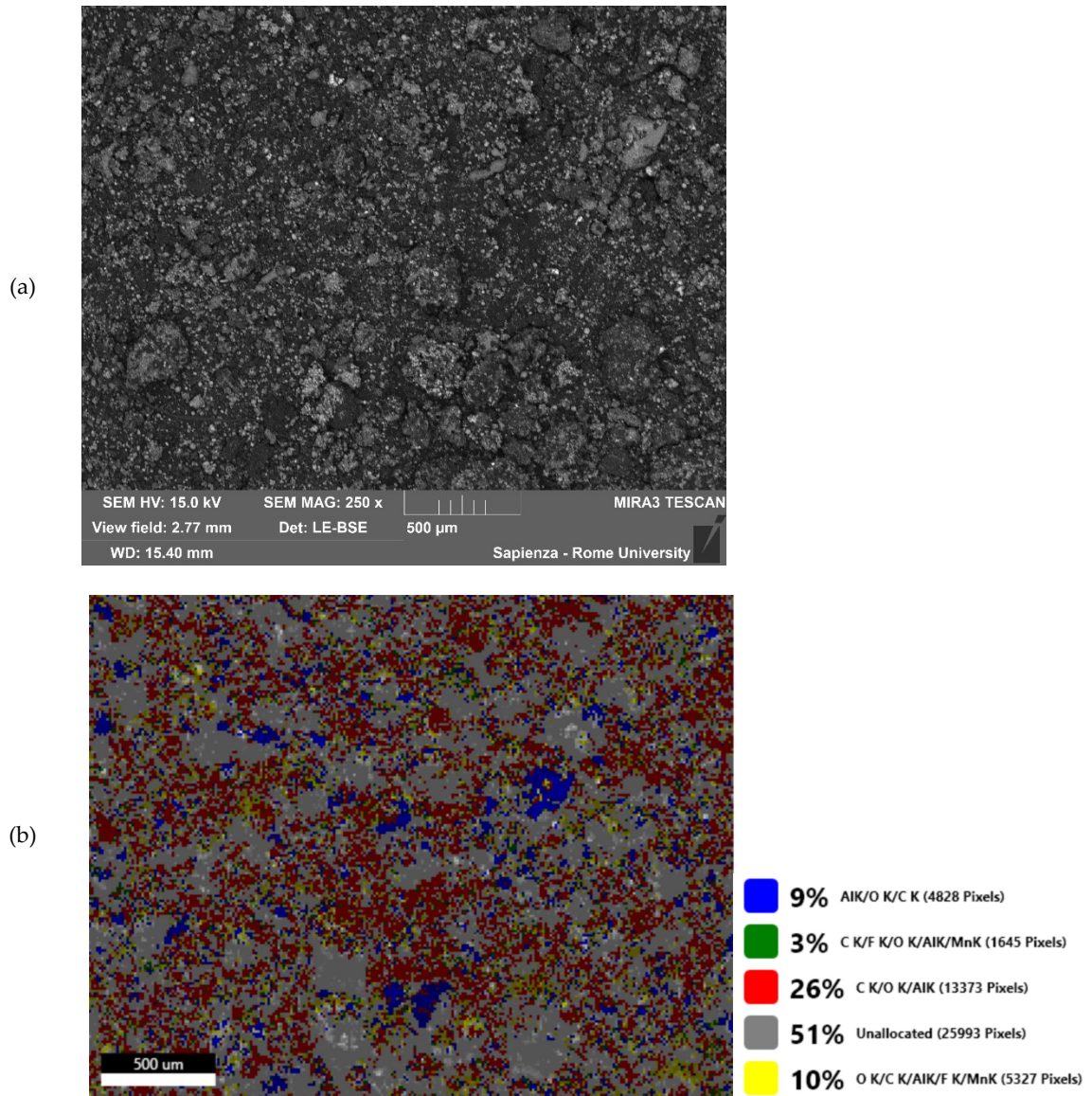
Figure 68: filters after the thermal abuse test on C/LCO at 100 %: (a) SEM-BSE; (b) EDX map..

From both figures it is possible to observe the presence of solid particles dispersed over the entire area under investigation while the filter textures and pores are not visible. So, EDX analyses were therefore conducted on the particles, and the most significant image for the filter is reported in Figure 69, with the diameter of the particles and the respective EDS spectra for compositional analysis.

(a)

(b)

Element	C K	O K	Al K	P K	Mn K	Co K	Ni K
Weight %	0.79	0.07	0.16	0.28	30.38	22.57	45.75
Atomic %	3.66	0.24	0.34	0.50	30.71	21.27	43.28

Lsec: 20.0   1 Cnts   1.260 keV   Det: Octane Elect Plus

(c)

Element	C K	O K	F K	Cu K	Al K
Weight %	0.96	0.91	0.44	2.20	95.49
Atomic %	2.55	1.81	0.74	1.11	112.98

Lsec: 20.0   175 Cnts   1.260 keV   Det: Octane Elect Plus

(d)

Element	C K	O K	Al K	P K	Mn K	Co K	Ni K	Cu K
Weight %	1.54	1.30	14.75	1.00	24.84	16.69	38.26	1.62
Atomic %	5.84	3.69	24.82	1.47	20.52	12.85	29.58	1.16

Lsec: 20.0   38 Cnts   1.260 keV   Det: Octane Elect Plus

168

Element	C K	O K	F K	Al K	P K	Mn K
Weight %	2.05	39.05	6.00	47.62	1.85	3.42
Atomic %	3.55	50.69	6.56	36.66	1.24	1.29

(e)

Lsec: 20.0   58 Cnts   1.260 keV   Det: Octane Elect Plus

Figure 69: powder after the thermal abuse test on C/NMC at 100 %. (a) Areas analyzed by EDX and dimension of the particles; (b) EDX of Spot 1; (c) EDX of Spot 2; (d) EDX of Spot 3; (e) EDX of Spot 4.

The four particles analyzed have different diameters, d_1 = 25.99 µm, d_2 = 17.48 µm, d_3 = 9.07 µm, and d_4= 12.14 µm, with an average diameter of 16.17 ± 7.41 µm. The chemical composition also varies slightly in terms of identified species and weight %. In general, all compounds due to internal composition have been identified; the anode, such as C and Cu, the cathode material, such as Al, Co, Mn, Ni and O, and the electrolyte, such as C, O, P and F. In the case of the largest particle, Spot 1, it is possible to observe the preferential contribution of only the cathode material, Ni, Co, and Mn, while in the case of particle 2, Spot 2, the composition is due to the components of the anode and the electrolyte solution together with the aluminum, given by the cathode collector.

4.3.4   Discussion: Cathode composition impact on the thermal behavior

The four chemistries investigated so far, considering even the C/NCA, have the same anode composition, graphite deposited on a copper current collector, with a different composition of the active cathode material which is deposited on an aluminum collector. In fact, the cathode of the NCA is made of lithium nickel cobalt aluminum oxide, the LFP is made of lithium iron phosphate, the NMC by lithium nickel manganese cobalt oxide, while the LCO is composed by lithium cobalt oxide, with nickel and manganese under the 3 %, all deposited on an aluminum current collector. So, a comparison can be made on the effect of the composition of the cathode on the thermal behavior of Li-ion cells, according to the SoC.

169

In fact, the first thing that it is possible to observe is the effect of the SoC, which determines the strength of the electrical abuse when the opposite poles enter in contact due to the melting of the separator. For each cell the relative voltage range as indicated in the SDS is reported in Table 63.

Table 63: electrochemical parameter, voltage (V), for the different Li-ion cells.

Voltage (V)	C/NCA	C/LFP	C/NMC	C/LCO
Soc 50 %	3.60	3.20	3.65	3.45
SoC 100 %	4.20	3.70	4.20	4.20

From Table 60 it is possible to observe that the voltage ranges for the four chemistries considered are quite similar, with a wider range for the C/NCA, C/NMC, and C/LCO, while the C/LFP shown the lower range, so the voltage range can give back a first evaluation of the TR strength.

So, from the voltage comparison and the results of the thermal abuse tests on the same chemistry at different SoC, it is possible to observe that regardless of the chemistry a lower SoC, i.e., 50%, showed a lower impact on the main parameters, i.e. temperature and pressure, and on the ejected products, i.e. composition of the gases and size of the solid particles, compared to a higher SoC, i.e., 100%. So, the SoC range can be divided in low and unstable states, from 50 to 0 %, and high states, from 50 to 100 % [159]. The reason is due to the different voltage values available inside the cell, according to the relative voltage reported in each technical specification (Table 63), which may or may not favor the achievement of the TR with the relative jet fire from the cell and the complete combustion of the species present. So, the chemical composition of the internal components effects the internal reaction that can occur due the heating between the components.

A first comparison can be made between the temperature values of the main events for the thermal abuse tests at different SoC and the temperature values obtained by the thermal stability tests UN/ECE Regulation N°100 for the relative chemical composition. The comparison between the temperature of CID-vent disk activation , venting and TR for the two anode composition is shown in Figure 70,

Figure 70a for C/NCA, Figure 70b for C/LFP, Figure 70c for C/NMC, and Figure
70d for C/LCO.

(a)

(b)

(c)
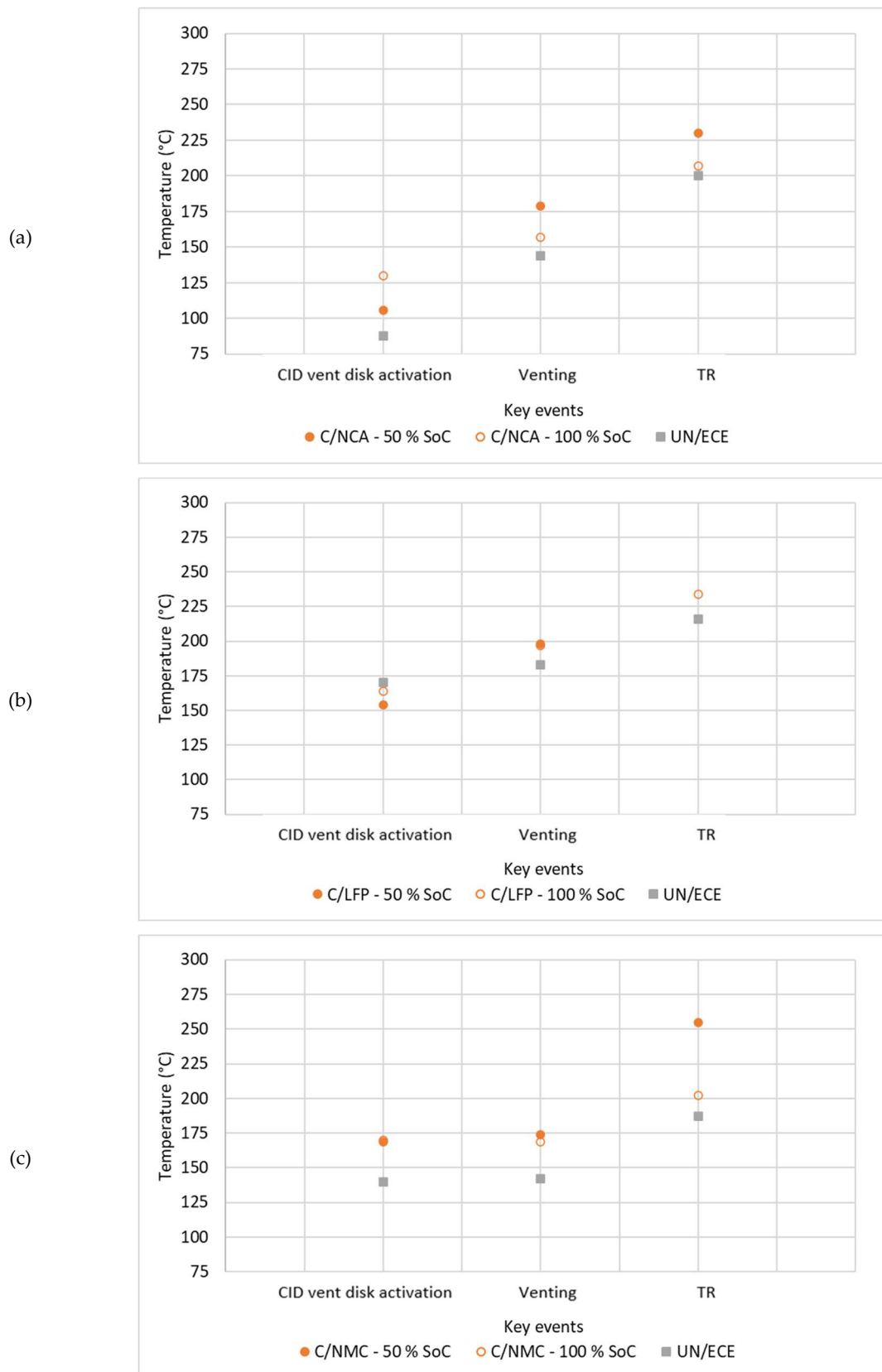
(d)
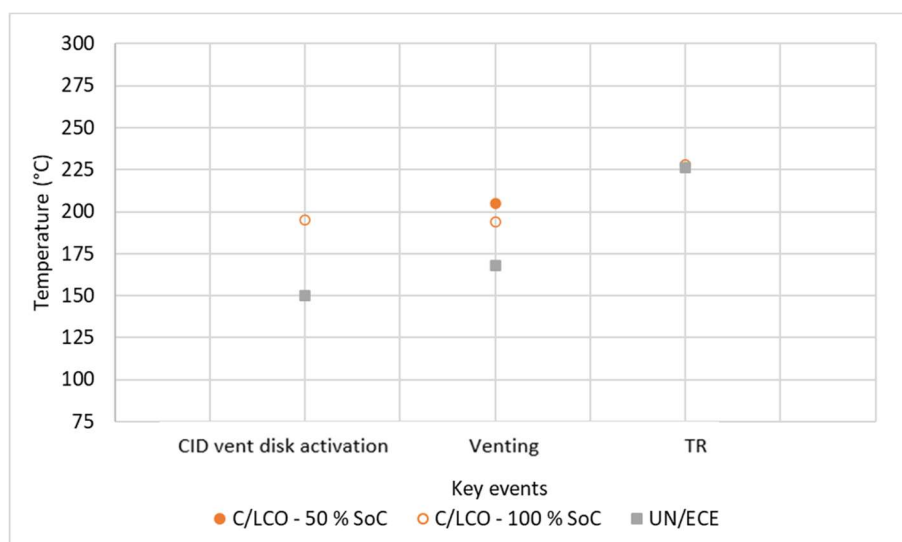
Figure 70: Comparison between the temperatures obtained by the UN/ECE N°100 and thermal abuse tests for: (a) C/NCA; (b) C/LFP; (c) C/NMC; (d) C/LCO..

The temperature values recorded for the key events, CID-vent disk activation, venting and TR, for all the cathode chemistries, except C/LFP, are higher than the limit values obtained by applying the thermal stability test reported in the UN/ECE Regulation N°100. This result shows that in the test conditions investigated, the key events occur at higher temperatures than those predicted by the thermal stability test, confirming the ability of this latter to give conservative estimation of the key temperatures. On the other hand, the activation of the protective systems of the cell at higher temperatures, increases the possibility of secondary reactions inside the cell with consequent increase of dangerous emissions.

The comparison between the different cathode chemical compositions is reported according to the SoC, in Table 64 for the 50 % SoC and in Table 65 for the 100 % SoC. Both tables are divided in five sections, the first reports the voltage, the second describes the main events reached during the abuse with the relative maximum temperature and pressure reached, while the other three report the physical-chemical characterization of the emissions.

Table 64: Comparison between the safety relevant parameters observed for the different chemistries at 50 % SoC.

Parameters	C/NCA	C/LFP	C/NMC	C/LCO
Soc 50 % (V)	3.60	3.20	3.65	3.45
CID-vent disk activation	106	154	169	n.d.
Venting	179	198	174	205
TR	230	n.d.	255	n.d.
Tmax (°C)	535	310	491	350
(source)	(self heating)	(external heating)	(self heating)	(external heating)
SHR (°C/s)	0.300	n.p.	0.256	n.p.
P_{max} (barg)	2.312	0.090	0.880	0.746
Weight loss (g)	5.8223	4.3885	8.8928	4.2860
Total gas (g) - 30 min	6.3433	4.3182	6.9489	4.4294
CCO (ppmv) - 30 min	10462	6501	7693	1203
CHF (ppmv) - 30 min	344	106	155	276
Total solid (g)	0.0504	0.0017	0.0876	0.0058
Organic part	PEO, paraffin	-	Paraffin	EC
Inorganic part	Al, Cu, Ni	-	Al	Ni, Al, Cu, Co, Li, P, Mn
Particle size (µm)	1.633	-	40	-
Total liquid (g)	n.p.	0.3984	n.p.	0.1409
Organic part	-	EC	-	EC

n.d.: not detected. n.p.: not present. - : no information.

For the 50 % SoC, it is observed that the TR occurred only for the C/NCA and the C/NMC cells and not for the C/LFP and the C/LCO cells and the products emitted were different in terms of nature and total amount. In fact, the TR in the case of the first two cells occurred with a SHR around 0.300 °C/s with a maximum of 535 °C and 2.312 barg for the C/NCA and a maximum of 491 °C and 0.880 barg for the C/NMC. These temperature and pressure caused the loss in weight of 5.8223 g from the C/NCA and of 8.8928 g for the C/NMC, in the form of gas and solid products. While, in the case of the C/LTO and the C/LCO, even if the furnace temperature was maintained over 300 °C the TR was not detected.

Table 65: Comparison between the safety relevant parameters observed for the different chemistries at 100 % SoC.

Parameters	C/NCA	C/LFP	C/NMC	C/LCO
SoC 100 % (V)	4.20	3.70	4.20	4.20
CID-vent disk activation	130	164	170	195
Venting	157	197	169	194
TR	207	234	202	228
Tmax (°C)	579	310	721	563
(source)	(self heating)	(self heating)	(self heating)	(self-heating)
SHR (°C/s)	0.600	0.400	0.600	0.700
P_{max} (°C)	5.071	0.108	5.858	3.692
Weight loss (g)	18.3600	12.3725	17.3341	12.3725
Total gas (g) - 30 min	8.2230	6.6576	9.1373	8.6807
CCO (ppmv) - 30 min	15760	10952	9421	10106
C_{HF} (ppmv) - 30 min	101	200	605	298
Amount of solid (g)	4.0103	0.066	5.4487	0.0976
Organic composition	-	PEO, Paraffin	-	-
Inorganic composition	Al, Co, Cu, Li, Mn	C, O, Al, Fe, Cu, P, F.	Ni, Al, Li, Co, Cu, Mn, P	Ni, Al, Li, Cu, Co
Particle size (µm)	n.a.	4.89	35.5	16.17
Amount of liquid (g)	n.p.	0.0453	n.p.	n.p.
Organic composition	-	EC	-	-

n.a.: not available. n.d.: not detected. n.p.: not present. - : no information.

For higher SoC, 100 %, the TR occurred for all the cells under investigation and the products emitted were similar in terms of nature and total amount, except for the small amount of liquid collected after the thermal abuse test on the C/LFP. The first events, CID-vent disk activation , occurred for all the chemistries in a range of temperature between 130 °C for the C/NCA and 195 °C for the C/LCO, while the venting occurred between 157 °C (C/NCA) and 197 °C (C/LFP). So, the safety devices are activated by different values of internal pressure which correspond to different temperature of the cell surface. Anyway, the SHR which initiate the TR, defined as TR onset, for the four cells is similar and between 0.4 and 0.6 °C/s which is higher compared to the SHR observed for the cells at the 50 % SoC. The maximum temperature and pressure reached at the peak of the TR are significantly different, from the lower values of 310 °C and 0.108 barg (C/LFP), to the higher values of 721 °C and 5.858 barg (C/NCA).

To define the safety of the Li-ion cells under investigation usually is defined the safety operating windows, so the area of temperature and voltage inside which the cell use can be defined safe. The upper limit for the temperature can be defined by the CID-vent disk activation temperature. In the case of the C/NCA the activation is between 106 and 130 °C, according to the SoC, while for the C/LCO is around 200 °C. A higher temperature value in this case is synonymous of greater stability, with a wider operating safety window in terms of temperatures and lower risk during use. The other two cells, the C/LFP and the C/NMC, showed the CID-vent disk activation between 150 and 170 °C. From the temperature values for the main events, summarized below and extracted from Table 64 and Table 65, the safest cell can be considered the C/LFP, for both the SoCs while the more unstable are the C/NCA and the C/NMC, in fact:

$T_{CID50\%}$: C/NMC (169 °C) > C/LFP (154 °C) >> C/NCA (106 °C).

$T_{V50\%}$: C/LCO (205 °C) > C/LFP (198 °C) >> C/NCA (179 °C) > C/NMC (174 °C).

$T_{TR50\%}$: C/LCO (255 °C) > C/NCA (230 °C).

$T_{CID100\%}$: C/LCO (195 °C) > C/ NMC (170 °C) > C/LFP (164 °C) >> C/NCA (130 °C).

$T_{V100\%}$: C/LFP (197 °C) > C/LCO (194 °C) >> C/NMC (169 °C) >> C/NMC (157 °C).

$T_{TR100\%}$: C/LFP (243 °C) > C/LCO (228 °C) >> C/NCA (207 °C) > C/NMC (202 °C).

These results are in line with the voltage ranges, in fact the higher voltage for the C/NCA and the C/NMC can explain the lower temperature observed for the CID-vent disk activation and the venting and the higher temperature reached at the end of the TR during the thermal abuse tests.

Even the products emitted can be considered to define the safety of the cells during an abuse. For the 50 % SoC, regardless of whether the TR is reached or not, a weight loss of the cell is observed due to the emission of gases, solids and in some cases even liquids, as for the C/LFP and the C/LCO. The higher weight loss is observed for the cells that reached the TR, between 5 and 8 g, due to the higher

temperature and the reactions activated between the internal components, while the liquid was collected, between 0.1 and 0.3 g collected, only for the cells that did not reach the maximum event, the TR. Independently from the temperature and the TR the main products emitted from the cells during the thermal abuse test is the gas phase, with an amount between 4 and 6 g, constituted by CO, CO_2, and CH_4 correlated to the combustion reactions and by HF, DMC, and EC due to the electrolyte. Of these species the most dangerous are the HF and the CO due to their intrinsic toxicity, and in fact their exposure is limited by the NIOSH (30 ppm for HF and 1200 ppm for the CO). These two limit values were exceeded during the thermal abuse tests of all the chemistries, usually of one order of magnitude except for the CO in the C/NMC.

The toxic substances are not the only risk for the human health, in fact even the size of the metallic particles must be evaluated to assess whether or not they are capable of being breathed (d < 4 μm) and/or inhaled (10-100 μm). For the tests at the 50 % SoC only the C/NCA release metallic powder with a diameter, measured by the SEM-EDX, of 1.63 μm which can therefore be breathed in, affecting human lungs.

The emissions are worse as the SoC increases, in fact there is an increase in material losses from the cell in terms mainly of gases and solids. In fact, the weight loss from the cells is between 12 and 18 g, almost 10 grams of difference with half charged cells, with an increase especially of the solid components. Even in this case a small amount of liquid, 0.0453 g, was collected at the end of the thermal abuse test on the LFP due to the lower temperature reached during the TR compared to the boiling temperature of the EC. About the toxic gases, HF and CO, the concentration exceed the NIOSH (30 ppm for HF and 1200 ppm for the CO) similarly to the 50 % SoC, so all the values are one order of magnitude higher than IDHL for the HF and CO (the latter except for the C/NMC). As mention before, the increase in health risk is due to the increase in solid particulate released. In fact, at

100% SoC, around 4/5 g of solid material are observed with particle diameters between 4.89 μm for the C/LFP, 16.17 μm for the C/LCO and 35.5 μm for the C/NMC. The latter particles, due to their coarse diameter, are only respirable while the first particles, due to their fine particle size, are both inhalable and respirable with very serious effects on human health.

So, among the Li-ion cells under investigation with the same anode material the more stable cathode material resulted the C/LFP, for the lower temperature and pressure observed during the TR, reached only for the higher SoC, and the typology of products emitted, liquid and condensate phase compared to respirable metallic powder. The worst cell in term of safety it can be defined the C/NCA, due to the lower temperature of the CID-vent disk activation and the large amount of products emitted, with physical-chemical properties that are very dangerous for human health.

4.4 Additional thermal abuse test on C/NCA 18650 cells

From the obtained results it emerged that the most dangerous Li-ion cell is the C/NCA, due to both the higher temperature and pressure values reached already at 50 % SoC and the products emitted during the TR, in terms of gases and solid particulate.

For this reason additional thermal abuse tests varying the test conditions, i.e., feed gas (N_2 or air), and the heating rates (5 or 10 °C/min), were performed to evaluate on one hand if the inert atmosphere can lead to a reduction both of the maximum temperature and pressure values reached and the danger of the products emitted and on the other how the behavior changes as consequence of an increased heating rate.

Differences between the gas compositions allow to distinguish the products that are generated inside the cells, in N_2, and those that are formed outside the cells by reaction with air. While the difference between the temperature values reached

can give back an idea of the severity of the internal reactions and severity according to the external energy supplied.

4.4.1 Results: heating rate and environmental impacts

In Table 66 are reported the parameters of the main events occurring during the tests at both the heating rate, 5 and 10 °C/min, and the atmosphere, air and N_2 (see also Figure 102 (Appendix 5)).

Table 66: temperature (°C) and pressure (barg) of the main events of the different thermal abuse tests on C/NCA.

Key event	Air – 10 °C/min	Air – 5 °C/min	N_2 – 10 °C/min	N_2 – 5 °C/min
CID-vent disk activation	1260	1672	1184	1745
	$132 \pm 20°C$	$106 \pm 2°C$	$128 \pm 23°C$	$107 \pm 4°C$
	0.01 barg	0.175 barg	0.25 barg	0.11 barg
Venting	1687	2770	1793	2585
	$194 \pm 11°C$	$179 \pm 16°C$	$195 \pm 23°C$	$171 \pm 5°C$
	0.18 barg	1.43 barg	3.70 barg	0.34 barg
TR	1917	3122	2115	3015
	$226 \pm 24°C$	$230 \pm 6°C$	$221 \pm 11°C$	$213 \pm 6°C$
	0.73 barg	1.50 barg	4.10 barg	0.83 barg
Maximum	2049	3181	2250	3107
	$564 \pm 85°C$	$535 \pm 17°C$	$497 \pm 68°C$	$554 \pm 11°C$
	1.48 barg	2.31 barg	5.10 barg	1.19 barg

From the comparison, the CID-vent disk activation temperatures and venting temperatures are not significantly different for tests conducted at the same heating rate in air or N_2, but are higher for test performed at higher heating rate (10 °C/min). On the contrary the TR and the peak temperatures are more affected by the feed gas used in the tests than by heating rate. In air the cell temperature is affected by the combustion of the organic compounds, mainly electrolyte, emitted by the cell that occurs outside the cell. In fact, in addition to the increase in temperature and pressure, the heating rate causes the emission of gases.

The emission profiles of the main species, such as HF, EC, DMC, CO, CO_2, CH_4 are reported in Figure 103 (Appendix 5) whith the concentration values expressed in ppmv.

The total quantities of the gases, expressed in ppm, are reported in Table 67, and compared with the IDLH limits reported by the NIOSH.

Table 67: concentration (ppm) of gas emitted for thermal abuse test on NCA at 50 % SoC in air and N$_2$ at 5 and 10 °C/min in 30 min.

ppm / Tests	DMC	EC	HF	CH$_4$	CO	CO$_2$
Air – 10 °C/min	37	15	308	304	21017	26422
Air – 5 °C/min	55	n.d.	344	349	10462	13118
N$_2$ – 10 °C/min	59	36	92	92	4751	3986
N$_2$ – 5 °C/min	51	n.d.	172	32	3903	3070
IDLH [51]	-	-	30	-	1200	-

So, the concentration values significantly exceed the IDLH values reported by the NIOSH for HF and for CO by an order of magnitude in the case of the tests in air for both the substances. For the test in N$_2$ the concentration values for the HF and the CO exceed the limits but are significantly lower than those measured in air

For these tests the quantities collected and the type of residues are reported in Table 68 and showed in Figure 72.

Table 68: weight of the cell and the products collected (g) after the thermal abuse test on NCA at 50 % SoC in air and N$_2$ at 5 and 10 °C/min in 30 min.

g / Tests	Initial cell weight	Final cell weight	Δcell	Gases weight	Condensate phase weight	Solid weight	Liquid weight
Air – 10 °C/min	45.2854	39.7100	5.5754	7.0432	0.0612	n.p.	n.p.
Air – 5 °C/min	45.6600	39.8367	5.8223	6.3433	0.0504	n.p.	n.p.
N$_2$ – 10 °C/min	45.4701	39.6900	5.7801	2.2439	0.0183	n.p.	n.p.
N$_2$ – 5 °C/min	45.1898	39.6104	5.5794	1.8066	0.0375	n.p.	n.p.

n.p.: not present.

From Table 68 it is possible to observe that the loss of material from the cells is constant, in terms of amount, and similar in nature, as condensed phase on the filter, independently from the conditions. The nature and composition of the residues released on the filter is shown in Figure 72. In the case of tests in air the condensate phase is darker compared to the condensate phase in N$_2$, probably due to the combustion of the electrolyte.

The characterization of the condensed phases collected on the filters permitted to obtain the composition, by ATR-FT-IR analysis, and the quantification, by ICP and AAS analysis, and the size of the particle emitted, by SEM-EDX analysis.

(a)   (b)   (c)   (d)
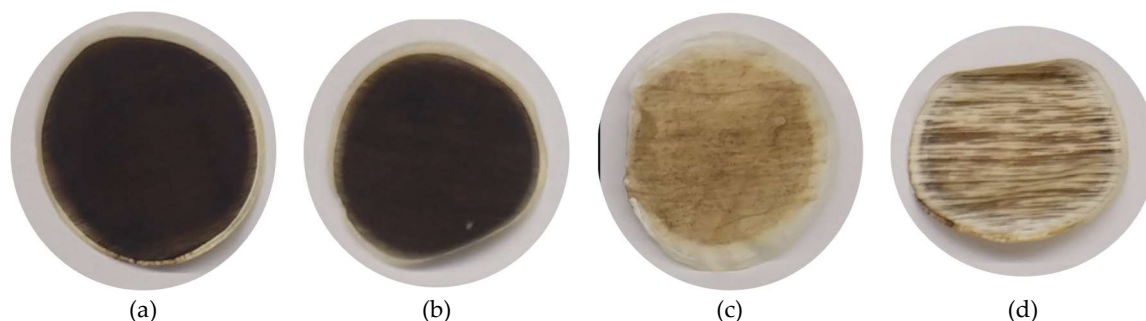
Figure 71: filters after the thermal abuse test on NCA at 50 % SoC: (a) 10 °C/min in air; (b) 5 °C/min in air; (c) 10 °C/min in N_2; (d) 5 °C/min in N_2.

Even the external case showed a similar aspect, with some bubble outside the venting valve due to the release of the electrolyte during the TR, as shown in Figure 72.

(a)   (b)   (c)   (d)
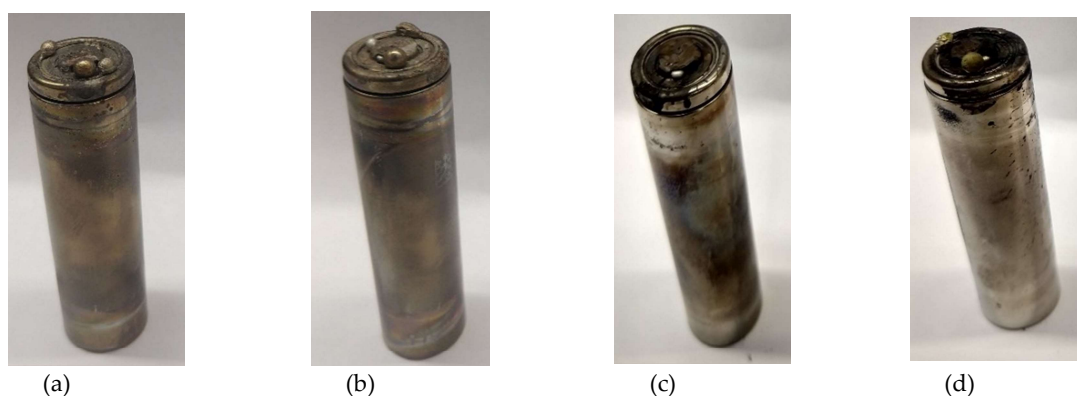
Figure 72: cells after the thermal abuse test on NCA at 50 % SoC: (a) 10 °C/min in air; (b) 5 °C/min in air; (c) 10 °C/min in N_2; (d) 5 °C/min in N_2.

The ATR-FT-IR analysis were performed on the condensed phase collected during the tests on the filters, and the ATR-FT-IR spectra are shown in Figure 104 (Appendix 5), while in able 69 are reported the peaks with the relative identification and force.

The analysis showed the presence of paraffin and PEO, used as explained before as protective layer of the anode material or separator to improve the battery cycling. In addition, PEO can be produced even by the EC degradation.

Identification		Air – 10 °C/min		Air – 5 °C/min		N$_2$ – 10 °C/min		N$_2$ – 5 °C/min	
Paraffin oil	s	2951.76	m	2951.19	m	2951.70	m	2951.14	m
Paraffin oil – PEO	vs	2917.87	vs	2918.01	vs	2917.35	vs	2918.16	vs
Paraffin oil – PEO	vs	2849.63	s	2849.62	s	2849.15	s	2849.77	s
Paraffin oil	vw	2724.01	vw	2737.23	vw	n.d.	-	2722.61	vw
PEO	w	1712.88	m	1714.37	m	1711.40	w	1713.75	w
PEO	w	1644.21	vw	1642.61	vw	1642.32	vw	1642.91	vw
PEO	w	1614.47	w	n.d.	-	n.d.	-	1602.36	vw
Paraffin oil – PEO	s	1461.48	s	1461.66	s	1462.57	m	1461.97	m
Paraffin oil – PEO	m	1376.48	s	1376.06	s	1376.72	m	1375.86	m
Paraffin oil	w	1273.84	w	1267.92	vw	1201.19	s	1212.49	s
PEO	w	1167.09	vw	1163.74	m	1145.29	vs	1154.36	vs
Paraffin oil	vw	1074.22	vw	1068.87	vw	1085.88	vw	1081.13	vw
PEO	w	908.95	w	909.60	w	909.63	m	909.28	m
Paraffin oil	w	887.25	w	886.26	w	885.48	m	887.05	m
Paraffin oil	m	730.22	m	729.99	m	729.56	m	730.00	m
Paraffin oil – PEO	s	719.48	m	719.27	m	719.48	m	719.47	m

n.d.: not detected.

The results obtained by the ICP-OES and AAS-OES were reported in Table 70 as milligrams of metal over the gram of solid collected.

Table 70: quantification of metals (mg) in the filters after the thermal abuse tests on NCA at 50 % in air and N$_2$ at 5 and 10°C/min.

	Al (mg)	Co (mg)	Cu (mg)	Li (mg)	Mn (mg)	Ni (mg)	P (mg)
Air – 10 °C/min	0.0026	< LOD	< LOD	0.0007	< LOD	< LOD	< LOD
Air – 5 °C/min	0.0057	< LOD	< LOD	0.0012	< LOD	0.1505	< LOD
N$_2$ – 10 °C/min	0.0049	< LOD	< LOD	0.0010	< LOD	< LOD	< LOD
N$_2$ – 5 °C/min	0.0047	< LOD	< LOD	0.0005	< LOD	< LOD	< LOD

LOD: limit of detection.

The difference between the total solid ejected and the sum of the metals is due to the loss of the information about carbon and oxygen. The main metals found were Al from the cathode collector and Li. The lower concentration values are due to the low amount of material collected on the filters.

SEM-EDX analyses were conducted on the filters collected after the thermal abuse tests. In Figure 73 are reported the SEM images of the surface of the filters. From the images obtained with the BSE detector it is possible to highlight the compositional contrast at the expense of the structural morphology, which can be

evaluated with the SE detector. From the images obtained on the test filters, shown in Figure 73, no compositional difference is observed between the various samples. In fact, in all the samples there are small particles, lighter points with an almost spherical shape, dispersed on the filter surface. The composition of the filter is constant, even if acquired in BSE from the images it is possible to observe the fibers and their texture, and the dimensions of the particles are significantly smaller than the filtering section.

(a)

(b)

(c)

(d)
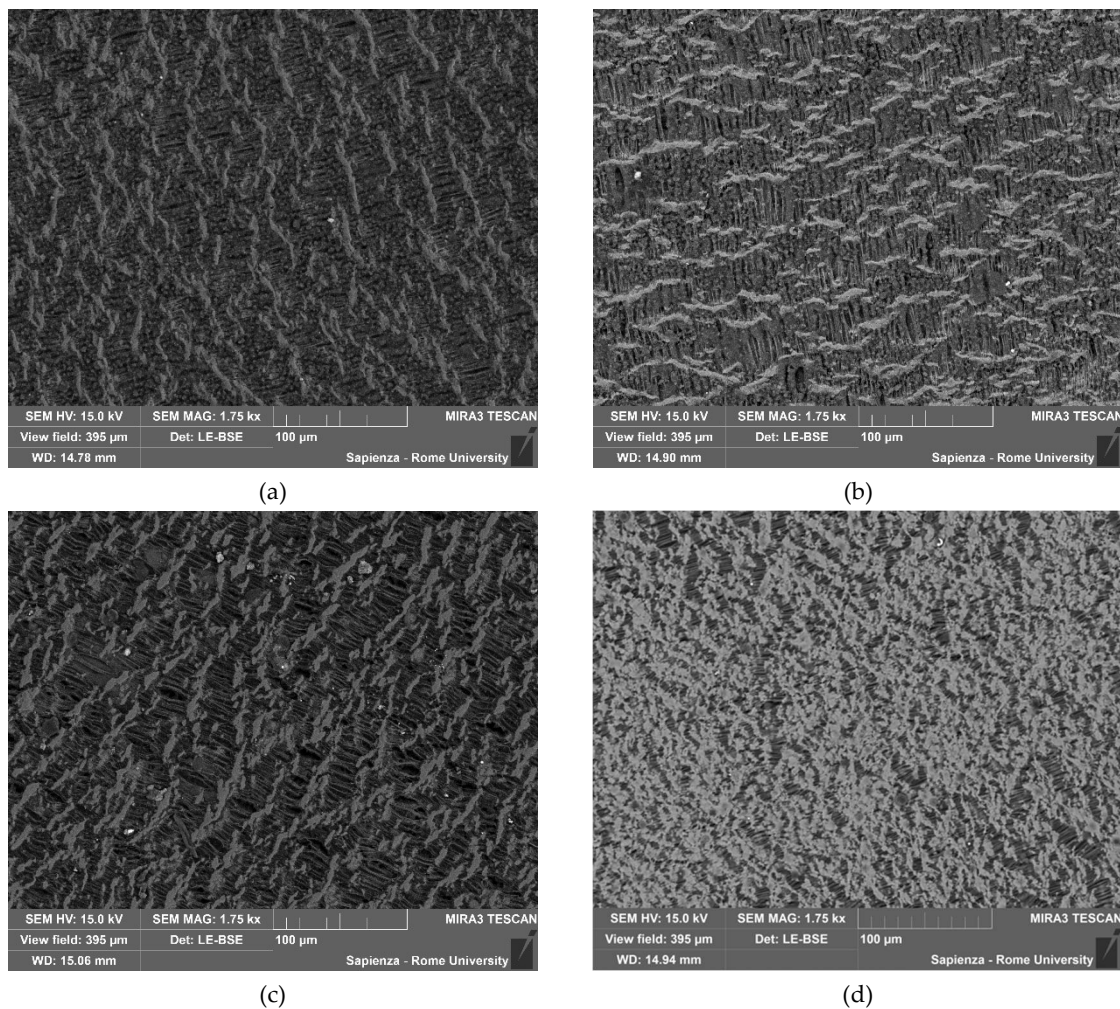
Figure 73: SEM on the filters after test: (a) 10°C/min in air; (b) 5°C/min in air; (c) 10°C/min in N_2; (d) 5°C/min in N_2.

By magnifying the different filter areas, it was possible to identify particles with different compositions and diameters. In the following figures are reported the most significant image of each filter with the magnification and its spot and/or area analyzed, the diameter of the particles and the respective EDX spectra for

compositional analysis. The results of the analyses are reported in Figure 74 for the 10 °C/min in air, in Figure 75 for the 5 °C/min in air, in Figure 76 for the 10 °C/min in N_2 and in Figure 77 for the 5°C/min in N_2.

The chemical composition and diameters of particles observed in the sample of Figure 74 are homogeneous. In fact there is the same chemical composition: Al, O, F and P with similar percentage of these elements among the investigated spots, and also diameters are comparable, d_1= 1.48 μm, d_2 = 1.04 μm and d_3 = 2.54 μm, between the different particles with an average value of 1.68 μm. The presence of F and P is common and is traceable to the electrolyte solution in which the Li-salt ($LiFP_6$) is dissolved in organic carbonates (i.e., DEC and EC). The presence of Li has been demonstrated by the ICP and AAS analysis later reported. Al and O are instead attributable to the composition of the cathode made of lithium nickel cobalt aluminum oxides (NCA). The presence of C is due to the initial treatment of the sample, graphitization, so it is therefore not possible to distinguish it from the graphite of the anode material.

The agglomerate in Figure 75 can be divided into two distinct particles, the up-per one with a d = 1.10 μm and the inferior one with a d_1 = 2.55 μm and d_2 = 1.78 μm. The main difference between the two particles in terms of composition is the presence of Al in the upper one and a greater amount of oxygen in the inferior one. Also, in this case P and F are found and attributable to the electrolyte salt while the material coming from the electrodes, specifically the cathode, is confirmed by the copresence, in Spot 1, of Ni, Co and Al, presumably in oxidized form, while in Area 1 to the copresence of Ni and Co.
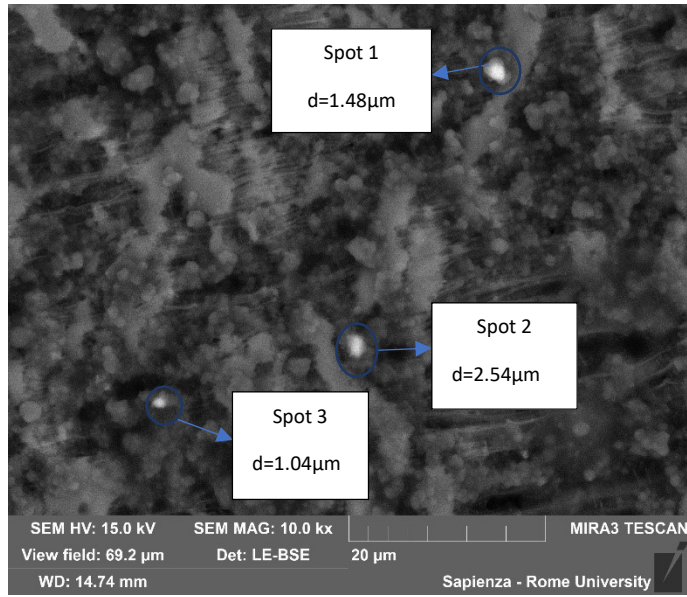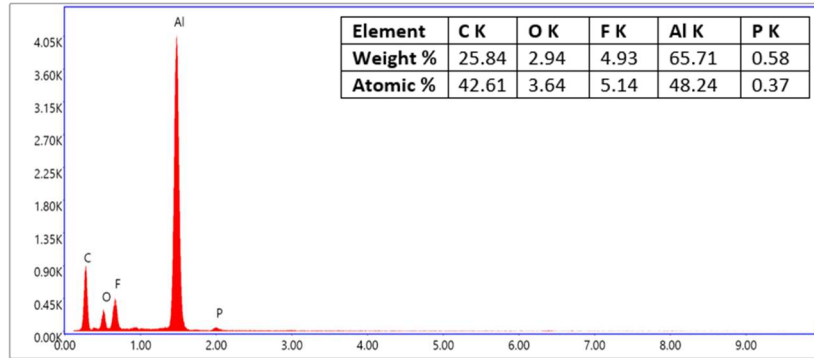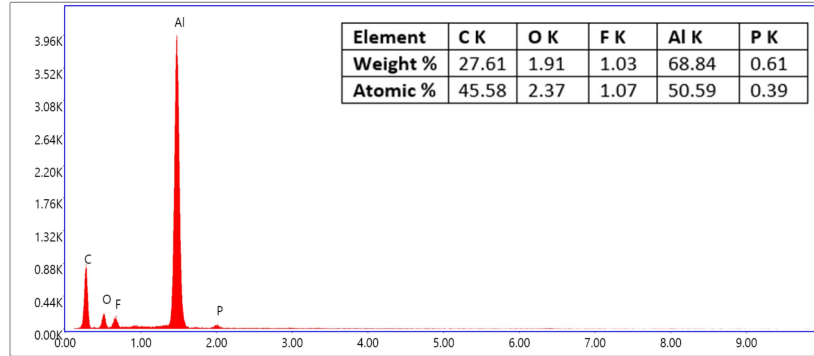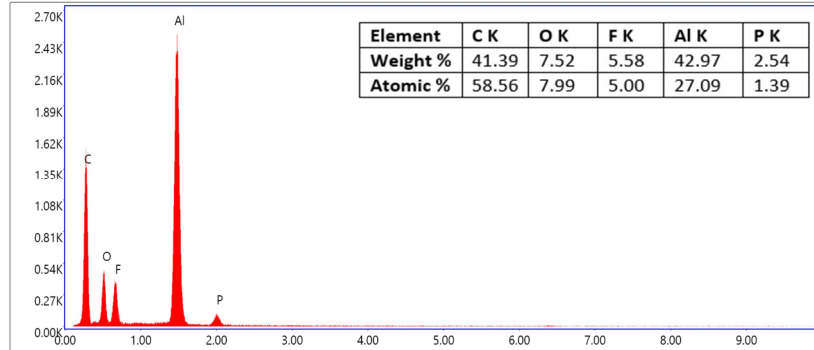
Figure 74: Condensed phase collected during the test at 10°C/min in air. (a) Areas analyzed by EDX and dimension of the particles; (b) EDX of Spot 1; (c) EDX of Spot 2: (d) EDX of Spot 3.
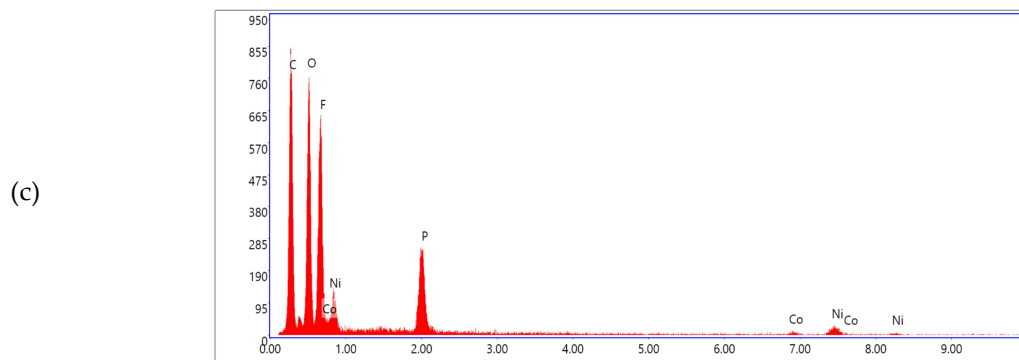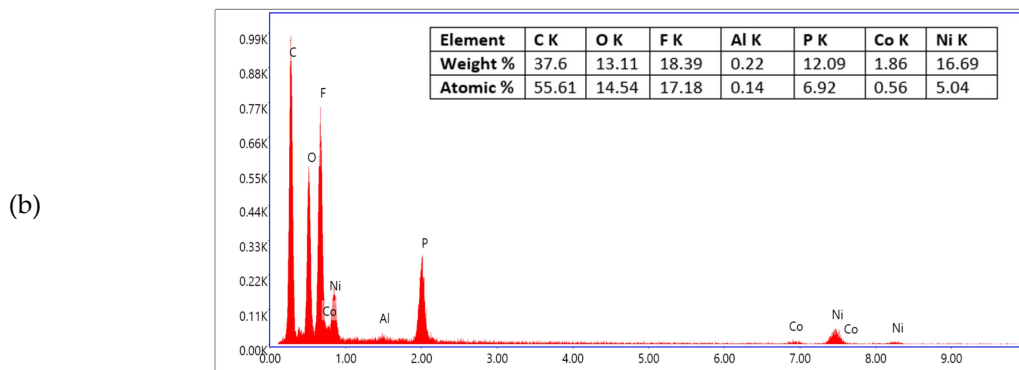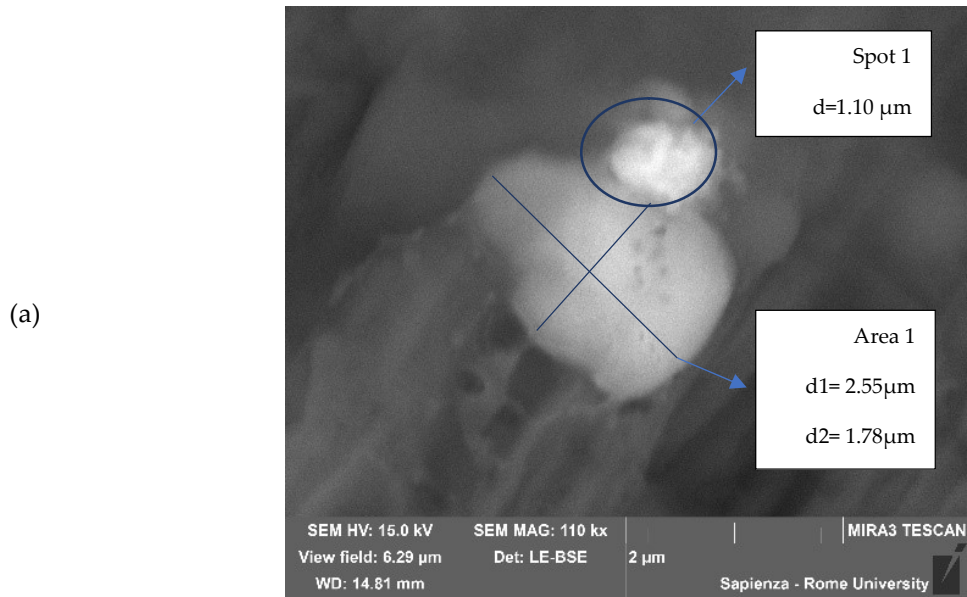
Figure 75: Condensate phase collected during the test at 5°C/min in air. (a) Areas analyzed by EDX with dimension of the particles; (b) EDX of Spot 1; (c) EDS of Area 1.
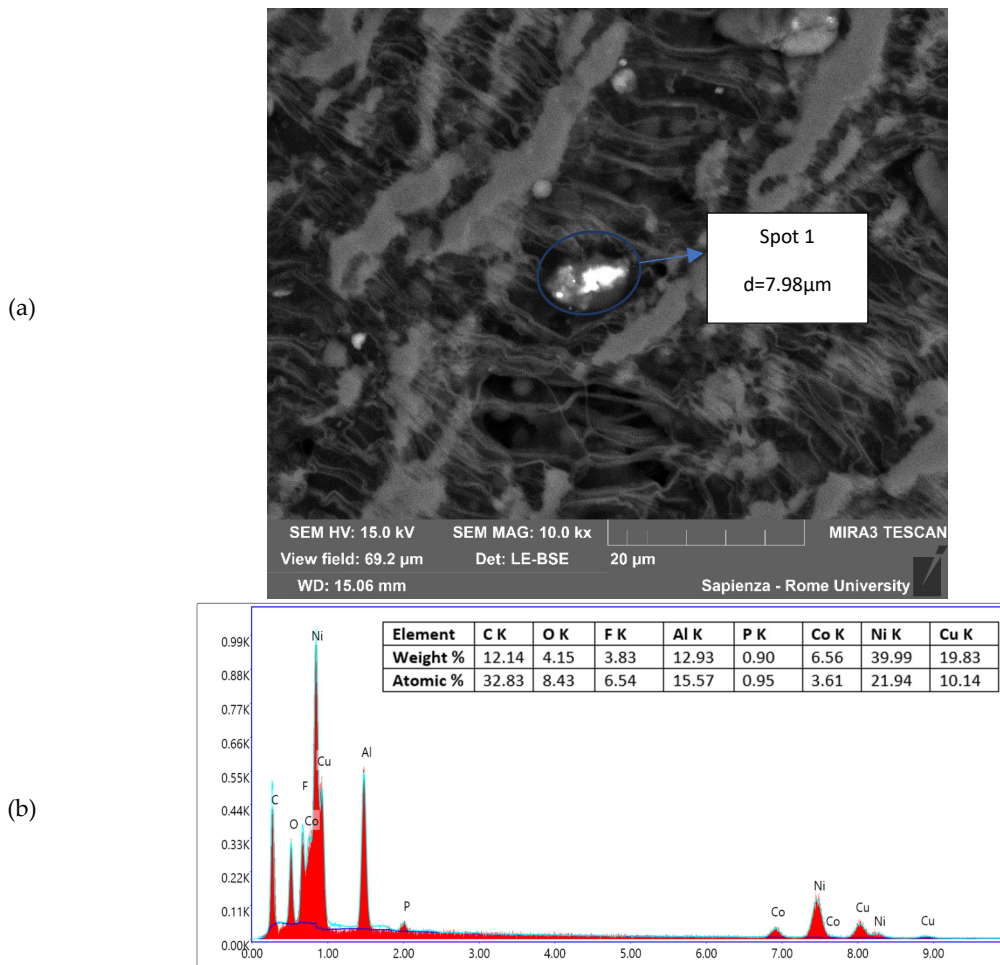
Figure 76: Condensed phase collected during the test at 10°C/min in N_2. (a) Spot analyzed by EDX and dimension of the particle; (b) EDX of Spot 1.

In the latter sample, Figure 76, the particle has no perfectly spherical geometry, d = 7.98 μm, and compounds from both electrodes (Al, Ni, Co from cathode and Cu from anode), which can always be in the form of oxides for the oxygen copresence, and from electrolyte salt (P and F) are present. In this sample the contribution of the electrodes, specifically the active cathode material and the anode collector, is higher, in weight %, than the previous samples. The presence of Al, Co and Ni, tendentially in oxidized form, are due to the degradation of the cathode active material, while the Cu is due to the degradation of the anode collector.
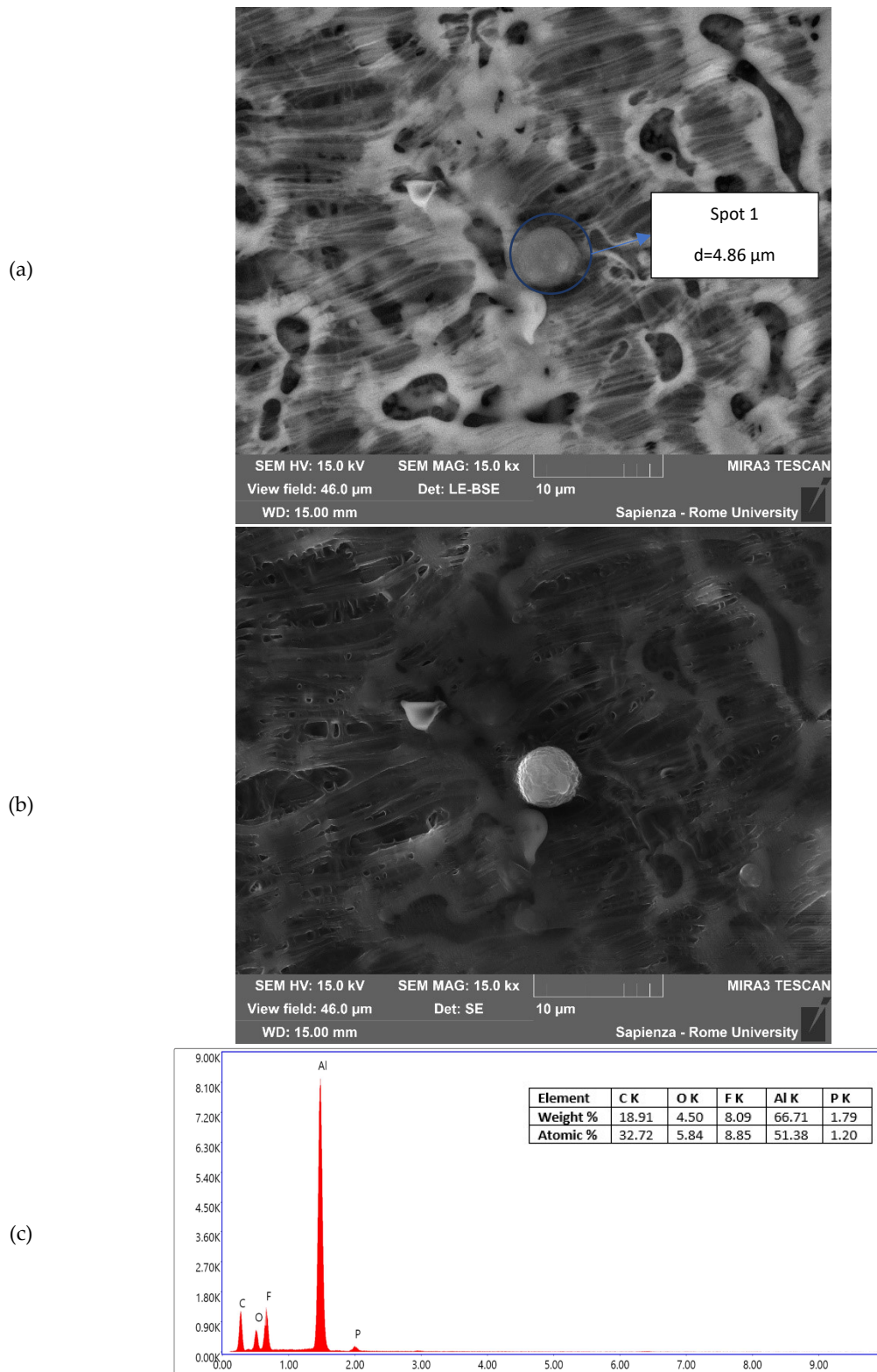
Figure 77: Condensate phase collected after the test at 5°C/min in N₂. (a) Spot analyzed by EDS and dimension of the particle; (b) EDS of Spot 1; (c) Same spot analyzed by SE.

Also, in this sample, Figure 77, is observed a spherical particle, d = 4.86μm, composed mainly of Al, in the form of an oxide due to the copresence of O, and F and P attributable to the electrolyte solution.

Comparing the results of different feed gas composition, it is observed that in air the particles have a more spherical shape and smaller diameters, around an average value of 1.54 ± 0.69 μm. In nitrogen, instead, the particles have a less spherical shape, agglomeration, and much larger diameters, 6.42 ± 2.21 μm. In terms of composition, however, there is the constant presence of F, P, O, Al while the presence of Ni, Co and Cu vary depending on the sample.

4.4.2 Discussion: heating rate and environmental impacts

The temperature and pressure values of the main events for the different thermal abuse tests, shown in Figure 78, were compared with the values obtained by the thermal stability tests UN/ECE Regulation N°100 in air and N_2. The Figure 78 show the comparison of results (a) in air and (b) in N_2 for the temperature of the key events, i.e., CID-vent disk activation , venting and TR.

In terms of temperature the values recorded for the key events, CID-vent disk activation , venting and TR, in all test conditions are higher than the limit values obtained by applying the thermal stability test reported in the UN/ECE Regulation N°100. This result shows that in the test conditions investigated, the key events occur at higher temperatures than those predicted by the thermal stability test, confirming the ability of this latter to give conservative estimation of the key temperatures. On the other hand, the activation of the protective systems (CID, and venting) of the cell at higher temperatures, increases the possibility of secondary reactions inside the cell with consequent increase of dangerous emissions.

The profiles of the emitted gases are similar in air and N_2 for most of the gases. In fact, due to the combustion reactions of electrolyte solvents in air the concentration of CO_2 is higher than in N_2, where the CO is the main product of the carbonate's decomposition. For CO and HF, the concentration values significantly exceed the IDLH values reported by the NIOSH by an order of magnitude in the case of the tests in air for both the substances. For the tests in N_2 the concentration value for

the HF and the CO exceed the limits but are of the same order of magnitude of the NIOSH limit values, except for the HF at 5 °C/min.
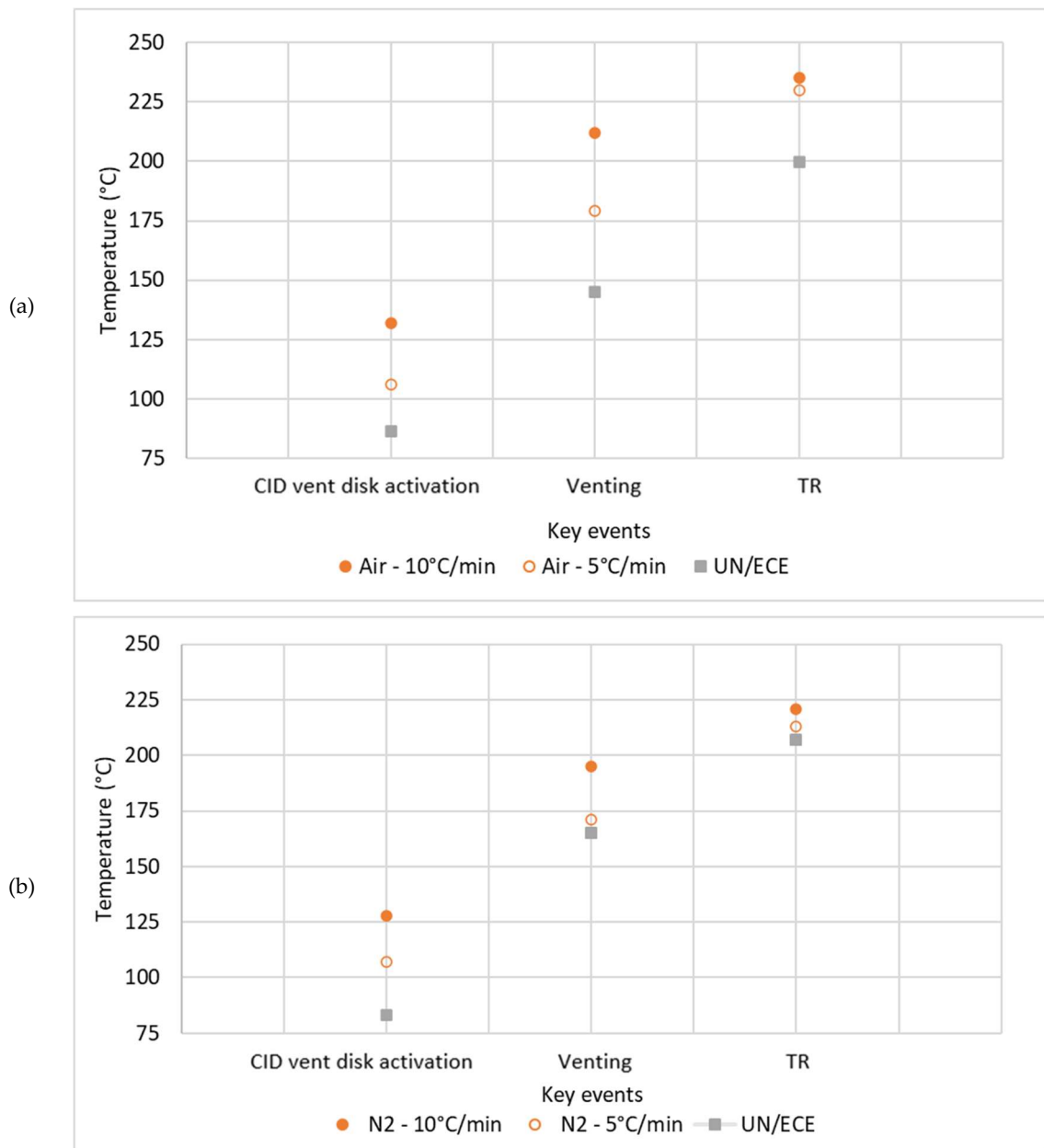
Figure 78: Comparison between the temperatures by the UN/ECE N°100 and thermal abuse tests in: (a) air and (b) N_2.

A similar analysis can be made for metals, both in particle size and chemical composition. By cross-checking the data obtained from ATR-FT-IR analyses, SEM images with related EDX analyses and ICP-OES and AAS-OES analyses, it is possible to trace the condensed phase emitted by the electrolyte solution, i.e., Li, P

and F, the degradation of the separator, i.e., paraffinic wax and PEO, and the electrode material, i.e., Al, Ni, Co and O.

The filters were analyzed by ATR-FT-IR and both the PEO and the paraffin oil were identified. From Figure 72 it is possible to observe that the condensate phase is deposited differently; in particular, the brown deposit results homogeneously dispersed on the filter surface in tests performed in air than in N_2. The difference is due to the combustion reactions that occurred in an oxidative atmosphere.

From the EDX analysis it is possible to obtain an identification and a distribution of the metals. In terms of composition there is the presence of F, P, O is observed in all the samples, while Al, Ni and Co vary depending on the sample, but their distribution similar to that of O allow to assume that the electrode metals, Ni, Co and Al, are present as oxides. For Co, Mn and Li emissions, the reference IDLH value are not reported from NIOSH. Regardless an important aspect that must be evaluate is the dimension of the particles or metal agglomerates. SEM images showed the presence of particles, of spherical shape, and/or metal agglomerates, with an average diameter of particles of 1.54 ± 0.69 μm. These particles if dispersed in the air during a fire of Li-ion batteries contribute to the rise of PM 2.5, which can be inhaled and breathed causing effects both in the short and long-term depending on the toxicity of the compounds. For the analyzed NCA cell, the particles can be composed of different metal (Li, Ni and Co) oxides, carbonates, fluorinates and phosphates. From the quantification through the ICP-OES and AAS it was possible to evaluate the metal concentration in emissions and the main metals release are the Li and the Al, due to the higher amount as chemical components.

4.5   Conclusions from thermal stability and thermal abuse tests

In conclusion the thermal stability tests allowed to obtain information about the temperature limit of the safety windows for the different chemistries investigated and the safety concern due to the emission products. Therefore, evaluating all the

data obtained by the characterization analysis, the safest cell turns out to be the C/LFP compared to the C/NMC and the C/NCA which are the most dangerous.

The thermal abuse tests allowed to obtain information about the temperature and pressure on the cell when subjected to a similar external heating abuse (5 °C/min) at two SoC (50 and 100 %). The two SoCs represent the more unstable level, 50 %, and the higher energy level of charge, 100 %. Independently from the SoC the products emitted resulted dangerous both in the form of gases and solids. The danger can be defined by the exposure concentration, compared to the IDLH, and the size of the particles, inhalable ($10 < d < 100$ μm) and/or breathable ($d < 4$ μm).

Between the different anode active materials investigated, graphite and LTO, the more stable resulted the LTO. While among the cathode active materials, NCA, LFP, LCO, and NMC, the more stable resulted the LFP.

The additional tests conducted on the C/NCA, which is the most unstable cell between the chemistries investigated, were conducted to understand the impact of different heating rate (5 vs 10 °C/min) and the environment (air vs N_2). The higher heating rate showed an increase of the temperature on the cell surface at which the key events occurred with respect to the slower heating rate, anyway both the temperature-pressure and the emission profiles resulted similar. The main difference was observed between the oxidative and the inert atmosphere, as expected, in presence of air the amount of CO and CO_2, due to the combustion reactions, increased compared to the amounts detected in the inert atmosphere. The study in the inert atmosphere was conducted for two reasons, first to evaluate the products produced just from the internal reactions occurring inside the cells and then to evaluate the impact of the atmosphere on the safety concerns. From the analysis of data resulted that an inert atmosphere reduces, albeit slightly, the temperatures at which the key events occur and the products emitted.

The results obtained on the cells taken into consideration in the study are in line with what is reported by other studies in the literature. In fact, the greater stability of LFPs compared to other chemistries, such as NCA, LCO and NMC, was also verified by Golubkov et al. [169]. They found for the LFP cells the highest onset temperature (195 °C), the smallest temperature increase during the thermal runaway (210 °C), the lowest amount of produced gas (50 mmol) and the lowest percentage of toxic CO in the gas (4%) [169]. This is due to the higher stability of the cathode materials and the relative degradation temperature. In fact, comparing the commercial chemical composition it emerged that the LFP is the most thermally stable material due to the high temperature of degradation of the material [63]. Inside the LFP cells the production of oxygen, due to degradation of the internal materials, occurred above 500 °C, also causing a slower heating rate [62]. For the other chemistries the degradation reactions that lead to the oxygen production occurred at lower temperature, between 140 and 160 °C for NCA, as reported in Equation (11) or around 260 °C for NMC, as reported in Equation (12) [11].

Even the SoC impact observed for the Li-ion cells under investigation is in accordance with the literature studies already available. In fact, the severity of the thermal runaway increased with increasing SOC [170]. In fact, at different SoC it is possible to observe that regardless of the chemistry a lower SoC (i.e., 50 %) showed a lower impact on the main parameters, i.e. temperature and pressure, and on the ejected products (i.e., composition of the gases and size of the solid particles) compared to a higher SoC (i.e., 100 %). So, the SoC range can be divided in low and unstable states, from 50 to 0 %, and high states, from 50 to 100 % [159].

The combination of the results relevant to emission's characterization can be used to identify the personal protective equipment (PPE) that can be adopted by firefighters to operate in complete safety on the LIBs fire scene. The most efficient equipment in the case of LIBs fire is the gas masks, so-called air-purifying

respirators, which protect from inhaling dangerous substances, such as chemicals particles. The selection of the more efficient respirator must be done in accordance with the hazard and the airborne concentrations [171]. Gas filters provide protection against vapors, chemical substances and toxic gases. They usually consist of a bed of activated carbon. They are described according to 2 criteria: filter type and capacity, as reported in Table 71.

Table 71: Filter color and code, filtered contaminant and terms of use and filter capacity or efficiency [172].

Filter color		Filter type	Filtered contaminant	Terms of use Filter capacity er efficiency
Dark brown		AX	Gases and vapors organic compounds with boiling point < 65 °C such as methyl acetate, acetone, butane, chloroform, methanol, freons, etc.	Use immediately after opening, for single use only. Group 1: 100 ppm max 40 min, 500 ppm max 20 min. Group 2: 1000 ppm max 60 min, 5000 ppm max 20 min.
Light brown		A	Gases and vapor of organic compounds with boiling point < 65 °C mainly solvents and hydrocarbons such as acetates, acetic acid, acrylics, alcohols, benzene, phenols, styrene, etc.	Class 1: 1000 ppm Class 2: 5000 ppm Class 3: 10000 ppm With a ventilated system: Class 1: 500 ppm Class 2: 1000 ppm
Grey		B	Inorganic gases and vapor except CO: bromine, cyanide, chlorine, hydrogen sulfide, fluorine, isocyanates, formol, hydrocyanic acid...	
Yellow		E	Acid gases and vapors: sulphuric anhydride, sulphur dioxide, hydrochloric acid, hydrofluoric acid, formic acid, etc.	
Green		K	Ammonia and organic ammonia derivates: hydrazine, methylamine, aziridine, etc.	
Black		CO	Carbon monoxide	Single use (max. 10000 ppm)
Red		Hg	Mercury vapors	Maximum operating time: 50 h
Blue		NO	Nitrous vapors and nitrogen oxides	Maximum use time: 20 min single use
Orange		Reactor	Radioactive iodine, including radioactive methane iodine	Depending on the level of radioactivity
White		P	Particles	P1: filter efficiency > 80 % P2: filter efficiency > 94 % P3: filter efficiency > 99.95 %

So, the most efficient gas filter can be obtained by the combined filters: A1E1P3 + CO.

5. Nanomaterials (NMs) safety characterization

From the literature review, the NMs most frequently used as active materials for the anode are silicon, LTO and graphite, while the carbon black (CB) is used as an additive to increase the conductivity and therefore the electrical performance of LIBs.

For each material, the flammability behavior, the explosivity and the impact of ecotoxicity were evaluated. These results must be correlated with the physical properties of both the pristine material and the dispersed material in the ISO solution, so a complete characterization was carried out in terms of size, such as granulometry and SSA, and stability of the dispersion in solvent, such as zeta potential.

The aim is to identify the risks from the first phases of the LIBs production to subsequent assembly and use, to ensure the safety of both production and consumer during processing and use. Indeed, even if these parameters are already available for the respective micro-sized materials, the reduction in size can significantly influence the behavior. Finally, to evaluate the decrease in safety, the results obtained for NMs were compared with the available data of the respective micro materials, either from previous studies or from the ECHA dossier [122].

This part represents the preliminary study of a larger project funded in the framework of Saf€ra call. For this reason the results reported in this section will show a comparison between nano and micro results, and the conclusion serves as the first step for the subsequent phases of the project.

5.1. Materials and methods
5.1.1. Materials
5.1.1.1. NMs powders

The NM powders for the characterization, explosivity and eco-toxicity analysis have been purchased by MTI (United State of America) and Nanographenex (United Kingdom). Specifically from the Nanographenex were bought Natural

Graphite (C) Nanopowder/Nanoparticles (purity: 99.9 % size: 400 nm - 1.2 µm) [173], Silicon (Si) Nanopowder/Nanoparticles (purity: 98+ %, size: 40-60 nm) [174] and Vulcan XC72 Conductive Carbon Black (size: 30 nm) [175], while from the MTI were bought MesoCarbon MicroBeads (MCMB) graphite powder for Li-ion battery anode (50 nm) [176] and Titanate ($Li_4Ti_5O_{12}$) powder for Li-ion battery anode (10 nm) [177].

5.1.1.2. *Daphnia coltures*

The Daphnia organisms were cultivated at the INERIS toxicology department. The organisms are stored in a room at temperature and light controlled and in pools with ISO medium and with fresh nutrients every 24 h. Before the ecotoxicity tests the organisms were filtered to just the organisms younger than 24 h.

5.1.2. Methods

Both the explosivity behavior and the ecotoxicity impact for the NMs are strictly linked to the particle physical-chemical properties and to the dispersion conditions in which they are.

5.1.2.1. *Characterization of the NMs*

The NMs characterization was carried out on the pristine powder, on the NMs dispersed in water, after the dispersion treatment, and in the ISO medium, to understand how these conditions effect the intrinsic properties of the NMs.

5.1.2.1.1. Pristine NMs

The most important properties that must be evaluated for the pristine NMs are the granulometry, the specific surface area (SSA) and the density. For all these measurements there are standard regulations that can be applied to uniform the data obtained with the reference ones.

Qualification and size distribution measurement of particles, granulometry, can be evaluated following the ISO 13320:2020 [178]. The granulometry tests were performed with a HELOS-KR equipped with Quixel or Rodos dispersing units (Sympatec).

To determine the overall specific surface area of porous solids it is necessary to measure the amount of physically adsorbed gas (N_2) according to the Brunauer, Emmett and Teller (BET) method, following the ISO 9277:2010 [179]. The SSA tests were performed with a 3-Flex (Micromeritics).

Finally, the density can be evaluated correlating the quantities of technical gas adsorbed by the sample according to the ASTM B923-22 [180]. The density tests were performed with a Accupyc II 1340 (Micromeritics).

5.1.2.1.2. NMs dispersed in water and in ISO medium

The most important properties that must be evaluated for the NMs dispersed in a solvent, such as water or ISO medium are the zeta potential and the hydrodynamic size. In fact, these properties change significantly according to the solvent in which the NMs are dispersed.

The zeta potential and the hydrodynamic size analysis were performed with a ZetaSizer nano series Nano – ZS (Malvern). The results obtained were evaluated by the Malvern ZetaSizer software.

5.1.2.2. Explosivity and flammability risk of the NMs

The main parameters that can define the flammability and the explosivity severity of a material are the MIE, the MIT, the MEC and the deflagration index, calculated by the cube-root law, according to Equation (*26*). The tools used to determine the different explosiveness factors are reported in Section "1.7.2.2. Explosivity and flammability risk" in the Introduction.

The MIT can be evaluated according to the NF EN ISO/IEC 80079-20-2, *Explosive atmospheres – Part 20-2: Material characteristics – Combustible dusts test methods* [96]. The tests were performed in a Godbert-Greenwald furnace (Intertek), a constant temperature furnace, with 600 °C. The MIE can be evaluated by the Hartmann tube [95], called even MIKE, according to the standard references NF EN ISO/IEC 80079-20-2, *Explosive atmospheres – Part 20-2: Material characteristics – Combustible dusts test methods* [96]. The tests were performed in a MIKE 3 (Kuhner) with a

196

capacitor discharge spark as ignition source. The test consists in the evaluation of the ignition energy necessary for explosion, observing for a given powder concentration the flame propagation at least 6 cm away from the spark electrodes. Finally, the MEC and the explosivity factors, such as maximum explosion pressure (P_{max}), assessed the severity of the explosion, can be evaluated according to the NF EN ISO/IEC 80079-20-2, *Explosive atmospheres – Part 20-2: Material characteristics – Combustible dusts test methods* [96], and the NF EN 14034, *Determination of explosion characteristics of dust clouds*, in part 1, *Determination of the maximum explosion pressure pmax of dust clouds*, part 2, *Determination of the maximum rate of explosion pressure rise (dp/dt)max of dust clouds*, and part 3, *Determination of the lower explosion limit LEL of dust clouds* [98]. The tests were performed inside a 20-L sphere (Kuhner) and the electrical ignition source, placed in the center of the sphere, has an energy between 2 and 10 kJ according to the analysis .

5.1.2.3.   Eco-toxicity of the NMs

The ecotoxicity of NMs was evaluated by conducing in-vitro test on the *Daphnia magna*, to determine the NM-induced changes in cells. The tests were conducted according to the OECD TG 202, *Daphnia sp. Acute Immobilization Test* [110]. The ecotoxicological end point after the 48 h of test is the immobilization of the organisms that can be evaluated both visually and by microscope.

5.2. Results

The physical properties, the explosivity risk, and the eco-toxicity impact of the different NMs has been evaluated following the same standard procedures to highlight any significant differences between theme and with the relative material in the micro size.

5.2.1. Explosivity and flammability of the NMs

The flammability and explosivity parameters must be related to the main physical properties of the pristine materials, such as the particle size, as per ISO 13320:2020 [178], the SSA, as per ISO 9277:2010 [179], and the density, as per ASTM B923-22

[180]. The results obtained for the various materials at the different size are reported in Table 72.

Table 72: physical properties of the different materials at the micro and nano size.

Parameters	Size (d$_{50}$)	Granulometry (VMD)	Pycno gas (g/cm^3)	SSA (m^2/g)	VSSA (m^2/cm^3)
Micro-CB	17 μm	n.a.	n.a.	n.a.	n.a.
Nano-CB	40 nm	-	0.167	1142	190.71
Micro-C	17.79 μm	19.17 μm	2.3	0.7426	1.7080
Nano-C	3.86 μm	4.11 μm	2.4	9.6971	23.2730
Micro-LTO	2.46 μm	n.a.	n.a.	n.a.	n.a.
Nano-LTO	1.13 μm	1.78 μm	3.6	4.599	16.556
Micro-Si	25 μm	-	0.36	18.6	6.70
Nano-Si	40 nm	-	-	-	-

VMD: . Volume mean diameter. n.a.: not available on ECHA.

From the data reported in Table 72 it is possible to observe the main difference between the physical properties of the same material at the micro and the nano scale. The size of the material can be obtained by the d$_{50}$, so the diameter of the 50 % of the material, anyway, to classify the scale of the material other parameters must be evaluated, such as the VSSA. The VSSA value is obtained multiplying the specific surface area (SSA) and the porosity (pycno gas) and if the result is higher than 6 m^2/cm^3 the material under investigation can be considered a nano scale material. This parameter so permits to distinguish the nanomaterial from the micromaterials. The complete investigation of the materials permits to better correlate the physical-chemical properties with the explosivity risk and the flammability behavior, as an example the size can affect the interaction between the particles if released in atmosphere.

The main parameters, such as MIT, MIE, MEC, and K$_{st}$, that define the flammability and the explosivity were evaluated by the standard procedures. The results obtained for the materials at different size are reported in Table 73.

Table 73: flammability and explosivity parameters of the different materials at the micro and nano size.

Parameters	MIT_{cloud} (°C) MIT_{layer} (°C)	MIE (mJ)	MEC (g/m³)	P_{max} (bar)	$\left(\frac{dp}{dt}\right)_{max}$ (bar/s)	K_{st} (mbar/s)
Micro-CB [122]	600; > 450	> 1000	125	3	n.a.	6
Nano-CB	860; -	> 1000	60	7.6	248	67
Micro-C	760; > 410	> 1000	0	*	*	*
Nano-C	740; > 410	n.c.	80	7.1	234	63
Micro-LTO [122]	n.a.	n.a.	n.a.	n.a.	n.a.	n.a.
Nano-LTO	> 1000; > 410	> 1000	0	*	*	*
Micro-Si	> 1000; -	> 1000	135	7.9	249	68
Nano-Si	360; 390	3< MIE<10	n.a.	9.2	1389	377

n.a.: not available by ECHA dossier. n.c.: not conducted due to the conductivity of the powder. *: not conducted, due to the MEC=0.

From the parameters reported in Table 73 it is possible to observe the difference between the same material but with different sizes, micro and nano. The reduction of the size, from micro to nano in the majority of the case enhances the explosivity risk, as observed for the Si, the CB, and the graphite, while in the case of the LTO any comparison can be done. The main parameter that classifies the severity of the explosion is the K_{st}; if the value is 0 the explosion feature is nil, for values between 1 and 200 the feature is weak, between 201 and 300 is strong while when the valuer is higher than 300 the explosion feature is classified has very strong.

In the case of the Si and the CB the trend is similar, with an increase of the risk of explosivity anyway the extent of the variations is significantly different between Si and CB. In fact, for the CB passing from the micro to the nano size there is a decrease of 1 order of magnitude of the MEC and an increase of 1 order of magnitude for the K_{st}, anyway the severity of the explosion is always classified as weak (between 1-200 mbar/s). For the Si the passage from the micro to the nano shows significantly decrease of the MIE and the K_{st}. The minimum ignition energy for the micro-Si is higher of 10000 mJ while for the nano-Si is lower than 10 mJ, 3

orders of magnitude lower, and the severity of the explosion for nano-Si is not weak, as for the micro, but very strong (> 300 mbar/s).

In the case of the graphite the behavior between the micro and the nano size for similar regarding the ignition temperature, both for the material in cloud and in layer, while the explosivity parameters are significantly different. The temperatures obtained for the cloud are between 740 and 760 °C, while for the layer are higher than 410 °C, which is the limit temperature according to the standard procedure. Anyway the most significantly difference between the two size is in term of explosivity, in fact while the micro-C dispersed in the air does not generate an explosive atmosphere (ATEX) due to the MEC equals to zero, the nano-CB can caused a weak explosion, K_{max} equal to 63 mbar/s.

The comparison between the micro and the nano LTO is more complex due to the not availability of data for the microsize. The data relative to the micro-LTO are not available because according to REACH, Annex VII, column 2, the study does not need to be conducted if there are no chemical groups associated with explosive properties present in the molecule. The substance contains none of the reactive groups known to cause possibly explosive properties, therefore explosive properties of LTO are unlikely. Anyway, a similar trend has been observed for the nano-LTO, in fact, if dispersed in the air it does not generate an explosive atmosphere being the MEC equals to zero, and even the ignition temperature and energy are higher than 1000 °C and 3 mJ, indicating the thermal stability of the LTO material.

5.2.2. Eco-toxicity of the NMs

Ecotoxicity results also need to be related to the main physical properties of the NM, but in this case related to the NM dispersed in the ISO medium used for Daphnia testing. The characterization, such as hydrodynamic dimension and surface potential, according to ISO 22412:2017 [13], is performed on the ISO medium and compared with the initial SDS characteristics.

NMs are considered difficult materials, according to the definition reported in OECD TG 23 [113], therefore several pretreatment steps were performed to improve the stability of the dispersion in the ISO medium throughout the duration of the test. Usually, a sonication step in an ice bath is sufficient, however if the material has critical values another possibility to avoid agglomeration and sedimentation is the addition of humic acid to the ISO medium. Humic acid allows to obtain a greater dispersion and a higher stability of the suspension, due to the increase in the charge on the surface of the particles. Humic acid in this experiment was added to nano graphite and the best dispersion, expressed as Zeta potential (mV), is shown in Figure 79.

From Figure 79 it is possible to observe the significant difference between the zeta potential obtained without (Figure 79a) and with the addition of humic acid (Figure 79b). In the second case, the NM particles dispersed in the ISO solution showed higher stability than the particles in the ISO medium without humic acid. In fact, the closer the zeta potential distribution is to zero, the more unstable the suspension is, causing agglomeration and precipitation, while a value higher than 25, in absolute value, indicates greater stability of the particles in the medium.

By applying the different pretreatments, it is possible to achieve the improvement of the physical characteristics of the ISO medium solution with the dispersed NMs. The parameters evaluated are both cumulative, such as the Z-average size and the polydispersity, the so-called polydispersity index PdI, and the size of the distribution, all expressed as particle diameter in nm (d.nm), and the Z-potential, expressed in mV, reported in Table 74.
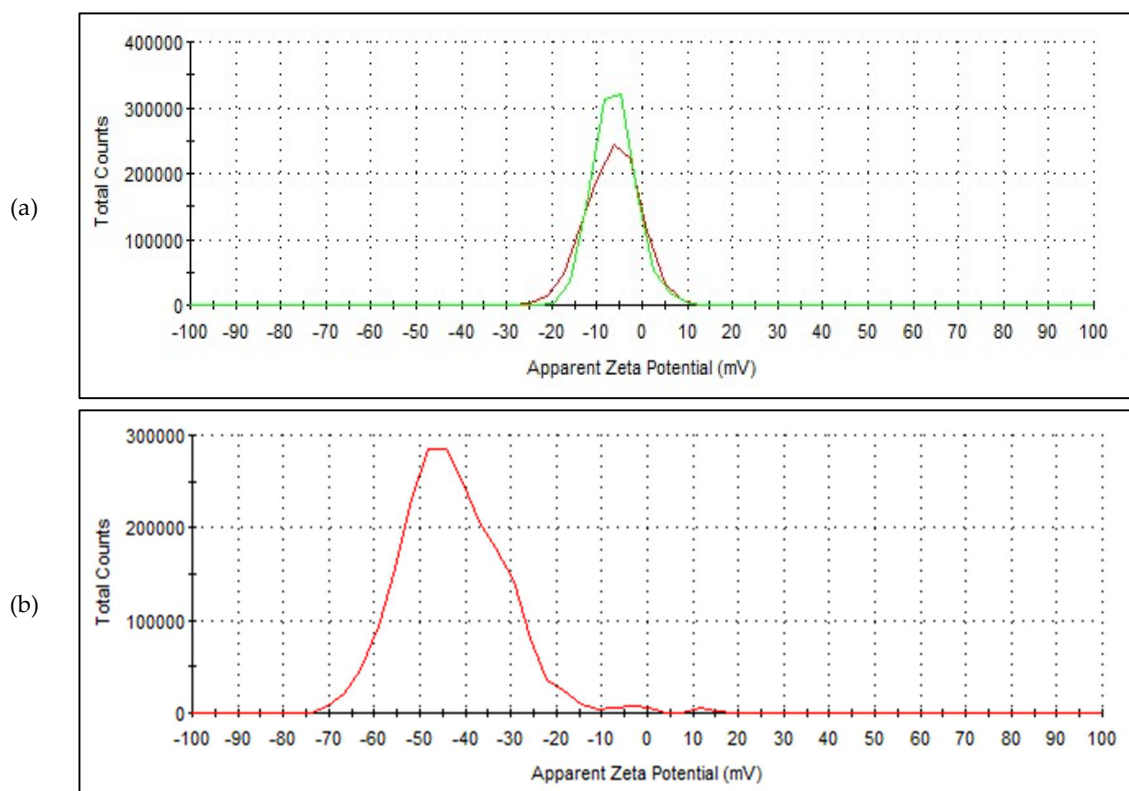
Figure 79: Zeta potential distribution for nano-graphite: (a) without hummic acid; (b) with hummic acid.

Table 74: hydrodynamic properties of the ISO medium solution with the different NMs.

Parameter	Size (d_{50})	Z-average (d.nm)	PdI (d.nm)	1st peak (d.nm)	Z-potential (mV)
Micro-CB [122]	17 µm	n.a.	n.a.	n.a.	n.a.
Nano-CB	40 nm	1657 ± 393.9	0.888 ± 0.158	147.75 ± 62.15	-19.30 ± 0.0577
Micro-C	17.79 µm	1533	0.846	629.6	-42.6
Nano-C	3.86 µm	5820 ± 1105	1.000 ± 0.0	271.45 ± 40.94	-24.8 ± 0.854
Micro-LTO [122]	2.46 µm	n.a.	n.a.	n.a.	n.a.
Nano-LTO	1.13 µm	2393.0 ± 365.4	0.385 ± 0.039	1501.00 ± 186.68	-4.37 ± 0.205
Micro-Si [122]	n.a.	n.a.	n.a.	n.a.	n.a.
Nano-Si	40 nm	690.8 ± 9.457	0.287 ± 0.039	951.17 ± 17.13	-14.5 ± 0.700

n.a.: not available by ECHA dossier.

From these results of the Z-average, the PdI, and the first peak it is possible to obtain information on the mono or polydispersity of the sample. In fact, if the Z-average is lower than or similar to the first peak, the sample can be considered monodisperse while a higher value represents a polydisperse sample. The PdI also returns information on dispersion, and if the value is greater than 0.5 the solution can be considered with a wide size distribution. The information are useful for the

better knowledge of the behavior of the materials when dispersed in the ISO medium, however, it is possible to observe from Table 74 that this information is normally not available. For the materials tested the nano-Si and the nano-LTO showed a monodispersity of NMs in the ISO medium, with a PdI lower than 0.5, and the Z-average like the first peak of the size distribution, while nano-C and nano-CB showed a broad size distribution, with PdI around 0.8 and a significantly difference between the Z-average and the 1st peak values.

Comparing the dimensional values reported in the SDS with the Z-averaged values, significant differences between them are noted, and this is due to the solvation and agglomeration of the particle in the medium. Therefore, even if the pristine material had nanometric dimensions after pretreatment in the ISO medium the dimensions increased significantly, for example for the CB the size went from 30 nm to 1657 nm (equal to 1.657 µm). For this type of alteration, the ecotoxicity results must always be correlated to the ISO characteristics of the medium and not just the original ones. The Z-potential, however, returns information on the surface charge of the particles, and therefore the repulsive force between them. If the values are higher than 25, in absolute value, the repulsion between the particles in the solution is high and therefore they are stable. And this value, as shown before, can be improved by external addition of organic solvents or humic acid.

Another possibility is also to increase the contact surface between the NMs and the Daphnia. Ecotoxicity tests are usually performed in tubes but to increase contact the tubes can be replaced with Petri dishes, as shown in Figure 80 for the CB.

Figure 80: eco-toxicity tesst for CB in the: (a) tube; (b) petri dish.

Using Petri dishes instead of tubes reduces the effect of CB sedimentation on the bottom of the tube which could cause an alteration of the immobilization values. In fact, the Daphnia could be brought to the bottom by precipitation causing mechanical immobilization and not by biological interaction with the NM. The different impacts of the NMs on the Daphnia after 48 h are shown in Figure 81, where Daphnia after different tests condition are compared.
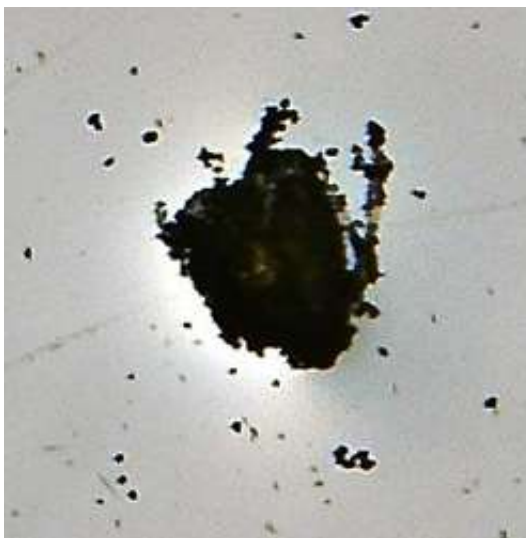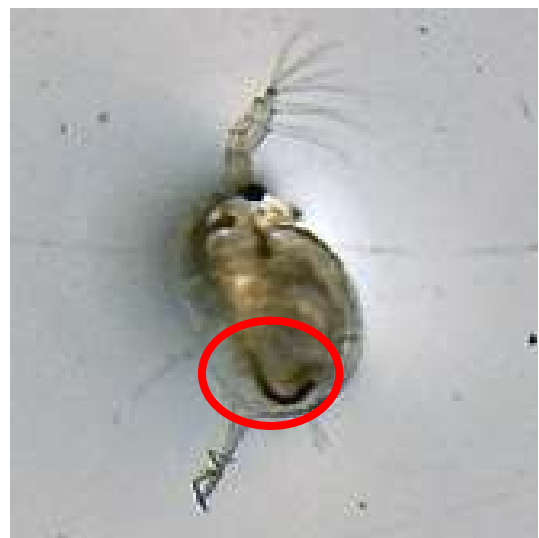
Figure 81: Daphnia after 48 h: (a) mechanical effect of the NMs; (b) biological interaction of the NMs.

Figure 81a shows the mechanical effect, therefore the Daphnia completely covered externally by the NM while in Figure 81b the biological interaction between the internal organism of the Daphnia and the NM, circle in red.

After 48 h of testing, according to OECD TG 202 [110], the ecotoxicity endpoint for each concentration can be assessed by imaging. The toxicology endpoint of Daphnia is immobilization, therefore the inability of the organism to move through the tube or Petri dish. All those movements that allow you to reach two distinct points are considered movement, while the movement of the antennas alone is not considered sufficient. By calculating the number of daphnia immobilized for each concentration it is possible to obtain the dose-effect curve and therefore the related ecotoxicity parameters, such as NOEC, EC_{50}, and EC_{100}, as reported in Table 75.

Table 75: eco-toxicity parameters for the different materials.

Parameter	NOEC (ppm)	EC_{50} (ppm)	EC_{100} (ppm)
Micro-CB [122]	3200 (24 h)	> 5600 * (24 h)	n.a.
Nano-CB (tube)	3.75 < NOEC < 7.5	7.5 < EC_{50} < 15	> 30 *
Nano-CB (Petri dish)	7.5 < NOEC < 15	15 < EC_{50} < 30*	> 30 *
Micro-C	220 < NOEC < 1000 *	220 < NOEC< 1000 *	> 1000 *
Nano-C	100 < NOEC < 220	220 < NOEC< 1000 *	> 1000 *
Micro-LTO [122]	100	> 100 *	n.a.
Nano-LTO	245.8 < NOEC < 307	384 < EC_{50} < 480	> 600 *
Micro-Si [122]	n.a.	n.a.	n.a.
Nano-Si	> 1000 *	> 1000 *	> 1000 *

n.a.: not available by ECHA dossier. *: maximum concentration tested.

In Table 75 are reported the eco-toxicity parameters obtained from the NMs with those for the micromaterials indicated in the ECHA dossier, when available. The comparison between the concentration values obtained experimentally and the concentration values indicated in the ECHA is not always possible because some data are not reported in the dossier. The reason is given by the fact that 100 ppm is usually considered as eco-toxicity limit, beyond this concentration if no effects are observed, so NOEC > 100 ppm, the substance can be considered non-toxic, as in the case of the micro-LTO where 100 ppm is the maximum concentration tested. Otherwise, if some effects are observed the concentration values tested can be higher than 100 ppm to define at least the EC_{50} or even the EC_{100}.

The difference between the concentration values for the nano and the micro size in the case of the graphite is not too evident although present. In fact, the NOEC is observed in a lower range of concentration for the nano, between 100 and 220 ppm, compared to the micro, between 220 and 1000 ppm. The other parameter, especially the EC100 are instead observed in the same range. These evaluations shown an increase of the eco-toxicity with the decreasing of the material size.

The opposite behavior has been observed in the case of the LTO, in fact the NOEC for the nano-LTO it was identified among 245.8 and 307 ppm while for the micro-LTO it was identified at 100 ppm. In any case, the following parameter, the EC_{50}, was identified in a very close range of concentrations, between 384 and 480 ppm. This indicates that although the NOEC is higher than for the micro material, the eco-toxicity increases sharply for the nano material.

The results obtained by the nano-Si can not be compared with the micro-Si, anyway the nano material did not show any eco-toxic effects during the tests on the daphnia. In fact, all the parameters are higher than 1000 ppm and as said before usually the limit for the nom-toxicity of the material is fixed at 100 ppm, so 1 order of magnitude lower compared to the nano-Si concentrations.

The most interesting data in term of eco-toxicity are observed by CB, where a significantly decrease of the concentration values indicated an increase of the eco-toxicity of the NMs. Nevertheless, some clarifications must be made regarding the data indicated by ECHA and reported in all SDSs for CBs. The values reported refer both to the tests conducted following OECD TG 202 but since CB is classified as a difficult material, according to the TG 23, the tests were conducted for 24 hours, and not 48 hours, and the daphnia were not placed in the solution containing the different concentrations of dust but in a previously filtered solution, and therefore free of material dust. So, the comparison between the data reported in the ECHA dossier and the experimental data is not possible. Anyway, comparing the data obtained for the nano-CB with the other nano materials it is

possible to observe a drastic reduction in concentrations especially related to NOEC and EC$_{50}$. In fact, both the NOEC and the EC$_{50}$ for the nano-CB were identified between 3.75 and 15 ppm, concentration values lower than the other values by 1 if not 2, in the case of Si, orders of magnitude. Comparing the two conditions investigated, powder dispersed in the tube or in the Petri dish, it is possible to observe a slight decrease in concentrations in the tubes. For this reason additional tests were done to identify the EC$_{100}$ value. This value was not included in the table as it was obtained from a different study and therefore with another stock solution, even though the tests were conducted in the same conditions and according to the same regulation. The EC$_{100}$ value obtained from this second experiment appears to be between 20.66 and 45.45 ppm.

5.3. Discussion

The most studied active materials for the anode, to improve the performance of LIBs, are nano-Si, nano-LTO and nano-graphite, while nano-CB can be used as an additive to increase their conductivity.

The characterization of NMs, both as original materials and as materials dissolved in a medium, is useful for having more precise information on the physical properties that influence the risk of explosiveness and eco-toxicity. Physical properties can be expressed in terms of d$_{50}$, diameter of particles in pure powder, and Z-mean, hydrodynamic diameter of particles dispersed in a medium.

In terms of explosive risk, numerous parameters were assessed, such as MEC, P$_{max}$ and K$_{st}$, according to the relevant standard procedures. By reducing the size of the material, from the micro size to the nano size, a significant increase in the severity of the explosivity was observed related to a lower concentration required for initiation, MEC. This behavior is increasingly evident from CB, to Si up to the extreme case of graphite. In fact, for the CB the severity of the explosion is classified as weak for both dimensions while for the Si as the dimensions decrease the severity goes from weak to very strong. For graphite, the micro material does

not have explosive behavior while the nano one showed a weak explosive severity related to a low concentration of material, 80 g/m^3. Both nano and micro LTO, however, due to the absence of chemical groups associated with explosive properties in the molecule, showed a zero risk of explosivity.

Also in terms of ecotoxicity, the most significant results were obtained from the tests conducted on nano-CB. In fact, for the ecotoxicity parameters, such as NOEC and EC50, a very low concentration was observed, between 3.75 and 15 ppm, compared to the concentration ranges observed for the other nanomaterials, from 100 to over 1000 ppm. The main physical property that must be evaluated for the stock solution containing NMs is the Z-mean of the particles. In fact, the interaction between the particles and the ISO medium can create, depending on the specific surface and the surface forces, an agglomerate with a larger diameter than the original material and/or the deposition of the material, thus reducing the suspension of the NM in solution. This behavior was observed for the NMs under examination and in fact the Z-average of the particle in the ISO medium also increases by 2 orders of magnitude compared to the initial material, as for the nano-CB which went from 40 nm to 1657 nm in the medium ISO. In any case, the attractive and repulsive forces are also present in the real case of release into water and therefore the results obtained evaluate the impacts of NMs on the environment, as the physical properties of the medium vary.

So, the reduction in size therefore resulted in an increase in the severity of the explosion and simultaneously a reduction in the concentration needed to observe an ecotoxic effect on the organism in the aquatic ecosystem.

6. Investigation on effective fighting technology for LIB fire

The fire tests were conducted on Kokam SLPB. The tests were performed to determine the effective fighting technology for LIB fire of three different agents, i.e., water mist, F-500, and CO_2, and the chemical composition of the solid and liquid residues after the extinction in terms of VOCs and metal, by SPME-GC-MS and ICP-OES analysis.

6.1. Materials and Methods

6.1.1. Materials

6.1.1.1. Li-ion cells

The fire tests were conducted on Kokam lithium- ion pouch (Li-Po) battery Superior Lithium Polymer Battery (SLPB), as reported in Table 7.

6.1.1.2. Extinguishing agents

The extinguishing agents for the fire test were provided by ENEA (Italy). The three extinguishing agents were two water-based, water mist and F-500 water additive 2 % (v/v) [137], and one gaseous, CO_2, as shown in Figure 82 According to the physical state and the drops size the lance are different, as shown in Figure 19.

| (a) | (b) | (c) |
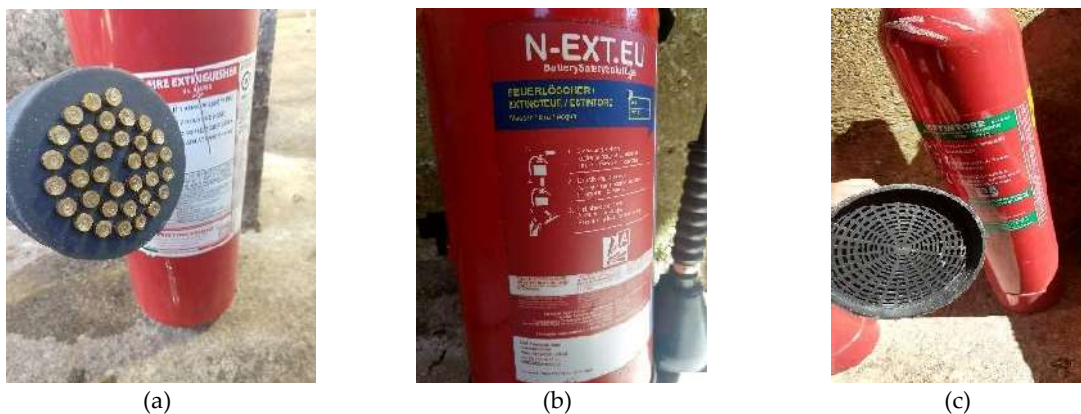
Figure 82: extinguishing agents: water mist (a); F-500 water additive 2 % (v/v) (b); CO_2 (c).

6.1.2. Methods

6.1.2.1. Fire test

The fire tests were carried out in an open space surrounded by perimeter walls and protective mesh as a ceiling to minimize the risk of projection of solid fragments. The cell was placed on a grate placed over a propane flame burner, as shown in Figure 83. Specifically, the fire tests were carried out following the

following phases: (i) the cell was positioned in the center of a metal grid placed above a propane burner (7.5 kW), (ii) two TCs were fixed on the upper surface of the cell, (iii) the propane flame was lit, (iv) an extinguishing agent was applied, i.e., water mist, F-500 water additive 2 % (v/v) and CO_2, after the catastrophic failure of the cell occurred, for 10 s. The propane burner was turned off once cell venting was observed. A tank was positioned below the metal grid to collect the liquid residues after each fire test.

Figure 83: fire test system.

From the combination of the temperature, acquired by the two TCs placed on the surface of the cell, and the video, recorded by a high-speed camera, the surface temperature of the cell and the relative ignition, vent, flame, catastrophic failure times were obtained. At the end of each test, both the solid samples, the burnt Li-ion cell, and the liquid samples, the extinguishing agent collected in the tank, were taken for subsequent analyzes to determine the chemical composition of these samples.

6.1.2.2. Characterization of liquid and solid residues after the fire test

Both the solid and the liquid residues were collected to determine the chemical composition by different analytical techniques, such as the GC-FID, the SPME-GC-MS, and the ICP-OES.

6.1.2.2.1. GC-FID method

The analysis on liquid samples, the extinguishing agent collected in the tank after the extinction, was carried out by GC-FID, according to the EPA method 8015D [145] to identify and eventually quantify the following compounds: benzene, toluene, ethylbenzene, m-xylene, p-xylene, and o-xylene (BTEX).

A Perkin Elmer Clarus 500GC with autosampler and coupled with an FID was used for the analyses. The column used was a StabilWax-DA - Restek (30 m x 0.25 mm i.d. x 0.25 μm). For each test 1 mL of liquid residue was aliquoted in 1.5 mL vials, without pre-treatment. A standard solution which contains 200 μg/ml of benzene, toluene, ethylbenzene, m-xylene, p-xylene, and o-xylene in methanol (BTEX, Restek), was used as standard to obtain the retention time (t_R) of each compound, the calibration line, and the limits of quantification (LOQ) and LOD. The GC-FID analysis method was performed with helium as the carrier gas with a flow rate of 1 mL/min. The injector was set at 200 °C and 1.0 μL of sample was injected with a split ratio of 70:1. The analysis involves a programmed temperature: from 100 °C (2.5 min) up to 200 °C (10 min) with a heating rate of 30 °C/min. The detector was set at a temperature of 270 °C.

6.1.2.2.2. SPME-GC-MS method

To identify and quantify the VOCs in the solid and liquid samples, analysis was carried out by GC-MS according to the EPA 8260D method [146]. For this analysis the samples do not require a pre-treatment process and are extracted by SPME, according to the EPA 5012A method [147, p. 501].

An Agilent Technologies 7890B GC System was used for analysis, with an EST (Flex) analytical autosampler coupled to an Agilent 5977B GC/MSD. The column used was a HP-5MS Agilent Technologies Inc. (30 m x 0.25 mm i.d. x 0.25 μm). For each test 10mL of liquid residue and 5 g of solid residue were aliquoted in separate 20 mL headspace vials. In addition, an ISTD, was added to all samples prior to the analysis, specifically 3 μL for the solid samples and 10 μL for the liquid samples of BTEX (Restek). The extraction method was based on SPME,

using a 100 μm polydimethylsiloxane (PDMS) fiber (Supelco), which allows adsorption of non-polar compounds. At the beginning of each analysis session the PDMS fiber was conditioned for 30 min at 200 °C. Before the analysis in GC-MS, the samples were subjected to heating in a heated oven maintained at a temperature of 75 °C for 15 min and subjected to stirring. The fiber was then exposed in the headspace of the samples for 15 min at 75 °C. The operating conditions of the gas chromatograph were the transfer line at 250 °C and helium as the carrier gas. The analysis involves a programmed temperature: from 45 °C (3 min) to 250 °C (10 min) with a heating rate of 1 °C/min, for a total run of 33 min. The mass spectrometry works in EI mode at 70 eV and the source was maintained at a temperature of 230 °C. The mass spectra were acquired in scan mode, with m/z between 40 and 400. The mass spectra were compared with the NIST library.

6.1.2.2.3.   ICP-OES method

The procedure applied is the same reported in section Electrode's characterization, according to the EPA 200.8-1 method [148, p. 200].

6.2. Results

In Table 76 are reported the fire test code with the relative conditions, such as Kokam cell capacity and extinguishing agents applied.

Table 76: Experimental test conditions and relative test code.

Test code	Li-ion cell	SOC (%)	Burner	Extinguishing agent
K25-W	Kokam 25Ah	100	Propane	Water mist
K25-F5	Kokam 25Ah	100	Propane	F-500
K25-CO$_2$	Kokam 25Ah	100	Propane	CO$_2$
K40-W	Kokam 40Ah	100	Propane	Water mist
K40-F5	Kokam 40Ah	100	Propane	F-500
K40-CO$_2$	Kokam 40Ah	100	Propane	CO$_2$

From the combination of the temperature, acquired by the two TCs placed on the surface of the cell, and the video, recorded by a high-speed camera, the surface temperature of the cell and the relative time for the key events, such as ignition, venting, catastrophic failure and extinguishing application were obtained. At the end of each test, both the solid samples, i.e., the burnt Li-ion battery, and the

liquid samples, the extinguishing agent present inside the tank, were collected for subsequent analyzes to determine the chemical composition.

The tests were conducted for each chemical composition and here is reported the data obtained for Kokam 25 Ah (K25) extinguished with CO_2 to shown how the temperature values has been obtained and the residues has been analyzed.

6.2.1. Fire test on Kokam 25 Ah extinguished with CO_2 (K25-CO_2)

Figure 84 shown the key events of the test conducted on the K25 extinguished with CO_2 extinguishant (K25-CO_2): (a) the propane flame was lit, (b) the venting of the gas/vapor, (c) the catastrophic failure of the cell, (d) fist application of the CO2 extinguishing agent, (e) cooling of the system, (f) second application of the CO2 extinguishing agent, (g) cooling of the system, (h) first application of the water mist extinguishing agent, (i) cooling of the system, (l) samples collection.

Under continuous heating (Figure 84a) the internal pressure of the LIB increases leading to the opening of the zone with a lower resistance seal and the venting of the gas/vapor (Figure 84 b). The venting phase is characterized by swelling of the cell followed by an explosion and spraying of a large amount of white aerosol mainly consisting of the electrolyte solution, which ignites instantly. Due to the exothermic reaction, the temperature increased becoming more dramatic and involving the whole system, causing the catastrophic failure of the cell (Figure 84c). The first application of the CO_2 agent was applied immediately for 10 s and the flame was extinguished (Figure 84e). Anyway, monitoring the temperature registered by the TCs was possible to notice an increase of the temperature, so a second application of the CO_2 agent was applied for 10 s (Figure 84f) and the system was leave on the grid (Figure 84g) to cool it but again the temperature increased so a third application was applied but with the water mist agent (Figure 84h). After this third application the system temperature dropped to below 100°C (Figure 84i) and them the solid residue was collected for the subsequent analysis (Figure 84l).

(a) ignition at 0 s

(b) venting at 10 s
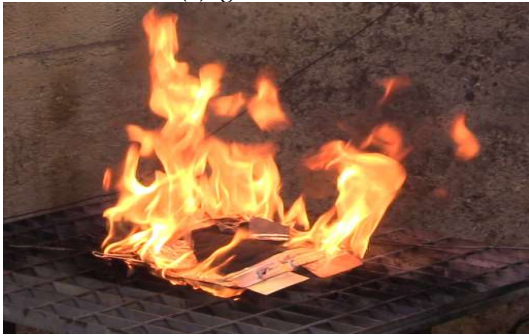
(c) catastrophic rupture at 40 s

(d) first extinction at 40 s

(e) post first extinction 50 s

(f) second extinction 115 s

(g) post second extinction 125 s

(h) third extinction 175 s

(i) post third extinction 185 s
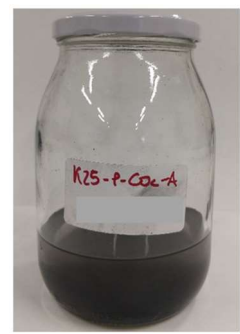
(l) sample collection

Figure 84: key events for K25-CO₂ fire test.

6.2.1.1.   K25-CO₂: Extinguishing agent efficiency

In Figure 85 is reported the temperature profile registered by the TCs on the cell surface, and the extinction events are label.
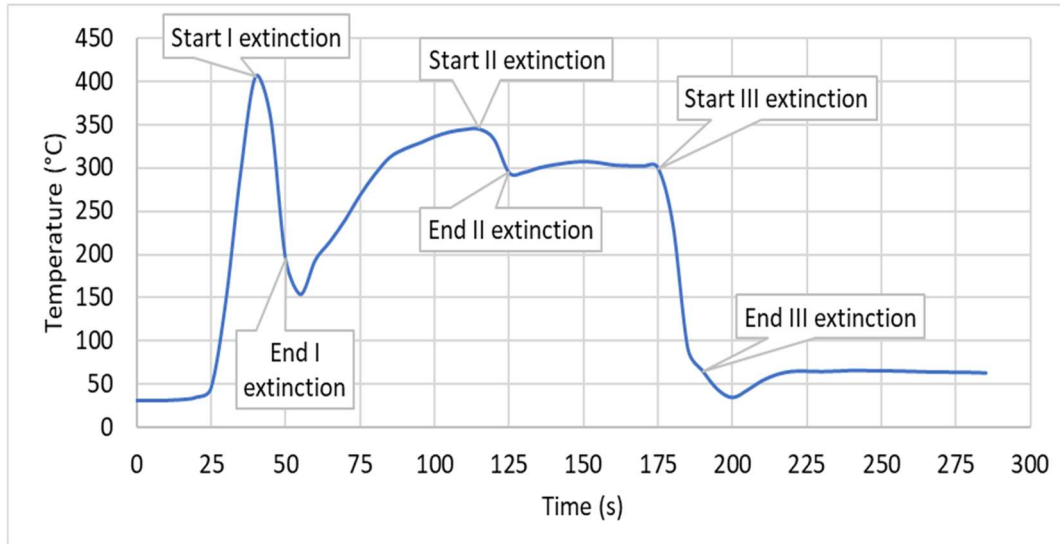
Figure 85: temperature profile (°C) for the fire test on K25-CO₂.

From Figure 85 it is possible to identify the time and the relative temperature of the key events occurring during the fire test, such as venting, catastrophic rupture, and extinction phases, as reported in Table 77.

Table 77: time (s) and temperature (°C) of the key events for the fire test on K25-CO₂.

Events	t (s)	T (°C)
Initial	0	29
Venting	10	35
Catastrophic rupture	40	406
Start I extinction	40	406
End I extinction	50	195
Start II extinction	115	345
End II extinction	125	295
Strat III extinction	175	300
End III extinction	185	91

It is important to underline that in the fire tests conducted with CO_2 as an extinguishing agent, three extinguishing steps were necessary: two with CO_2 and one at the end with water mist to definitively cool the system. This because in the case of CO_2 the temperature after the application did not reach temperature similar to the environmental one and it is not maintained over the time. In fact, after the two-extinguishing application with CO_2, a rise in temperature is observed

in a short time. After the first extinguishing application, a minimum temperature of 195 °C at 50 s is recorded, but then in about 60 s the temperature increases up to a maximum of 345 °C. The same behavior is observed in the second extinguishing phase, where a minimum temperature of 295 °C at 125 s is reached and then rise to 300 °C in 50 s. The third phase, with water mist, allows instead to lower the temperature below 100 °C and to maintain it in the time. From the data reported in Table 77 it is possible to calculate the cooling rate v_c, according to Equation (28), for the CO_2 extinguishing agent. The various extinguishing phases have the following cooling rate: 21 °C/s, 5 °C/s, both for CO_2 application and 21 °C/s, respectively for water mist.

Another important aspect that must be considered, especially for the safety of the rescue team, is that after the extinguishing the temperature increase is not linked to a reappearance of the flame or to a significant increase in the vapors and/or gases emitted, as shown in Figure 84e and Figure 84g. Therefore, CO_2 has only a surface cooling effect as recorded by the IR thermal imaging camera, shown in Figure 86.

So, after the first and the second application the temperature rises rapidly, and this can pose a great risk in terms of toxic emissions and heat propagation. The increase in temperature is due to the exothermic reactions that inside the battery.
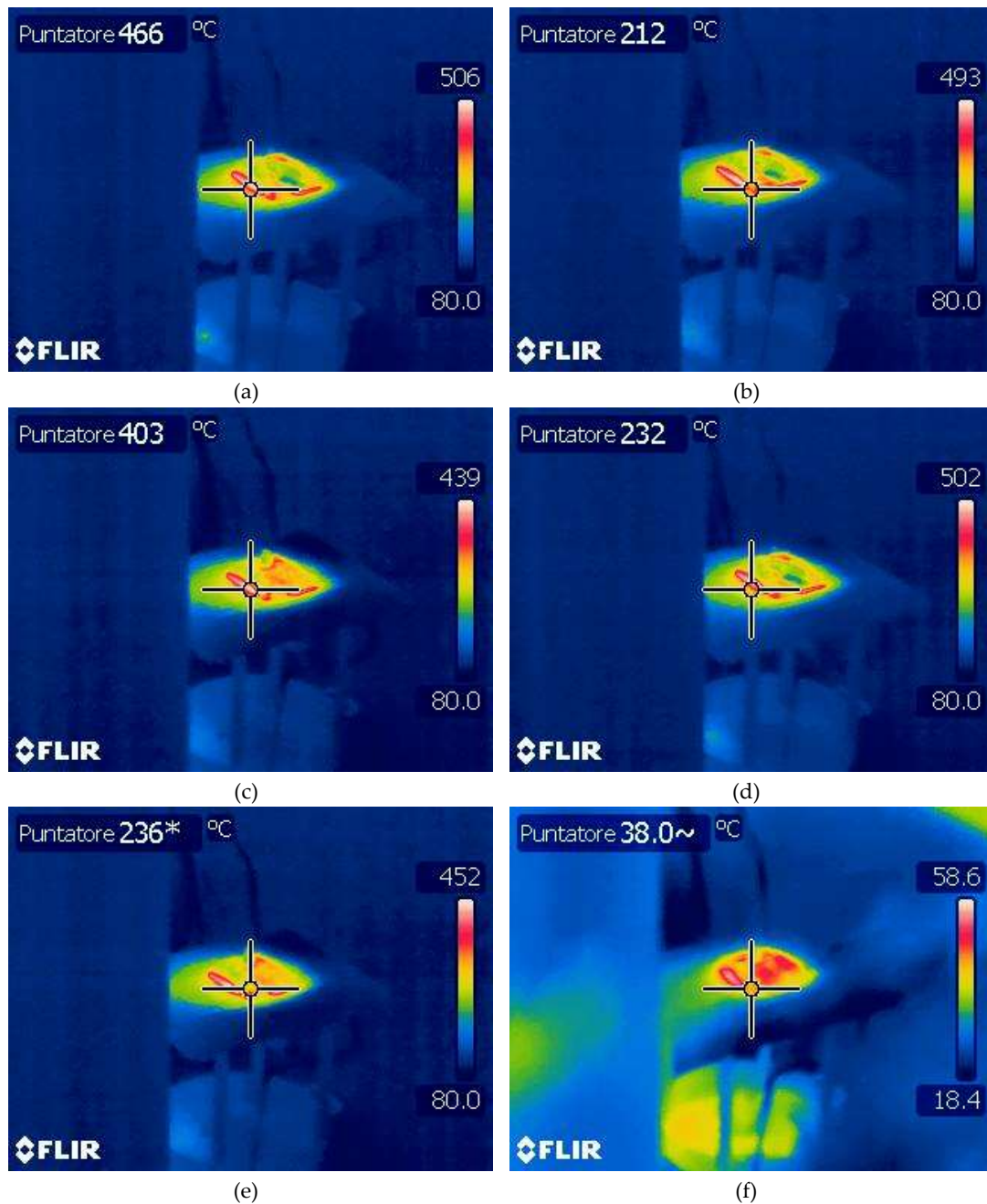
Figure 86: thermal images of K25-CO₂: start (a) and end (b) of I extinction phase, start (c) and end (d) of II extinction phase, start (e) and end (f) of III extinction phase.

6.2.1.2. K25-CO₂: Characterization of the residues

Another safety aspect that must be considered is even the impact on the human health and the environmental of the residue. Once the system reached a safety temperature, solid residue has been collected. In Table 78 are reported the weight of the cell after the test (g), the humidity of the sample (%), the weight of the dry cell after the test (g), the weight loss, indicated with the term Δcell and expressed

in g, calculated considering the initial weight of 555 g for K25, and the volume of liquid collected by the tank, expressed in ml.

Table 78: Residues weight (g) after the fire test on the K25-CO₂.

Weight cell pretest (g)	Weight cell posttest (g)	Humidity of sample (%)	Dry weight cell posttest (g)	Δcell (g)	Volume liquid (ml)
555	463.30	31.00	319.68	235.32	1092.02

The lost in weight, 235.32 g, is given both by the evaporation of the electrolyte, around 60.49 g for the K25, as obtained by the characterization of the Kokam cells, and the emission of gases and solid particulate.

The residue were analyzed according to the SPME-GC-MS (EPA 5012A [147] and EPA 8260D [146] methods) and ICP-OES (EPA 200.8-1 method [148, p. 200]).

The VOCs in the residues were identify and quantify by SPME-GC-MS analysis and the results are reported in Table 79 for the solid, expressed in ppm, and in Table 80 for the liquid, with the respective retention time (t_R) expressed in min.

Table 79: VOCs identified in the solid sample or the fire test K25-CO₂ with the t_R (min) and the quantification (ppm).

Compound	t_R (min)	K25-CO₂
1-butanol	2.24	1581
2,4-dimethyl-1-heptene	4.91	5439
undecane, 2,2-dimethyl	7.16	434
terephthalic acid	16.58	1397

The compounds belonging to the hydrocarbon class are underlined.

Table 80: VOCs identified in the liquid sample or the fire test K25-CO₂ with the t_R (min) and the quantification (ppb).

Compound	t_R (min)	K25-CO₂
1-hexanol, 2-ethyl	7.64	1.1
nonanal	8.55	1.2
1-decanol	10.28	4.0
biphenyl	11.38	74
phenanthrene	14.71	0.8

The compounds belonging to the hydrocarbon class are underlined.

The low number of VOCs identify can be due to the application for two times of a gases extinguisher and then of a water based one. These operations favor the removal of the VOCs from the solid decreasing the numbers and the quantities.

Regarding the liquid the low quantities can be due to a lower affinity between the VOCs and the water.

To identify and quantify the metals the analysis was carry out by ICP-OES. The metal concentrations in the solid and liquid samples are reported in Table 81.

Table 81: Metals concentrations (ppm) in the solid and liquid sample of the fire test K25-CO₂.

ppm Sample	Co	Cu	Li	Mn	Ni
Solid	1356 ± 723	3491 ± 239	6305 ± 386	1030 ± 163	3434 ± 205
Liquid	85 ± 9	20 ± 2	58 ± 6	49 ± 5	127 ± 11

The concentrations values can be traced back to the percentages of metals present in the initial Kokam cell, as obtained by the characterization of the electrodes. In fact, the anodic material including the copper metallic collector is about 43 % while the cathodic material instead represents about the 53 %. About the single metal the lithium is the most concentrated metal due to its presence into cathode material and in the electrolyte, as salt ($LiPF_6$), followed by the Cu, Ni and Co, while Mn is the less abundant. Even, for this results the lower concentration in the liquid can be attribute to the lower affinity of the metals in water.

From the quantification of both the VOCs and the metals it is possible to classify the waste in accordance with the HP code defined in the European Regulation N. 2008/98/CE [142] and reported in Table 5. The hydrocarbon class is regulated, and the limits and thresholds values for the relative codes varying according to the sample matrix. In fact, in solid samples the hydrocarbons are separated according to the number of carbons in C5-C8 and C11-C39 hydrocarbons while in liquid samples all C5-C39 hydrocarbons are considered together. The compounds belonging to the hydrocarbon class are underlined in Table 79 and in Table 80 and in this case no light hydrocarbons were identified, just heavy hydrocarbons. For this reason, in Table 82 is reported the total concentrations of the 10<C<40 hydrocarbons in comparison with the relative concentration limit. While the limit values for metals in waste, from European Regulation N° 2008/98/EC [142], refer

only to copper, expressed as $CuSO_4$, and nickel, expressed as $NiSO_4$, with different limit concentrations which, and therefore a different specific danger. The concentration of the different species and the relative limit values are compared in Table 82.

Table 82: concentration in the solid of the regulated compounds and relative concentration limit (ppm) for the purpose of danger according to the EU Regulation N. 1375/2014 [132].

Compound	Concentration (ppm)	Concentration limit (ppm) for the purpose of danger according to the EU Regulation N. 2008/98/EC [132]
Hydrocarbons 10<C<40	5873	250000 (HP14) threshold 10000.
Cu, as $CuSO_4$	**8129**	250000 (HP6) threshold 10000; 200000 (HP4) thresholds 10000; 250000 (HP14) threshold **1000**.
Ni, as $NiSO_4$	_9054_	1000 (HP7); 10000 (HP11); _3000_ (HP10); 10000 (HP5); 250000 (HP6) threshold 10000; 200000 (HP4) threshold 1000; 100000 (HP13); 250000 (HP14) threshold 1000.

The concentration values of the heavy hydrocarbons in the solid residue are under the threshold values of the HP14 code (eco-toxic), while for the metals analysis the comparison is more complexed, due to the higher number of codes and even the definition of the threshold limit. The Cu concentration exceed the threshold value of the code HP14 without anyway exceed the limit value for the purpose of danger according to the EU Regulation, while is under the threshold values of the code HP4 (irritant - skin irritation and eye damage), HP6 (acute toxicity). The Ni concentration value in solid sample, as reported in Table 82, exceed the threshold value of the HP4 and HP14 codes without anyway exceed the limit values, while the concentration limit of the HP7 (carcinogenic) and HP10 (toxic for reproduction) codes were exceed.

So, the solid sample must be classified with the following codes: HP5 and HP10. Therefore, the solid must be isolated and handled so that there are no material losses and disposed of in a manner compliant with the codes just identified.

The same evaluation must be done for the liquid residues, and the concentration of the different species and the relative limit values are compared in Table 83.

Table 83: concentration in the liquid of the regulated compounds and relative concentration limit (ppm) for the purpose of danger according to the EU Regulation N. 1375/2014 [132].

Compounds	Concentration (ppm)	Concentration limit (ppm) for the purpose of danger according to the EU Regulation N. 2008/98/EC [132]
Hydrocarbons 5<C<39	0.149	250000 (HP14) threshold 10000.
Cu, as $CuSO_4$	47	250000 (HP6) threshold 10000; 200000 (HP4) thresholds 10000; 250000 (HP14) threshold 1000.
Ni, as $NiSO_4$	335	1000 (HP7); 10000 (HP11); 3000 (HP10); 10000 (HP5); 250000 (HP6) threshold 10000; 200000 (HP4) threshold 1000; 100000 (HP13); 250000 (HP14) threshold 1000.

The concentration values of the heavy hydrocarbons in the solid residue are significantly lower than the threshold values of the HP14 code, while for the metals analysis the comparison is more complexed, due to the higher number of codes and even the definition of the threshold limit. Both for the Cu and Ni the concentrations in the sample are significantly lower compared to the threshold value of the respective codes, such as HP14, HP6, and HP4 for Cu and HP7, HP5, HP13, and HP11 for the Ni.

Therefore, liquid residues do not require any identification code according to the EU Regulation.

6.3. Discussion

The fire tests were conducted according to the scheme summarized in Table 76, under the same operating conditions, and the same analyzes were carried out. The comparisons of the various analyzes are reported below to understand how the extinguishing agent affects the temperature values during the extinction and the relative emissions composition. The first data are the one about the temperature profile, from the venting to the catastrophic rupture and the final extinction phase. Even the residues, both solid and liquid, were collected and analyzed to identify and quantify the VOCs and the metal to compare that results with the limits

established for waste by the European Regulation N. 1357/2014 to evaluate the environmental impact of wastes and the land remediation management, according to the identification HP code.

6.3.1. Comparison of the efficiency of extinguishing agents

In Figure 87 are reported the temperature profiles of the tests conducted of the K25 (a) and K40 (b) cells obtained with the three extinguishing agents, water mist (blue line), F-500 (orange line) and CO_2 (gray line).
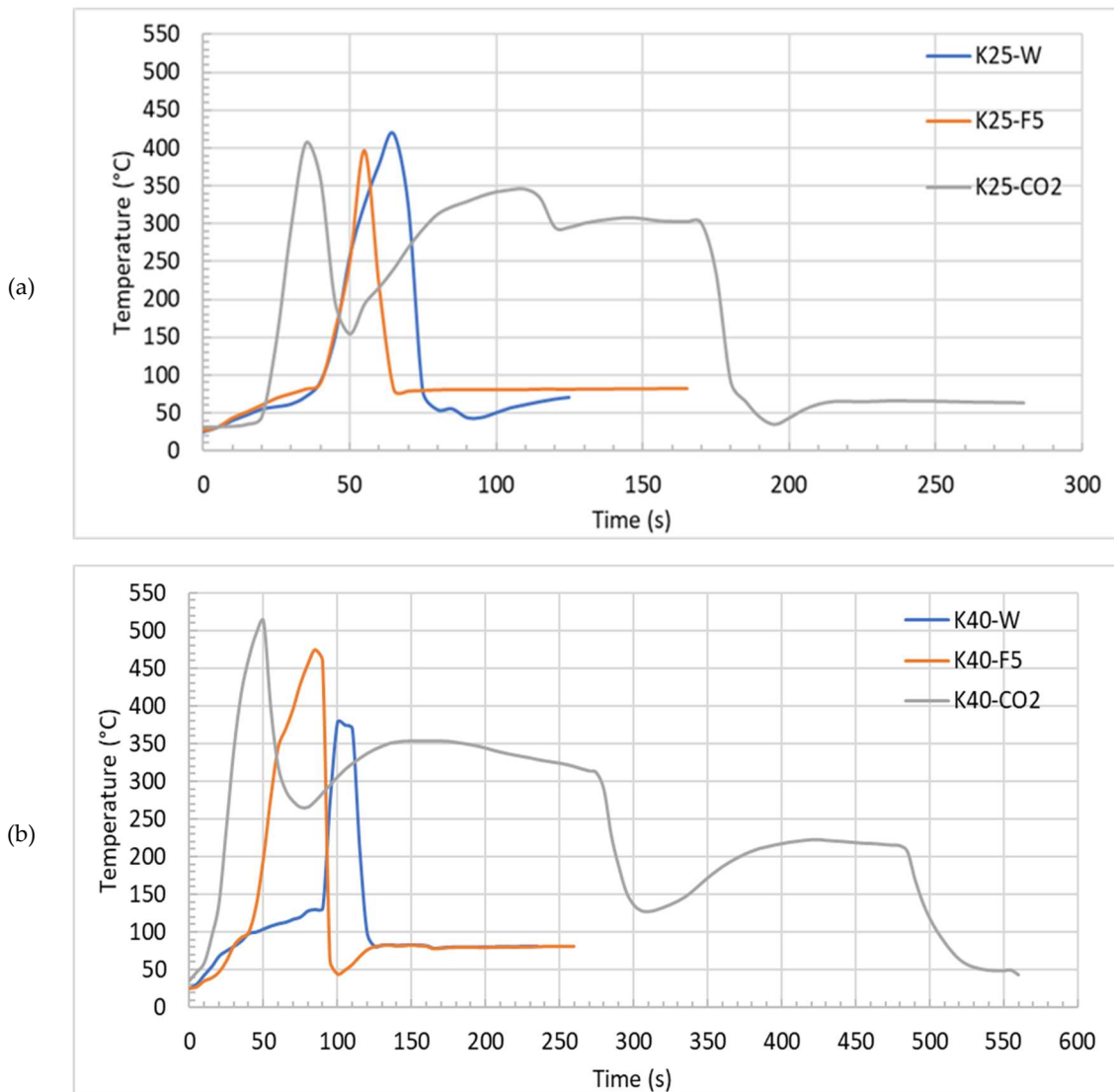

Figure 87:Temperature profile (°C) for fire tests on cells: (a) K25; (b) K40.

A similar behavior between the extinguishing agents used, regardless of the capacity of the cell, is observed. For both the K25 and the K40 the fire tests conducted with CO_2 needed three extinguishing applications, two with CO_2 and

one with water mist to definitively cool the system. The major events, in terms of time at which occur, and temperature reached, are shown in Table 84.

Table 84: Temperature (°C) of key events with temperature for each fire test.

T key events (°C)	K25-W	K25-F5	K25-CO$_2$	K40-W	K40-F5	K40-CO$_2$
T$_{initial}$	25	26	29	25	26	26
T$_{venting}$	150	89	35	132	100	31
T$_{catastrophic\ rupture}$	419	396	406	379	475	406
T$_{start\ extinction}$	419	396	406	370	459	512
T$_{end\ extinction}$	78	80	195	98	45	319
T$_{start\ extinction'}$	-	-	345	-	-	289
T$_{end\ extinction'}$	-	-	295	-	-	187
T$_{start\ extinction''}$	-	-	300	-	-	207
T$_{end\ extinction''}$	-	-	91	-	-	101

From the data reported in Table 84 it is possible to make some considerations both on the effect of the cell capacity, 25 and 40 Ah, and on the efficacy of the various extinguishing agents. To evaluate the effect of the capacity, it is necessary to compare the time of the key events, such as venting and catastrophic rupture. For the effectiveness of the extinguishing agents, on the other hand, the cooling rate and the temperature maintained at the end of the application of the extinguishing agent are evaluated. From the comparison of the data between the cells with different capacities, it comes that the average time and temperature to reach the venting are 32 s and 91°C for 25 Ah, while 47 s and 88 °C for K40. Even the average temperature for reaching the catastrophic rupture does not differ significantly, in fact 407 °C is reached in 53 s for the K25 and 420 °C in 82 s for the K40. Thus, the different capacities of the cells did not significantly affect the occurring of the venting and of the catastrophic rupture.

About the extinguishing agents, from the experimental data it emerges that the first significant difference between water-based and gaseous extinguishing agents lies in the number of extinguishing phases required. After, the effectiveness of the extinguishing agents can be evaluated by the cooling rate, v_c, calculated by the Equation (28). The values of the cooling rate s are reported in Table 85.

Table 85: Values of the cooling rate vc (°C/s) for the different fire tests.

Test code	v_c (°C/s)	$v_{c'}$ (°C/s)	$v_{c''}$ (°C/s)
K25-W	34	-	-
K25-F5	32	-	-
K25-CO$_2$	21	5	21
K40-W	27	-	-
K40-F5	41	-	-
K40-CO$_2$	19	10	10

Significant difference was observed in the cooling rate varying the agents, in fact, the rate changed from 30.5 ± 4.9 °C/s for water mist, 36.5 ± 6.4 °C/s for F-500 to a lower value of 20.0 ± 1.4 °C/s for CO$_2$, in reference to the first extinction. These values highlight a greater cooling ability and inhibition capacity of the water-based agents compared to the gaseous one.

The different in the effect can be explained both by the physical characteristic of the agents and the cooling mechanism. In fact, the water mist and the F-500 being liquid, sprayed in the form of micro-drops, can penetrate inside the cell, allowing internal cooling. The greater cooling effect of the F-500 on water mist is due to the F-500's ability to wrap the fuel elements of combustion in the micelles, inhibiting combustion and consequently the release of heat. Although CO$_2$ could suppress LIBs fire by suffocation, but it is not able to reduce the internal temperature of LIBs stopping the exothermic reactions inside. This is the reason why the heat capacity of carbon dioxide is such low that it cannot cool the battery down for a durable time.

So, the water-based have a faster and more effective cooling effect due to their ability to penetrate inside the cell, reaching temperatures below 100 °C after the first application but the higher cooling rate of F-500 is due to ability of encapsulating the fuel compounds.

6.3.2. Comparison of residues characterization

Once the system reached a safety temperature, solid and liquid residues have been collected. In Table 86 are reported the weight of the cell after the test (g), the humidity of the sample (%), the weight of the dry cell after the test (g), the weight loss, indicated with the term Δcell and expressed in g, calculated considering the initial weight of 555 g for the K25 and 835 g for K40, and the volume of the liquid samples (ml).

Table 86: Solid (g) and liquid (ml) samples collected after each fire test.

Test id	Weight cell posttest (g)	Humidity of sample (%)	Dry weight cell posttest (g)	Δcell (g)	Volume liquid (ml)
K25-W	446.90	24.00	339.64	215.36	184.96
K25-F5	488.46	20.00	390.77	164.23	298.00
K25-CO_2	463.30	31.00	319.68	235.32	1092.02
K40-W	755.66	28.00	544.08	290.92	482.51
K40-F5	639.50	18.00	524.39	310.61	158.47
K40-CO_2	681.50	31.00	470.24	470.24	n.c.

n.c.: not collected.

Weight loss increases with the increase of the capacity of the cells, in fact for the K25 there is an average loss of 204.97 ± 36.67 g while in the case of K40 the loss is of 322.10 ± 38.24 g. The lost is given both by the evaporation of the electrolyte, around 60.49 g for K25 and 180.01 g for the K40, as obtained by the characterization of the Kokam cells, and the emission of gases and solid particulate. While, the amount of liquid residue collected from the containment tank at the end of the tests varies significantly. This variability may be due to evaporation of the extinguisher and exit from the tank in the case of tests with water mist and F-500 while in the case of the test with CO_2 the final water has been applied in abundance to extinguish the fire.

Liquid samples were analyzed both by GC-FID to evaluate the presence of benzene, toluene, ethylbenzene, p-xylene, m-xylene and o-xylene (BTEX) and by SPME-GC-MS to determinate the VOCs.

From the analysis by GC-FID, in all samples the concentrations of BTEX are below the LOD, 200 ppb for benzene and 1 ppm for the other compounds, except in the sample K40-F5 which has a benzene concentration of 500 ppb. The limit values in waste for these substances, according to the European Regulation N. 2008/98/CE [142], are 100 ppm for benzene, 30000 ppm for toluene, $2.25*10^5$ ppm for ethylbenzene and $2.00*10^5$ ppm as the sum of the xylenes. The values obtained are significantly lower than the legal limits, so there is any classification.

While the SPME-GC-MS analysis, both on solid and liquid, shown an higher number of compounds and the identification and quantification are reported in Table 87 for the solid, expressed in ppm, and in Table 88 for the liquid, expressed in ppb, with the relative t_R expressed in min.

Table 87: Compounds identified in solid samples with their respective t_R (min) and quantification (ppm).

Compound	t_R (min)	K25-W	K25-F5	K25-CO$_2$	K40-W	K40-F5	K40-CO$_2$
1-butanol	2.24	n.d.	n.d.	1581	n.d.	n.d.	n.d.
2,4-dimethyl-1-heptene	4.91	n.d.	n.d.	5439	n.d.	n.d.	n.d.
1,3-propanediamine	7.14	99	n.d.	n.d.	89	n.d.	n.d.
undecane, 2,2-dimethyl	7.16	n.d.	n.d.	434	n.d.	n.d.	n.d.
1-hexanol, 2-ethyl	7.63	n.d.	725	n.d.	n.d.	147	n.d.
tetradecane	9.55	n.d.	494	n.d.	n.d.	413	n.d.
decane, 3-bromo	9.57	n.d.	n.d.	n.d.	176	n.d.	110
tridecane	10.55	n.d.	743	n.d.	n.d.	415	n.d.
biphenyl	11.40	n.d.	42030	n.d.	n.d.	n.d.	n.d.
octadecane	11.45	n.d.	1127	n.d.	n.d.	222	n.d.
undecane, 4,7-dimethyl	11.47	n.d.	n.d.	n.d.	n.d.	n.d.	389
biphenyl-ether	11.59	47	n.d.	n.d.	93	n.d.	n.d.
5-octadecene	13.06	n.d.	926	n.d.	n.d.	n.d.	n.d.
1,4-butanediol	13.10	56	n.d.	n.d.	n.d.	n.d.	n.d.
hexane, 3,3-dimethyl	13.12	n.d.	n.d.	n.d.	n.d.	n.d.	346
hexadecane	13.13	n.d.	1962	n.d.	n.d.	177	n.d.
undecane, 5,7-dimethyl	13.17	n.d.	n.d.	n.d.	250	n.d.	n.d.
heptadecane	13.83	n.d.	1027	n.d.	n.d.	n.d.	n.d.
isophthalic acid	14.93	1401	n.d.	n.d.	2434	3789	n.d.
terephthalic acid	16.58	n.d.	n.d.	1397	2264	n.d.	1949

n.d.: not detected. The compounds belonging to the hydrocarbon class are underlined.

Table 88: Compounds identified in liquid samples with their respective t_R (min) and quantification (ppb).

Compound	t_R (min)	K25-W	K25-F5	K25-CO$_2$	K40-W	K40-F5
octanal	7.32	0.2	n.d.	n.d.	n.d.	n.d.
1-hexanol, 2-ethyl	7.64	1.0	n.d.	1.1	2.1	n.d.
1-octanol	8.14	1.4	n.q.	n.d.	0.6	73
nonanal	8.55	0.4	n.d.	1.2	0.2	n.d.
hexanoic acid, 2-ethyl	8.62	0.2	n.d.	n.d.	0.5	n.d.
decanal	9.64	0.5	n.d.	n.d.	1.0	n.d.
1-decanol	10.28	6.8	444	4.0	4.4	1387
undecanal	10.63	0.1	n.d.	n.d.	0.2	n.d.
<u>biphenyl</u>	11.38	7.5	14	74	0.6	173
<u>tetradecane</u>	11.46	0.5	n.d.	n.d.	0.2	n.q.
biphenyl-ether	11.59	0.6	n.d.	n.d.	0.2	n.d.
acenaphthylene	12.07	0.4	n.d.	n.d.	n.d.	n.d.
<u>1-heptadecene</u>	12.24	n.d.	6.6	n.d.	n.d.	n.d.
<u>hexadecane</u>	13.13	n.d.	n.d.	n.d.	0.2	n.d.
<u>3-heptadecene</u>	13.83	n.d.	7.2	n.d.	n.d.	n.d.
<u>phenanthrene</u>	14.71	1.2	n.d.	0.8	n.d.	n.d.
1-octadecanol	14.56	n.d.	5.7	n.d.	n.d.	n.d.
hexadecanal	14.75	n.d.	9.6	n.d.	n.d.	14

n.d.: not detected; n.q.: under the limit of quantification (LOQ). The compounds belonging to the hydrocarbon class are underlined.

Both in solid and liquid residues the compounds identified are similar, in terms of classes, but it is different the order of the concentration, in the solid they are in the order of ppm while in the liquid of ppb, so 3 order lower.

For the same extinguishing agent, the compounds identified for different capacities are similar and even the concentration level. There is a difference between solid and liquid residues due to the ability of the VOCs to remain in the solid samples. In fact, the lower concentration, ppb, in the liquid can be due to the lack of affinity between the matrix and the compounds. According to that it can be noticed that the solid sample obtained by the tests with F-500, for both capacities, present compounds of the petroleum distillate, such as tetradecane, tridecane, octadecane and hexadecane. On the contrary, water mist samples contain acid and phenyl, such as isophthalic acid and diphenyl ether. Finally, the CO$_2$ results, in the case of liquid, are related to the water mist used after two extinctions with gas and these two steps led to a high loss of VOCs. So, after F-500 application the solid

residues are shown the higher concentration compared to the other solid samples, and this can be caused by the property of the agent to encapsulate some specific class of compounds, such as hydrocarbons. In fact, especially for the test K25-F5 the ppm of hydrocarbons is one orders of magnitude higher than the concentration of the other compounds: 1127 ppm for octadecane, 1962 ppm for hexadecane and 1027 ppm for heptadecane.

This class of compounds is regulated under the EU Regulation N. 1375/2014 [143] and the limits and thresholds values of the relative HP codes, reported in Table 5, depend on the sample matrix. In fact, in solid samples the hydrocarbons are separated according to the number of carbons in C5-C8 and C11-C39 hydrocarbons while in liquid samples all C5-C39 hydrocarbons are considered together. The compounds belonging to the hydrocarbon class are underlined in Table 87 and Table 88 and in the case of the solid samples analyzed no light hydrocarbons were identified but only heavy hydrocarbons for these reason in Table 89 are reported the sums of the concentrations of 10<C<40 hydrocarbons for solid samples and the sum of 5≤C<40 hydrocarbons for liquid samples with the relative concentration limits.

Table 89: Hydrocarbons concentration in solid and liquid samples compared to the limit of the EU Regulation N. 1375/2014 [143] (ppm).

Sample matrix	Test code	Hydrocarbons 10<C<40 (ppm)	Concentration limit (ppm) for the purpose of danger according to the EU Regulation N. 1375/2014
Solid samples	K25-W	0	250000 (HP14) threshold **10000**
	K25-F5	**48309**	
	K25-CO$_2$	5873	
	K40-W	250	
	K40-F5	1227	
	K40-CO$_2$	735	
Sample matrix	Test code	Hydrocarbons 5≤C<40 (ppm)	Concentration limit (ppm) for the purpose of danger according to the EU Regulation N. 1375/2014
Liquid samples	K25-W	0.017	100000 (HP5)
	K25-F5	0.049	
	K25-CO$_2$	0.149	
	K40-W	0.002	
	K40-F5	0.346	

The concentration values of the solid samples are all under the threshold values of the HP14 code except for the sample of the test fire K25-F5 that is higher than the

threshold values of the HP14 code but significantly lower than the limit values. In the liquid samples the concentrations are significantly lower respect to the limit of the HP5 code. Therefore, for the class of hydrocarbons there is no correlated hazard code, both for solid and liquid samples.

Then, the metals are quantified by ICP-OES analysis and the metal concentrations for the solid are reported in Table 90 while for the liquid are reported in Table 91.

Table 90: Metals concentrations (ppm) in solid samples.

ppm \ Test code	Co	Cu	Li	Mn	Ni
K25-W	1052 ± 380	1886 ± 131	7669 ± 500	826 ± 48	2936 ± 173
K25-F5	1671 ± 515	3364 ± 232	9274 ± 587	1107 ± 174	3018 ± 546
K25-CO$_2$	1356 ± 723	3491 ± 239	6305 ± 386	1030 ± 163	3434 ± 205
K40-W	1085 ± 196	7521 ± 522	4898 ± 315	909 ± 57	2480 ± 234
K40-F5	1554 ± 130	8788 ± 614	5607 ± 332	860 ± 76	2983 ± 665
K40-CO$_2$	1216 ± 502	7091 ± 495	7282 ± 466	902 ± 63	4330 ± 146

From the quantification values it is possible to observe how the contribution of each single metal in the different solid samples is similar in terms of total amount. These trend between the metals can be traced back to the percentages of metals present in the initial cells, as obtained by the characterization of the Kokam cells. In fact, the anodic material including the copper metallic collector is about 43 % while the cathodic material instead represents about 51 %. Lithium is the most concentrated metal due to its presence into cathode material and in the electrolyte, as salt (LiPF$_6$) followed by the Cu while the Mn is the less abundance.

Table 91: Metals concentrations (ppm) in liquid samples.

ppm \ Test code	Co	Cu	Li	Mn	Ni
K25-W	66 ± 6	48 ± 5	73 ± 7	111 ± 12	62 ± 6
K25-F5	106 ± 11	30 ± 3	142 ± 14	59 ± 6	96 ± 9
K25-CO$_2$	85 ± 9	20 ± 2	58 ± 6	49 ± 5	127 ± 11
K40-W	108 ± 11	89 ± 10	116 ± 12	122 ± 12	88 ± 8
K40-F5	80 ± 8	66 ± 6	68 ± 7	35 ± 4	31 ± 3

Although, two orders of magnitude lower, traces of the same metals were also found in the post-extinction liquid samples. The range of concentrations for the different samples changes significantly from 860 ± 76 to 9274 ± 587 ppm for the

solid and from 20 ± 2 to 142 ± 14 ppm for liquid. The higher concentrations in the solids are due to the chemical composition of the cathode, made of lithium-nickel-manganese-cobalt-oxides.

The limit values for metals in waste, from European Regulation N° 2008/98/EC, refer only to Cu, expressed as $CuSO_4$, and Ni, expressed as $NiSO_4$, with different limit concentrations which, for the purposes of dangerousness, lead to a different code and therefore a different specific danger. In Table 92 are reported the concentration values of $CuSO_4$, in the solid and liquid samples and the reference limits, concentration limit for the purpose of danger according to the EU Regulation N. 1375/2014 [143]. The same results are reported in Table 93 for $NiSO_4$.

Table 92: $CuSO_4$ concentration in solid and liquid compared to the limit of the EU Regulation N. 1375/2014 [143].

Sample matrix	Test code	Cu, as $CuSO_4$ (ppm)	Concentration limit (ppm) for the purpose of danger according to the EU Regulation N. 1375/2014 [143]
Solid samples	K25-W	4392	250000 (HP6) threshold **10000** 200000 (HP4) threshold **10000** 250000 (HP14) threshold 1000
	K25-F5	7833	
	K25-CO_2	8129	
	K40-W	**17513**	
	K40-F5	**20463**	
	K40-CO_2	**16511**	
Liquid samples	K25-W	112	
	K25-F5	70	
	K25-CO_2	47	
	K40-W	207	
	K40-F5	154	

The Cu concentrations for the solid samples from the fire test on K25, as reported in Table 92, are below the threshold value for the HP4 and HP6 codes but not of HP14 code without exceed the limit values, while the solid samples from the fire test on K40 exceed the threshold values of all the codes, HP4, HP6 and HP14, without anyway exceed the limit values for the purpose of danger according to the EU Regulation N. 1375/2014 [143]. The difference between the two capacities is due to higher amount of metal in the K40 than the K25. In the liquid samples the Cu concentrations are all, independently from the capacity, significantly below the threshold limits, therefore liquid samples do not have to be classified according to the waste EU Regulation.

The Ni concentration values in solid samples, as reported in Table 93, are all exceed the threshold value of the HP4 and HP14 codes without anyway exceed the limit values, while the concentration limit of the HP7 and HP10 codes were exceed. In addition, the concentration values of the solid sample obtained from the fire test K40-CO$_2$ is higher than the threshold of the HP6 code and higher than the concentration limit of the HP5 and HP11 codes. So, all the solid samples must be classified as carcinogenic and toxic to reproduction, and in addition the solid sample K40-CO$_2$ is even STOT/aspiration toxicity and mutagenic. Even for the Ni the concentration in the liquid samples is significantly below all the threshold limits of the code. So, they do not have to be classified for the EU Regulation.

Table 93: NiSO$_4$ concentration in solid and liquid compared with the limit of the EU Regulation N. 1375/2014 [143].

Sample matrix	Test code	Ni, as NiSO$_4$ (ppm)	Concentration limit (ppm) for the purpose of danger according to the EU Regulation N. 1375/2014 [143]
Solid samples	K25-W	_7741_	**1000** (HP7)
	K25-F5	_7957_	**10000** (HP11)
	K25-CO$_2$	_9054_	_3000_ (HP10)
	K40-W	_6539_	**10000** (HP5)
	K40-F5	_7865_	250000 (HP6) threshold 10000
	K40-CO$_2$	**11416**	200000 (HP4) threshold 1000
Liquid samples	K25-W	163	100000 (HP13)
	K25-F5	253	250000 (HP14) threshold 1000
	K25-CO$_2$	335	
	K40-W	232	
	K40-F5	82	

So, the extinguishing agent, in addition to extinguishing the fire, carries with it metal particles which therefore modify the initial composition of the agent itself, also varying its environmental impact. Combining the results obtained it is possible to draw a first assessment of the environmental impact of extinguishing agents once engaged on LIB fires. In fact, both the water mist and the F-500 are classified, based to their composition, as not harmful to the environment, non-toxic and completely biodegradable, while CO$_2$ has the advantage of leaving no sample being applied in the gaseous phase. From the results obtained, however, it emerges that both the solid and the liquid samples, cannot longer be considered in this classification due to the enrichment of the VOCs and the metals significantly higher than the legal limits.

7. Conclusions

The present work touched many aspects regarding the LIBs, from the active materials present inside the cells to the extinguishing capacity of some extinguishing agents during a LIBs fire passing through the identification of the key events and the main products that can be emitted during the TR of Li-ion cells.

The preliminary analysis and tests were performed to characterize the principal components present inside the Li-ion cells and to determine the thermal stability of the whole cell. In fact, in the SDS of the Li-ion cell is not usually reported the precise composition, in terms of weight and species, of the main internal components, especially regarding the electrolyte. From the characterization of the 18650 Li-ion some data were confirmed, such as the active materials of the anode and the cathode, while some discoveries have been made. In fact, some additives were added to the electrolyte to enhance both the safety and the performance, such as the tetrahydrofuran. Even if, these substances are added to the chemical composition to enhance the safety and the performance of the cells, their presence must be reported in the SDS to have a better understanding of the reactions that can occur inside the cell and the species that can be released outside the cell during a generical abuse.

The characterization of cells was made to identify and quantify the products and to understand the origin of the products during a thermal abuse. The tests were conducted in a laboratory scale apparatus equipped with a stainless-steel reactor placed inside an electrical furnace to induce an external heating with controlled heating and connected to sensors (TCs) and online analytical instrument (FT-IR). While other instruments off-line (SEM-EDX, and ICP-OES) were used to complete the characterization analysis of the liquid and/or solid resides.

Firstly, the thermal stability tests, according to the UN/ECE-R100.02:2022, returned information on the temperature values for the safety windows, meaning the temperature value after which the thermal stability of the cells is not more

guaranteed. By comparing the temperature and pressure values for the main events it was possible to draw up the following safety scale, from safest to least safe:
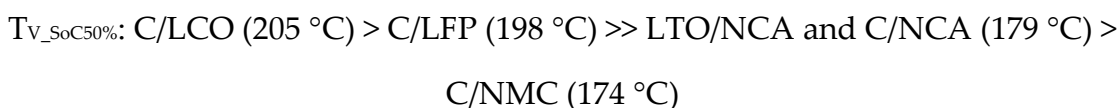
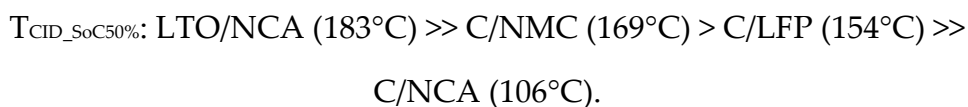C/LFP > LTO/NCA >> C/LCO > C/NMC >> C/NCA
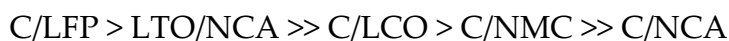
Applying an external abuse, 5 °C/min, it was possible to evaluate the thermal behavior of different chemistries, C/NCA, LTO/NCA, C/LFP, C/NMC, and C/LCO. A complete investigation of the thermal parameters and the physical-chemical properties of the main products had been obtained for each Li-ion cell under investigation.

The parameters that has been considered to evaluate the thermal behavior are the SoC and the chemical composition, of the anode and the cathode.

Independently from the chemistries, it was observed that a lower SoC, i.e., 50%, showed a lower impact on the main parameters, i.e., temperature and pressure, and on the ejected products, i.e., composition of the gases and size of the solid particles, compared to a higher SoC, i.e., 100%. So, the SoC range can be divided in low and unstable states, from 50 to 0 %, and high states, from 50 to 100 %. The reason is due to the different electrical energy available inside the cell, according to the relative voltage reported in each technical specification, which may favor the achievement of the TR with the relative jet fire from the cell and the complete combustion of the emitted species.

The temperature and pressure at which the key events are observed rise as the SoC increases, and for some chemistries the effects are more evident that for other, as reported in the following scheme:

$T_{CID\_SoC50\%}$: LTO/NCA (183°C) >> C/NMC (169°C) > C/LFP (154°C) >> C/NCA (106°C).

$T_{V\_SoC50\%}$: C/LCO (205 °C) > C/LFP (198 °C) >> LTO/NCA and C/NCA (179 °C) > C/NMC (174 °C)

$T_{TR\_SoC50\%}$: C/LCO (255 °C) > C/NCA (230 °C).

$T_{CID\_SoC100\%}$: C/LCO (195 °C) > C/NMC (170 °C) > C/LFP (164 °C) >> C/NCA (130 °C).

$T_{V\_SoC100\%}$: C/LFP (197 °C) > C/LCO (194 °C) > LTO/NCA (187 °C) >>

C/NMC (169°C) >> C/NMC (157 °C).

$T_{TR\_SoC100\%}$: C/LFP (243 °C) > LTO/NCA (233 °C) > C/LCO (228 °C) >>

C/NCA (207°C) > C/NMC (202 °C).

On the contrary, the emissions worsen as the SoC increases, in fact there is an increase in material losses from the cell in terms mainly of gases and solids. Among the gases emitted, CO_2, CO, CH_4, HF, DMC, and EC were found . About the toxic gases, HF and CO, the concentration exceed the NIOSH (30 ppm for HF and 1200 ppm for the CO) with a similar trend between the 50 % and the 100 % SoC, so all the values are 1 order of magnitude higher for the HF while for the CO the exceed is of one order of magnitude except for the C/NMC. The increase in health risk is due to the increase in solid particulate released. In fact, in addition to the metallic composition, due to the composition of the mixed oxides that constitute the positive electrode, there is also the aspect of size which is not negligible since depending on the diameter if dispersed in the air they can be inhalable (10 < d < 100 μm) and/or breathable (d < 4 μm). For example, from the test at the 50 % SoC the NCA released metallic powder with a diameter, measured by the SEM-EDX, of 1.63 μm which can therefore be breathed in, affecting human lungs, while from the test at 100 % the LCO released metallic powder with a diameter of 16.17 μm which due to their coarse diameter, are only respirable.

The additional tests conducted on the C/NCA, that resulted the worst cell between the chemistries investigated, were conducted to understand the impact of different heating rate (5 vs 10 °C/min) and the environment (air vs N_2). The different heating rate shown an increase of the temperature on the cell surface compared to the slower heating rate, anyway both the temperature-pressure and the emission

profiles resulted similar. The main difference was observed between the oxidative and the inert atmosphere, in fact, in presence of air the amount of CO and CO_2, due to the combustion reactions, increased compared to the amounts detected in the inert atmosphere. The study in the inert atmosphere was conducted for two reasons, the first to evaluate the products produced just from the internal reactions occurring inside the cells and after to evaluate the impact of the atmosphere on the safety concerns. From the data obtained an inert atmosphere reduced, albeit slightly, the temperatures reached, and the products emitted. Anyway, it is difficult to think of modules and/or battery packs surrounded by nitrogen and not air, both from the point of view of the design of the external cases and of maintenance and maintenance.

The combination of the products characterization was used to identify the PPE that can be adopted by firefighters who must operate on the scene of a LIBs fire to be able to operate in complete safety. The most efficient equipment in the case of LIBs fire is the gas masks, with the following combined filters: A1E1P3 + CO.

Moreover, to increase the performance of the LIBs, the NMs are under investigation. In fact, the use of NMs in the internal chemical composition is showing an improvement on the global capacity of the LIBs enhancing the performance. Anyway, the NMs decrease the safety properties increasing the explosivity and thermal risks and the eco-toxicity impact. For these reasons, a study on the thermal and the explosivity behaviors and the environmental impact, of the most interesting NMs, i.e., Si, LTO, and graphite, has been conducted to guarantee an improvement in the performance of the electrical device without losing in terms of safety.

The first step was the characterization of NMs, both as pristine and as materials dissolved in a medium, is useful for having more precise information on the physical properties that influence the risk of explosiveness and eco-toxicity. This evaluation is important because according to the environment the properties can

significantly change, for example the Z-average of the particle in the ISO medium can increases by 2 orders of magnitude compared to the initial material.

In terms of explosive risk, the reduction of the size of the material, from the micro size to the nano size, determined a significant increase in the severity of the explosion, from nil or weak to very strong. This behavior is increasingly evident from CB, to Si up to the extreme case of graphite. By the explosivity results it was possible to draw up the following safety scale, from safest to least safe: LTO >> CB > Si > graphite.

The most significant results, in terms of eco-toxicity, were obtained for the nano-CB. In fact, the NOEC and EC50, were observed between 3.75 and 15 ppm, compared to the concentration ranges observed for the other nanomaterials, from 100 to over 1000 ppm. By the eco-toxicity results it was possible to draw up the following safety scale, from safest to least safe: Si >> LTO > graphite >> CB.

So, the reduction in size therefore resulted in an increase in the severity of the explosion and simultaneously a reduction in the concentration necessary to observe an ecotoxic effect in the aquatic ecosystem.

The last aspect investigated is the fire management to identify the most suitable and efficient extinguishing agents, in terms of cooling and inhibition effect.

Fire tests were conducted on commercial NMC pouch cells, Kokam 25 Ah and 40 Ah, to establish the efficiency of the extinguishing agents and the chemical composition of the liquid and solid samples. From the monitoring of the temperatures in the different fire tests it emerged that the cell capacities, 25 and 40 Ah, do not significantly affect the venting and catastrophic rupture temperatures of the cell. In term of extinguishing agents, the water-based, i.e., water mist and F-500, show a greater efficiency than gaseous one, i.e., CO_2, after the first application. Water-based have a faster and more effective cooling effect due to their ability to penetrate inside the cell, reaching temperatures below 100 °C after the first

application. The higher cooling rate of F-500 is due to ability of encapsulating the fuel compounds. The instrumental analyses for the identification and quantification of VOCs, by GC-FID and SPME-GC-MS, and metal, by ICP-OES, in the solid and liquid samples demonstrate the dangerous of solid and liquid sample after a LIB fire. In solid samples from tests with F-500 application, due to the higher ability of micelles to encapsulate hydrocarbons compounds, the concentration of these class is for many compounds higher than 1000 ppm. Finally, there are differences between liquid and solid samples, in terms of metal concentration. The presence is due to the composition of the cathode of the batteries, containing lithium, nickel, cobalt, and manganese. In conclusion, from the point of view of cooling efficiency, water-based agents are the better solution than gaseous ones.

From the point of view of the environmental impact, criticalities emerged from the analysis of the post fire test solid and liquid samples, especially due to the high metal content. These species, together with the VOCs, modify the initial composition of both the fuels and the extinguishing agents and therefore require a new cataloging for subsequent disposal.

Although the topics covered are broad and cover various problems related to the use and abuse of batteries, they all fall within the scope of an increasingly safe and conscious transition towards electrical devices. Often, in fact, conditions of abuse are reached due to users unawareness of the risks related to batteries. Correct information and a more conscious use of these devices are the basis for correct use and obtaining maximum performance.

Acknowledgment

References

[1] J.-M. Tarascon and M. Armand, "Issues and challenges facing rechargeable lithium batteries," *Nature*, vol. 414, no. 6861, pp. 359–367, Nov. 2001, doi: 10.1038/35104644.

[2] L. Lu, X. Han, J. Li, J. Hua, and M. Ouyang, "A review on the key issues for lithium-ion battery management in electric vehicles," *Journal of Power Sources*, vol. 226, pp. 272–288, Mar. 2013, doi: 10.1016/j.jpowsour.2012.10.060.

[3] Y. Qiu and F. Jiang, "A review on passive and active strategies of enhancing the safety of lithium-ion batteries," *International Journal of Heat and Mass Transfer*, vol. 184, p. 122288, Mar. 2022, doi: 10.1016/j.ijheatmasstransfer.2021.122288.

[4] Q. Wang, P. Ping, X. Zhao, G. Chu, J. Sun, and C. Chen, "Thermal runaway caused fire and explosion of lithium ion battery," *Journal of Power Sources*, vol. 208, pp. 210–224, Jun. 2012, doi: 10.1016/j.jpowsour.2012.02.038.

[5] C. F. Lopez, J. A. Jeevarajan, and P. P. Mukherjee, "Characterization of Lithium-Ion Battery Thermal Abuse Behavior Using Experimental and Computational Analysis," *J. Electrochem. Soc.*, vol. 162, no. 10, pp. A2163–A2173, 2015, doi: 10.1149/2.0751510jes.

[6] B. Xu, L. Kong, G. Wen, and M. G. Pecht, "Protection Devices in Commercial 18650 Lithium-Ion Batteries," *IEEE Access*, vol. 9, pp. 66687–66695, 2021, doi: 10.1109/ACCESS.2021.3075972.

[7] T. Hettesheimer *et al.*, "Entwicklungsperspektiven für Zellformate von Lithium-Ionen-Batterien in der Elektromobilität", doi: 10.24406/PUBLICA-FHG-298745.

[8] J. Ming *et al.*, "New Insight on the Role of Electrolyte Additives in Rechargeable Lithium Ion Batteries," *ACS Energy Lett.*, vol. 4, no. 11, pp. 2613–2622, Nov. 2019, doi: 10.1021/acsenergylett.9b01441.

[9] A. K. Shukla and T. P. Kumar, "Materials for next-generation lithium batteries," *CURRENT SCIENCE*, vol. 94, no. 3, 2008.

[10] S. Hess, M. Wohlfahrt-Mehrens, and M. Wachtler, "Flammability of Li-Ion Battery Electrolytes: Flash Point and Self-Extinguishing Time Measurements," *J. Electrochem. Soc.*, vol. 162, no. 2, pp. A3084–A3097, 2015, doi: 10.1149/2.0121502jes.

[11] M. Kaliaperumal *et al.*, "Cause and Mitigation of Lithium-Ion Battery Failure—A Review," *Materials*, vol. 14, no. 19, p. 5676, Sep. 2021, doi: 10.3390/ma14195676.

[12] "BU-205: Types of Lithium-ion - Battery University." Accessed: Aug. 08, 2023. [Online]. Available: https://batteryuniversity.com/article/bu-205-types-of-lithium-ion

[13] S. S. Williamson, P. A. Cassani, S. Lukic, and B. Blunier, "Energy Storage," in *Power Electronics Handbook*, Elsevier, 2011, pp. 1331–1356. doi: 10.1016/B978-0-12-382036-5.00046-X.

[14] Y. Mekonnen, A. Sundararajan, and A. I. Sarwat, "A review of cathode and anode materials for lithium-ion batteries," in *SoutheastCon 2016*, Norfolk, VA, USA: IEEE, Mar. 2016, pp. 1–6. doi: 10.1109/SECON.2016.7506639.

[15] W. Li, K. R. Crompton, C. Hacker, and J. K. Ostanek, "Comparison of Current Interrupt Device and Vent Design for 18650 Format Lithium-ion Battery Caps," *Journal of Energy Storage*, vol. 32, p. 101890, Dec. 2020, doi: 10.1016/j.est.2020.101890.

[16] IEC, "Inetrnational Standard IEC 62133 - Secondary cells and batteries containing alkaline or other non-acid electrolytes – Safety requirements for portable sealed secondary cells, and for batteries made from them, for use in portable applications." 2002. [Online]. Available: https://webstore.iec.ch/preview/info_iec62133%7Bed1.0%7Den_d.pdf

[17] N. Anderson, M. Tran, and E. Darcy, "18650 Cell Bottom Vent: Preliminary Evaluation into its Merits for Preventing Side Wall Rupture," presented at the S&T Meeting, San Diego, California, Dec. 07, 2016. [Online]. Available: https://ntrs.nasa.gov/api/citations/20160014008/downloads/20160014008.pdf

[18] "IEEE Standard for Rechargeable Batteries for Cellular Telephones," IEEE. doi: 10.1109/IEEESTD.2011.5930304.

[19] D. Lisbona and T. Snee, "A review of hazards associated with primary lithium and lithium-ion batteries," *Process Safety and Environmental Protection*, vol. 89, no. 6, pp. 434–442, Nov. 2011, doi: 10.1016/j.psep.2011.06.022.

[20] W. Waag and D. U. Sauer, "SECONDARY BATTERIES – LEAD– ACID SYSTEMS | State-of-Charge/Health," in *Encyclopedia of Electrochemical Power Sources*, Elsevier, 2009, pp. 793–804. doi: 10.1016/B978-044452745-5.00149-0.

[21] J.-K. Park, Ed., *Principles and applications of lithium secondary batteries*. Weinheim, Germany: Wiley-VCH, 2012.

[22] C.-H. Yim, F. M. Courtel, and Y. Abu-Lebdeh, "A high capacity silicon–graphite composite as anode for lithium-ion batteries using low content amorphous silicon and compatible binders," *J. Mater. Chem. A*, vol. 1, no. 28, p. 8234, 2013, doi: 10.1039/c3ta10883j.

[23] G.-A. Nazri and G. Pistoia, Eds., *Lithium batteries: science and technology*, First softcover printing. New York, NY: Springer, 2009.

[24] R. Zhang *et al.*, "State of the Art of Lithium-Ion Battery SOC Estimation for Electrical Vehicles," *Energies*, vol. 11, no. 7, p. 1820, Jul. 2018, doi: 10.3390/en11071820.

[25] D. Kong, H. Lv, P. Ping, and G. Wang, "A review of early warning methods of thermal runaway of lithium ion batteries," *Journal of Energy Storage*, vol. 64, p. 107073, Aug. 2023, doi: 10.1016/j.est.2023.107073.

[26] "Shepherd's Bush high-rise fire caused by e-bike prompts safety warning from firefighters | London Fire Brigade." Accessed: Aug. 28, 2023. [Online]. Available: https://www.london-fire.gov.uk/news/2022-news/june/shepherd-s-bush-high-rise-fire-caused-by-e-bike-prompts-safety-warning-from-firefighters/

[27] "Tesla crash may have triggered battery fire: Swiss firefighters | Reuters." Accessed: Sep. 02, 2023. [Online]. Available: https://www.reuters.com/article/us-swiss-tesla-crash-idUSKCN1IF2WN

[28] "Une Dacia Spring s'embrase en Roumanie." Accessed: Aug. 29, 2023. [Online]. Available: https://insideevs.fr/news/667505/dacia-spring-incendie-batterie-roumanie/

[29] X. Wu *et al.*, "Safety Issues in Lithium Ion Batteries: Materials and Cell Design," *Front. Energy Res.*, vol. 7, p. 65, Jul. 2019, doi: 10.3389/fenrg.2019.00065.

[30] G. Zhang, X. Wei, S. Chen, J. Zhu, G. Han, and H. Dai, "Revealing the Impact of Slight Electrical Abuse on the Thermal Safety Characteristics for Lithium-Ion Batteries," *ACS Appl. Energy Mater.*, vol. 4, no. 11, pp. 12858–12870, Nov. 2021, doi: 10.1021/acsaem.1c02537.

[31] X. Feng, M. Ouyang, X. Liu, L. Lu, Y. Xia, and X. He, "Thermal runaway mechanism of lithium ion battery for electric vehicles: A review," *Energy Storage Materials*, vol. 10, pp. 246–267, Jan. 2018, doi: 10.1016/j.ensm.2017.05.013.

[32] A. Jana, D. R. Ely, and R. E. García, "Dendrite-separator interactions in lithium-based batteries," *Journal of Power Sources*, vol. 275, pp. 912–921, Feb. 2015, doi: 10.1016/j.jpowsour.2014.11.056.

[33] C. Fear, D. Juarez-Robles, J. A. Jeevarajan, and P. P. Mukherjee, "Elucidating Copper Dissolution Phenomenon in Li-Ion Cells under Overdischarge Extremes," *J. Electrochem. Soc.*, vol. 165, no. 9, pp. A1639–A1647, 2018, doi: 10.1149/2.0671809jes.

[34] L. He, Q. Sun, L. Lu, and S. Adams, "Understanding and Preventing Dendrite Growth in Lithium Metal Batteries," *ACS Appl. Mater. Interfaces*, vol. 13, no. 29, pp. 34320–34331, Jul. 2021, doi: 10.1021/acsami.1c08268.

[35] C. Menale, S. Constà, V. Sglavo, L. Della Seta, and R. Bubbico, "Experimental Investigation of Overdischarge Effects on Commercial Li-Ion Cells," *Energies*, vol. 15, no. 22, p. 8440, Nov. 2022, doi: 10.3390/en15228440.

[36] J.-B. Jung, M.-G. Lim, J.-Y. Kim, B.-G. Han, B. Kim, and D.-S. Rho, "Safety Assessment for External Short Circuit of Li-Ion Battery in ESS Application Based on Operation and Environment Factors," *Energies*, vol. 15, no. 14, p. 5052, Jul. 2022, doi: 10.3390/en15145052.

[37] G. Zhang, X. Wei, X. Tang, J. Zhu, S. Chen, and H. Dai, "Internal short circuit mechanisms, experimental approaches and detection methods of lithium-ion batteries for electric vehicles:

A review," *Renewable and Sustainable Energy Reviews*, vol. 141, p. 110790, May 2021, doi: 10.1016/j.rser.2021.110790.

[38] Y. Xiao *et al.*, "Review of mechanical abuse related thermal runaway models of lithium-ion batteries at different scales," *Journal of Energy Storage*, vol. 64, p. 107145, Aug. 2023, doi: 10.1016/j.est.2023.107145.

[39] H. Wang, S. Simunovic, H. Maleki, J. N. Howard, and J. A. Hallmark, "Internal configuration of prismatic lithium-ion cells at the onset of mechanically induced short circuit," *Journal of Power Sources*, vol. 306, pp. 424–430, Feb. 2016, doi: 10.1016/j.jpowsour.2015.12.026.

[40] D. Ouyang, M. Chen, Q. Huang, J. Weng, Z. Wang, and J. Wang, "A Review on the Thermal Hazards of the Lithium-Ion Battery and the Corresponding Countermeasures," *Applied Sciences*, vol. 9, no. 12, p. 2483, Jun. 2019, doi: 10.3390/app9122483.

[41] M. Chen, J. Liu, D. Ouyang, and J. Wang, "Experimental investigation on the effect of ambient pressure on thermal runaway and fire behaviors of lithium-ion batteries," *Int J Energy Res*, vol. 43, no. 9, pp. 4898–4911, Jul. 2019, doi: 10.1002/er.4666.

[42] C. Essl *et al.*, "Comprehensive Hazard Analysis of Failing Automotive Lithium-Ion Batteries in Overtemperature Experiments," *Batteries*, vol. 6, no. 2, p. 30, May 2020, doi: 10.3390/batteries6020030.

[43] M. Wakihara, "Recent developments in lithium ion batteries," *Materials Science and Engineering: R: Reports*, vol. 33, no. 4, pp. 109–134, Jun. 2001, doi: 10.1016/S0927-796X(01)00030-4.

[44] H. Abdi, B. Mohammadi-ivatloo, S. Javadi, A. R. Khodaei, and E. Dehnavi, "Energy Storage Systems," in *Distributed Generation Systems*, Elsevier, 2017, pp. 333–368. doi: 10.1016/B978-0-12-804208-3.00007-8.

[45] D. Lisbona and T. Snee, "A review of hazards associated with primary lithium and lithium-ion batteries," *Process Safety and Environmental Protection*, vol. 89, no. 6, pp. 434–442, Nov. 2011, doi: 10.1016/j.psep.2011.06.022.

[46] V. Ruiz, A. Pfrang, A. Kriston, N. Omar, P. Van den Bossche, and L. Boon-Brett, "A review of international abuse testing standards and regulations for lithium ion batteries in electric and hybrid electric vehicles," *Renewable and Sustainable Energy Reviews*, vol. 81, pp. 1427–1452, Jan. 2018, doi: 10.1016/j.rser.2017.05.195.

[47] United Nations, "Agreement - Concerning the Adoption of Harmonized Technical United Nations Regulations for Wheeled Vehicles, Equipment and Parts which can be Fitted and/or be Used on Wheeled Vehicles and the Conditions for Reciprocal Recognition of Approvals Granted on the Basis of these United Nations Regulations." Mar. 23, 2022. [Online]. Available: https://unece.org/transport/documents/2022/03/standards/regulation-no-100-rev3

[48] "Incendie à Grand-Couronne. Les réponses d'experts sur le danger des batteries au lithium," actu.fr. Accessed: Aug. 29, 2023. [Online]. Available: https://actu.fr/normandie/grand-couronne_76319/incendie-a-grand-couronne-les-reponses-d-experts-sur-le-danger-des-batteries-au-lithium_56664541.html

[49] "Pure Ev Fire Accident: Electric scooter from Pure EV catches fire in Chennai, fourth such incident in four days, ET Auto." Accessed: Aug. 29, 2023. [Online]. Available: https://auto.economictimes.indiatimes.com/news/two-wheelers/scooters-mopeds/electric-scooter-from-pure-ev-catches-fire-in-chennai-fourth-such-incident-in-four-days/90524995?redirect=1

[50] "Audi e-tron: la batteria da 700 kg si stacca e vola via dopo incidente - SicurAUTO.it." Accessed: Aug. 29, 2023. [Online]. Available: https://www.sicurauto.it/news/auto-elettriche-ibride/audi-e-tron-la-batteria-da-700-kg-si-stacca-e-vola-via-dopo-incidente/?utm_source=dlvr.it&utm_medium=linkedin

[51] "Table of IDLH Values | NIOSH | CDC." Accessed: Sep. 04, 2023. [Online]. Available: https://www.cdc.gov/niosh/idlh/intridl4.html

[52] H. Chikh-Bled, K. Chah, Á. González-Vila, B. Lasri, and C. Caucheteur, "Behavior of femtosecond laser-induced eccentric fiber Bragg gratings at very high temperatures," *Opt. Lett.*, vol. 41, no. 17, p. 4048, Sep. 2016, doi: 10.1364/OL.41.004048.

[53] W. Yongqing, G. Zongqing, W. Shuonan, and H. Ping, "The temperature measurement technology of infrared thermal imaging and its applications review," in *2017 13th IEEE International Conference on Electronic Measurement & Instruments (ICEMI)*, Yangzhou: IEEE, Oct. 2017, pp. 401–406. doi: 10.1109/ICEMI.2017.8265833.

[54] M. Qiu, J. Liu, B. Cong, and Y. Cui, "Research Progress in Thermal Runaway Vent Gas Characteristics of Li-Ion Battery," *Batteries*, vol. 9, no. 8, p. 411, Aug. 2023, doi: 10.3390/batteries9080411.

[55] C. Essl, L. Seifert, M. Rabe, and A. Fuchs, "Early Detection of Failing Automotive Batteries Using Gas Sensors," *Batteries*, vol. 7, no. 2, p. 25, Apr. 2021, doi: 10.3390/batteries7020025.

[56] P. Russo and M. L. Mele, "Li-ion batteries: characterization of the thermal runaway reactions using a DSC," *Proceedings of the 13th International Symposium on Hazards, Prevention and Mitigation of Industrial Explosions (ISHPMIE 2020)*, pp. 166–174, 2020, doi: 10.7795/810.20200724.

[57] Y. Fernandes, A. Bry, and S. De Persis, "Identification and quantification of gases emitted during abuse tests by overcharge of a commercial Li-ion battery," *Journal of Power Sources*, vol. 389, pp. 106–119, Jun. 2018, doi: 10.1016/j.jpowsour.2018.03.034.

[58] F. Larsson, P. Andersson, and B.-E. Mellander, "Lithium-Ion Battery Aspects on Fires in Electrified Vehicles on the Basis of Experimental Abuse Tests," *Batteries*, vol. 2, no. 2, p. 9, Apr. 2016, doi: 10.3390/batteries2020009.

[59] M. L. Mele *et al.*, "Thermal Abuse Tests on 18650 Li-Ion Cells Using a Cone Calorimeter and Cell Residues Analysis," *Energies*, vol. 15, no. 7, p. 2628, Apr. 2022, doi: 10.3390/en15072628.

[60] Y. Peng *et al.*, "A comprehensive investigation on the thermal and toxic hazards of large format lithium-ion batteries with LiFePO4 cathode," *Journal of Hazardous Materials*, vol. 381, p. 120916, Jan. 2020, doi: 10.1016/j.jhazmat.2019.120916.

[61] H. M. Barkholtz *et al.*, "Multi-scale thermal stability study of commercial lithium-ion batteries as a function of cathode chemistry and state-of-charge," *Journal of Power Sources*, vol. 435, p. 226777, Sep. 2019, doi: 10.1016/j.jpowsour.2019.226777.

[62] D. H. Doughty and E. P. Roth, "A General Discussion of Li Ion Battery Safety," *Electrochemical Society Interface*, vol. 21, no. 37, p. 8, Jan. 2012, doi: 10.1149/2.F03122if.

[63] J. Sun *et al.*, "Toxicity, a serious concern of thermal runaway from commercial Li-ion battery," *Nano Energy*, vol. 27, pp. 313–319, Sep. 2016, doi: 10.1016/j.nanoen.2016.06.031.

[64] P. Andersson, P. Blomqvist, A. Lorén, and F. Larsson, "Using Fourier transform infrared spectroscopy to determine toxic gases in fires with lithium-ion batteries: FTIR to Determine Toxic Gases," *Fire Mater.*, vol. 40, no. 8, pp. 999–1015, Dec. 2016, doi: 10.1002/fam.2359.

[65] F. Diaz, Y. Wang, R. Weyhe, and B. Friedrich, "Gas generation measurement and evaluation during mechanical processing and thermal treatment of spent Li-ion batteries," *Waste Management*, vol. 84, pp. 102–111, Feb. 2019, doi: 10.1016/j.wasman.2018.11.029.

[66] P. Ribière, S. Grugeon, M. Morcrette, S. Boyanov, S. Laruelle, and G. Marlair, "Investigation on the fire-induced hazards of Li-ion battery cells by fire calorimetry," *Energy Environ. Sci.*, vol. 5, no. 1, pp. 5271–5280, 2012, doi: 10.1039/C1EE02218K.

[67] Y. Peng *et al.*, "A comprehensive investigation on the thermal and toxic hazards of large format lithium-ion batteries with LiFePO4 cathode," *Journal of Hazardous Materials*, vol. 381, p. 120916, Jan. 2020, doi: 10.1016/j.jhazmat.2019.120916.

[68] Perkin Elmer, "Spectrum 3 FT-IR, Perkin Elmer guide." Accessed: Nov. 08, 2021. [Online]. Available: https://resources.perkinelmer.com/lab-solutions/resources/docs/bro_spectrum3-ft-ir.pdf

[69] T. L. Barone, T. H. Dubaniewicz, S. A. Friend, I. A. Zlochower, A. D. Bugarski, and N. S. Rayyan, "Lithium-ion battery explosion aerosols: Morphology and elemental composition," *Aerosol*

Science and Technology, vol. 55, no. 10, pp. 1183–1201, Oct. 2021, doi: 10.1080/02786826.2021.1938966.

[70] S. Chen, Z. Wang, and W. Yan, "Identification and characteristic analysis of powder ejected from a lithium ion battery during thermal runaway at elevated temperatures," *Journal of Hazardous Materials*, vol. 400, p. 123169, Dec. 2020, doi: 10.1016/j.jhazmat.2020.123169.

[71] F. Larsson, P. Andersson, P. Blomqvist, and B.-E. Mellander, "Toxic fluoride gas emissions from lithium-ion battery fires," *Sci Rep*, vol. 7, no. 1, p. 10018, Aug. 2017, doi: 10.1038/s41598-017-09784-z.

[72] G. Wang *et al.*, "Revealing particle venting of lithium-ion batteries during thermal runaway: A multi-scale model toward multiphase process," *eTransportation*, vol. 16, p. 100237, Apr. 2023, doi: 10.1016/j.etran.2023.100237.

[73] P. G. Bruce, B. Scrosati, and J.-M. Tarascon, "Nanomaterials for Rechargeable Lithium Batteries," *Angew. Chem. Int. Ed.*, vol. 47, no. 16, pp. 2930–2946, Apr. 2008, doi: 10.1002/anie.200702505.

[74] M. Sivaramkrishnan *et al.*, "A Certain Investigation of Nanomaterial-Based Li-Ion Batteries for Electrical Vehicles," *Journal of Nanomaterials*, vol. 2022, pp. 1–6, Aug. 2022, doi: 10.1155/2022/2700050.

[75] B. D. Assresahegn and D. Bélanger, "Synthesis of binder-like molecules covalently linked to silicon nanoparticles and application as anode material for lithium-ion batteries without the use of electrolyte additives," *Journal of Power Sources*, vol. 345, pp. 190–201, Mar. 2017, doi: 10.1016/j.jpowsour.2017.01.135.

[76] V. Vishwakarma, S. S. Samal, and N. Manoharan, "Safety and Risk Associated with Nanoparticles - A Review," *JMMCE*, vol. 09, no. 05, pp. 455–459, 2010, doi: 10.4236/jmmce.2010.95031.

[77] C. Jiang, E. Hosono, and H. Zhou, "Nanomaterials for lithium ion batteries," *Nano Today*, vol. 1, no. 4, pp. 28–33, Nov. 2006, doi: 10.1016/S1748-0132(06)70114-1.

[78] C. Corcione and M. Frigione, "Characterization of Nanocomposites by Thermal Analysis," *Materials*, vol. 5, no. 12, pp. 2960–2980, Dec. 2012, doi: 10.3390/ma5122960.

[79] European Commission. Joint Research Centre., *The NanoDefine methods manual: 2020*. LU: Publications Office, 2020. Accessed: Jun. 14, 2023. [Online]. Available: https://data.europa.eu/doi/10.2760/79490

[80] L. Wang *et al.*, "Bamboo Leaves Derived Ultrafine Si Nanoparticles and Si/C Nanocomposites for High-performance Li-ion Battery Anodes".

[81] S. Chen, M. L. Gordin, R. Yi, G. Howlett, H. Sohn, and D. Wang, "Silicon core–hollow carbon shell nanocomposites with tunable buffer voids for high capacity anodes of lithium-ion batteries," *Phys. Chem. Chem. Phys.*, vol. 14, no. 37, p. 12741, 2012, doi: 10.1039/c2cp42231j.

[82] S. Chen, L. Shen, P. A. Van Aken, J. Maier, and Y. Yu, "Dual-Functionalized Double Carbon Shells Coated Silicon Nanoparticles for High Performance Lithium-Ion Batteries," *Adv. Mater.*, vol. 29, no. 21, p. 1605650, Jun. 2017, doi: 10.1002/adma.201605650.

[83] C. Erk, T. Brezesinski, H. Sommer, R. Schneider, and J. Janek, "Toward Silicon Anodes for Next-Generation Lithium Ion Batteries: A Comparative Performance Study of Various Polymer Binders and Silicon Nanopowders," *ACS Appl. Mater. Interfaces*, vol. 5, no. 15, pp. 7299–7307, Aug. 2013, doi: 10.1021/am401642c.

[84] S. Pinilla, S.-H. Park, K. Fontanez, F. Márquez, V. Nicolosi, and C. Morant, "0D-1D Hybrid Silicon Nanocomposite as Lithium-Ion Batteries Anodes," *Nanomaterials*, vol. 10, no. 3, p. 515, Mar. 2020, doi: 10.3390/nano10030515.

[85] M. S. Al Ja'farawy, D. N. Hikmah, U. Riyadi, A. Purwanto, and H. Widiyandari, "A Review: The Development of SiO2/C Anode Materials for Lithium-Ion Batteries," *J. Electron. Mater.*, vol. 50, no. 12, pp. 6667–6687, Dec. 2021, doi: 10.1007/s11664-021-09187-x.

[86] N. S. Hudak, "Nanostructured Electrode Materials for Lithium-Ion Batteries," in *Lithium-Ion Batteries*, Elsevier, 2014, pp. 57–82. doi: 10.1016/B978-0-444-59513-3.00004-2.

[87] W. Qi, J. G. Shapter, Q. Wu, T. Yin, G. Gao, and D. Cui, "Nanostructured anode materials for lithium-ion batteries: principle, recent progress and future perspectives," *J. Mater. Chem. A*, vol. 5, no. 37, pp. 19521–19540, 2017, doi: 10.1039/C7TA05283A.

[88] L. Sun, Y. Liu, R. Shao, J. Wu, R. Jiang, and Z. Jin, "Recent progress and future perspective on practical silicon anode-based lithium ion batteries," *Energy Storage Materials*, vol. 46, pp. 482–502, Apr. 2022, doi: 10.1016/j.ensm.2022.01.042.

[89] A. Enotiadis, N. J. Fernandes, N. A. Becerra, M. Zammarano, and E. P. Giannelis, "Nanocomposite electrolytes for lithium batteries with reduced flammability," *Electrochimica Acta*, vol. 269, pp. 76–82, Apr. 2018, doi: 10.1016/j.electacta.2018.02.079.

[90] L. J. Johnston, E. Mansfield, and G. J. Smallwood, "Physicochemical Properties of Engineered Nanomaterials," in *Metrology and Standardization of Nanotechnology*, E. Mansfield, D. L. Kaiser, D. Fujita, and M. Van De Voorde, Eds., Weinheim, Germany: Wiley-VCH Verlag GmbH & Co. KGaA, 2017, pp. 99–114. doi: 10.1002/9783527800308.ch5.

[91] S. Mourdikoudis, R. M. Pallares, and N. T. K. Thanh, "Characterization techniques for nanoparticles: comparison and complementarity upon studying nanoparticle properties," *Nanoscale*, vol. 10, no. 27, pp. 12871–12934, 2018, doi: 10.1039/C8NR02278J.

[92] J. X. Bouillard, "Fire and Explosion of Nanopowders," in *Nanoengineering*, Elsevier, 2015, pp. 111–148. doi: 10.1016/B978-0-444-62747-6.00005-1.

[93] O. Dufaud, A. Vignes, F. Henry, L. Perrin, and J. Bouillard, "Ignition and explosion of nanopowders: something new under the dust," *J. Phys.: Conf. Ser.*, vol. 304, p. 012076, Jul. 2011, doi: 10.1088/1742-6596/304/1/012076.

[94] C. Lin *et al.*, "Investigation into the Suppression Effects of Inert Powders on the Minimum Ignition Temperature and the Minimum Ignition Energy of Polyethylene Dust," *Processes*, vol. 8, no. 3, p. 294, Mar. 2020, doi: 10.3390/pr8030294.

[95] D. Castellanos, P. Bagaria, and C. V. Mashuga, "Effect of particle size polydispersity on dust cloud minimum ignition energy," *Powder Technology*, vol. 367, pp. 782–787, May 2020, doi: 10.1016/j.powtec.2020.04.037.

[96] ISO, "ISO/IEC 80079-20-2:2016 Explosive atmospheres — Part 20-2: Material characteristics — Combustible dusts test methods." 2016. [Online]. Available: https://www.iso.org/standard/66564.html

[97] P. Amyotte, *An introduction to dust explosions: understanding the myths and realities of dust explosions for a safer workplace*. Amsterdam Boston: Butterworth-Heinemann Elsevier, 2013.

[98] European Standard (EN), "BS EN 14034-3:2006+A1:2011 Determination of explosion characteristics of dust clouds Determination of the lower explosion limit LEL of dust clouds." Aug. 31, 2011. [Online]. Available: https://www.en-standard.eu/bs-en-14034-3-2006-a1-2011-determination-of-explosion-characteristics-of-dust-clouds-determination-of-the-lower-explosion-limit-lel-of-dust-clouds/

[99] T. Abbasi and S. A. Abbasi, "Dust explosions–Cases, causes, consequences, and control," *Journal of Hazardous Materials*, vol. 140, no. 1–2, pp. 7–44, Feb. 2007, doi: 10.1016/j.jhazmat.2006.11.007.

[100] P. R. Amyotte and R. K. Eckhoff, "Dust explosion causation, prevention and mitigation: An overview," *J. Chem. Health Saf.*, vol. 17, no. 1, pp. 15–28, Jan. 2010, doi: 10.1016/j.jchas.2009.05.002.

[101] R. K. Eckhoff, *Dust explosions in the process industries*, 3rd ed. Amsterdam Boston: Gulf Professional Pub, 2003.

[102] D. Castellanos, V. H. Carreto-Vazquez, C. V. Mashuga, R. Trottier, A. F. Mejia, and M. S. Mannan, "The effect of particle size polydispersity on the explosibility characteristics of aluminum dust," *Powder Technology*, vol. 254, pp. 331–337, Mar. 2014, doi: 10.1016/j.powtec.2013.11.028.

[103] S. Rana and P. T. Kalaichelvan, "Ecotoxicity of Nanoparticles," *ISRN Toxicology*, vol. 2013, pp. 1–11, Mar. 2013, doi: 10.1155/2013/574648.

[104]   F. Nasser and I. Lynch, "Updating traditional regulatory tests for use with novel materials: Nanomaterial toxicity testing with Daphnia magna," *Safety Science*, vol. 118, pp. 497–504, Oct. 2019, doi: 10.1016/j.ssci.2019.05.045.

[105]   D. Wilkinson, "Zooplankton – A Lake's best Friend." Accessed: Jul. 09, 2023. [Online]. Available: https://clp.indiana.edu/doc/fact-sheets/zooplankton.pdf

[106]   I.-S. Kwak and Y.-S. Park, "Food Chains and Food Webs in Aquatic Ecosystems," *Applied Sciences*, vol. 10, no. 14, p. 5012, Jul. 2020, doi: 10.3390/app10145012.

[107]   K. Mattsson, E. V. Johnson, A. Malmendal, S. Linse, L.-A. Hansson, and T. Cedervall, "Brain damage and behavioural disorders in fish induced by plastic nanoparticles delivered through the food chain," *Sci Rep*, vol. 7, no. 1, p. 11452, Sep. 2017, doi: 10.1038/s41598-017-10813-0.

[108]   I. Fekete-Kertész *et al.*, "Ecotoxicity Assessment of Graphene Oxide by Daphnia magna through a Multimarker Approach from the Molecular to the Physiological Level including Behavioral Changes," *Nanomaterials*, vol. 10, no. 10, p. 2048, Oct. 2020, doi: 10.3390/nano10102048.

[109]   A. Boughbina-Portolés *et al.*, "Reliable assessment of carbon black nanomaterial of a variety of cell culture media for in vitro toxicity assays by asymmetrical flow field-flow fractionation," *Anal Bioanal Chem*, vol. 415, no. 11, pp. 2121–2132, May 2023, doi: 10.1007/s00216-023-04597-8.

[110]   OECD, *Test No. 202: Daphnia sp. Acute Immobilisation Test*. in OECD Guidelines for the Testing of Chemicals, Section 2. OECD, 2004. doi: 10.1787/9789264069947-en.

[111]   OECD, *Test No. 211: Daphnia magna Reproduction Test*. in OECD Guidelines for the Testing of Chemicals, Section 2. OECD, 2012. doi: 10.1787/9789264185203-en.

[112]   OECD, *Test No. 201: Alga, Growth Inhibition Test*. in OECD Guidelines for the Testing of Chemicals, Section 2: Effects on Biotic Systems. OECD Publishing, 2006. doi: 10.1787/9789264069923-en.

[113]   OECD, *Guidance Document on Aquatic Toxicity Testing of Difficult Substances and Mixtures*. in OECD Series on Testing and Assessment. OECD, 2019. doi: 10.1787/0ed2f88e-en.

[114]   K. Hund-Rinke *et al.*, "Prioritising nano- and microparticles: identification of physicochemical properties relevant for toxicity to Raphidocelis subcapitata and Daphnia magna," *Environ Sci Eur*, vol. 34, no. 1, p. 116, Dec. 2022, doi: 10.1186/s12302-022-00695-z.

[115]   M. Sillanpää, T.-M. Paunu, and P. Sainio, "Aggregation and deposition of engineered TiO$_2$ nanoparticles in natural fresh and brackish waters," *J. Phys.: Conf. Ser.*, vol. 304, p. 012018, Jul. 2011, doi: 10.1088/1742-6596/304/1/012018.

[116]   L. J. Johnston, N. Gonzalez-Rojano, K. J. Wilkinson, and B. Xing, "Key challenges for evaluation of the safety of engineered nanomaterials," *NanoImpact*, vol. 18, p. 100219, Apr. 2020, doi: 10.1016/j.impact.2020.100219.

[117]   S.-H. Lee, K. Jung, W. C. Yoo, J. Chung, and Y.-W. Lee, "Dispersion Stability of 14 Manufactured Nanomaterials for Ecotoxicity Tests Using Raphidocelis subcapitata," *IJERPH*, vol. 19, no. 12, p. 7140, Jun. 2022, doi: 10.3390/ijerph19127140.

[118]   European Commission. Joint Research Centre., *NANoREG framework for the safety assessment of nanomaterials.* LU: Publications Office, 2017. Accessed: Jul. 17, 2023. [Online]. Available: https://data.europa.eu/doi/10.2760/245972

[119]   A. A. Keller *et al.*, "Stability and Aggregation of Metal Oxide Nanoparticles in Natural Aqueous Matrices," *Environ. Sci. Technol.*, vol. 44, no. 6, pp. 1962–1967, Mar. 2010, doi: 10.1021/es902987d.

[120]   H. Kim, K. Park, and M.-Y. Lee, "Biocompatible Dispersion Methods for Carbon Black," *Toxicological Research*, vol. 28, no. 4, pp. 209–216, Dec. 2012, doi: 10.5487/TR.2012.28.4.209.

[121]   K. Dhangar, M. Kumar, M. Aouad, J. Mahlknecht, and N. P. Raval, "Aggregation behaviour of black carbon in aquatic solution: Effect of ionic strength and coexisting metals," *Chemosphere*, vol. 311, p. 137088, Jan. 2023, doi: 10.1016/j.chemosphere.2022.137088.

[122]   "Homepage - ECHA." Accessed: Sep. 04, 2023. [Online]. Available: https://echa.europa.eu/home

[123]   K. Schwirn and D. Völker, "Hazard grouping of nanomaterials for daphnia and algae toxicity: lessons learned from scientific projects for regulatory applicability," *Environ Sci Eur*, vol. 31, no. 1, p. 48, Dec. 2019, doi: 10.1186/s12302-019-0226-9.

[124]   Y. M. Abd-Elhakim, M. M. Hashem, K. Abo-EL-Sooud, B. A. Hassan, K. M. Elbohi, and A. A. Al-Sagheer, "Effects of Co-Exposure of Nanoparticles and Metals on Different Organisms: A Review," *Toxics*, vol. 9, no. 11, p. 284, Nov. 2021, doi: 10.3390/toxics9110284.

[125]   F. Zhang, Z. Wang, W. J. G. M. Peijnenburg, and M. G. Vijver, "Review and Prospects on the Ecotoxicity of Mixtures of Nanoparticles and Hybrid Nanomaterials," *Environ. Sci. Technol.*, vol. 56, no. 22, pp. 15238–15250, Nov. 2022, doi: 10.1021/acs.est.2c03333.

[126]   "Corpo Nazionale dei Vigili del Fuoco." Accessed: Aug. 05, 2023. [Online]. Available: https://www.vigilfuoco.it/aspx/Page.aspx?IdPage=5374

[127]   Z. Xu, X. Guo, L. Yan, and W. Kang, "Fire-extinguishing performance and mechanism of aqueous film-forming foam in diesel pool fire," *Case Studies in Thermal Engineering*, vol. 17, p. 100578, Feb. 2020, doi: 10.1016/j.csite.2019.100578.

[128]   Y. Huang, Z. Wencheng, X. Dai, and Y. Zhao, "Study on Water-based Fire Extinguishing Agent Formulations and Properties," *Procedia Engineering*, vol. 45, pp. 649–654, 2012, doi: 10.1016/j.proeng.2012.08.217.

[129]   G. Zhao, G. Xu, S. Jin, Q. Zhang, and Z. Liu, "Fire-Extinguishing Efficiency of Superfine Powders under Different Injection Pressures," *International Journal of Chemical Engineering*, vol. 2019, pp. 1–7, May 2019, doi: 10.1155/2019/2474370.

[130]   M. Lou, H. Jia, Z. Lin, D. Zeng, and J. Huo, "Study on fire extinguishing performance of different foam extinguishing agents in diesel pool fire," *Results in Engineering*, vol. 17, p. 100874, Mar. 2023, doi: 10.1016/j.rineng.2023.100874.

[131]   "Fire Extinguishers – Classes, Colour Coding, Rating, Location and Maintenance : Firesafe.org.uk." Accessed: Sep. 04, 2023. [Online]. Available: https://www.firesafe.org.uk/portable-fire-extinguisher-general/

[132]   "GHS SDS Preparation Tip 3: How to Choose Suitable Fire Extinguishing Agents." Accessed: Aug. 08, 2023. [Online]. Available: https://www.chemsafetypro.com/Topics/GHS/GHS_SDS_section_5_how_to_choose_suitable _fire_extinguishing_agents_for_chemicals.html

[133]   L. Lu, X. Han, J. Li, J. Hua, and M. Ouyang, "A review on the key issues for lithium-ion battery management in electric vehicles," *Journal of Power Sources*, vol. 226, pp. 272–288, Mar. 2013, doi: 10.1016/j.jpowsour.2012.10.060.

[134]   "Electric car catches fire, burns passenger - YouTube." Accessed: Aug. 05, 2023. [Online]. Available: https://www.youtube.com/watch?v=Bqwh4yUyJuE

[135]   M. Ghiji *et al.*, "A Review of Lithium-Ion Battery Fire Suppression," *Energies*, vol. 13, no. 19, p. 5117, Oct. 2020, doi: 10.3390/en13195117.

[136]   S. Yuan *et al.*, "A review of fire-extinguishing agent on suppressing lithium-ion batteries fire," *Journal of Energy Chemistry*, vol. 62, pp. 262–280, Nov. 2021, doi: 10.1016/j.jechem.2021.03.031.

[137]   W. Luo, S. Zhu, J. Gong, and Z. Zhou, "Research and Development of Fire Extinguishing Technology for Power Lithium Batteries," *Procedia Engineering*, vol. 211, pp. 531–537, 2018, doi: 10.1016/j.proeng.2017.12.045.

[138]   Russo Paola, Di Bari Cinzia, Mazzaro Michele, De Rosa Armando, and Morriello Ilario, "Effective fire extinguishing systems for lithium-ion battery," *Chemical Engineering Transactions*, vol. 67, pp. 727–732, Sep. 2018, doi: 10.3303/CET1867122.

[139]   T. Liu, Y. Liu, X. Wang, X. Kong, and G. Li, "Cooling control of thermally-induced thermal runaway in 18,650 lithium ion battery with water mist," *Energy Conversion and Management*, vol. 199, p. 111969, Nov. 2019, doi: 10.1016/j.enconman.2019.111969.

[140]   "Hazard Control Technologies Europe srl - Incapsulazione." Accessed: Aug. 05, 2023. [Online]. Available: https://www.f-500.it/incapsulazione/

[141] W. Mrozik, M. A. Rajaeifar, O. Heidrich, and P. Christensen, "Environmental impacts, pollution sources and pathways of spent lithium-ion batteries," *Energy Environ. Sci.*, vol. 14, no. 12, pp. 6099–6121, 2021, doi: 10.1039/D1EE00691F.

[142] European Union, "Consolidated text: Directive 2008/98/EC of the European Parliament and of the Council of 19 November 2008 on waste and repealing certain Directives (Text with EEA relevance)." Jul. 05, 2018. [Online]. Available: https://eur-lex.europa.eu/eli/dir/2008/98/2018-07-05

[143] European Union, "Commission Regulation (EU) No 1357/2014 of 18 December 2014 replacing Annex III to Directive 2008/98/EC of the European Parliament and of the Council on waste and repealing certain Directives Text with EEA relevance." Dec. 19, 2014. [Online]. Available: https://eur-lex.europa.eu/legal-content/EN/TXT/?uri=celex%3A32014R1357

[144] Italian Ministry of the Environment, "Decreto Legislativo n. 152: Codice dell'Ambiente." Gazzetta Ufficiale della Repubblica Italiana No. 88, Apr. 03, 2006. [Online]. Available: https://www.fao.org/faolex/results/details/en/c/LEX-FAOC064213/

[145] U.S. EPA, "Method 8015C (SW-846): Nonhalogenated Organics Using GC/FID." 2003. [Online]. Available: https://www.epa.gov/esam/epa-method-8015d-sw-846-nonhalogenated-organics-using-gcfid

[146] U.S. EPA, "Method 8260D (SW-846): Volatile Organic Compounds by Gas Chromatography/Mass Spectrometry (GC/MS)." 2006. [Online]. Available: https://www.epa.gov/esam/epa-method-8260d-sw-846-volatile-organic-compounds-gas-chromatography-mass-spectrometry-gcms

[147] U.S. EPA, "Method 5021A: Volatile Organic Compounds in Various Sample Matrices Using Equilibrium Headspace Analysis, part of Test Methods for Evaluating Solid Waste, Physical/Chemical Methods." 2014. [Online]. Available: https://www.epa.gov/hw-sw846/sw-846-test-method-5021a-volatile-organic-compounds-vocs-various-sample-matrices-using

[148] U.S. EPA, "Method 200.8: Determination of Trace Elements in Waters and Wastes by Inductively Coupled Plasma-Mass Spectrometry." 1994. [Online]. Available: https://www.epa.gov/esam/epa-method-2008-determination-trace-elements-waters-and-wastes-inductively-coupled-plasma-mass

[149] M. Ermrich and D. Opper, *XRD for the analyst: getting acquainted with the principles*, 2nd revised edition. Almelo: PANalytical, 2013.

[150] S. Gražulis *et al.*, "Crystallography Open Database – an open-access collection of crystal structures," *J Appl Crystallogr*, vol. 42, no. 4, pp. 726–729, Aug. 2009, doi: 10.1107/S0021889809016690.

[151] F. Horsthemke *et al.*, "Fast screening method to characterize lithium ion battery electrolytes by means of solid phase microextraction – gas chromatography – mass spectrometry," *RSC Adv.*, vol. 7, no. 74, pp. 46989–46998, 2017, doi: 10.1039/C7RA08599K.

[152] B. Wiedemer, "Analysis of Ethylene Carbonate and Ethyl Methyl Carbonate by GC/FID on a Thermo Scientific TraceGOLD TG-35MS Column".

[153] J. M. Anderson and G. Voskerician, "The challenge of biocompatibility evaluation of biocomposites," in *Biomedical Composites*, Elsevier, 2010, pp. 325–353. doi: 10.1533/9781845697372.3.325.

[154] C. Di Bari *et al.*, "Test di caratterizzazione e di calorimetria a cono condotti su celle di interesse automotive," RdS/PAR2017/247, 2018. [Online]. Available: https://www.enea.it/it/Ricerca_sviluppo/documenti/ricerca-di-sistema-elettrico/adp-mise-enea-2015-2017/mobilita-elettrica/report-2017/rds-par2017-247.pdf

[155] D. P. Finegan *et al.*, "Identifying the Cause of Rupture of Li-Ion Batteries during Thermal Runaway," *Advanced Science*, vol. 5, no. 1, p. 1700369, Jan. 2018, doi: 10.1002/advs.201700369.

[156] T. Ohzuku, A. Ueda, and N. Yamamoto, "Zero-Strain Insertion Material of Li [Li1 / 3Ti5 / 3] O 4 for Rechargeable Lithium Cells," *J. Electrochem. Soc.*, vol. 142, no. 5, pp. 1431–1435, May 1995, doi: 10.1149/1.2048592.

[157] L. Zhao, H.-L. Pan, Y.-S. Hu, H. Li, and L.-Q. Chen, "Spinel lithium titanate (Li $_4$ Ti $_5$ O $_{12}$) as novel anode material for room-temperature sodium-ion battery," *Chinese Phys. B*, vol. 21, no. 2, p. 028201, Feb. 2012, doi: 10.1088/1674-1056/21/2/028201.

[158] N. Mao, Z.-R. Wang, Y.-H. Chung, and C.-M. Shu, "Overcharge cycling effect on the thermal behavior, structure, and material of lithium-ion batteries," *Applied Thermal Engineering*, vol. 163, p. 114147, Dec. 2019, doi: 10.1016/j.applthermaleng.2019.114147.

[159] H.-S. Kim, R. Verma, J. Kim, and C.-J. Park, "Effect of Urea as Electrolyte Additive for Stabilization of Lithium Metal Electrodes," *ACS Sustainable Chem. Eng.*, vol. 8, no. 30, pp. 11123–11132, Aug. 2020, doi: 10.1021/acssuschemeng.0c01513.

[160] A. La Monaca *et al.*, "1,3-Dioxolane: A Strategy to Improve Electrode Interfaces in Lithium Ion and Lithium-Sulfur Batteries," *ChemElectroChem*, vol. 5, no. 9, pp. 1272–1278, May 2018, doi: 10.1002/celc.201701348.

[161] A. G. Paul-Orecchio, J. A. Weeks, A. Dolocan, and C. B. Mullins, "High-Stability Lithium Metal Batteries Enabled by a Tetrahydrofuran-Based Electrolyte Mixture," *ACS Appl. Energy Mater.*, vol. 5, no. 8, pp. 9437–9446, Aug. 2022, doi: 10.1021/acsaem.2c00993.

[162] D. Bresser, E. Paillard, and S. Passerini, "Lithium-ion batteries (LIBs) for medium- and large-scale energy storage:," in *Advances in Batteries for Medium and Large-Scale Energy Storage*, Elsevier, 2015, pp. 125–211. doi: 10.1016/B978-1-78242-013-2.00006-6.

[163] W. Zhang *et al.*, "Combustion calorimetry of carbonate electrolytes used in lithium ion batteries," *Journal of Fire Sciences*, vol. 33, no. 1, pp. 22–36, Jan. 2015, doi: 10.1177/0734904114550789.

[164] K. Liu, Y. Liu, D. Lin, A. Pei, and Y. Cui, "Materials for lithium-ion battery safety," *SCIENCE ADVANCES*, 2018.

[165] N. H. Almousa *et al.*, "Paraffin Wax [As a Phase Changing Material (PCM)] Based Composites Containing Multi-Walled Carbon Nanotubes for Thermal Energy Storage (TES) Development," *Crystals*, vol. 11, no. 8, p. 951, Aug. 2021, doi: 10.3390/cryst11080951.

[166] C. Bergeron, E. Perrier, A. Potier, and G. Delmas, "A Study of the Deformation, Network, and Aging of Polyethylene Oxide Films by Infrared Spectroscopy and Calorimetric Measurements," *International Journal of Spectroscopy*, vol. 2012, pp. 1–13, Feb. 2012, doi: 10.1155/2012/432046.

[167] J. Mo *et al.*, "Polyethylene Oxide as a Multifunctional Binder for High-Performance Ternary Layered Cathodes," *Polymers*, vol. 13, no. 22, p. 3992, Nov. 2021, doi: 10.3390/polym13223992.

[168] Y.-B. He *et al.*, "Gassing in Li4Ti5O12-based batteries and its remedy," *Sci Rep*, vol. 2, no. 1, p. 913, Dec. 2012, doi: 10.1038/srep00913.

[169] A. W. Golubkov *et al.*, "Thermal-runaway experiments on consumer Li-ion batteries with metal-oxide and olivin-type cathodes," *RSC Adv.*, vol. 4, no. 7, pp. 3633–3642, 2014, doi: 10.1039/C3RA45748F.

[170] A. W. Golubkov *et al.*, "Thermal runaway of commercial 18650 Li-ion batteries with LFP and NCA cathodes – impact of state of charge and overcharge," *RSC Adv.*, vol. 5, no. 70, pp. 57171–57186, 2015, doi: 10.1039/C5RA05897J.

[171] "Respiratory Protection - Overview | Occupational Safety and Health Administration." Accessed: Oct. 24, 2023. [Online]. Available: https://www.osha.gov/respiratory-protection

[172] "Respiratory protective filters: colour code, class, etc. | Be Atex." Accessed: Oct. 24, 2023. [Online]. Available: https://www.be-atex.com/en/respiratory-protective-filters-colour-code-class-etc

[173] "Natural Graphite (C) Nanopowder/Nanoparticles, Purity: 99.9% Size: 400 nm-1.2 um." Accessed: Jul. 19, 2023. [Online]. Available: https://nanographenex.com/natural-graphite-c-nanopowder-nanoparticles-purity-99.9-size-400-nm-1.2-um-nanoparticles?search=carbon&description=true&category_id=60&sub_category=true

[174] "Silicon (Si) Nanopowder/Nanoparticles, Purity: 98+%, Size: 40-60 nm, Laser Synthesized." Accessed: Jul. 19, 2023. [Online]. Available: https://nanographenex.com/silicon-si-

nanopowder-nanoparticles-purity-98-size-40-60-nm-laser-synthesized-
nanoparticles?search=silicon%2040%20-%2060%20nm

[175]   "Vulcan XC72 Conductive Carbon Black." Accessed: Jul. 19, 2023. [Online]. Available:
https://nanographenex.com/vulcan-xc72-conductive-carbon-black-
nanoparticles?search=carbon%20black&description=true&category_id=60&sub_category=tru
e

[176]   "MCMB (MesoCarbon MicroBeads) Graphite Powder for Li-ion Battery Anode, 250g/bag -
EQ-Lib-MCMB." Accessed: Jul. 19, 2023. [Online]. Available:
https://www.mtixtl.com/MCMBMesoCarbonMicroBeadsGraphitePowderforLi-
ionBatteryAnode250g.aspx

[177]   "Li4Ti5O12 Powder for Li-ion battery anode, 200g/bag - EQ-Lib-LTO." Accessed: Jul. 19,
2023. [Online]. Available: https://www.mtixtl.com/Li4Ti5O12PowderforLi-
ionbatteryanode200g/bag-EQ-Lib-LTO.aspx

[178]   ISO, "ISO 13320:2020 Particle size analysis — Laser diffraction methods." 2020. [Online].
Available: https://www.iso.org/standard/69111.html

[179]   ISO, "ISO 9277:2010 Determination of the specific surface area of solids by gas adsorption
— BET method." 2010. [Online]. Available: https://www.iso.org/standard/44941.html

[180]   ASTM, "ASTM B923-22 Standard Test Method for Metal Powder Skeletal Density by
Helium or Nitrogen Pycnometry." Apr. 07, 2022. [Online]. Available:
https://www.astm.org/b0923-22.html

Appendix

Appendix 1 – LTO/NCA thermal abuse tests

In this section are reported all the graphs relative to the thermal abuse tests of the LTO/NCA at two different SoCs, 50 and 100 %.

Specifically, in Figure 88 are shown the graphs of the temperature-profile, in Figure 89 are shown the gas emission profiles and finally in Figure 90 and Figure 91 are shown the ATR-FT-IR spectra of the products emitted for the thermal abuse test, both liquid and solid.
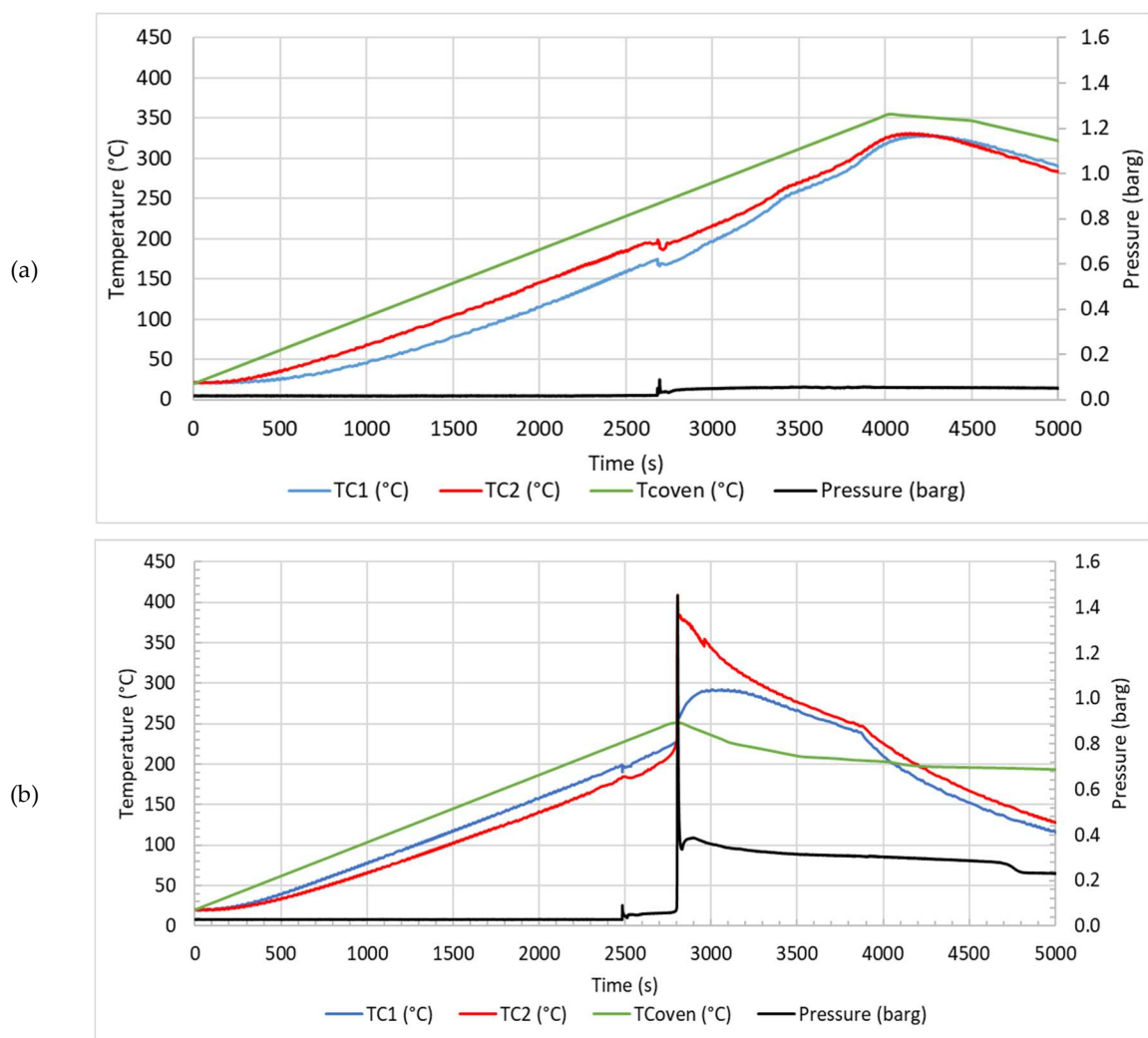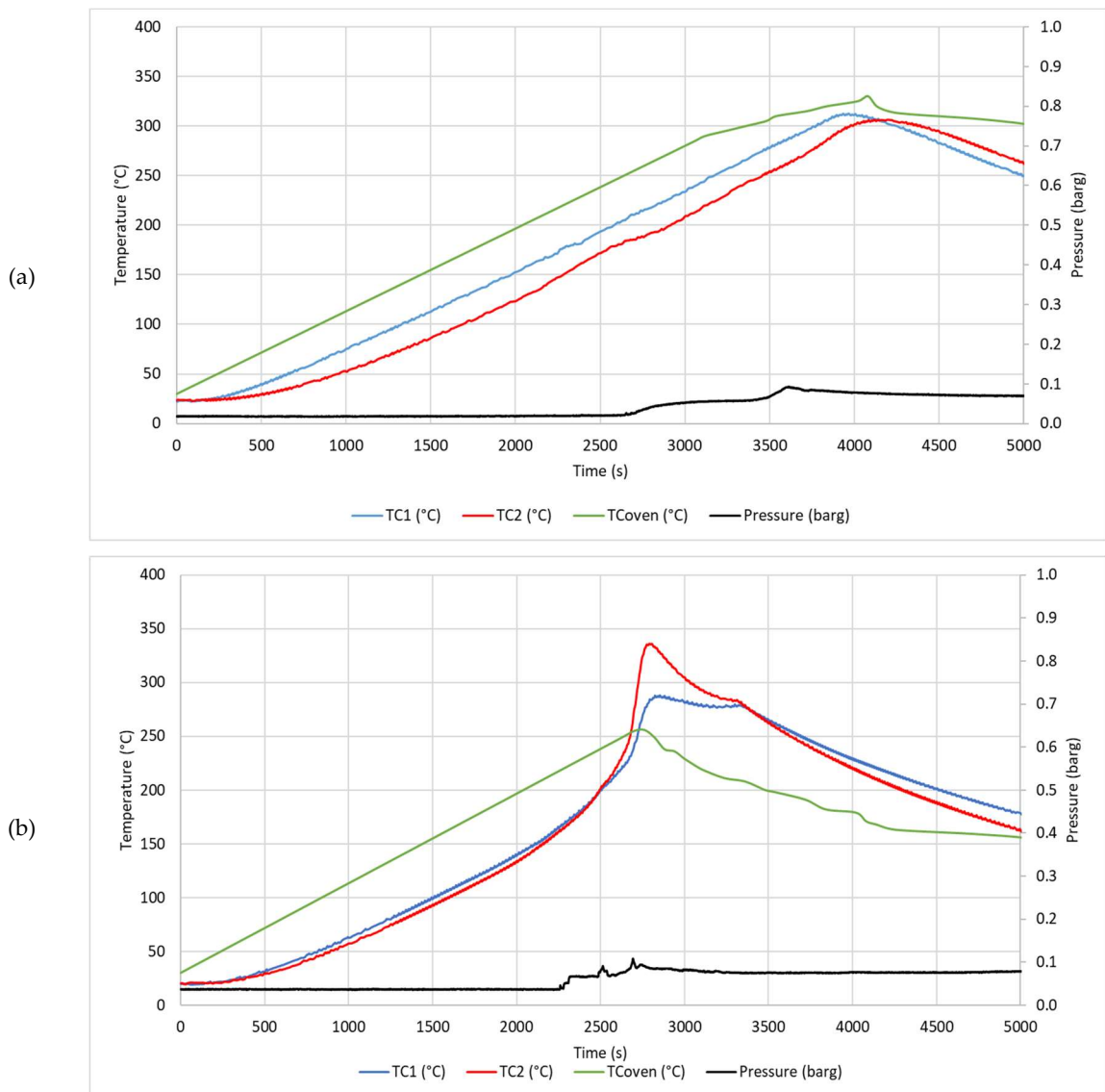

Figure 88: temperature (°C) and pressure (barg) profiles for thermal abuse test on LTO at SOC: (a) 50 %; (b) 100 %.
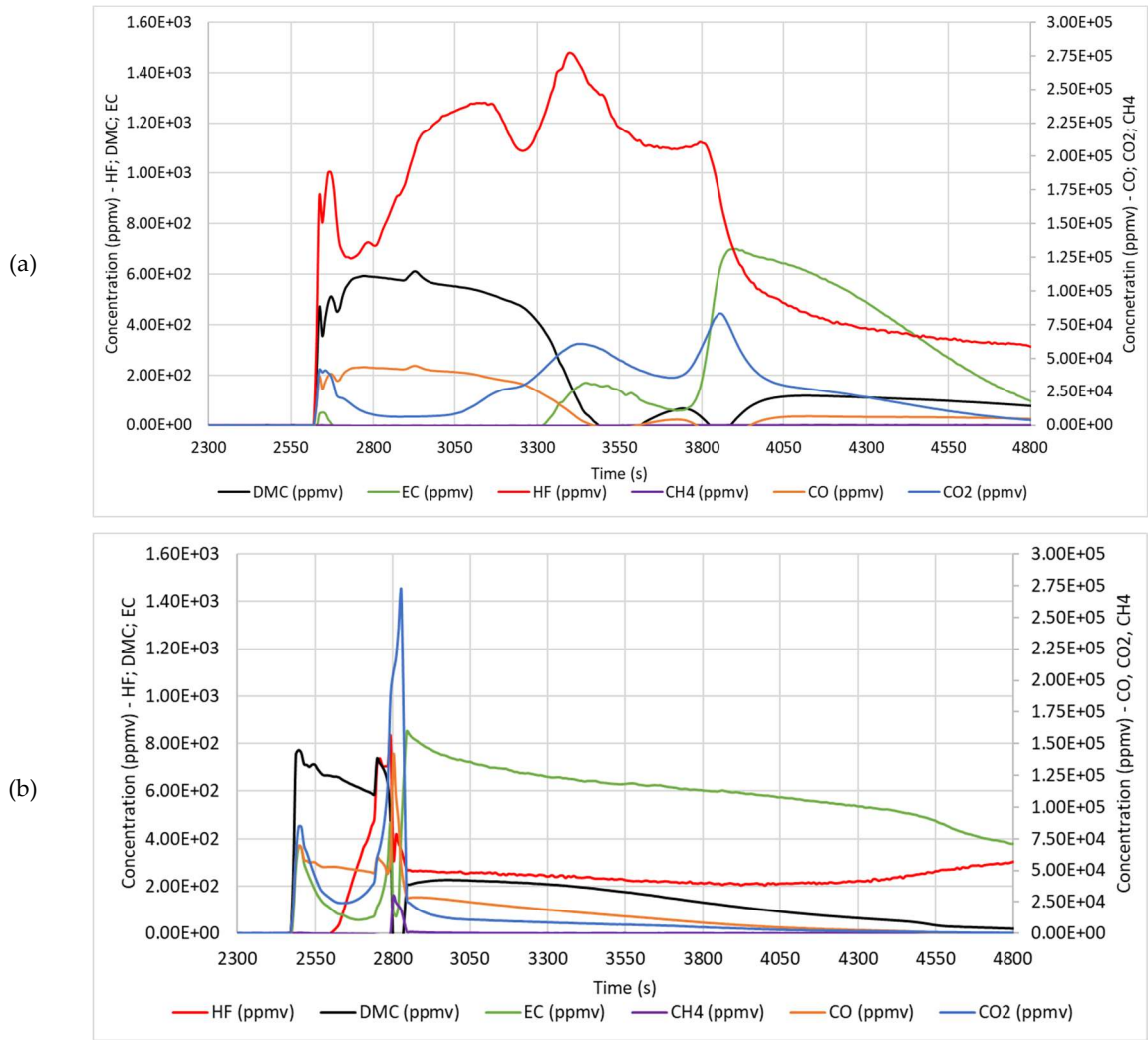
Figure 89: concentration profiles (ppmv) of DMC, EC, HF, CH$_4$, CO and CO$_2$ for thermal abuse test on LTO at SOC: (a) 50 %; (b) 100 %.
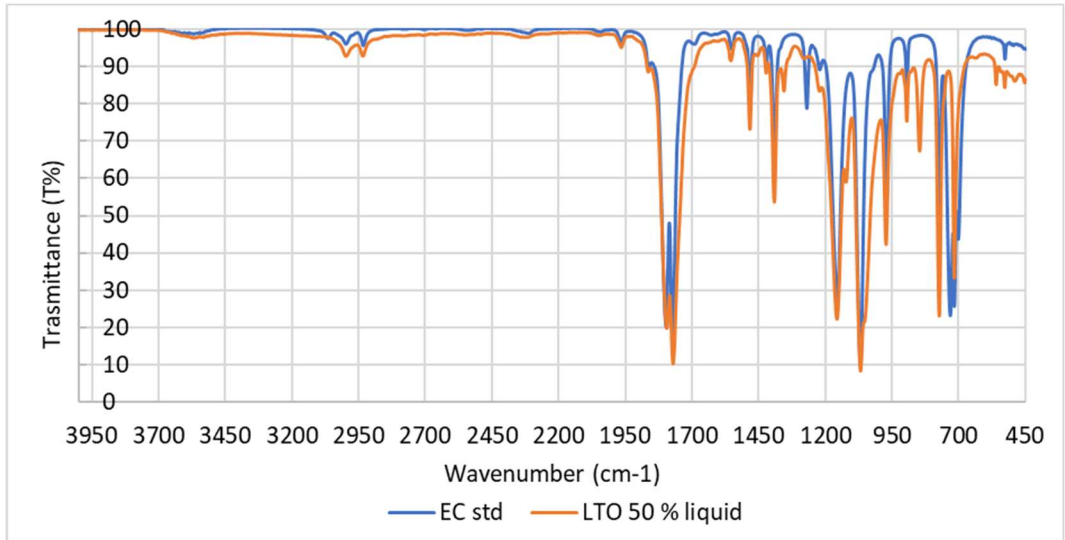
Figure 90: comparison between the spectra of the liquid residue collected after the thermal abuse test on LTO at 50 % and the EC standard spectra.
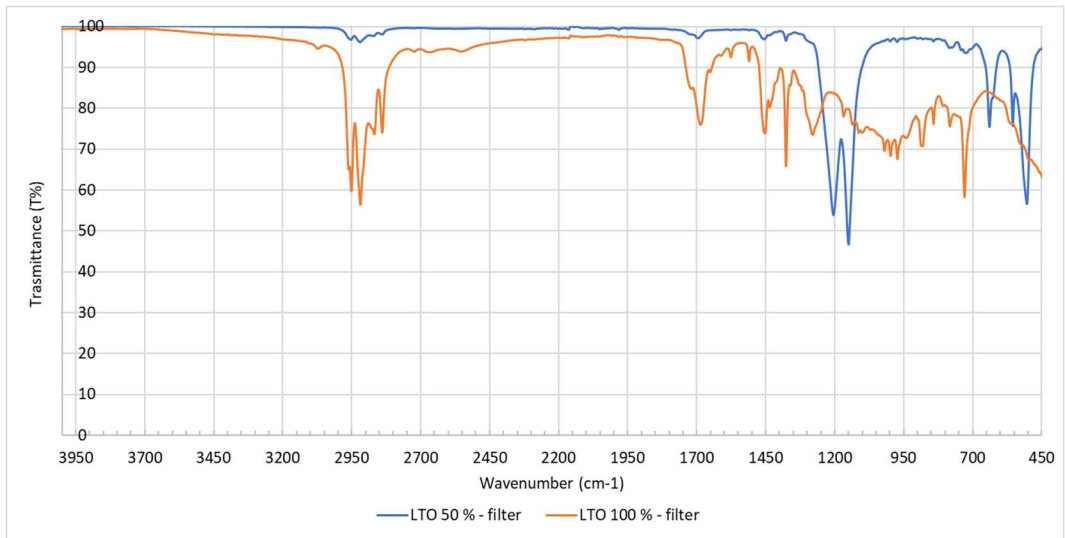

Figure 91: spectra of the solid residue collected after the thermal abuse test on LTO at 50 % and the 100 %.

Appendix 2 – C/LFP thermal abuse tests

In this section are reported all the graphs relative to the thermal abuse tests of the C/LFP at two different SoCs, 50 and 100 %.

Specifically, in Figure 92 are shown the graphs of the temperature-profile, in Figure 93 are shown the gas emission profiles and finally in Figure 94 and Figure 95 are shown the ATR-FT-IR spectra of the products emitted for the thermal abuse test, both liquid and solid.

Figure 92: temperature (°C) and pressure (barg) profiles for thermal abuse test on LFP at SoC: (a) 50 %; (b) 100 %.
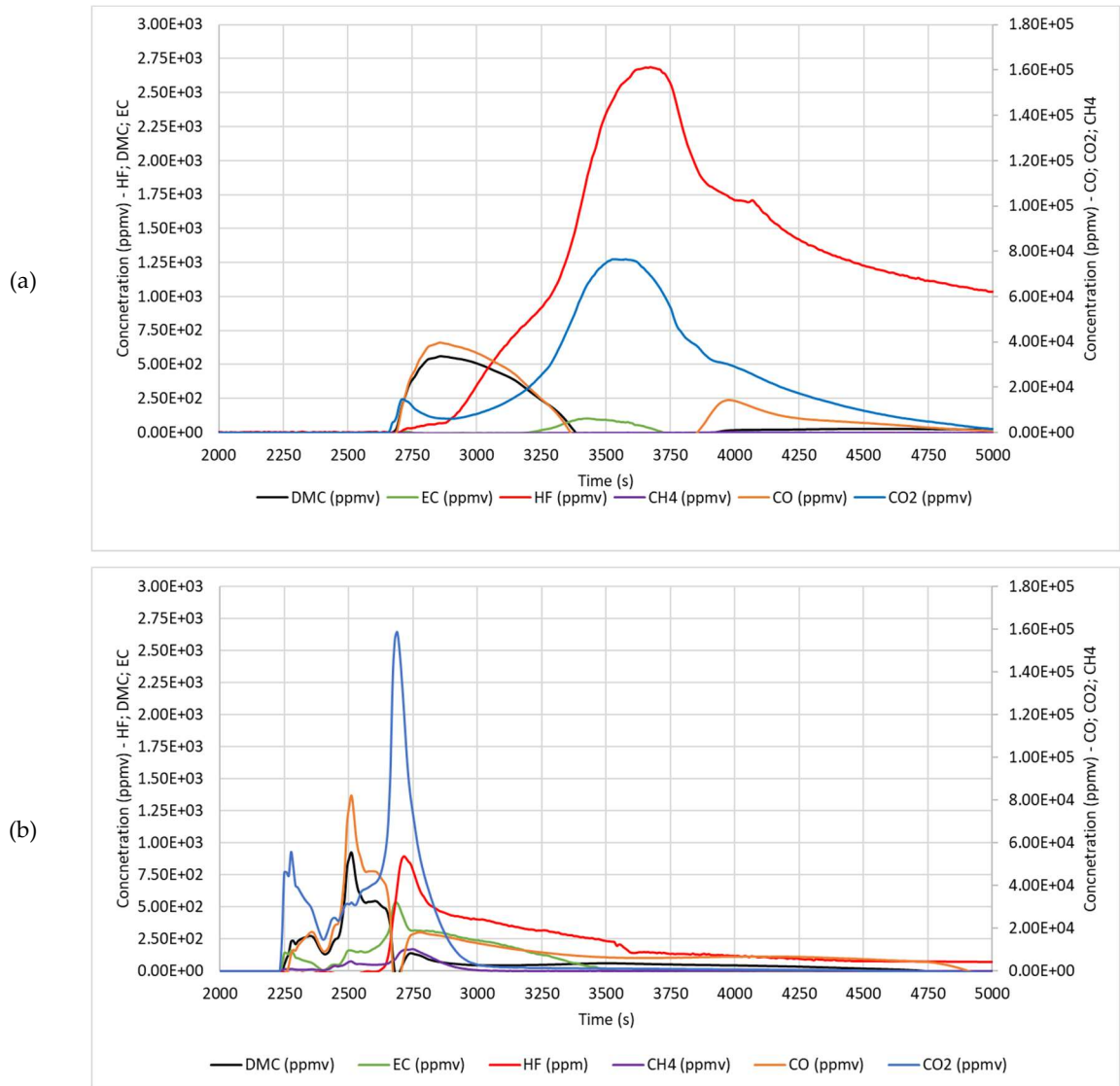
Figure 93: concentration profiles, expressed in ppmv, of DMC, EC, HF, CH₄, CO and CO₂ for thermal abuse test on LFP at SoC: (a) 50 %; (b) 100 %.
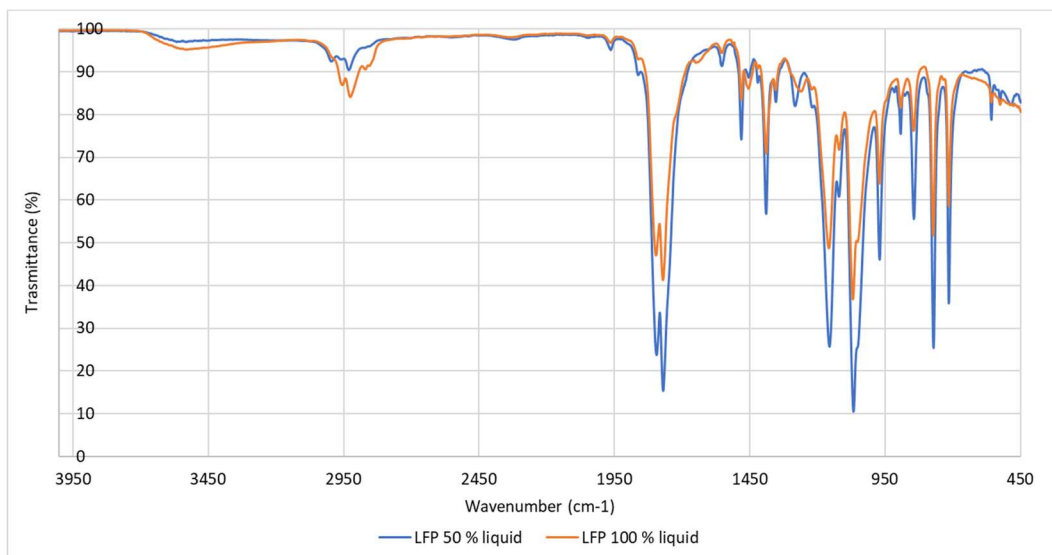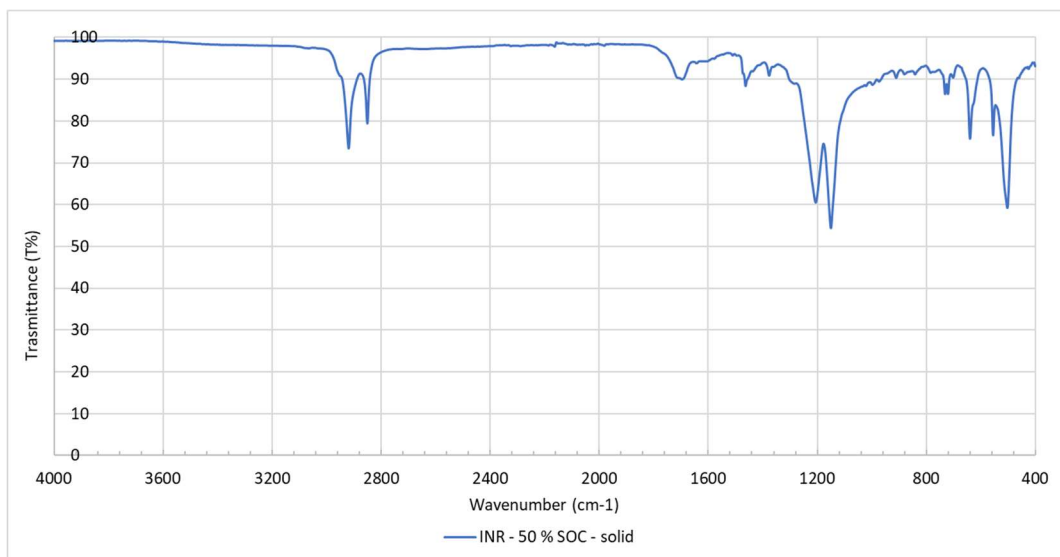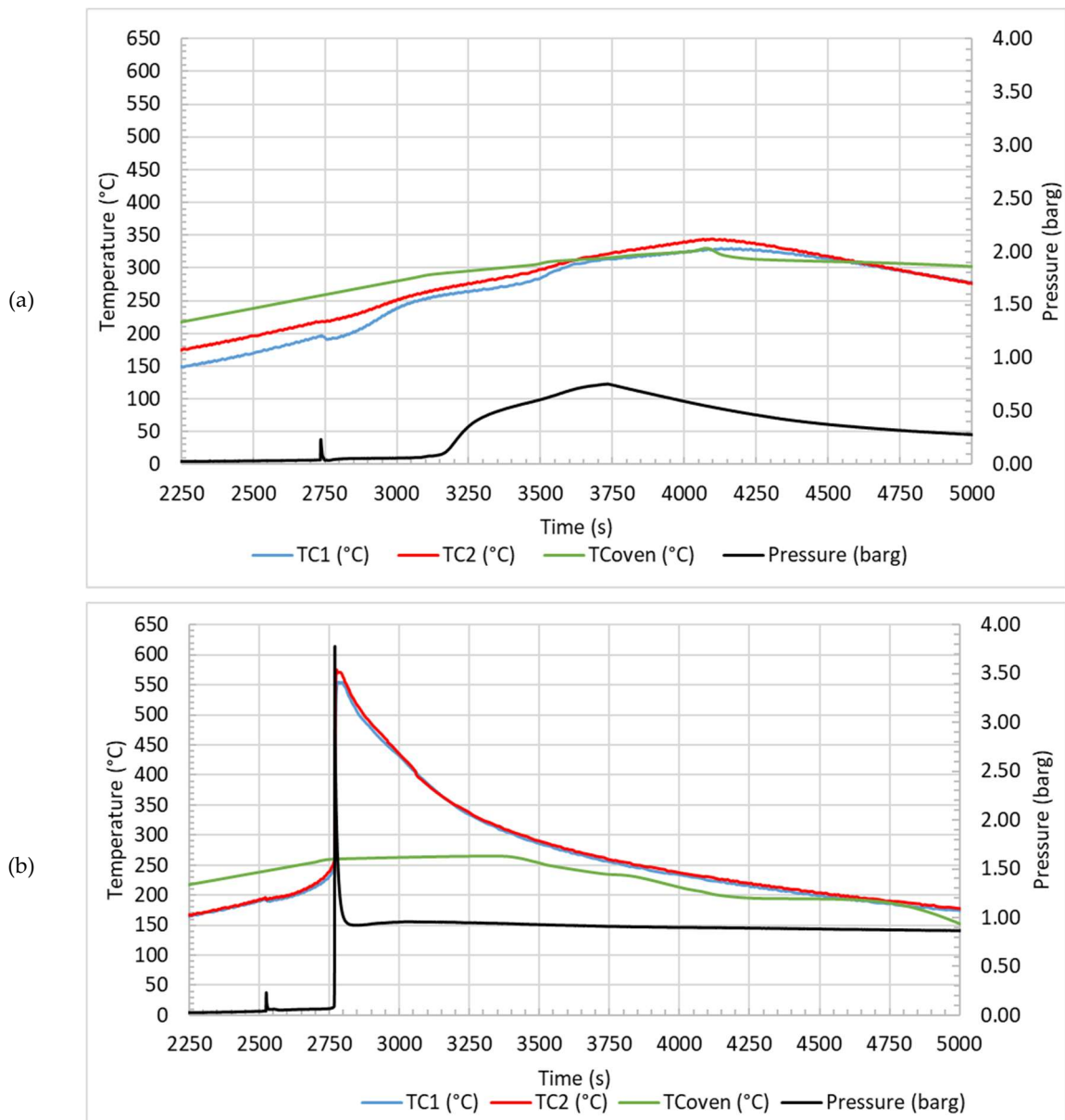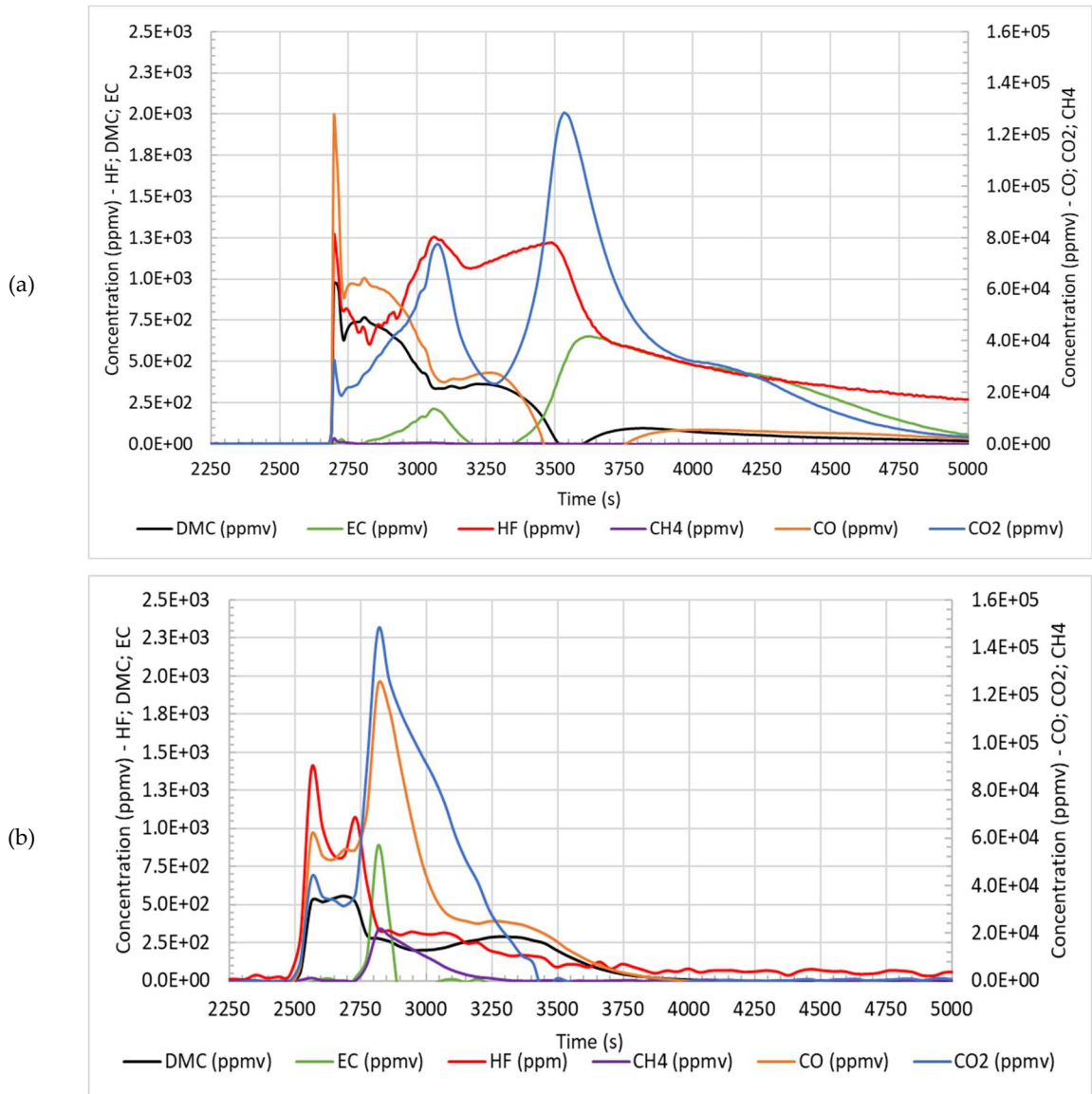
Figure 94: ATR-FT-IR spectra of the liquid obtained by the thermal abuse test on LFP at 50 % (blue) and 100 % (orange).
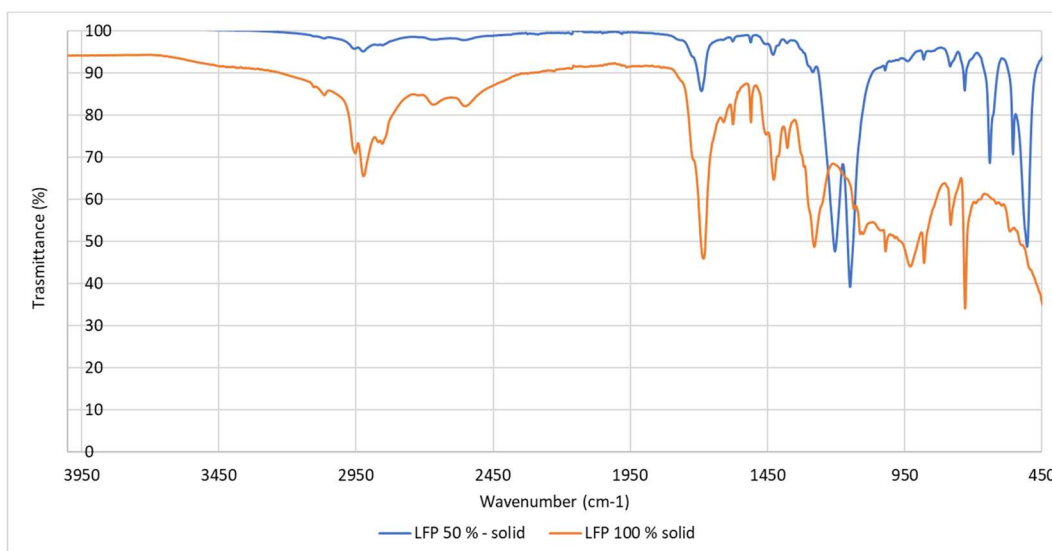
Figure 95: ATR-FT-IR spectra of the solid obtained by the thermal abuse test on LFP at 50 % (blue) and 100 % (orange).

Appendix 3 – C/NMC thermal abuse tests

In this section are reported all the graphs relative to the thermal abuse tests of the C/NMC at two different SoCs, 50 and 100 %.

Specifically, in Figure 96 are shown the graphs of the temperature-profile, in Figure 97 are shown the gas emission profiles and finally in Figure 98 is shown the ATR-FT-IR spectra of the solid product emitted for the thermal abuse test.
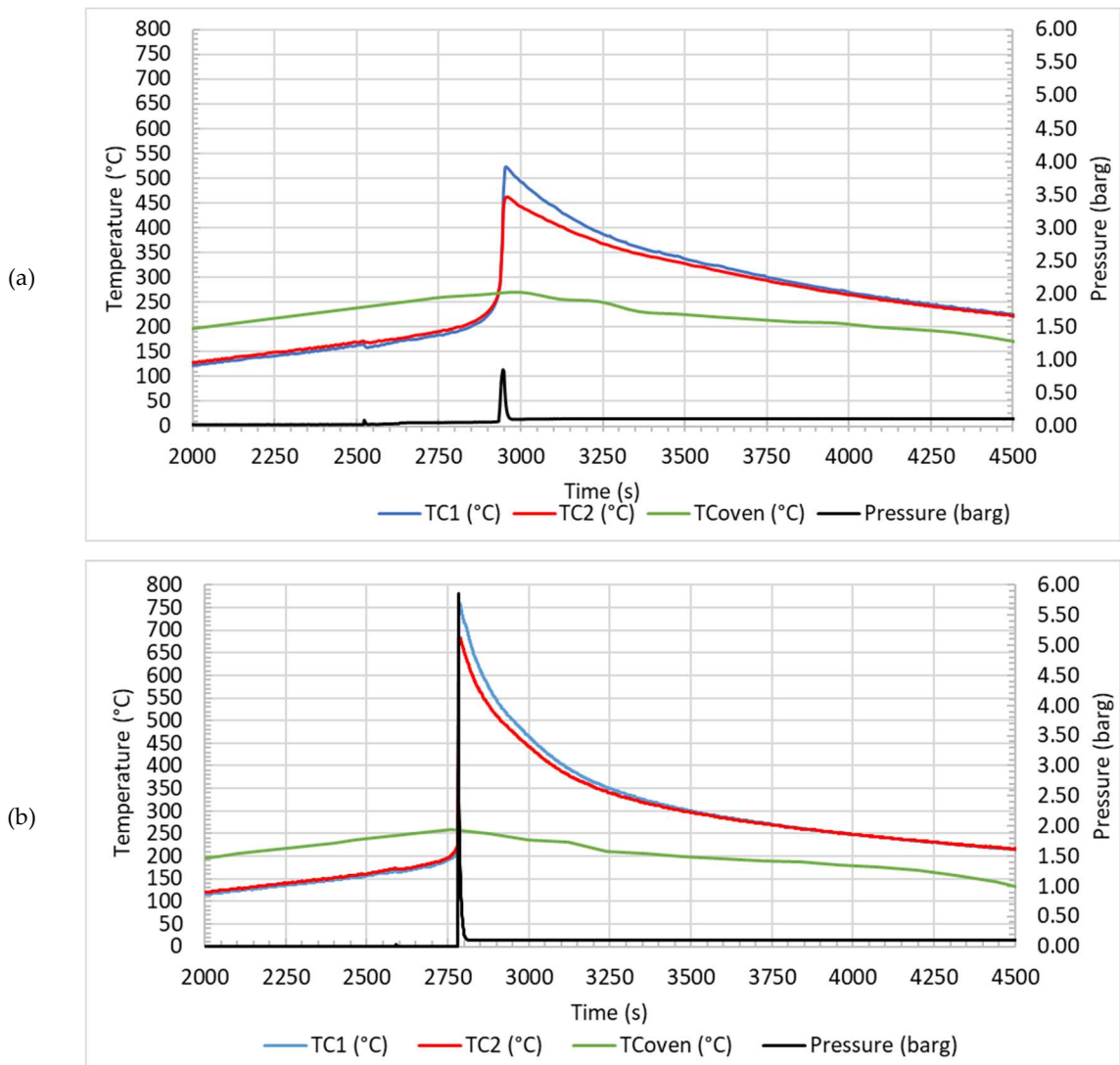
Figure 96: temperature (°C) and pressure (barg) profiles for thermal abuse test on NMC at SoC: (a) 50 %; (b) 100 %.
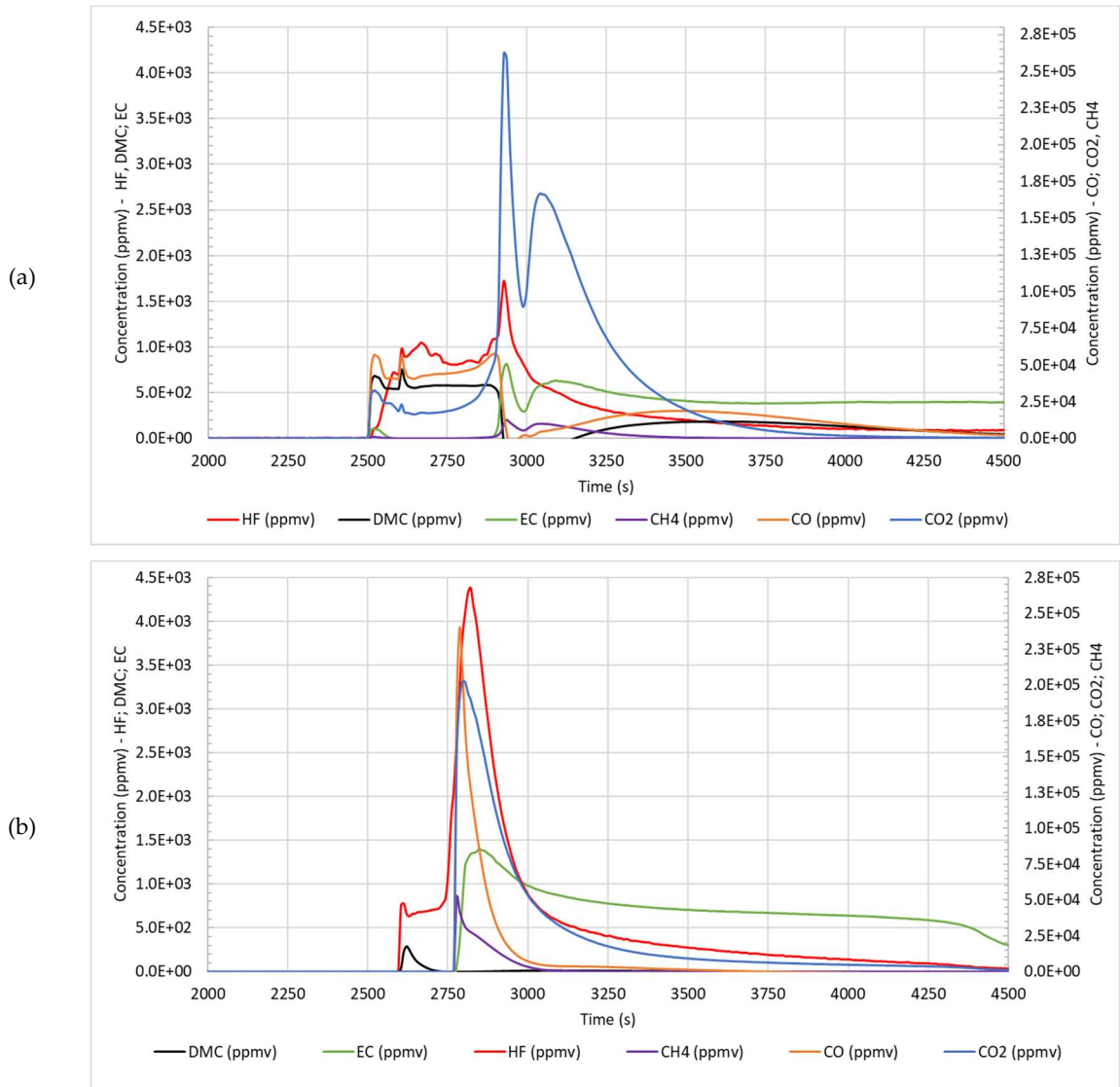
Figure 97: concentration profiles, expressed in ppmv, of DMC, EC, HF, CH$_4$, CO and CO$_2$ for thermal abuse test on NMC at SoC: (a) 50 %; (b) 100 %.
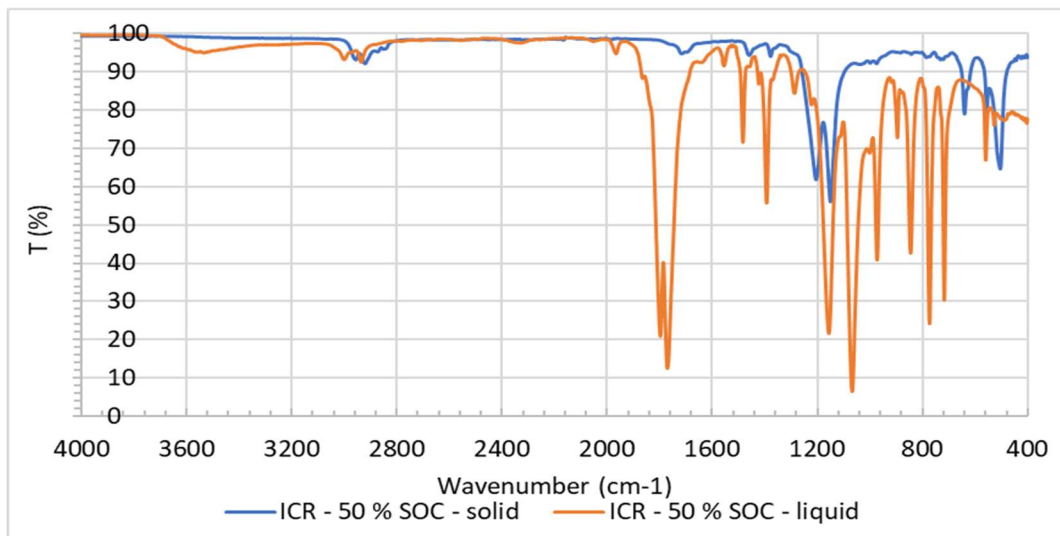

Figure 98: ATR-FT-IR spectra of the filter obtained by the thermal abuse test on NMC at 50 %.

Appendix 4 – C/LCO thermal abuse tests

In this section are reported all the graphs relative to the thermal abuse tests of the C/LCO at two different SoCs, 50 and 100 %.

Specifically, in Figure 99 are shown the graphs of the temperature-profile, in Figure 100 are shown the gas emission profiles and finally in Figure 101 are shown the ATR-FT-IR spectra of the products emitted for the thermal abuse test, both liquid and solid.

(a)

(b)

Figure 99: temperature (°C) and pressure (barg) profiles for thermal abuse test on LCO at SOC: (a) 50 %; (b) 100 %.

Figure 100: concentration profiles, expressed in ppmv, of DMC, EC, HF, CH$_4$, CO and CO$_2$ for thermal abuse test on LCO at SOC: (a) 50 %; (b) 100 %.


Figure 101: ATR-FT-IR spetra of the filter (blue line) and the liquid (orange line) obtained by the thermal abuse test on LCO at 50 %.

Appendix 5 – C/NCA additional thermal abuse tests

In this section are reported all the graphs relative to the additional thermal abuse tests of the C/NCA at 50 % SoC in two different atmosphere, air and N₂.

Specifically, in Figure 102 are shown the graphs of the temperature-profile, in Figure 103 are shown the gas emission profiles and finally in Figure 104 are shown the ATR-FT-IR spectra of the products emitted for the thermal abuse test, both liquid and solid.
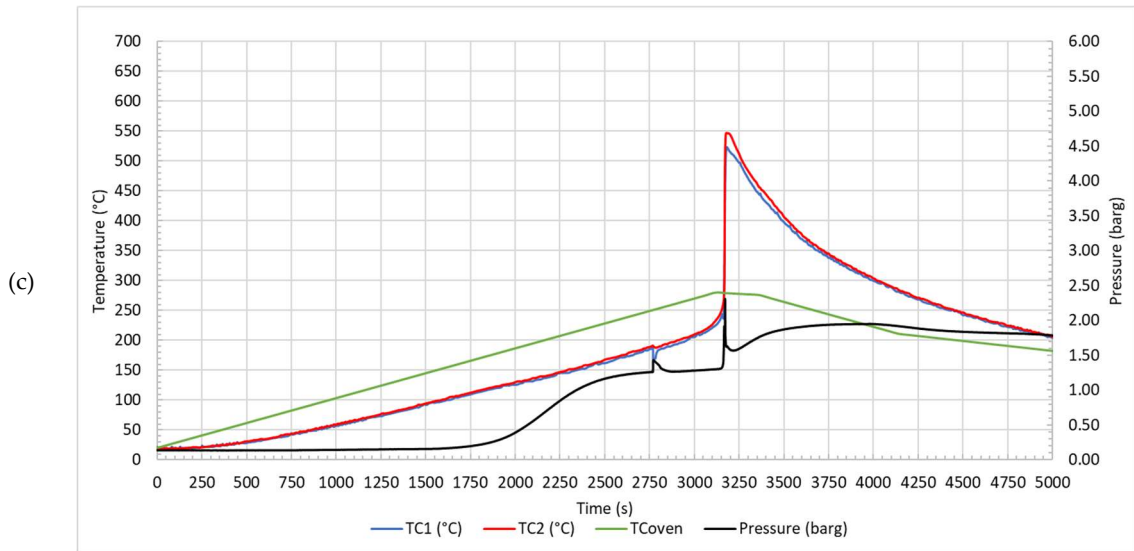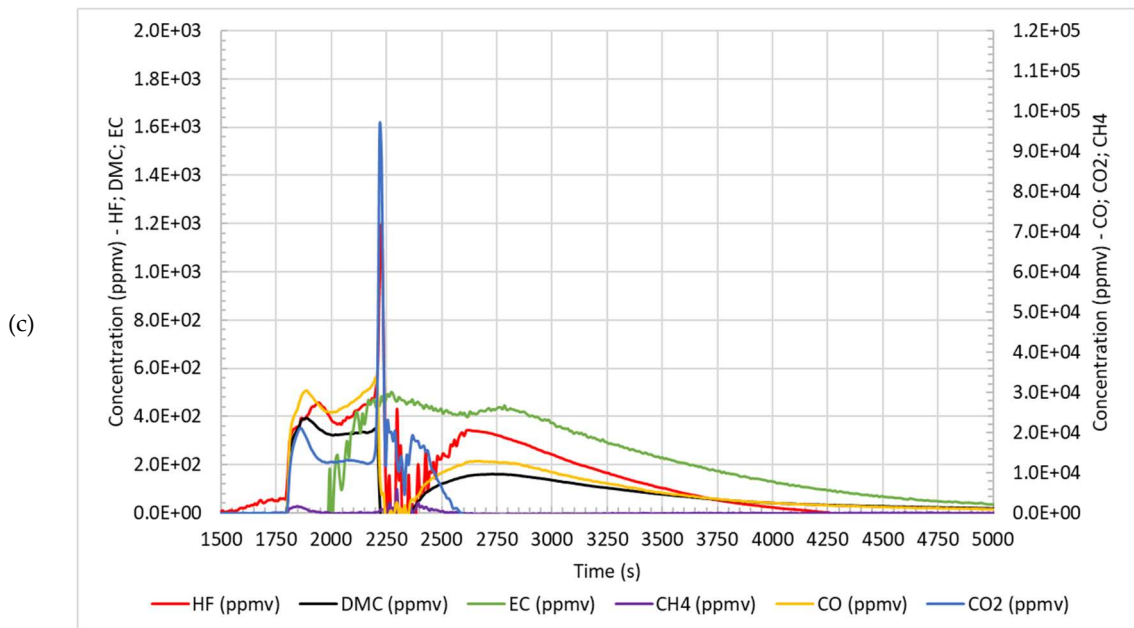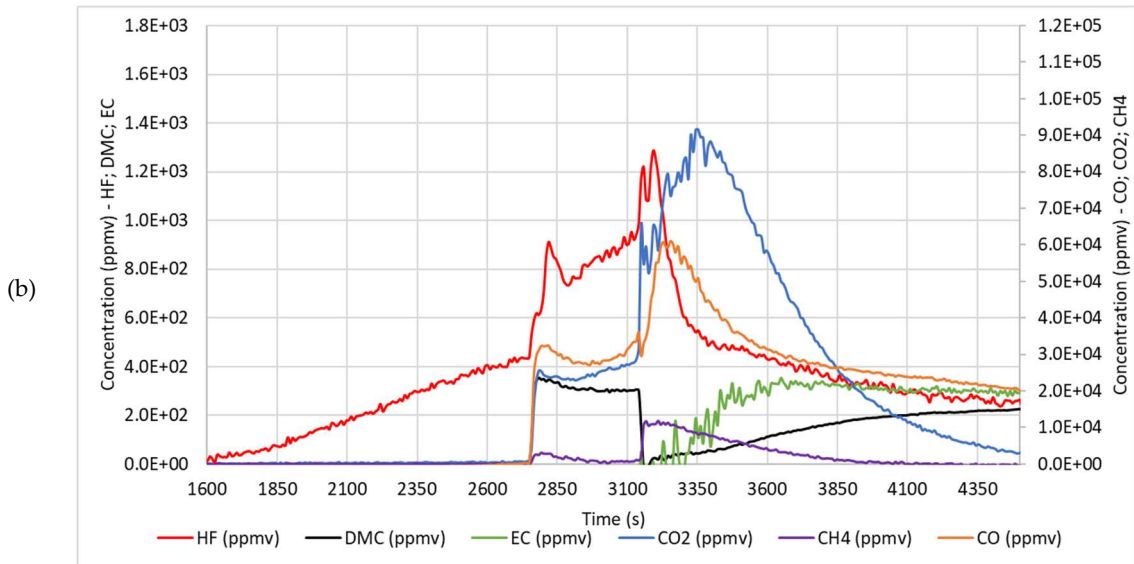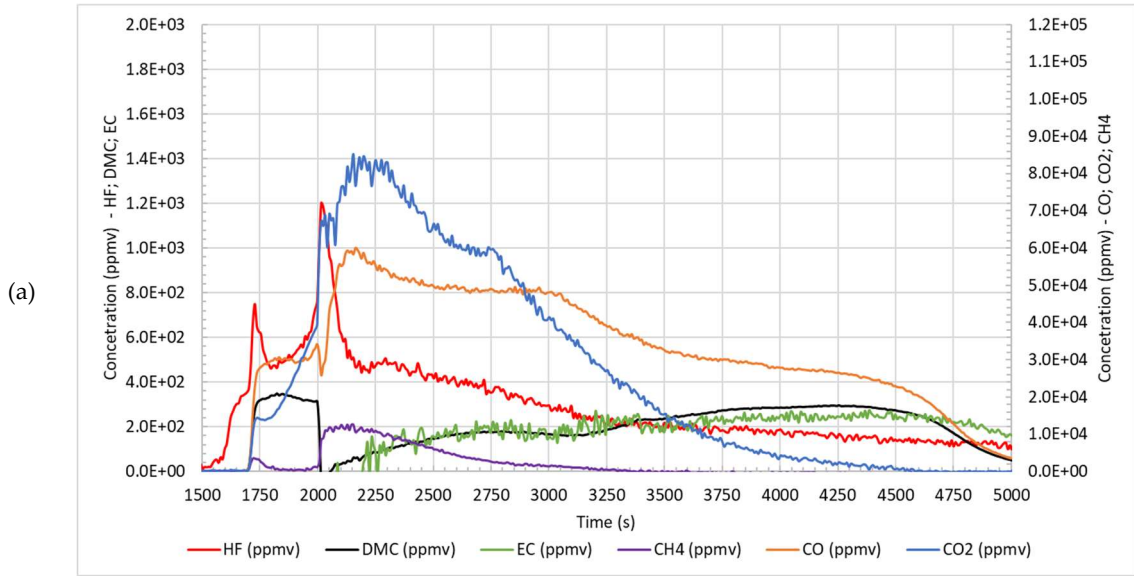
(c)

(d)
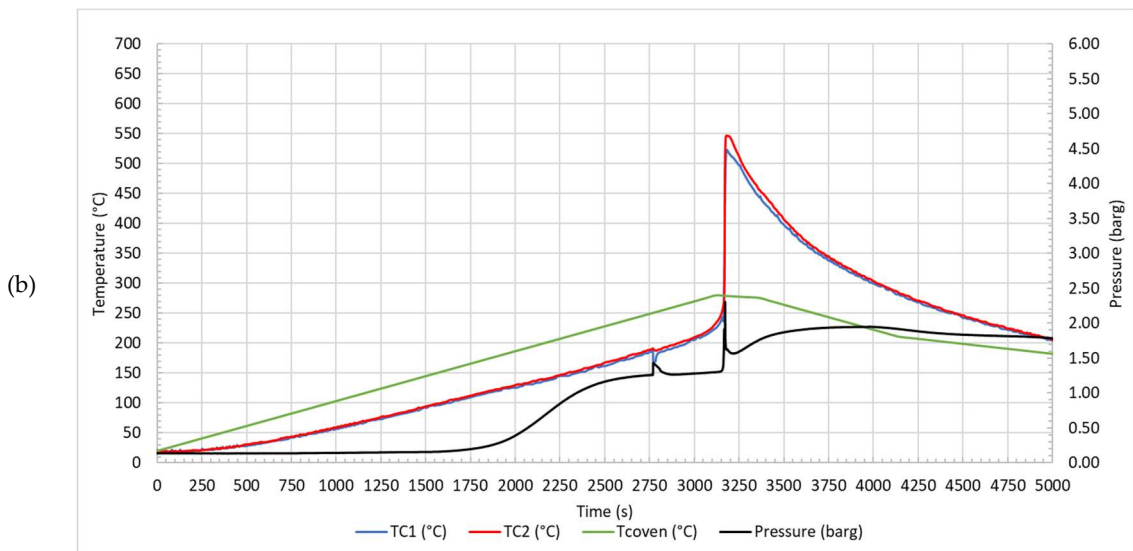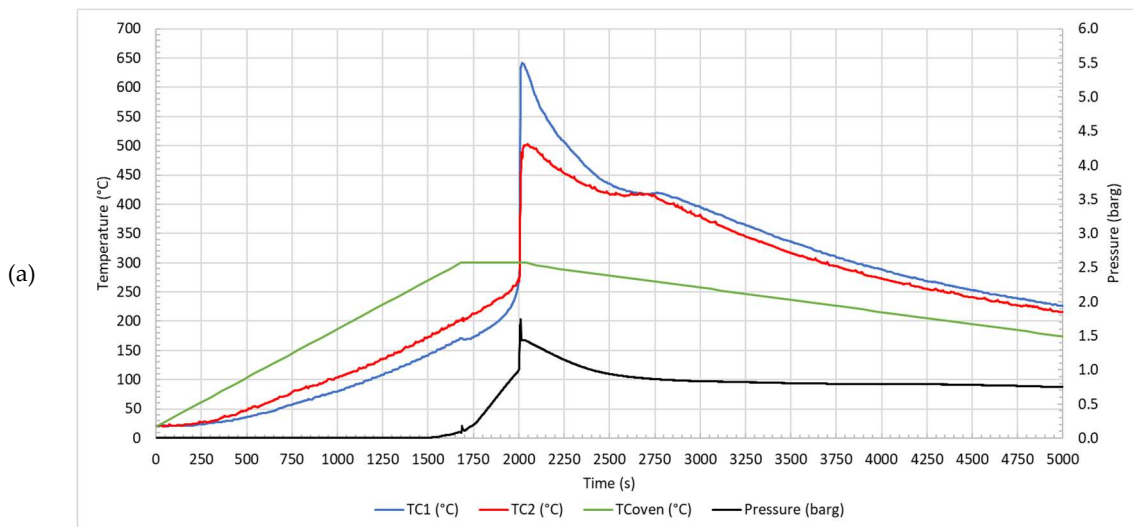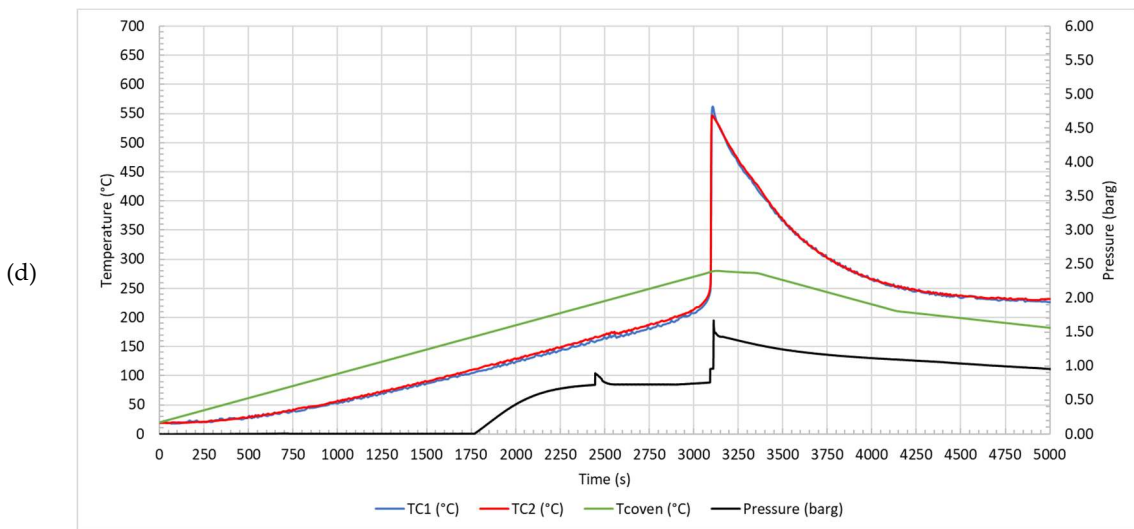
Figure 102: temperature and pressure profile for the thermal abuse test on NCA at 50 % SoC: (a) 10 °C/min in air; (b) 5 °C/min in air; (c) 10 °C/min in N2; (d) 5 °C/min in N2.
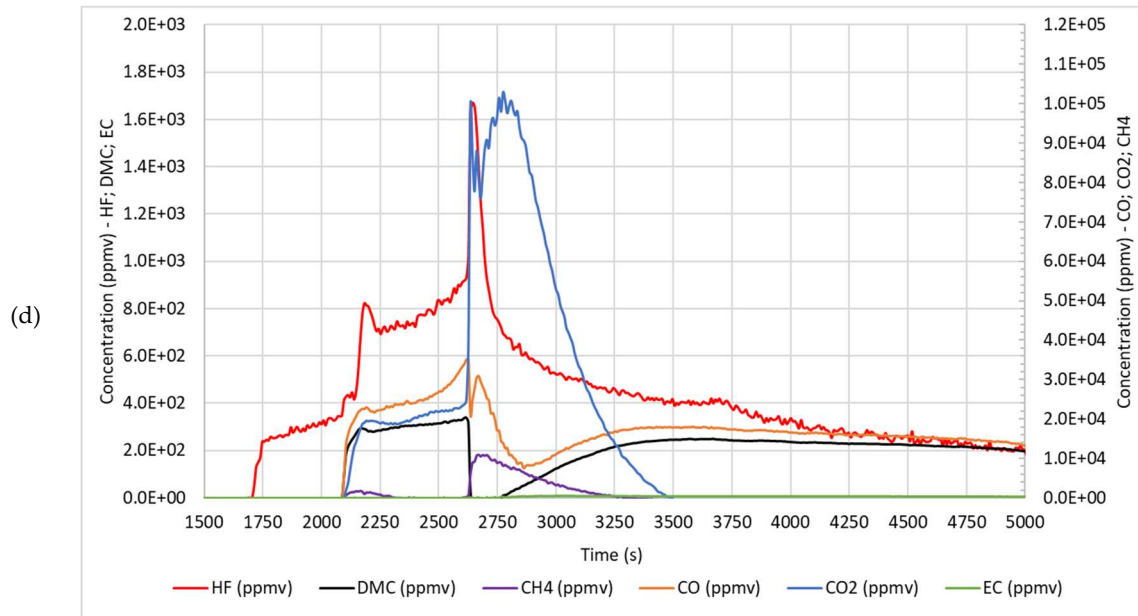
(a)

(b)

(c)

(d)

Figure 103: gas profile for the thermal abuse test on NCA at 50 % SoC: (a) 10 °C/min in air; (b) 5 °C/min in air; (c) 10 °C/min in N2; (d) 5 °C/min in N2.
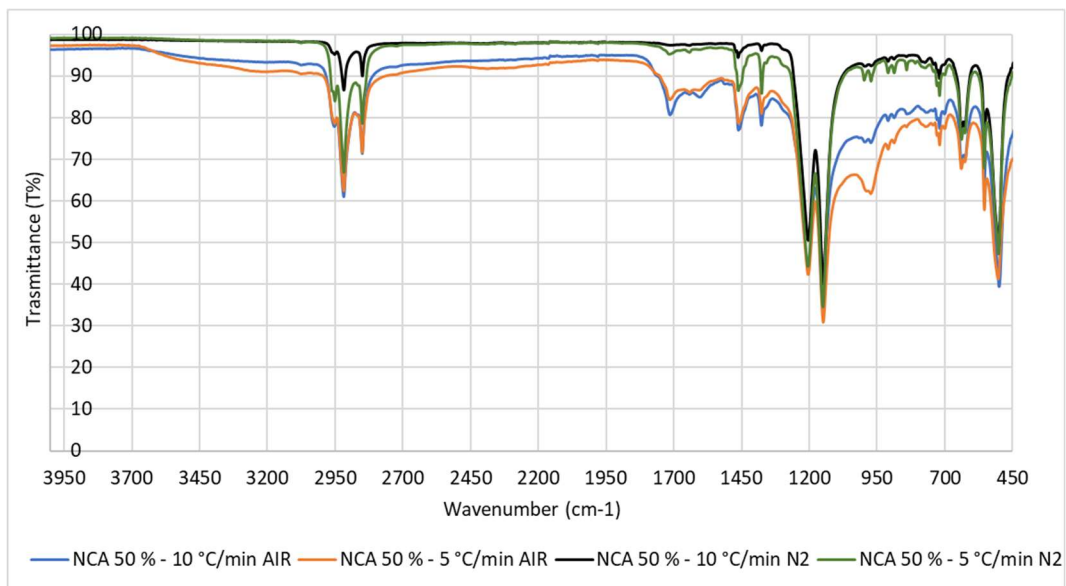

Figure 104: spectra of the condensate phase after the thermal abuse test on NCA at 50 % SoC: (blue) 10 °C/min in air; (orange) 5 °C/min in air; (black) 10 °C/min in N2; (green) 5 °C/min in N2.

Activities

Publications

S. Ubaldi, and P. Russo "Comparison between 18650 lithium-ion cells of different composition subjected to thermal abuse" Chemical Engineering Transactions, 2023, 104, pp. 49-54. doi:10.3303/CET23104009.

P. Russo, S. Ubaldi, and M. L. Mele, "Modeling of the Thermal Runaway Phenomenon of Cylindrical 18650 Li-Ion Cells," in ELECTRIMACS 2022, S. Pierfederici and J.-P. Martin, Eds., in Lecture Notes in Electrical Engineering, vol. 993. Cham: Springer International Publishing, 2023, pp. 515–527. doi: 10.1007/978-3-031-24837-5_39.

S. Ubaldi, M. Conti, F. Marra, and P. Russo, "Identification of Key Events and Emissions during Thermal Abuse Testing on NCA 18650 Cells", Energies, vol. 16, no. 7, p. 3250, Apr. 2023, doi: 10.3390/en16073250.

S. Ubaldi, C. Di Bari, A. De Rosa, M. Mazzaro, and P. Russo, "Investigation on Effective Fighting Technology for LIB Fire", Chem. Eng. Trans., vol. 91, pp. 505–510, Jun. 2022, doi: 10.3303/CET2291085.

M. L. Mele, M. P. Bracciale, S. Ubaldi, M. L. Santarelli, M. Mazzaro, C. Di Bari, and P. Russo, "Thermal Abuse Tests on 18650 Li-Ion Cells Using a Cone Calorimeter and Cell Residues Analysis," Energies, vol. 15, no. 7, p. 2628, Apr. 2022, doi: 10.3390/en15072628.

Presentations at congress

FEx23, 1st International Conference on Fires & Explosions in The Process Industry, 8-11 October 2023, Bologna, Italy. Speech "Comparison between 18650 lithium-ion cells of different composition subjected to thermal abuse" in the Fires (modelling, safety and experimental characterization) session of 9 October.

Chisa 26th International Congress of Chemical and Process Engineering, 21-25 August 2022, Prague, Czech Republic. Speech "Investigation on temperatures and gases emitted during thermal abuse tests of commercial Li-ion 18650 cells" in the Energy session of 23 May.

ISFEH10 10th International Seminar on Fire and Explosion Hazards, 22-27 May 2022, Oslo, Norway. Speech "A comparative study on the suppression capacity and the environmental impact of different extinguishing agents of lithium-ion battery fires" in the Highlighted Presentations session of 25 May.

Electrimacs 2022 14th International Conference of TC-Electrimacs Committee, 16-19 May 2022, Nancy, France. Speech "Modeling of the thermal runaway phenomenon of cylindrical 18650 Li-ion cells" in the session of 18 May.

CISAP10 International Conference on Safety & Environment in Process & Power Industry, 8-11 May 2022, Florence, Italy. Speech "Investigation on effective fighting technology for LIB fire" in the Multirisk assessment, resilience and regulatory issues session of 10 May.

Visiting period

INERIS (Institut national de l'environnement industriel et des risques), Verneuil-en-Halatte, Hauts-de-France, France, from June to September 2023.

Projects

Project report

Russo P., Bubbico R., and Ubaldi S. "Caratterizzazione delle reazioni coinvolte nel thermal runaway di celle Li-ione per lo sviluppo di un modello delle conseguenze", RdS/PTR2021/194, December 2021.

Russo P., Bubbico R., Mele M.L. and Ubaldi S. "Analisi critica dei modelli di reazione e realizzazione di un apparato sperimentale per lo studio del thermal runaway di celle Li-ione", Report RdS/PTR2020/051, April 2021.

Project funded

Evaluation of the fire risk of end-of-life Lithium-Ion Batteries (LIBs) in waste treatment plants" within the Type 1 Research Startup Projects and funded by Sapienza in the year 2022.

Master Thesis co-supervisor

Di Sabato E. "Valorizzazione degli scarti agroindustriali del kiwi con il recupero di composti bioattivi mediante l'impiego di processi a membrana e tecniche di estrazione in un modello di economia circolare" master Thesis in Chemical engineering, Sapienza, 25/05/2022.

The thesis work received two awards:

December 2023: Second Prize in the contest "Premi di Laurea in ricordo di Annalisa Romani", University of Firenze.

May 2023: First Prize in the contest "Innovative Master's Thesis", AIDIC.

Activities for credits achievement

PhD Schools

PhD School on "Educational Learning Modules on Li-ion batteries (ELMO-LION)", Online.

PhD School on "Fondamenti dei Processi di Elettrochimica e loro Applicazione e Catalisi", GRICU (GRuppo dell'Ingegneria Chimica dell'Università), July 6-9, 2022, Ischia, Italy.

PhD School on "Digitalization Tools for the Chemical and Process Industries", GRICU (GRuppo dell'Ingegneria Chimica dell'Università), March 11-12-18-19 2021, Politecnico di Milano's Cisco Webex Platform.

PhD Lessons

Topics in Chemical Engineering (4 CFU).

Topics in Chemical, Biochemical and Environmental Processes (4 CFU).

Methods of Research and Technology Transfer (3 CFU).

Topics in chemical engineering (4 CFU).

Topics in chemical, biochemical and environmental processes (4 CFU).

Methods of research and technology transfer (3 CFU).

Seminars

"Lithium-ion Battery Separator: Pore Structure Determination Using Mercury Intrusion Porosimetry", Micromeritics, Online, 23/03/2023.

"Physical Characterization Methods for Cathode Powders", Micromeritics, Online, 08/03/2023.

"Modeling and understanding of nanostructured materials: an advanced electron nanoscopy overview", Sapienza, 20/01/2023.

"e-bikes on trains/fire safety", Max Lakkonen, Institute for Applied Fire Safety Research (IFAB), Online, 05/10/2022.

"Complex chemistry models for circular economy processes and decarbonization" - Matteo Pelucchi (Dipartimento di Chimica Materiali e Ingegneria Chimica, Politecnico di Milano) – Sapienza, 04/10/2022.

"Fire Dynamics and Modeling", Prof.ssa Luisa Giuliani, Sapienza, 19/07/2022.

"Hierarchical macro-nanoporous metals for energy applications: thermal energy storage, boiling assisted heat transfer, superhydrophobic surfaces", Dr. Yarik Grosu, Sapienza, 01/06/2022.

"Electrochemical Energy Storage into the future: an Italian perspective", GISEL-INSTM, Webinar, 01/07/2021.

"Virtual Battery Exhibition", second edition, VDMA Battery Production and FVA Gmbhs, virtual conference and exhibition, 27/04/2021 - 03/05/2021.

"The Lifecycle of EV Batteries: batteries technological innovation are going to help end the ICE Age", AVERE, Webinar, 17/03/2021.

"Analisi termica, tutto quello che c'è da sapere", PerkinElmer, 12/03/2021.

"Europe's new battery regulation and its implications for the European battery value chain", EBA Virtual Meetup, 15/12/2020.

"Gestione dei rifiuti in ottica di economia circolare (parte inorganica)", Camera di commercio di Varese e Lombardia Circolare, Webinar, 02/12/2020.

Training course

Training course FT-IR, PerkinElmer Italia Spa, 08/11/2021.

Educational activities

Tutoring activities for teaching Process and Product Safety in the Chemical Industry, A.A. 2023/2024 and 2022/2023.

Tutoring activities for the Industrial and Organic Chemistry laboratory, Bachelor's degree in Chemical Engineering, A.A. 2022/2023.

PTCO introductory activities for teaching Process and Product Safety in the Chemical Industry, A.A. 2021-2022.